ISSN 1173-5996

Membrane Action in Fire Exposed Concrete Floor Systems

by

Linus C. S. Lim

Supervised by:

Professor Andre
Associate Professo

Fire Engineering Res

April 2(

This report is a reproduction of the thesis submitted in partial fulfilment for the degree of PhD (Fire) at the University of Canterbury

School of Engineering
University of Canterbury
Private Bag 4800
Christchurch, New Zealand
Phone +64-3 364-2250, Fax +64-3 364-2758
www.civil.canterbury.ac.nz

ABSTRACT

The behaviour of reinforced concrete slabs in fire conditions strongly depends on the support conditions and the interaction of the slabs with the surrounding structure. Previous research has shown that compressive restraint forces from the surrounding structure can increase the fire resistance of heated slabs, and fire resistance can also be considerably enhanced if tensile membrane behaviour is mobilised.

This study was carried out to investigate the effects of compressive membrane action and tensile membrane action on the behaviour of reinforced concrete flat slabs in fire conditions. The investigation into compressive membrane action was performed on single span, one-way flat slabs with a non-linear finite element program, SAFIR. The slabs were subjected to the ISO fire from below. The height of the line of thrust at the supports and the axial restraint stiffness were varied to model different support conditions. The investigation on tensile membrane action was performed on unrestrained two-way flat slabs and composite slabs. The study was performed with experimental fire tests and 3D finite element analyses with SAFIR, which was used to predict the behaviour of the tested slabs and also used to model different slab configurations. The experimental fire tests were carried out for six reinforced concrete and composite steel-concrete slabs on a fire resistance furnace, each of them exposed to the ISO standard fire while carrying a live load.

The SAFIR analyses of one-way flat slabs showed that their behaviour in fire conditions was very sensitive to the end support conditions and the axial restraint stiffness. The experimental tests and SAFIR analyses of two-way slabs showed that tensile membrane action significantly increased the fire resistance. The finite element predictions of the experimental fire tests with SAFIR showed good agreement.

It is concluded that one-way slabs with flexural continuity at the end supports and low axial restraint have excellent fire resistance. Compressive membrane action can increase the fire resistance of pin-supported slabs if the axial restraint stiffness is very high and if the line of thrust at the supports is located near the slab soffit.The fire resistance of unrestrained simply supported concrete slabs is significantly increased if tensile membrane action can be mobilised.

ACKNOWLEDGEMENTS

I would like to extend my appreciation and gratitude to the following people who have helped me with my research:

- My supervisors, Professor Andrew Buchanan and Associate Professor Peter Moss, for their invaluable support and guidance over the years.
- Professor Jean-Marc Franssen of the University of Liege, Belgium, for his invaluable help and advice with the SAFIR program.
- Mr. Geoff Bird of BHP NZ Steel and Mr. Charles Clifton of HERA for their enthusiasm and advice throughout this research project.
- The Board of BHP NZ Steel Limited for financially supporting me with the *BHP NZ Steel Research Scholarship*.
- The Department of Civil Engineering at the University of Canterbury for its support and excellent research facilities.
- Dimond Industries for providing the comprehensive test data of the ambient load tests on the *Hibond* slab.
- Colleen Wade, Mervyn Godkin and Paul Wong from BRANZ for their help during the experimental testing.
- The technicians from the University of Canterbury, Collin Bliss, Russell McConchie and Michael Weavers, and the technicians from BRANZ, Rik Engel and Brett Millin for their assistance during the experimental fire tests of the slabs.
- Dr. James Mackechnie for his advice during the construction of the slabs.
- My friends at the Department of Civil Engineering, particularly Ee Yii and Tony Parkes for their support, advice and company.
- Yee Thien for her patience and support during my research.
- And finally, to my dad and mum and my sisters, Lynette and Jane, for their unwavering support, patience and belief in me.

TABLE OF CONTENTS

LIST OF FIGURES

LIST OF TABLES

GLOSSARY OF TERMS

ΔL	Horizontal movement of slab
ε_σ	Stress related strain (Mechanical strain)
$\varepsilon_{c,1}$	Strain corresponding to peak stress of concrete
$\varepsilon_{c,u}$	Ultimate strain
ε_{cr}	Creep strain
ε_i	Initial strain
ε_{th}	Thermal strain
ε_{total}	Total strain
ε_{tr}	Transient thermal strain
λ	Thermal conductivity
σ	Stress
$\tilde{\sigma}$	Stress history
a_c	Thermal diffusivity
b	Slab width
c_c	Concrete cover
c_p	Specific heat
d_b	Reinforcing bar diameter
E_c	Elastic modulus of concrete
E_s	Elastic modulus of steel
f_p	Proportional stress limit
f'_c	Concrete cylinder compressive strength
f_t	Concrete tensile strength
f_y	Yield stress
G	Dead load
h	Slab thickness
k	Axial spring stiffness
$k_c(T)$	Strength reduction factor for concrete
L	Clear span
L_d	Development length of reinforcing bars
L_x	Short span of two-way slab

L_y	Long span of two-way slab
M_Δ	Moment due to axial restraint force and deflection
M^+_{fire}	Applied positive moment under fire conditions
$M^+_{fire,Red}$	Redistributed positive moment under fire conditions
M^-_{fire}	Negative moment under fire conditions
M_{th}	Moments due to rotational restraint against thermal curvature
N_x	Membrane traction in x-direction
N_y	Membrane traction in y-direction
Q	Live load
r_{load}	Load ratio
R_{cold}	Design resistance in ambient conditions
R_{fire}	Design resistance in fire conditions
s	Reinforcing bar spacing
t	Time
T	Axial force
U^*_{fire}	Design action in fire
w	Uniformly distributed load
w_u	Ultimate load capacity
x_o	Distance of line of thrust from the soffit
z_o	Distance of line of thrust from centroidal axis of slab

1. INTRODUCTION

1.1. Reinforced concrete slabs

Reinforced concrete slabs are one of the most common structural engineering elements. They are used as floors and roofs to carry vertical loads in commercial structures such as buildings and bridges. They can be constructed in several different structural forms such as solid flat slabs, waffle slabs or as composite slabs with steel decking. In addition to resisting vertical loads, their design has to take account of other environmental factors such as corrosion, harsh temperature conditions and fire.

An important design consideration for slabs in buildings is the effect of fire. The behaviour of reinforced concrete slabs under fire conditions is complex. When a fully developed fire occurs in a compartment, the floor slab above the compartment is subjected to heating due to the hot gases. In addition to preventing fire spread to the upper floors, the slab has to carry the applied loads and prevent collapse during and after the fire.

The most obvious consequence of the fire on the slab is strength degradation which may lead to collapse. Another effect of the fire which is not normally considered in typical structural design is the high thermal expansion of the slab. This will cause the surrounding structure to react against the thermal expansion and induce compressive forces in the heated slab. These compressive forces will affect the behaviour of the slab very significantly.

The behaviour of the heated slab also depends on how it is supported and built into the surrounding structure. Flexural continuity has been shown by previous researchers to increase the fire resistance of slabs as it allows load redistribution to the unheated parts of the structure. In recent years, fires in buildings and full scale fire tests have shown that slabs supported on four sides have much higher fire resistance than slabs supported at the two ends due to two way action and tensile membrane action.

1.2. Impetus of the research

The thrust of this research is to investigate two aspects which influence the behaviour of fire exposed slabs, which are compressive membrane action and tensile membrane action.

1.2.1. Compressive membrane action

The effects of compressive membrane forces in slabs subjected to fire are not well understood. The study on compressive axial restraint of fire exposed slabs started in the 1960's through experimental fire tests conducted at the Portland Cement Association (PCA) (Selvaggio et al., 1963; Issen et al., 1970). These tests showed that compressive axial restraint can increase the fire resistance of prestressed and reinforced concrete slabs. Based on these tests, the Prestressed Concrete Institute (PCI) (Gustaferro et al., 1989) developed a simple hand method to assess the effects of compressive axial restraint on the fire resistance of slabs. Currently, this remains the only available simple hand method but has not been verified by any published computer analysis. The applicability of this method to other types of floor systems other than those tested has been questioned by other researchers (Anderberg et al., 1980; Harmathy, 1993). Therefore, the behaviour of reinforced concrete slabs with different support and restraint conditions has been analysed with a special finite element program in this research project.

1.2.2. Tensile membrane action

Tensile membrane behaviour in slabs has been known for over 30 years and has remained as a scientific interest for structural engineers. Recently, several real fires in composite steel framed buildings in the U.K. have shown that tensile membrane action in composite slabs plays a very significant role in maintaining structural stability. The composite slabs, supported on unprotected beams, suffered very large midspan deflections but did not collapse. Full scale fire tests at the Cardington Large Building Test Facility have also confirmed this behaviour. This phenomenon has initiated a great deal of interest in the steel industry around the world because it has the potential to reduce the amount of passive fire protection in steel framed structures. Sophisticated computer programs have been developed to analyse tensile membrane behaviour in slabs under fire conditions. Simple design methods have been proposed by Bailey (2001) to utilise tensile membrane action in structural design for fire conditions but these have not been verified experimentally. There is a lack of data for fire

tests on two-way slabs in a controlled furnace environment. This research on tensile membrane behaviour consists of fire tests of two-way slabs in a controlled furnace environment and finite element modelling of the tested slabs.

1.3. Objectives

The objectives of this research are:

1. To determine whether axial restraint can increase the fire resistance of one-way reinforced concrete slabs.
2. To determine whether tensile membrane forces can prevent collapse of simply supported two-way slabs in fire.

1.4. Scope of research

The scope of this research covers:

Compressive restraint of reinforced concrete slabs

The slabs that are studied span in one direction and are axially restrained by the surrounding structure while being exposed to a fire from below. The slabs are heated with the ISO standard fire. Various boundary conditions are analysed to simulate the different types of support conditions in real structures. This study is conducted using plane frame analysis with the SAFIR finite element program.

Tensile membrane action of reinforced concrete slabs

The investigation into tensile membrane action in two-way slabs consists of:

1. Finite element predictions with SAFIR.
2. Experimental fire tests; six concrete and composite slabs are tested on a large furnace. The slabs span in two directions and are axially unrestrained. The slabs are loaded with a uniformly distributed load and heated with the ISO fire from below.
3. Comparison of the fire test results with the SAFIR predictions.
4. Extension of the SAFIR modelling to analyse other configurations and geometries.

1.5. Outline of thesis

In this thesis, Chapter 1 gives an introduction to the research project and outlines the objectives and scope of the research. Chapter 2 provides a review of the literature related to this research project. Chapter 3 summarises the behaviour of reinforced concrete slabs under fire conditions. Chapter 4 describes the SAFIR program and its capabilities.

Chapter 5 investigates the effects of compressive membrane action through the analyses of restrained one-way slabs with the SAFIR program.

The experimental fire tests of the two-way slabs are presented in Chapter 6. Chapter 7 discusses the verification of the shell element at ambient conditions while Chapter 8 investigates the behaviour of a two-way slab in fire conditions. Chapter 9 describes the 3D modelling of the tested slabs with SAFIR and compares the results with the experimental results. The 3D analyses of slabs with different geometries and support conditions are presented in Chapter 10. The conclusions and recommendations from this research can be found in Chapter 11. Full details of the experimental testing have been published in a separate report (Lim et al., 2002).

2. REVIEW OF FIRE BEHAVIOUR OF CONCRETE SLABS

2.1. Introduction

This chapter presents the literature relevant to this research project. This literature review covers extracts of various design codes, properties of concrete and steel at elevated temperatures, experimental studies and computer programs. The effects of membrane action and flexural continuity of the fire resistances of reinforced concrete slabs are summarised in this chapter and will be presented in detail in the next chapter.

2.2. Reinforced concrete floor systems

Reinforced concrete floor systems come in numerous different structural forms. Among some of them are solid slabs (Figure 2-1), prestressed slabs (Figure 2-2) and composite steel/concrete systems on steel decking (Figure 2-3). The choice of the type of slab for construction depends on several factors such as economy of construction, span, and strength and serviceability requirements.

Precast prestressed concrete systems and composite steel/concrete systems have increasingly become very popular forms of construction in recent decades. Precast prestressed slabs offer the advantage of speed and economy of prefabrication and the ability to reach large spans. Composite steel/concrete slabs on steel decking are popular because they can be rapidly constructed without heavy lifting machinery. In addition, the steel decking acts as permanent formwork and as external reinforcing.

Apart from resisting vertical loads, another important consideration which needs to be accounted for in the design of slabs is the effect of fire. Section 2.3 will present some recommendations by several different codes of construction to account for the effects of fire in slab design. Section 2.4 will present different design and analysis methods, ranging from simple hand methods to sophisticated computer programs.

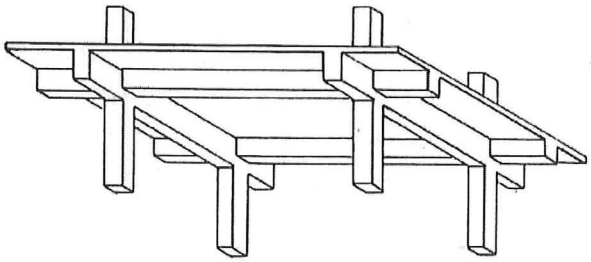

Figure 2-1: Two-way solid slab construction (Park et al., 2000)

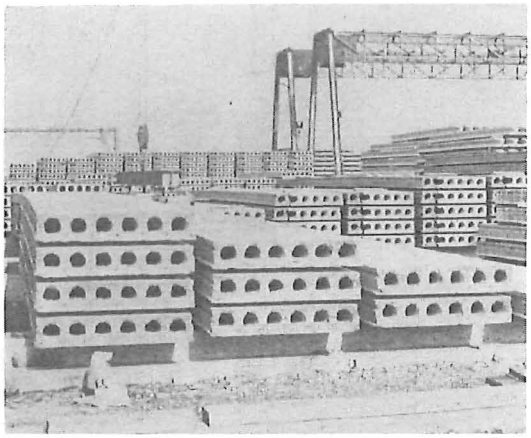

Figure 2-2: Precast prestressed hollow core slabs (FIP, 1986)

Figure 2-3: Composite steel/concrete floor system (Dimond Industries, 1997)

2.3. Code recommendations for fire design of concrete slabs

2.3.1. National codes

Most national design codes specify generic fire resistance ratings for the fire resistances of slabs, by specifying minimum thicknesses and concrete cover to the reinforcing steel. In some design codes, the fire resistance listings differentiate between normal weight and light weight concrete. Some codes further distinguish between siliceous and calcareous aggregate concrete for normal weight concrete. The fire resistances are based on exposure to the standard fire and do not usually account for the level of applied load.

2.3.2. The New Zealand Building Code

The New Zealand Building Code (BIA, 1992) specifies the fire resistance ratings of any element by three criteria: stability, integrity and insulation. Not all these criteria apply to all types of elements.

- The stability criterion applies to primary elements: e.g.: columns, beams, floors and load bearing walls. It requires the elements to maintain its load bearing capacity during a fire.
- The integrity criterion applies to secondary elements such as fire separations and floors. These elements are required to prevent the penetration of flame or hot gases during a fire.
- The insulation criterion applies to both primary and secondary elements. This criterion requires elements to prevent an average temperature rise of 140°C or a local maximum of 180°C on the unexposed face.

2.3.3. New Zealand Concrete Structures Standard (NZS 3101)

The Concrete Structures Standard NZS 3101 (NZS, 1995) requires reinforced concrete slabs to fulfil three criteria to satisfy the fire resistance requirements stated by the New Zealand Building Code (Section 2.3.2). The requirements to fulfil these criteria are:

Insulation

The insulation criteria of slabs depend on the effective thickness of the slabs and the type of aggregate of the concrete. For solid slabs, the effective thickness is the actual thickness.

Integrity

The integrity of the slab is its ability to prevent passage of flames through the slab. The standard specifies that the slab has a fire resistance rating for integrity if the requirements for both insulation and stability are met.

Stability

The code specifies a minimum concrete cover to the reinforcing steel in order to achieve a particular fire resistance rating.

The standard also provides different fire resistances for slabs with different support conditions, with reductions in thicknesses and concrete cover for slabs which are continuous or designed as two-way slabs.

2.3.4. Eurocode

Eurocode 2 (EC2, 1995) has similar fire resistance criteria to those in the New Zealand Concrete Structures Standard (NZS, 1995). Eurocode 2 also differentiates between one-way slabs and two-way slabs, and specifies different amounts of concrete cover for different aspect ratios in two-way slabs. It also gives several provisions and guidelines for continuous slabs.

Eurocode 2 provides guidelines for simple calculation methods for evaluating the strengths of fire exposed members based on the temperatures in the members. The strength of the members is calculated based on a reduced cross-section consisting of the cooler sections. It also requires proper detailing of the structural members to reduce the likelihood of spalling and other failure modes apart from bending, shear and axial loads. The Eurocode requires complex structures such as frames to be analysed with a suitable computer program.

Eurocode 2 provides details on the thermal and mechanical properties of concrete and reinforcing steel when they are subjected to elevated temperatures. Eurocode 3 (EC3, 1995) describes the behaviour of structural steel at elevated temperatures. The properties of steel and concrete at elevated temperatures based on the Eurocode (EC2, 1995; EC3, 1995) will be used in the analyses in this research project and will be explained in detail in sections 2.5 to 2.8.

2.3.5. ASTM E119 and Underwriters Laboratories

The ASTM E119 (ASTM, 1999) and the *Fire Resistance Directory* (UL, 1988) provides fire resistance ratings for various proprietary floor systems and also differentiates the ratings for restrained and unrestrained support conditions. ASTM E119 (ASTM, 1999) states that a restrained system is one in which expansion of the heated member is resisted by the external forces and an unrestrained system is one which is free to expand and rotate at its supports. ASTM E119 (ASTM, 1999) states that adequate restraint can occur in interior bays and exterior bays of framed buildings when:

> *"The space between the ends of precast units and the vertical faces of the supports, or between the ends of solid or hollow-core slab units does not exceed 0.25 percent of the length for normal weight concrete members or 0.1 percent of the length for structural lightweight concrete members."*

The above definition is schematically illustrated in Figure 2-4.

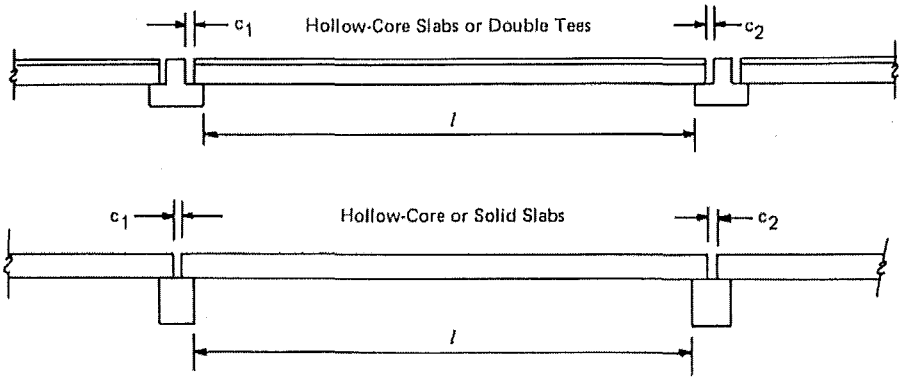

Figure 2-4: Definition of restraint by ASTM E119 (1999) for precast systems (Gustaferro et al., 1989).

The definitions of restraint in both ASTM E119 and the Underwriters Laboratories directory are confusing because they have mixed flexural continuity and axial restraint in the definitions and have not considered the effects of axial restraint and the stiffness of the supporting structure (Buchanan, 2001). A method for calculating the required stiffness of the supporting structure to provide axial restraint is presented in section 2.4.2.

2.4. Review of design methods

2.4.1. Simplified calculation methods

There are several hand methods available for the design of concrete slabs for fire exposure, depending on the type of slab and their support conditions. These different design methods are summarised by CRSI (1980), Purkiss (1996), Buchanan (2001) and Fleischmann et al. (2002) and will also be briefly presented in the following section.

The design of slabs under fire conditions is normally in the strength domain which requires the design resistance under fire conditions, R^*_{fire}, to be greater than the design action U^*_{fire}, at a particular duration of fire exposure. For simply supported slabs, only the strength reduction of the reinforcing steel needs to be considered to assess the strength of the slab. The strength of the concrete at elevated temperatures only needs to be considered in continuous slabs or where the heated concrete is in compression. Eurocode 2 (1995) recommends the calculation to be done with a reduced cross section for the fire damaged concrete and ignores the concrete in the zone above a limiting temperature. Buchanan (2001) has recommended using a limiting temperature of 500°C for large members.

The temperatures of the reinforcing steel in a fire exposed concrete member are assumed to be equal to the temperatures of the concrete at a particular distance from the fire exposed surface. From the temperatures of the heated reinforcing steel, its reduced strength can be determined from strength reduction factors such as those published in Eurocode 2. The temperatures in the concrete can be calculated with simple formulae such as those proposed by Wickström (1986), or by using published generic temperature contours for structural elements such as those by FIP (1978), Wade (1992) and the Eurocode (EC2, 1995). The applicability of these simple methods is limited to the standard fire. For fire conditions other than standard fires, the temperatures should be determined with computer programs such as TASEF (Wickström, 1979) or SAFIR (Franssen, 2002a).

2.4.2. Restrained one-way slabs

The simplified design method in section 2.4.1 does not take into account the effects of restraint. The effect of restraint is generally accepted as beneficial for the performance of flexural elements under fire conditions. However, quantifying this beneficial effect is not simple. The only available simple hand method was proposed by the Prestressed Concrete

Institute (Gustaferro et al., 1989). This method was developed based on numerous tests at the Portland Cement Association (PCA) furnace. It is a step-by-step method which incorporates design nomograms, shown in Figure 2-5. This method calculates the amount of thrust required to prevent collapse of a floor system, and the required stiffness of the surrounding structure to provide that amount of restraint.

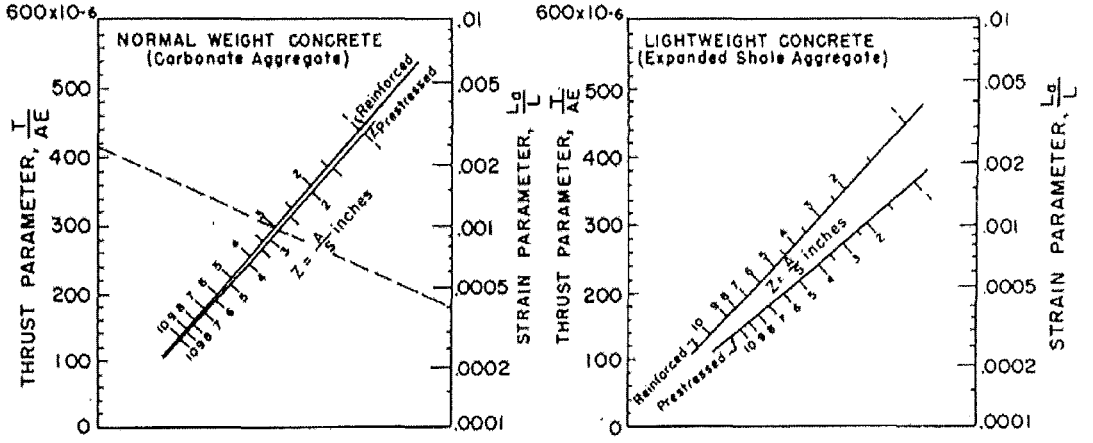

Figure 2-5: Nomograms developed by the PCI for calculating restraint of concrete floor systems (Gustaferro et al., 1989).

The Concrete Reinforcing Steel Institute (CRSI, 1980) has provided a step-by-step procedure for analysing structures exposed to fires. This procedure is directed to beams, slabs and joist systems and uses the PCI method or the "thick walled" cylinder analysis, if the floor system forms part of an interior bay. CRSI (1980) also provides generic recommendations for evaluating the position of the line of thrust at the slab supports. However, Harmathy (1993) has questioned the general applicability of these nomograms, formulas and tables.

2.4.3. Two way slabs

The ultimate load of two-way slabs at ambient conditions can be determined by yield-line theory (Park et al., 2000). Yield line theory can also be applied to slabs at elevated temperatures based on the strength reduction of the reinforcing steel due to the temperatures. However, yield-line theory does not take account of the membrane effects in the slab which has been shown by experimental tests (Bailey et al, 2000; Lim et al, 2002) to significantly increase the fire resistance of two-ways slabs. Bailey (2001) has recently developed a design method to determine the ultimate load capacity of two-way slabs at elevated temperatures, taking account of tensile membrane enhancement. Further details of the design method will be described in section 3.8.3.

2.4.4. Computer programs

This section describes some of the previous research on structures in fire using computer programs. Numerous computer programs have been developed for the analysis of steel and concrete structures under fire conditions, most of which are based on the finite element method. The existing computer programs relevant to this research project will be briefly described.

Sullivan et al. (1994) performed a review of the available computer programs for thermal and structural analysis of structures exposed to fire conditions. Among some of the earlier programs developed for 3D analysis of fire-exposed steel structures is FASBUS II (Jeanes, 1985, 1986). FASBUS II is based on the finite element method and was designed specifically to analyse the fire resistance of floor slabs in steel frames. The program uses beam elements and triangular plate bending elements to represent the frame and slab, respectively. The program uses an incremental-iterative approach to determine the displacements required to bring the structure to a point of equilibrium under the conditions imposed at each temperature. The temperature distributions in the structural members were determined with another program, FIRES-T3 (Iding et al., 1977).

Terro (1998) has developed the programs, TEMP and STRUCT, for 3D analysis of concrete structures in fire. The TEMP program is used for the thermal analysis of the structural members. The temperature distributions are then fed into the program STRUCT, to perform the structural analysis. STRUCT was developed under the shell of LUSAS (London University Structural Analysis System).

The VULCAN program has been developed at the University of Sheffield over recent years to model the 3D behaviour of composite buildings in fire (Huang et al., 1999a, 2000a). The program has been successfully verified with several experimental results of the Cardington full scale fire tests (Huang et al., 1999, 2000, 2001a). Some of the results of the VULCAN modelling will be briefly discussed in section 3.8.4.

SAFIR (Franssen, 2002a) is a non-linear finite element program which was developed at the University of Liege, Belgium, and is based on an earlier program, CEFICOSS. It consists of thermal and structural analysis components integrated into a single program. The thermal

analysis component is used to determine the temperature distributions of the structural members which are used in the structural analysis. SAFIR's structural analysis capabilities include 2D and 3D analysis of steel, concrete and composite members and can account for geometrical and material non-linearity. The SAFIR program will be used for the analyses of this research and will be described in further detail in chapter 4.

Other programs have also been developed by Wang (1994) and Jiang (2001) to perform 3D modelling of concrete slabs under fire conditions. Commercial general-purpose finite element packages, such as ABAQUS have also been used to model structures in fire (O'Callaghan et al., 2000; Lamont et al., 2001; Gillie et al., 2002; Moss et al., 2002). However, users have reported severe convergence problems using such commercial programs due to the non-linear nature of the analysis which includes the non-linear material properties and geometric non-linearity associated with large deflections (Gillie et al., 2001). Gillie et al. (2001) have developed a program, FEAST, which integrates with ABAQUS to analyse slabs at high temperatures with shell finite elements. The program uses a different analysis approach from other programs such as VULCAN and SAFIR. It uses the stress-resultant method in order to avoid the convergence problems associated with the non-linear material models (Gillie et al., 2001). Elghazouli et al. (2001) have developed a program ADAPTIC to model 3D steel frames using the grillage method.

Most of these programs are not user-friendly enough to be used as design tools and are typically used for research purposes. Graphical user interfaces have been developed in some programs, such as Supertemp-Calc (Anderberg, 1991), to simplify their use. Nevertheless, these programs require proper user knowledge and understanding of the structural behaviour in order to interpret the results correctly.

2.5. Thermal properties of concrete

2.5.1. Thermal conductivity

Thermal conductivity is the ability of a material to conduct heat and is defined as the ratio of heat flux to the temperature gradient. It represents the uniform flow of heat through concrete of unit thickness over a unit area subjected to a unit temperature difference between the two opposite faces (Bažant et al., 1996). Harmathy (1970) has calculated the thermal conductivities of four concretes in oven-dry conditions and the results of the calculations are shown in Figure 2-6. The four different concretes are referred to as Concretes 1, 2, 3 and 4 which were assumed to contain quartz, anorthosite and two lightweight shales, respectively. The thermal conductivity of normal weight concrete with siliceous and calcareous aggregates has been shown to lie between the theoretical lines of Concrete 1 and 2 in the above figure (Harmathy et al., 1973). For lightweight concrete, the results lie in between the lines of Concrete 3 and 4.

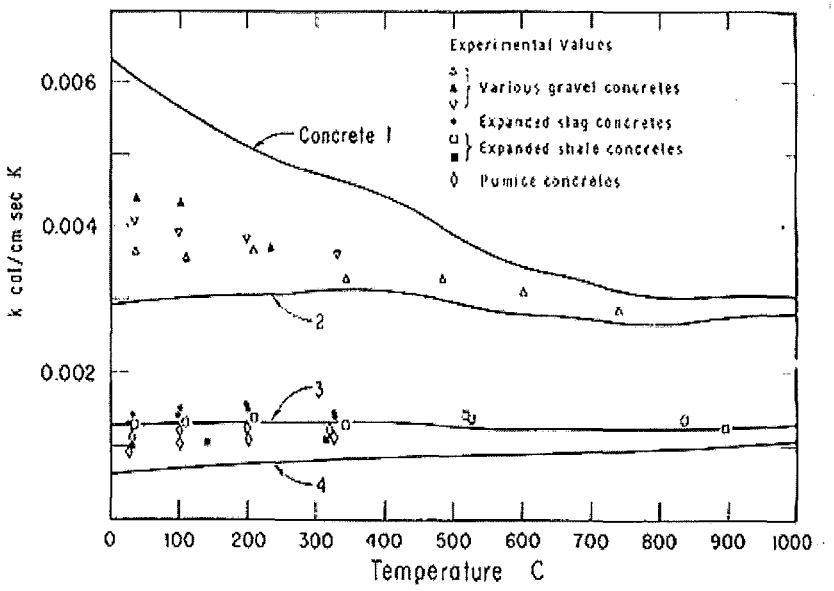

Figure 2-6: Thermal conductivities of various concretes (Harmathy, 1970).

The thermal conductivity of siliceous aggregate concrete based on the Eurocode (EC2, 1995) is shown in Figure 2-7 and is defined as:

$$\lambda = 2 - 0.24\,T/120 + 0.012\,(T/120)^2 \text{ (W/mK)} \qquad \text{For } 20°C < T \leq 1200°C$$

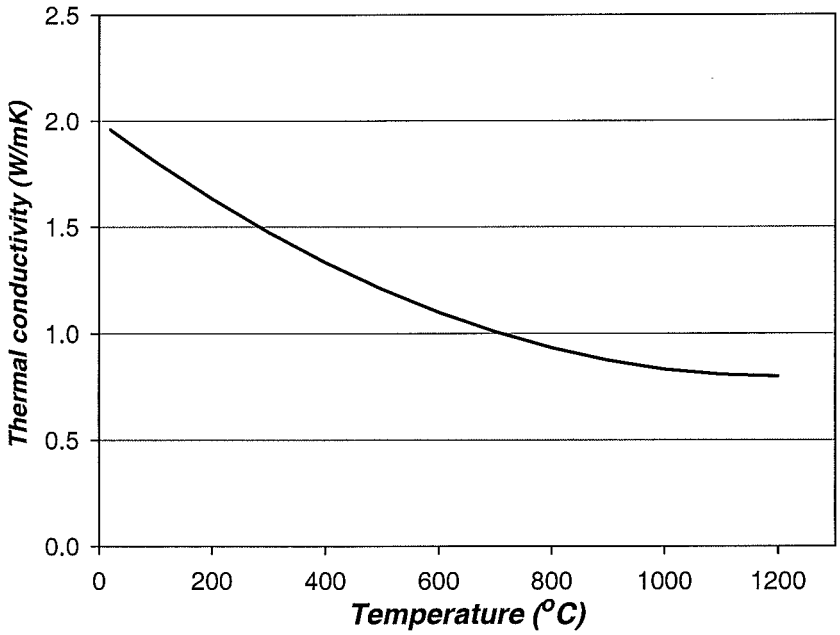

Figure 2-7: Thermal conductivity of siliceous aggregate concrete according to EC2 (1995).

2.5.2. Thermal diffusivity

Thermal diffusivity represents the rate of temperature change in a material and is used to calculate temperature distributions under transient conditions. Thermal diffusivity is expressed as $k/(\rho c_p)$, where k is the thermal conductivity, ρ is the material density and c_p is the specific heat of the material. The thermal diffusivity of normal and lightweight concrete is shown in Figure 2-8. The graph shows that the thermal diffusivity of the normal-weight concrete reduced by approximately 50 percent when the temperatures increased from ambient to 650°C. The reduction is approximately 25 percent for lightweight concrete. The thermal diffusivity of siliceous concrete, a_c, according to EC2 (1995) is considered to be independent of the concrete temperature and is taken as 0.69×10^{-6} m^2/s.

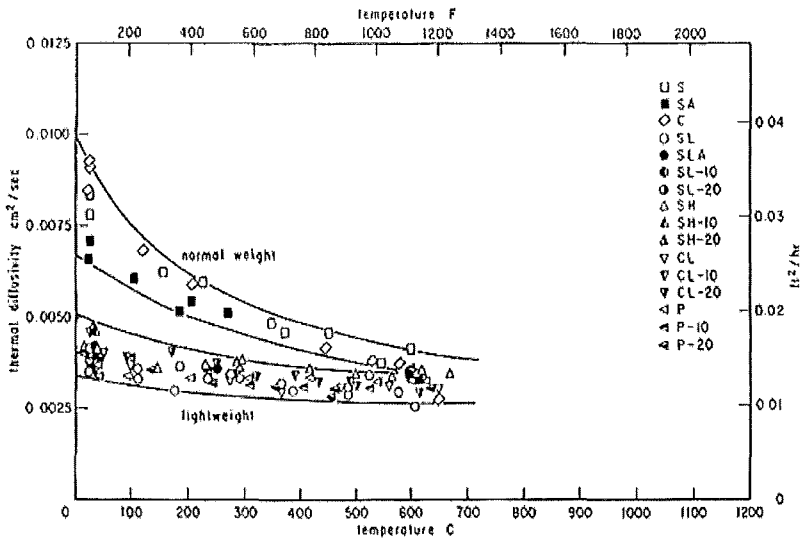

Figure 2-8: Thermal diffusivity of concrete (Harmathy et al., 1973).

2.5.3. Specific heat

The specific heat of a material is the amount of heat per unit mass which is required to change the temperature of the material by one degree. It is defined as (Harmathy et al., 1973):

$$c_p = \left(\frac{\partial H}{\partial T}\right)_p$$

where H= enthalpy, T= temperature and P=pressure. The specific heat of concrete is not very sensitive to either the aggregate type or the mix proportions but is very dependent on the moisture content. The effects of temperature on experimentally determined specific heats of various concretes are shown in Figure 2-9.

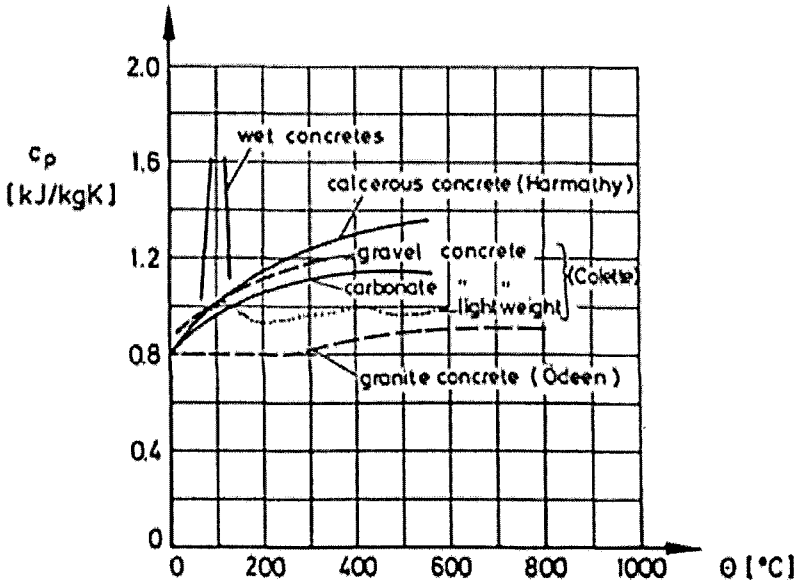

Figure 2-9: Effect of temperature on specific heats of different concretes (Schneider, 1985)

The specific heat of concrete with siliceous aggregates as a function of temperature according to EC2 (Figure 2-10) follows the equation below:

$$c_p = 900 + 80\,T/120 - 4(T/120)^2 \text{ (J/kgK)} \qquad \text{For } 20°C < T \leq 1200°C$$

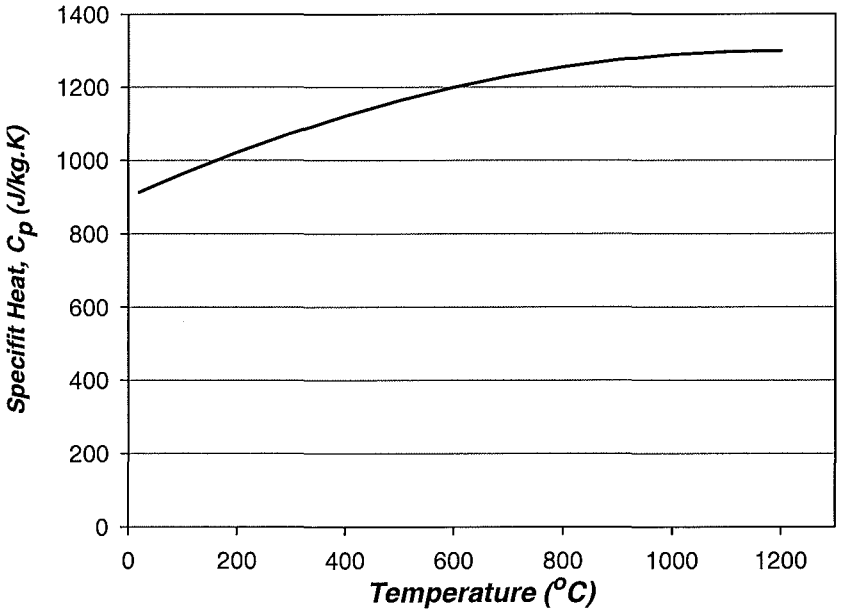

Figure 2-10: Specific heat of siliceous aggregate concrete according to EC2 (1995).

2.5.4. Thermal expansion of concrete

Concrete is an isotropic material and exhibits thermal expansion when it is subjected to a temperature change. Since it is an isotropic material, the thermal strain is the same in all directions. Stresses develop in concrete structures due to the non-uniform thermal expansion, which in turn leads to cracking and large scale spalling (Bažant et al., 1996).

i) Thermal expansion of aggregates

The thermal expansion of aggregates has a very important effect on the changes in the volume of concrete as they normally occupy between 65 percent and 80 percent of the total volume (Bažant and Kaplan, 1996). The main factor affecting the coefficient of thermal expansion of the aggregates is the percentage of silica present in them. Rocks with high contents of silica, such as quartzite and sandstone, have high coefficients of thermal expansion, ranging between 9×10^{-6} and 10×10^{-6} $°C^{-1}$ (Browne, 1972). The mineral composition of the rocks also plays an important part in their thermal expansion.

ii) Thermal expansion of hardened cement paste

At temperatures up to about 300°C, thermal shrinkage of the paste competes with thermal expansion to give a net expansion. At temperatures greater than 300°C, the thermal shrinkage exceeds the expansion and gives a net shrinkage. This competition of expansion and contraction affects the microstructure of the paste and its physical and mechanical properties (Bažant et al., 1996). The shrinkage at elevated temperatures has been attributed to the loss of moisture from the cement paste. When the cement paste is heated, the free pore water is driven out and if the temperatures are severe enough, the solid paste matrix will be dehydrated (Cruz et al., 1980).

iii) Thermal expansion of concrete

There is almost a linear relationship between the thermal expansion of the aggregates and the concretes made from them (Cruz et al., 1980; Bažant et al., 1996).

Figure 2-11 shows the thermal expansion for different types of concrete (Harmathy, 1993). Their data labels as shown in the diagram below are summarised in Table 2-1. Generally, expansion increases with temperature at temperatures greater than about 150°C to 300°C. Concretes made with siliceous aggregates show the highest expansion coefficients.

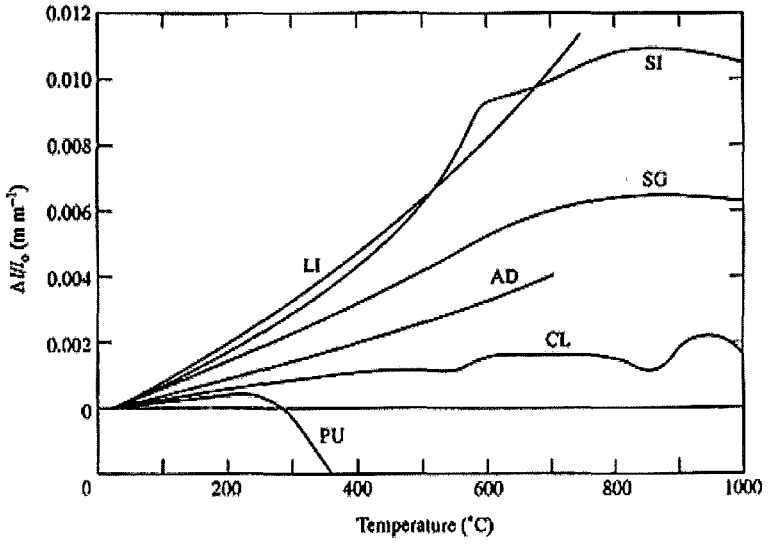

Figure 2-11 : Dilatometric curves for three normal weight concretes and three lightweight concretes (Harmathy, 1993).

Data label	Aggregate
LI	Limestone
SI	Siliceous rock
AD	Andesite
SG	Expanded slag
CL	Expanded clay
PU	Pumice

Table 2-1: Data labels for Figure 2-11 for concrete with different aggregates.

Khoury et al. (1985a, 1985b and 1986) have showed that there is considerable contraction for concrete under load compared with the free thermal strains (FTS). These contractions are referred to as "load-induced thermal strain" (LITS). The total thermal strain under load, expressed as a function of temperature (T) and stress (σ) is the difference between the FTS and the LITS.

$$\text{i.e.: Total thermal strain} = \text{FTS}(T,0) - \text{LITS}(T,\sigma)$$

The FTS of concrete is a non-linear function of temperature dominated by the aggregate type and content. The main contributor to LITS is the interaction with transient phenomena in drying creep. The equation above is valid only at low temperatures. At higher temperatures, there is a rapid increase in the rate of thermal expansion. This is due to the transformation of the aggregates and the failure of the bond between aggregate and cement paste (Blundell et al., 1976).

Concrete made of siliceous aggregates expand progressively up to about 700°C. There is a marked rate of expansion at about 570°C due to the conversion of α-quartz to β-quartz (Harmathy et al., 1973). This will cause micro-cracking with failure of the bond between the cement and the aggregate. At temperatures greater than 700°C, the concrete starts to contract. This contraction is due to the contraction of hardened cement paste and the dehydration and decomposition of the calcium silicate hydrates in the cement paste.

The coefficient of thermal elongation of concrete with siliceous aggregates according to EC2 (1995) is expressed as:

$$\Delta L/L_c = (-1.8 \times 10^{-4}) + (9 \times 10^{-6} T) + (2.3 \times 10^{-11} T^3) \qquad \text{For } 20°C < T \leq 700°C$$

$$\Delta L/L_c = (-14 \times 10^{-3}) \qquad \text{For } 700°C < T \leq 1200°C$$

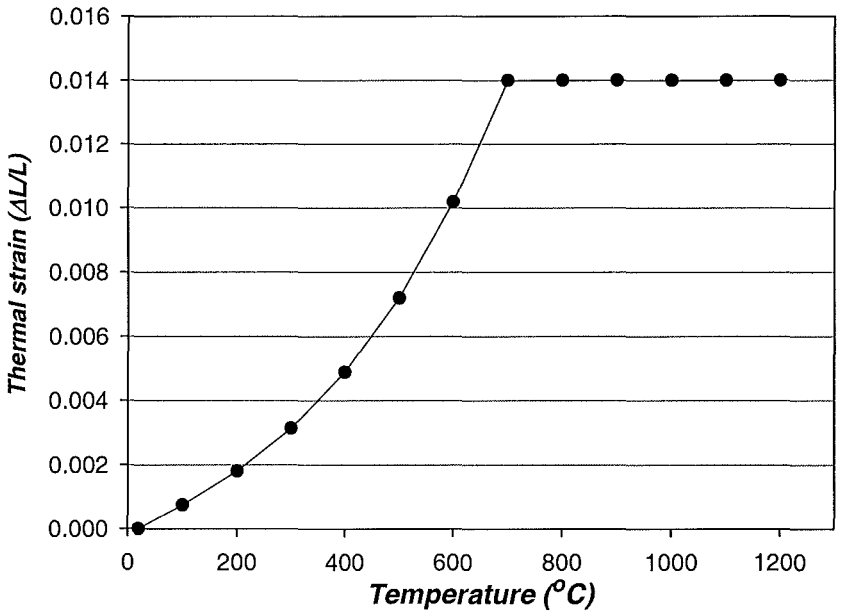

Figure 2-12: Thermal elongation of siliceous aggregate concrete according to EC2 (1995).

2.5.5. Spalling

Spalling is the separation of concrete from the surface in concrete structures when they are exposed to high temperatures. This phenomenon can seriously affect the fire resistance and stability of the structure and has been categorised into three categories (Institution of Structural Engineers, 1975):

- General or destructive spalling: This form of spalling is violent which usually occurs during the early stages of heating. It can result in extensive damage or complete destruction of the concrete element.
- Local spalling: This consists of surface pitting, aggregate splitting or corner break-off.
- Sloughing off: This is a progressive form of breakdown of the concrete elements after prolonged heating. Surface layers of concrete are separated from the main body of the member by long irregular cracks and cavities.

The factors that influence the occurrence of spalling are (Malhotra, 1984):

- The moisture content of the concrete.
- The number of faces exposed to heating.
- The level of stress in the concrete. High compressive stresses increase the probability of spalling and promote explosive spalling.
- The quantity of reinforcement in the member and the thickness of the member.
- The rate of heating of the structure. Rapid heating encourages spalling more than slow rates of heating.
- Cracking due to aggregate expansion, internal cracks or reinforcement expansion can also cause spalling.

Spalling can be prevented by:

- Reducing the moisture content.
- Reducing the compressive stresses.
- Constructing with lightweight concrete.
- Providing additional reinforcement.
- Incorporating polypropylene fibres into the concrete.

2.6. Thermal properties of steel

2.6.1. Thermal conductivity

The thermal conductivity of steel depends mainly on the amount of alloying elements and on the heat treatment. The thermal conductivity of steel λ_a for EC3 (1995) is determined from the following equations:

$$\lambda_a = 54 - 3.33 \times 10^{-2} T \text{ (W/mK)} \qquad \text{For } 20°C \leq T < 800°C$$

$$\lambda_a = 27.3 \text{(W/mK)} \qquad \text{For } 800°C \leq T \leq 1200°C$$

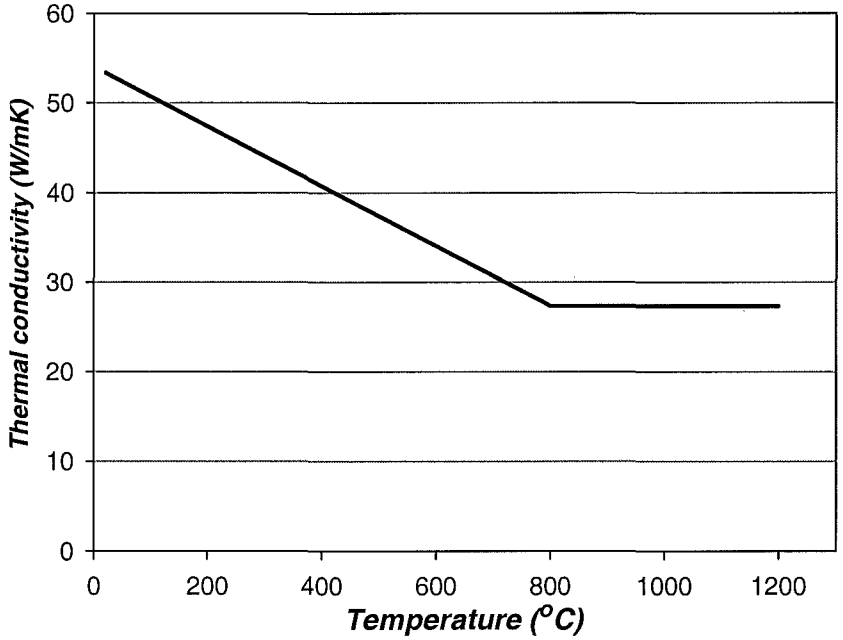

Figure 2-13: Thermal conductivity of steel as a function of temperature according to EC3 (1995).

2.6.2. Specific heat

The Eurocode (EC3, 1995) expresses the specific heat of steel c_p according to the following equations and is shown graphically in Figure 2-14.

$$c_p = 425 + 7.73 \times 10^{-1} T - 1.69 \times 10^{-3} T^2 + 2.22 \times 10^{-6} T^3 \text{ (J/kgK)} \qquad \text{For } 20°C \leq T < 600°C$$

$$c_p = 666 + 13002/(738\text{-}T) \times 9 \text{ (J/kgK)} \qquad \text{For } 600°C \leq T < 735°C$$

$$c_p = 545 + 17820(T\text{-}731) \times 10 \text{ (J/kgK)} \qquad \text{For } 735°C \leq T < 900°C$$

$$c_p = 650 \text{ (J/kgK)} \qquad \text{For } 900°C \leq T < 1200°C$$

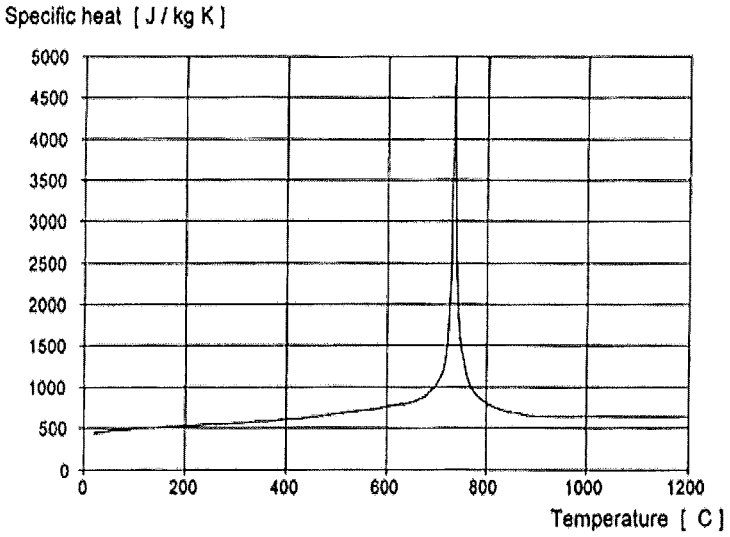

Figure 2-14: Specific heat of steel according to EC3 (1995).

2.6.3. Thermal expansion

The coefficient of thermal expansion of steel at room temperatures is about $11.4 \times 10^{-6} m^{-1} C^{-1}$ (Harmathy, 1993). The thermal expansion of various carbon and low- alloy steels depends on the carbon content and the heat treatment. The thermal elongation of structural and reinforcing steel according to EC3 (1995) is taken as:

$$\Delta L/L_s = (-2.416 \times 10^{-4}) + (1.2 \times 10^{-5} T) + (0.4 \times 10^{-8} T^2) \quad \text{For } 20°C < T \leq 750°C$$

$$\Delta L/L_s = 11 \times 10^{-3} \quad \text{For } 750°C < T \leq 860°C$$

$$\Delta L/L_s = (-6.2 \times 10^{-4}) + (2 \times 10^{-5} T) \quad \text{For } T > 860°C$$

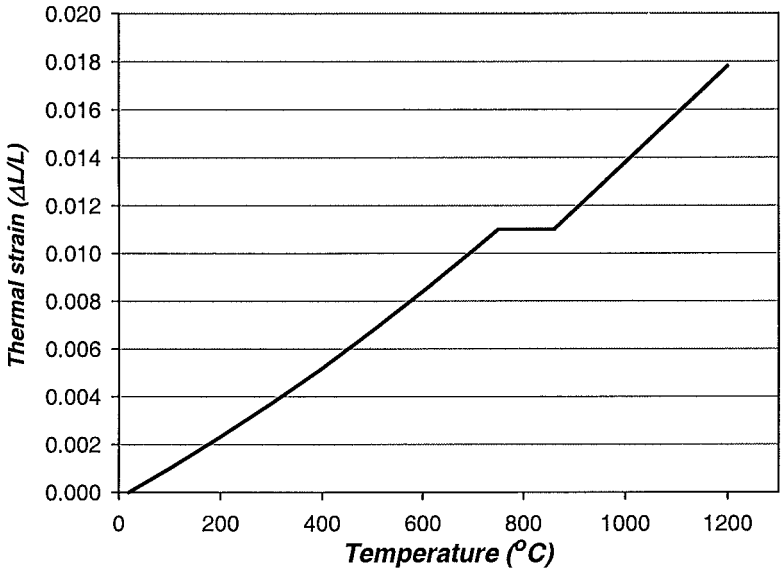

Figure 2-15: Thermal elongation of structural and reinforcing steel according to EC3 (1995).

2.7. Mechanical properties of concrete

2.7.1. Constitutive Law

Anderberg et al. (1976) proposed the constitutive law for concrete under transient high temperature conditions. The following equations in this section have been extracted from Anderberg et al. (1976), unless stated otherwise.

The constitutive law for concrete under high temperatures may be expressed as follows:

$$\varepsilon_T = \varepsilon_{th}(T) + \varepsilon_\sigma(\tilde{\sigma}, \sigma, T) + \varepsilon_{cr}(\sigma, T, t) + \varepsilon_{tr}(\sigma, T)$$

where ε_T = Total strain

ε_{th} = Thermal strain

ε_σ = Instantaneous, stress-related strain

ε_{cr} = Creep strain

ε_{tr} = Transient strain

T = Temperature

σ = Stress

$\tilde{\sigma}$ = Stress history

t = Time

2.7.2. Total strain, ε_T

The total strains of concrete in compression and under heating are illustrated in Figure 2-16. It shows the strains of specimens being stressed at different levels and heated to failure at a constant rate of 5°C/min. The thermal expansion is significantly reduced under stress and for a stress equal to about 40 percent of the ambient temperature strength, the thermal expansion is fully compensated by the stress induced deformation. As the temperature approaches a critical value, the compressive strain increases rapidly and finally failure occurs.

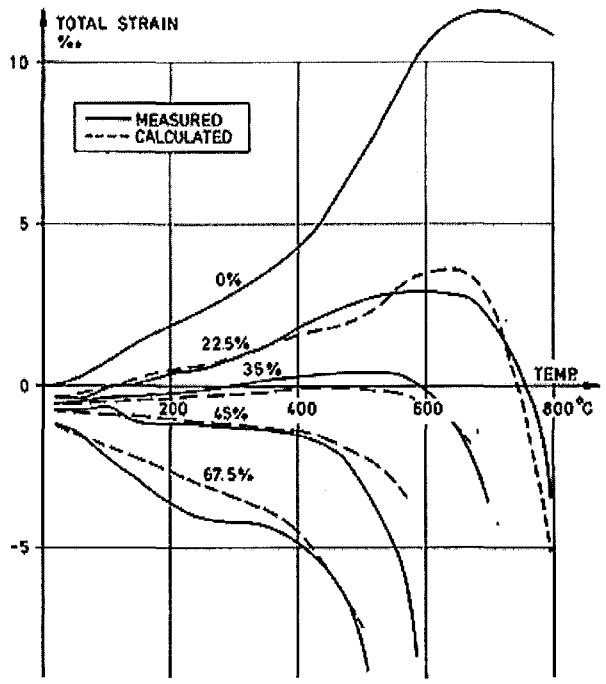

Figure 2-16: Deformation upon heating (5°C.min^{-1}) for different levels of compressive stress (percent of strength at ambient conditions) (Anderberg et al., 1978).

2.7.3. Thermal strain, ε_{th}

The thermal strain is the unrestrained thermal expansion of concrete. This component of the total strain has been explained in 2.5.4.

2.7.4. Instantaneous, stress-related strain, ε_{σ}

The stress-related strain is based on the concept that at every state, a specified stress-strain relation is valid for the material. The stress-strain behaviour is affected by two main factors: the current temperature and the prehistory of the stress. Anderberg et al. (1976) and Schneider (1985) have investigated the stress-strain relationships of concrete under elevated temperatures. The influence of temperature on the stress-strain curve is shown in Figure 2-17.

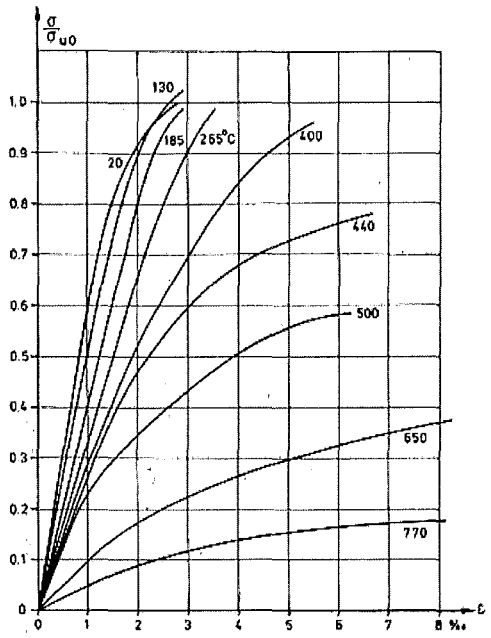

Figure 2-17: Stress-strain relations at different temperatures (Anderberg et al., 1976).

The high-temperature stress-strain relationship will be considerably different if the concrete is subjected to stress during the period of heating. Its deformability will be smaller and a slight increase in strength is observed. The general description of the stress-strain relation is shown in Figure 2-18.

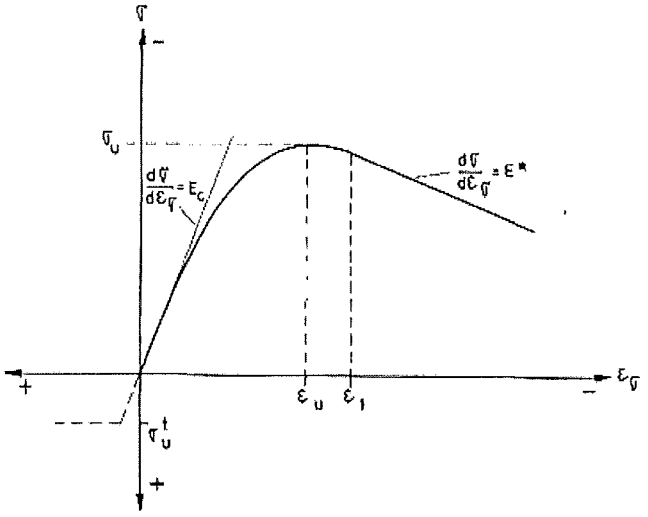

Figure 2-18: Stress strain relation of concrete (Anderberg et al., 1976).

The three parameters used to describe the envelope in Figure 2-18 are:

E_c = slope of rising branch

σ_u = compressive strength at the current state

ε_u = strain corresponding to maximum stress

E^* = slope of descending branch

The Eurocode (EC2, 1995) specifies the strength of uniaxial stressed concrete by a set of stress-strain relationships with a shape specified in Figure 2-19.

Range I of the model is expressed as

$$\sigma_c(\theta) = f_c(\theta) = \left[\frac{\varepsilon_c(\theta)}{\varepsilon_{c1}(\theta)} \times \frac{3}{2 + \left(\frac{\varepsilon_c(\theta)}{\varepsilon_{c1}(\theta)}\right)^3}\right];$$

$$\frac{f_c(\theta)}{f_c(20°C)} \text{ and } \varepsilon_{c1}(\theta) \text{ to be chosen according to table A.1 of EC2 (1995)}$$

Range II: For numerical purposes a descending branch should be adopted. Linear and non-linear models are permitted.

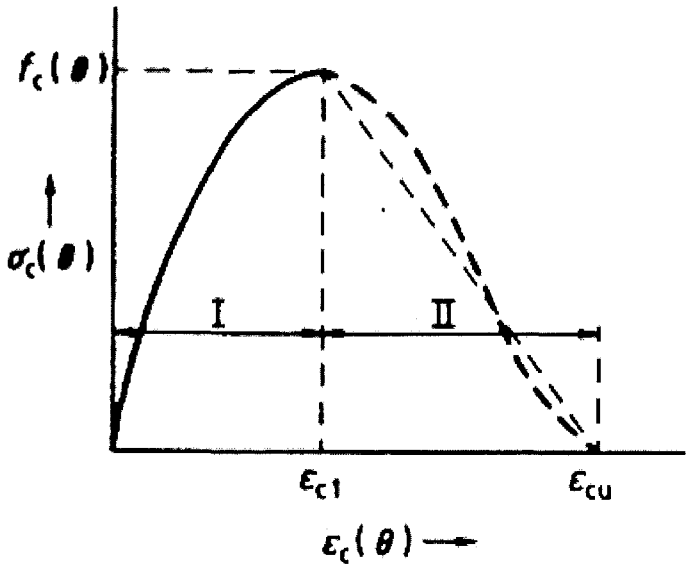

Figure 2-19: Model for compression stress-strain relationships for siliceous and calcareous concrete at elevated temperatures (EC2, 1995).

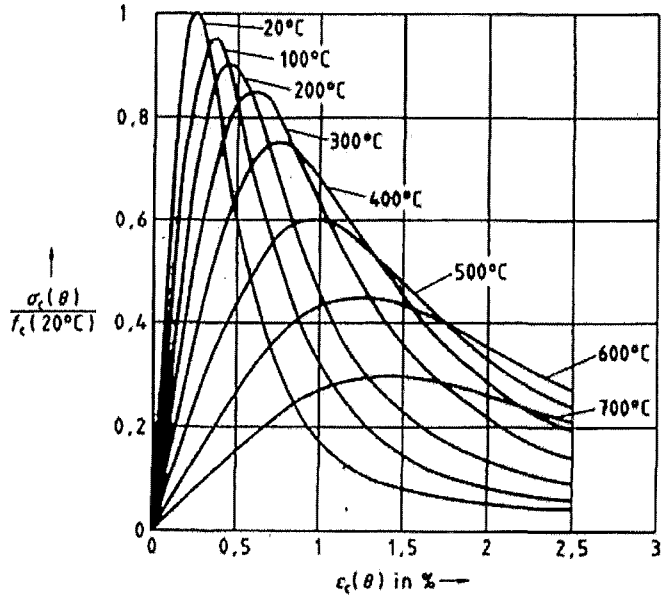

Figure 2-20: Stress strain relationships of siliceous aggregate concrete under elevated temperatures according to EC2 (1995).

2.7.5. Creep Strain, ε_{cr}

Figure 2-21 shows the variation of creep strain with time. It shows that when the temperature and stress vary with time, the evaluation of the creep strain is based on the strain hardening principle. The creep strain is not explicitly defined in the Eurocode and is implicitly included in the stress-strain relationships of the concrete.

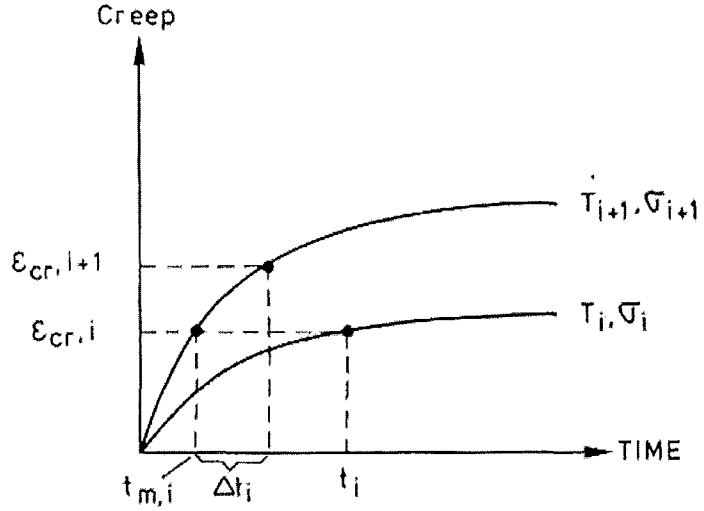

Figure 2-21: The principle of strain hardening for creep (Anderberg et al., 1976).

2.7.6. Transient strain, ε_{tr}

Anderberg et al. (1976) discovered that transient effects were important when they performed tests under constant stress and varying temperature and measured the resultant strain. Transient strain develops under stress when the temperature is increased. This strain has been shown to be irrecoverable and occurs only on the first heating of concrete.

Khoury et al. (1985a, 1985b and 1986) have explained the phenomenon of transient strain more clearly. Transient creep originates in the cement paste and is restrained by the aggregates. It provides the concrete some thermal stability by accommodating the considerable thermal incompatibility that develops between the aggregate and the cement paste during first heating. Transient creep causes a significant relaxation and redistribution of thermal stresses. Transient strain cannot be measured and must be determined from the remaining four strain components (Anderberg et al., 1976). Anderberg et al. (1976) have found that for siliceous aggregate concrete, the transient strain is of opposite sign to the thermal strain at temperatures below 500°C (which is the temperature at which the quartz phase change occurs).

$$\varepsilon_{tr} = \varepsilon_T - \varepsilon_{th} - \varepsilon_\sigma - \varepsilon_{cr}$$

Figure 2-22 shows the relative order of magnitude for the different components of strain, and shows that transient strain is a very important component.

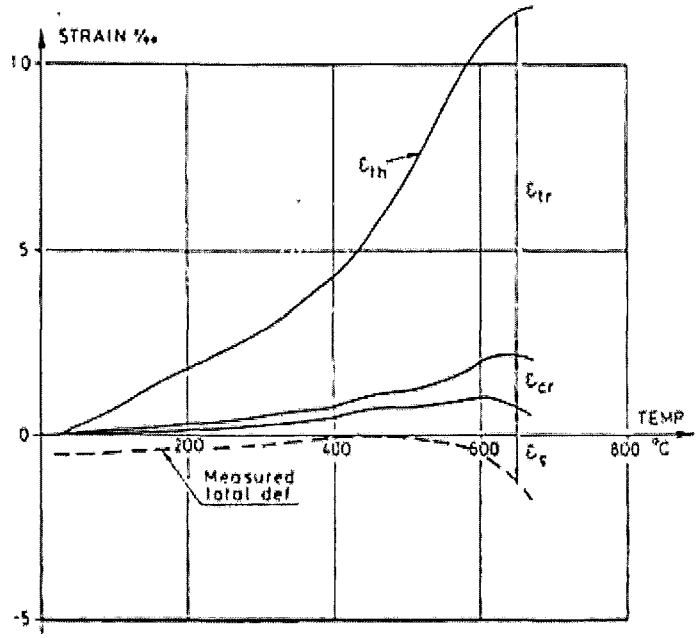

Figure 2-22: Relation between different strain components (Anderberg et al., 1976).

2.7.7. Modulus of Elasticity

The reduction of modulus of elasticity with temperature for various types of aggregates is shown in the figure below. The reduction of the modulus of elasticity is due to the breakage of bonds in the microstructure of the cement paste when the temperatures increase. Another cause of the reduction of the elastic modulus is the increase of rapid short-time creep.

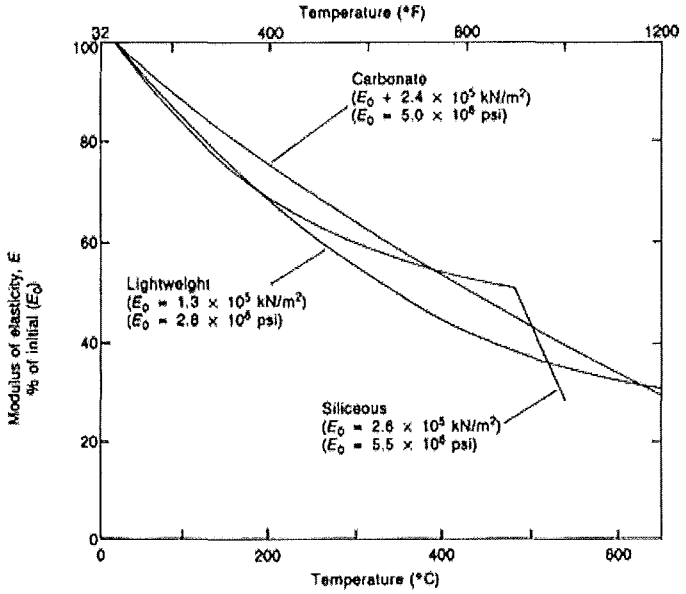

Figure 2-23: Reduction of modulus of elasticity for various types of aggregates with temperature (Bažant et al., 1996).

The type of aggregate used in the concrete has a strong influence on the reduction of the elastic modulus (Schneider, 1985). Although the data obtained from various investigators vary significantly, generally it is found that aggregates that are more compatible and chemically stable such as limestone exhibit a lower reduction (refer to Figure 2-23). Siliceous aggregates show a significant drop in the elastic modulus at temperatures above 500°C.

2.7.8. Compressive strength

The compressive strength of concrete is a function of temperature. The effects of the type of aggregate on the compressive strength of specimens that were unstressed during heating are shown in Figure 2-24. Figure 2-24 shows that from 450°C, the concrete with siliceous aggregates exhibited the greatest amount of strength reduction compared with that of calcareous or lightweight aggregates (Schneider, 1985). This trend was also observed when the concrete was stressed to $0.4\sigma_c$ and tested hot and to unstressed residual strengths.

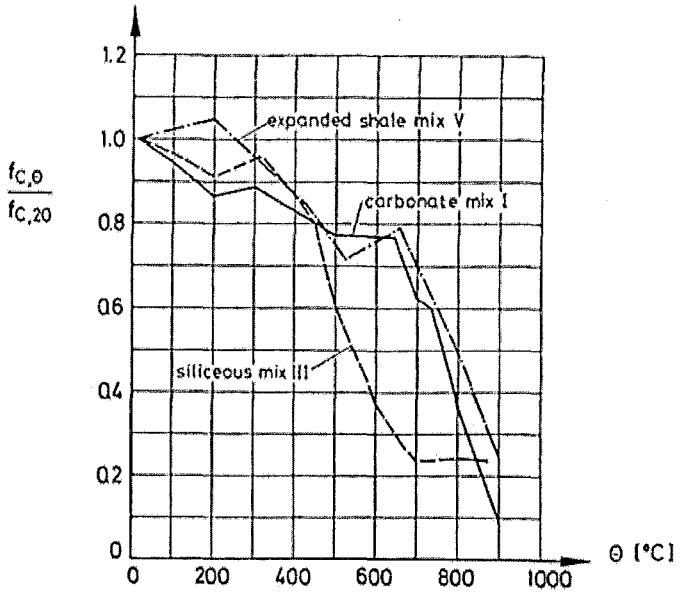

Figure 2-24: Variation of concrete compressive stress for different aggregates (Schneider, 1985).

The concrete compressive strength is also very dependent on the stress level (Schneider, 1985). The definitions of *unstressed, stressed* and *unstressed residual* shown in Figure 2-25 are explained below and have been directly extracted from Bazant et al. (1996).

1. *Unstressed: The loaded specimen was heated to the required temperature and then loaded to failure while hot.*
2. *Stressed: The specimen was loaded in compression and heated to the required temperature. The load was then increased until failure occurred.*
3. *Unstressed residual: The unloaded speciment was heated to the required temperature and then allowed to cool slowly to room temperature. After seven days, the specimen was loaded to failure in compression.*

The "stressed strength" of concrete is evidently higher than the "unstressed strength", as shown in Figure 2-25. The stress level itself has little effect on the ultimate strength as long as $\alpha > 0.20$, where α is the ratio of the applied stress to the uniaxial compressive strength at ambient conditions. It becomes significant once $\alpha < 0.20$.

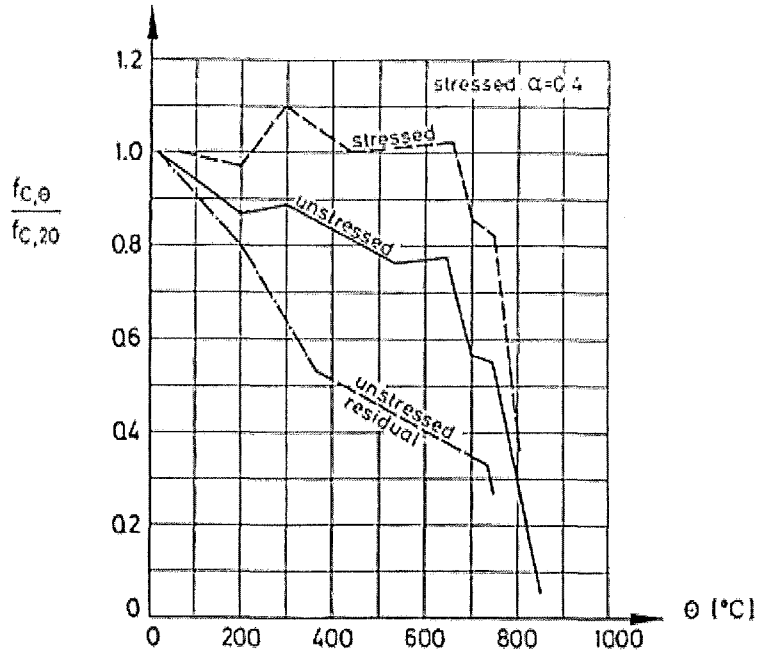

Figure 2-25: Stressed and unstressed calcareous concrete during heating (Schneider, 1985).

The Eurocode (EC2, 1995) expresses the reduction of the characteristic compressive strength of concrete by the coefficient $k_c(T)$.

$$f_c(T) = k_c(T).\ f_c(20°C)$$

The strength reduction coefficient $k_c(T)$ for siliceous aggregate concrete as obtained from EC2 is shown in Figure 2-26 and follows the equations:

$k_c(T) = 1.0$	for $20°C \leq T \leq 100°C$
$k_c(T) = (1600-T)/1500$	for $100°C < T \leq 400°C$
$k_c(T) = (900-T)/625$	for $400°C < T \leq 900°C$
$k_c(T) = 0$	for $900°C < T \leq 1200°C$

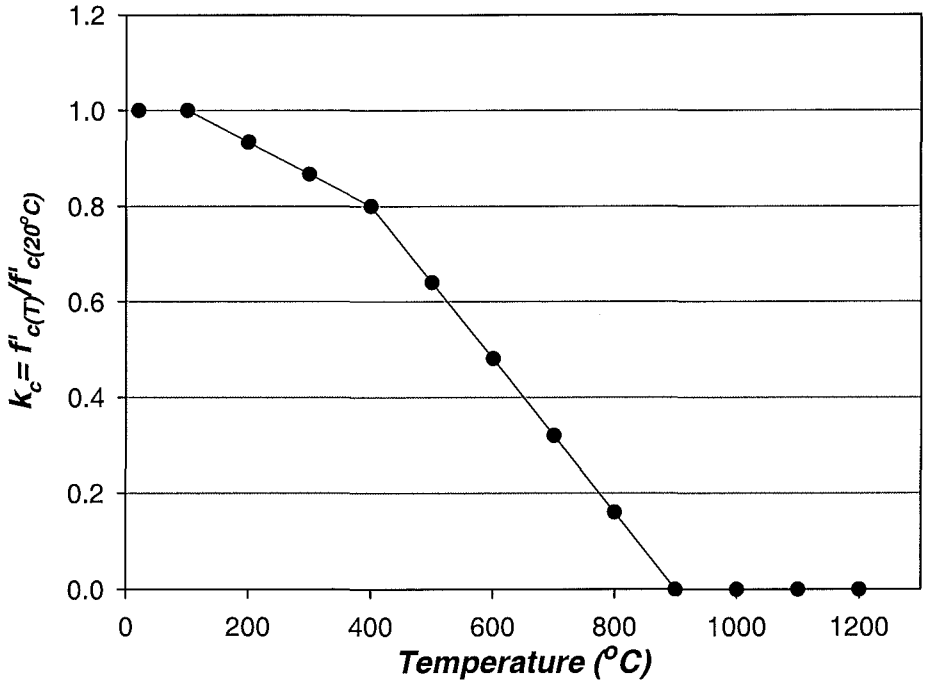

Figure 2-26: Coefficient $k_c(T)$ accounting for the decrease of compressive strength (f_c) for siliceous aggregate concrete at elevated temperatures according to EC2 (1995).

2.7.9. Biaxial properties of concrete at elevated temperatures

The compressive strength of concrete under biaxial stress at elevated temperatures is greater than its uniaxial strength. Figure 2-27 shows the typical failure envelope of concrete under biaxial stress from tests conducted by Ehm et al. (1985). The tests showed brittle, explosive failures of the concrete at ambient conditions and at 300°C. At 150°C and at temperatures above 450°C, the concrete failed in a more ductile and gradual manner. The tests showed that the mechanical properties of the concrete were very sensitive to the loads applied in the second axis whereby the ultimate strength of the concrete increased even under very low load levels in the second axis. The stress ratio, defined as the ratio between the principal stresses σ_1/σ_2, which gives the highest biaxial strength, increases to higher values with increasing temperature. The failure envelope changes from an elliptical shape at low temperatures to an egg-shaped envelope at higher temperatures.

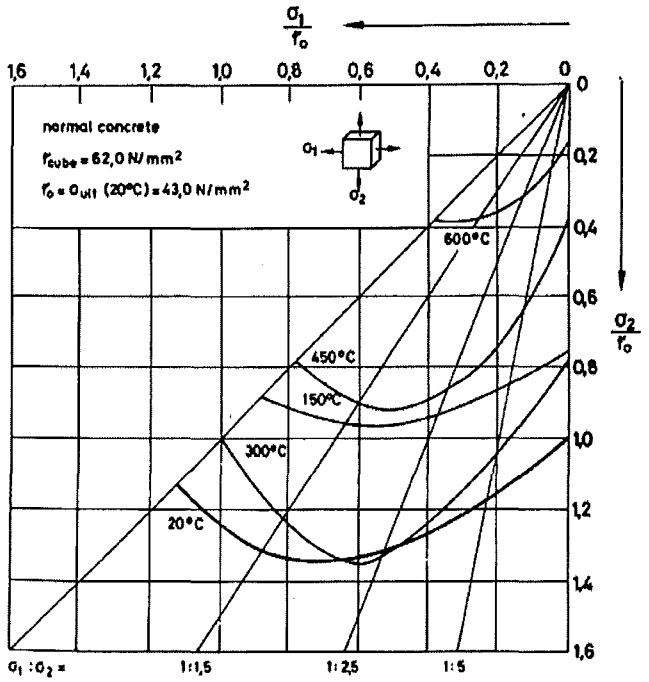

Figure 2-27: Biaxial strength envelopes of normal weight concrete at high temperatures (Ehm et al, 1985).

Figure 2-28 and Figure 2-29 show the concrete stress-strain relationships at high temperatures with biaxial stress ratios of zero (σ_1:σ_2 = 1:0) and unity (σ_1:σ_2 = 1:1), respectively. The graphs show that the principal strain, ε_2, at failure changes from positive under uniaxial loading to compression under equal biaxial loading. The strains, ε_1 and ε_2, which correspond to the ultimate strength, increase considerably with increasing temperature. Khennane et al. (1992a and 1992b) have developed a plasticity model for the behaviour of concrete at high temperatures. Their model was developed based on the experimental data from Ehm et al. (1985).

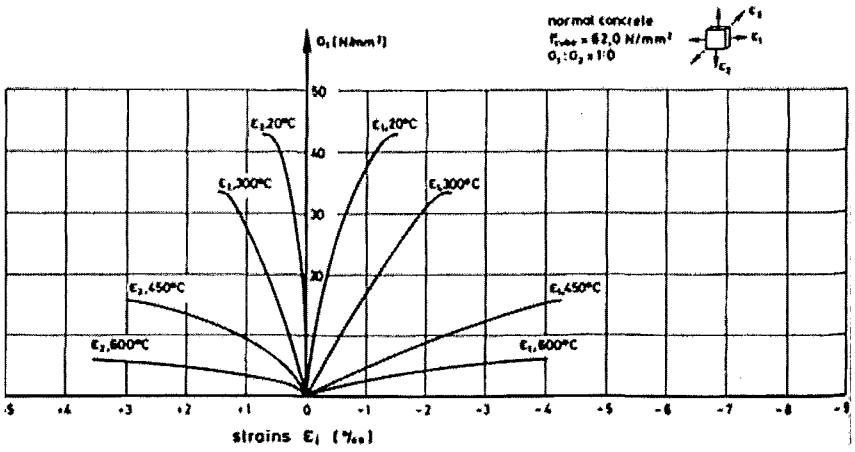

Figure 2-28: Concrete stress-strain relationships at high temperatures with biaxial stress ratios of zero.

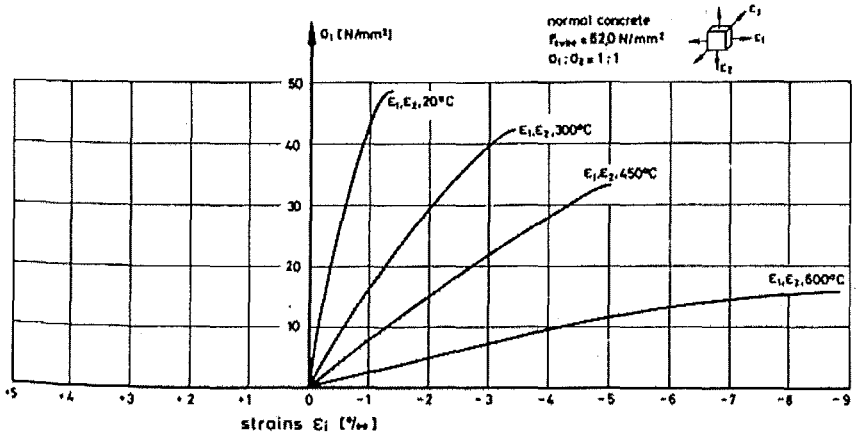

Figure 2-29: Concrete stress-strain relationships at high temperatures with biaxial stress ratios of unity.

2.8. Mechanical properties of steel

For steel sections, the thickness is such that their temperatures across the section may be considered uniform. Therefore, the problem encountered with concrete on heating rates is not as important.

2.8.1. Components of strain

The deformation of steel at elevated temperatures is given by the total strain as shown below. The transient strain component does not exist for steel.

$$\varepsilon_T = \varepsilon_{th}(T) + \varepsilon_\sigma(\tilde{\sigma}, \sigma, T) + \varepsilon_{cr}(\sigma, T, t)$$

where ε_{th} = Thermal strain

ε_σ = Instantaneous, stress-related strain

ε_{cr} = Creep strain

T = Temperature

σ = Stress

$\tilde{\sigma}$ = Stress history

t = Time

2.8.2. Thermal strain, ε_{th}

The thermal strain of steel is the thermal expansion of steel when it is heated up. Its behaviour under elevated temperatures is explained in section 2.6.3.

2.8.3. Stress-related strain, ε_σ

Typical stress–strain curves for structural steel elements at elevated temperatures at various temperatures as obtained by Harmathy et al. (1970) are shown in Figure 2-30. The graph shows that the yield plateau becomes less noticeable with temperature rise and disappears at about 300°C. After a slight decline at moderately elevated temperatures, the ultimate strength of the steel increases in the temperature range of 180°C to 370°C. Upon further temperature increase, the yield strength of the steel declines steadily.

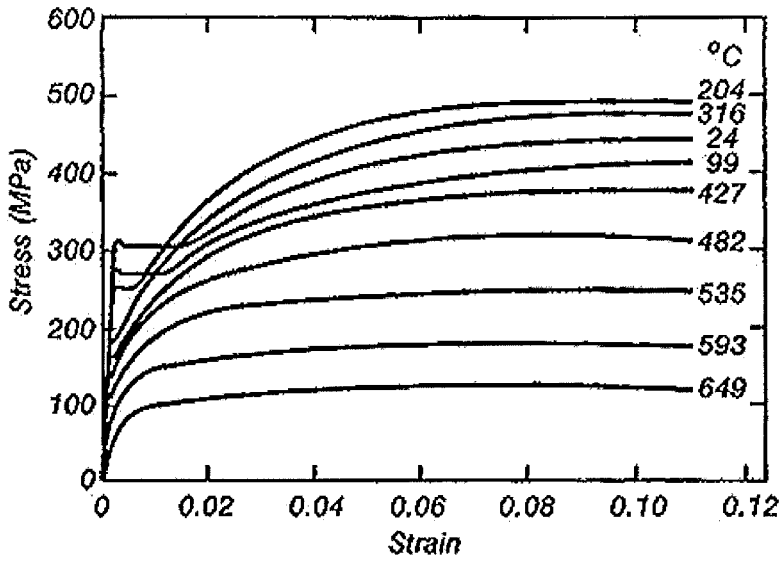

Figure 2-30: Stress strain curves at various temperatures for structural steel (Harmathy el al, 1970).

The stress-strain curve of steel according to EC3 (1995) at a given temperature is defined by three parameters.

i) The slope of the linear elastic range $E_s(T)$,

ii) The proportional limit $\sigma_{spr}(T)$, and

iii) The maximum stress level $f_y(T)$.

Figure 2-31 describes the stress-strain relationships of hot-rolled structural and reinforcing steels at elevated temperatures.

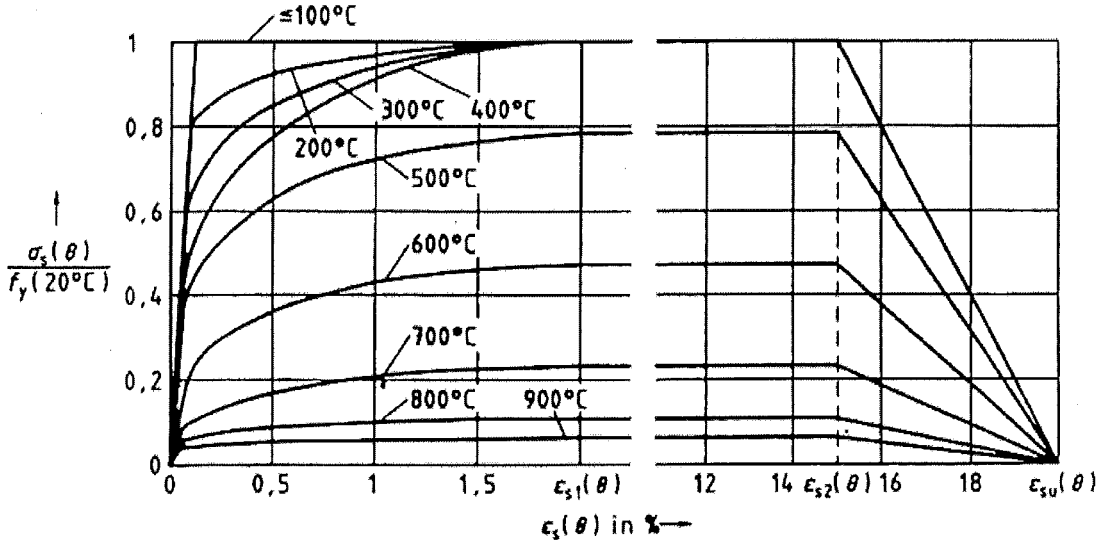

Figure 2-31: Stress strain relationships of hot rolled steel at elevated temperatures according to EC2 (1995).

2.8.4. Creep strain, ε_{cr}

Creep strain in structural steel elements only become significant at temperatures over 400-500°C. Kirby et al. (1988) have shown that the creep is highly dependant on the temperature and stress level of the steel. If a steel member of a particular stress level reaches a certain temperature, the member becomes plastic and runaway failure occurs (Figure 2-32).

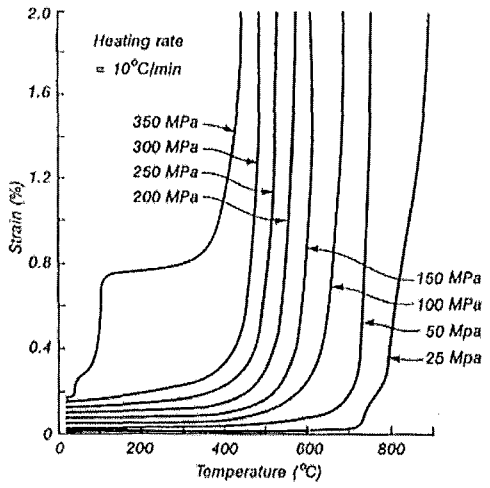

Figure 2-32: Creep of steel in tension (Kirby et al., 1988).

2.8.5. Modulus of Elasticity

The reduction of the modulus of elasticity with temperature for various types of steel is shown in Figure 2-33 below. Its reduction trend is similar to that of the yield strength. Harmathy (1993) has made a comparison by various researchers on the effect of temperature on various types of steel.

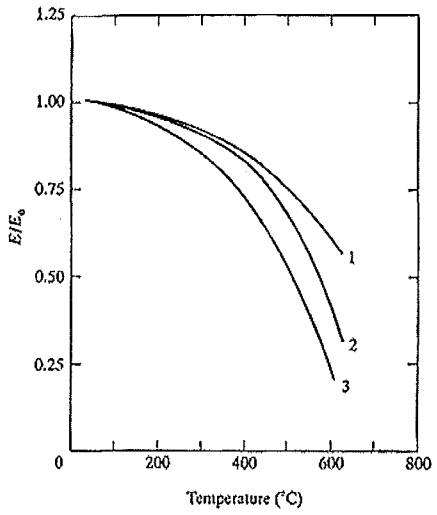

Figure 2-33: Variation of modulus of elasticity of steel with temperature 1) Structural steel, 2) Prestressing steel, 3) Reinforcing steel. (Harmathy, 1993).

2.8.6. Ultimate and yield strengths

Most normal construction steels have a well-defined yield strength at normal temperatures. However, this yield point disappears at elevated temperatures (Buchanan, 2001). The reduction of the ultimate and yield strengths of steel is shown in Figure 2-34 below. There is a significant amount of scatter shown with various curves recommended by various researchers. The vertically hatched and the horizontally hatched area represent the ultimate strength and yield strength of the steel. Curve *a* is the curve recommended by The Institution of Structural Engineers (1975) for both yield strength and ultimate strength.

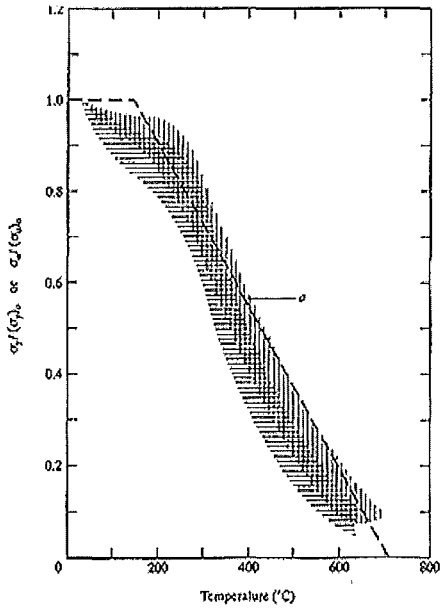

Figure 2-34: Ultimate and yield strengths of hot-rolled steel (Harmathy, 1993).

The variation of the elastic modulus, proportional limit and yield strength of hot-rolled steel and cold-drawn steel according to EC2 (1995) is shown in Figure 2-35 and Figure 2-36, respectively. The stress strain relationships may be applied to the steel in both tension and in compression. The stress-strain relationships account for, in an approximate manner, the effect of high temperature creep. The material model is applicable only for heating rates similar to those appearing under standard fire conditions.

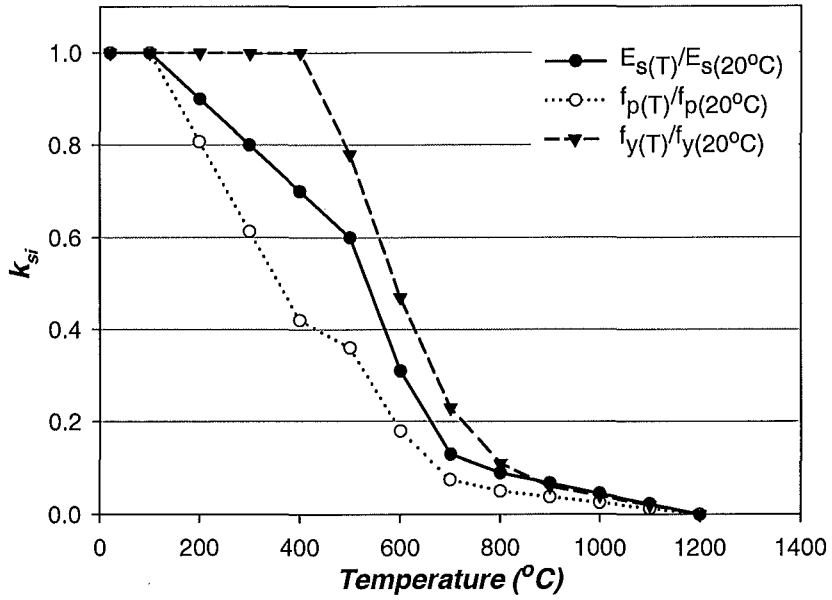

Figure 2-35: Parameters of stress-strain relationships of hot-rolled steels at elevated temperatures according to EC2 (1995).

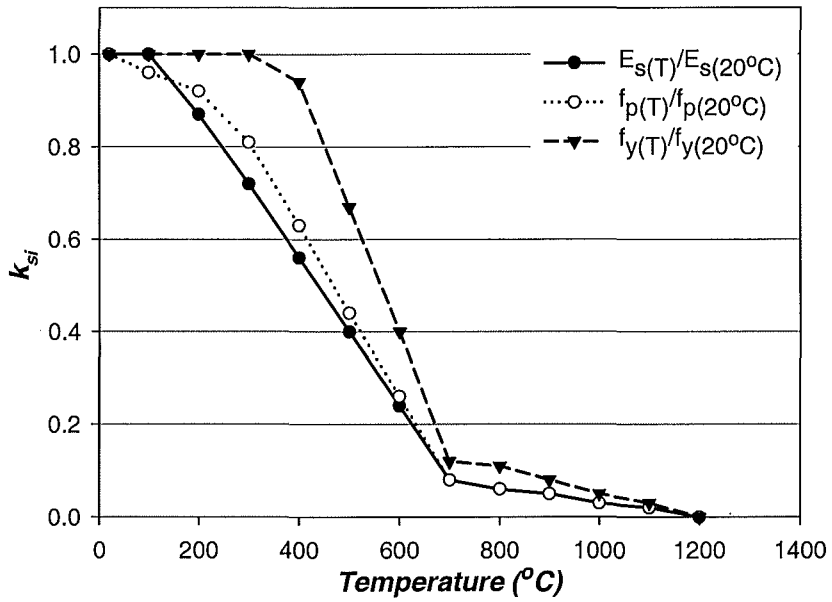

Figure 2-36: Parameters of stress-strain relationships of cold-worked steels at elevated temperatures according to EC2 (1995).

3. THE BEHAVIOUR OF REINFORCED CONCRETE SLABS UNDER FIRE CONDITIONS

3.1. Introduction

The behaviour of a slab exposed to high temperatures is highly dependent on its support conditions and the surrounding structure. This chapter discusses the effects of flexural continuity and tensile and compressive membrane action on the structural fire resistance of reinforced concrete slabs. This chapter also summarises the previous research by other researchers.

A few real fires in the past decades will be highlighted in section 3.2 to show the fire behaviour of slabs in multi-storey buildings. Section 3.3 will discuss the behaviour of slabs at ambient conditions due to the effects of compressive axial restraint and tensile membrane action. Section 3.4 briefly describes the behaviour of an unrestrained one-way slab exposed to fire while section 3.5 explains the fire behaviour of slabs subjected to compressive axial restraint. Sections 3.6 and 3.7 discuss the effects of flexural continuity and catenary action in slabs, respectively. Finally, the effect of tensile membrane enhancement on slabs subjected to fire exposure is presented in section 3.8.

3.2. Fires in multi-storey buildings

3.2.1. Introduction

This section presents several key incidents of fires in multi-storey buildings which emphasises the fire behaviour of slabs in multi-storey buildings.

3.2.2. Kimberley-Clark building

Vecchio et al. (1990a) have described a fire which occurred in the Kimberley-Clark building in 1978. The building was a four-storey concrete building used for paper manufacturing. The third storey of the building was used to store drums of nickel pellets and had been loaded up to 43kPa prior to collapse even though the floor was designed for a live load of 6kPa. At the time of the collapse, an explosion and a major fire occurred in the lower stories of the structure. It was not clear as to whether the collapse was caused by the fire and explosion or that the collapse triggered the explosion. The structural system consisted of a reinforced

concrete flat slab system with six bays in each direction. The floor slabs were 200mm thick. The third floor collapsed down to the basement level. The fire which occurred after the collapse of the third floor, raged for 48 hours due to the high fuel loads in the floors below the collapsed floor.

Vecchio et al. (1990a) have performed 2D analyses of the structure under fire conditions. The analyses were conducted with a program, TEMPEST, which can account for geometric and material non-linearity and material degradation at elevated temperatures and membrane forces in the slabs. Their analyses showed that the collapse could have been due to a fire in the floors below which weakened the overloaded floor. Their analyses also showed that the increased load carrying capacity of the slabs was attributed to the compressive membrane forces in the slab. The slabs would collapse only if they were allowed to elongate considerably. The elongation was resisted by the surrounding structure which resulted in high compression forces in the slab.

3.2.3. Kellogg Factory

The Institution of Structural Engineers and the Concrete Society (1975) and Cembureau and FIP (1979) have reported a fire which occurred in 1967 in the Kellogg factory in Manchester, U.K. The fire occurred on the ground floor of the five storey reinforced concrete factory. The fire burned for eight hours before it was brought under control. The fuel load was 1600 tonnes of paper and wax. The beams and slabs had 40mm and 20mm cover, respectively. The floors above the fire compartment which were supported on the concrete beams suffered very large vertical deflections and deformed as a two-way slab as shown in Figure 3-1 and Figure 3-2. Proper anchorage of the slab reinforcing to the surrounding structure and the adjacent beams enabled the slab to sustain large deflections. The slabs possibly developed tensile membrane action while they were supported on the beams which hung in a catenary.

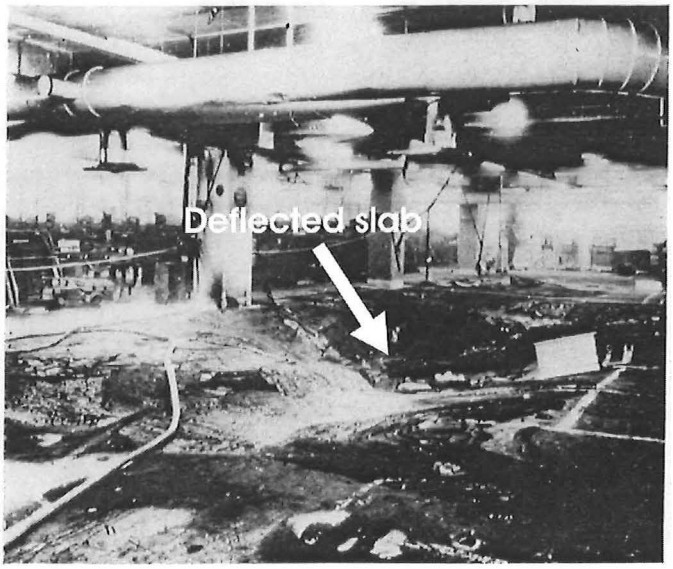

Figure 3-1: View of the floor above the fire (Institution of Structural Engineers and the Concrete Society, 1975).

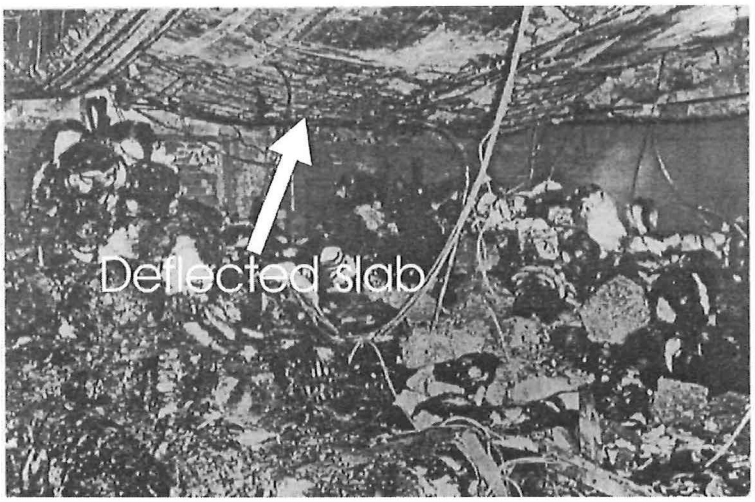

Figure 3-2: View of floor over fire (Cembureau and FIP, 1979).

3.2.4. Broadgate

In 1990, a fire occurred in a 14-storey office building on the Broadgate development in the U.K. (Newman et al., 2000). The office building was partly completed, with the active and passive fire protection features to the steelwork incomplete. The floor system was constructed with composite trusses and beams supporting a composite floor slab. The fire temperatures were estimated to have reached in excess of 1000°C.

The unprotected beams were distorted with permanent deflections as large as 270mm with local buckling of the bottom flanges and webs near their supports. The steel truss which spanned 13.5m, suffered deflections as large as 552mm and the supported composite floor

suffered deflections as large as 600mm. In various places, the reinforcement had failed and the steel decking debonded from the concrete. This is thought to be due to steam release of the concrete and restraint against thermal expansion. The catenary action of the deformed beams allowed membrane action to develop in the slabs.

Some of the unprotected steel columns deformed and shortened by 100mm, but the structure did not exhibit signs of collapse as the loads were redistributed to the stronger and cooler parts of the structure. Most of the connections did not fail despite suffering large deformations.

3.2.5. One Meridian Plaza

In 1991, a very severe fire occurred in the One Meridian Plaza in Philadelphia (Routley et al. 1991). The building was a 38 storey high rise office building built with a steel frame and a composite steel-concrete floor system. The structural steel was protected with spray-on fireproofing material. The columns had a 3-hour fire rating while the beams and floor system had a 2-hour rating. The fire occurred on the twenty-second storey and burned for 19 hours. The beams and floor systems suffered very large deflections but did not collapse, as shown in Figure 3-3. The fire demonstrated the beneficial effects of high levels of redundancy on the fire resistance of steel frame structures.

Figure 3-3: Large vertical deflections of the steel beams and floor system after the fire in the One Meridian Plaza (Routley et al., 1991).

3.3. Slab behaviour at ambient temperature

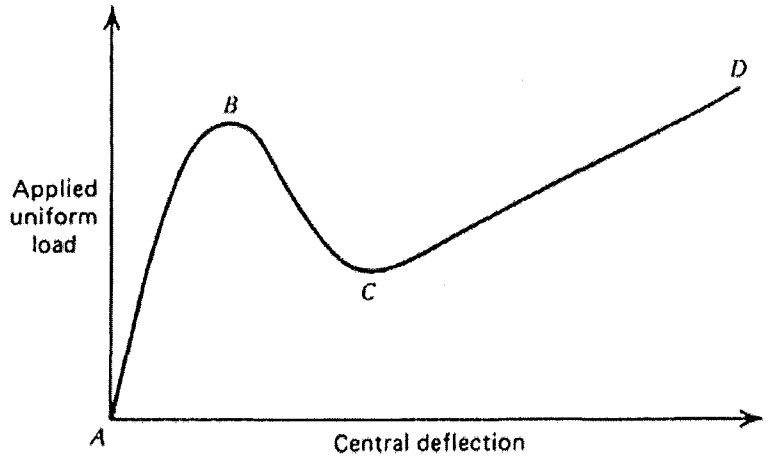

Figure 3-4: Load deflection curve of a two-way reinforced concrete slab (Park, 1964c).

The behaviour of one-way and two-way concrete slabs at ambient temperature has long been studied by many researchers. The behaviour of a two-way slab at ambient conditions, with laterally restrained edges can be divided into a few phases, described by Figure 3-4. As the loads on the slab are increased from A to B, the slab deflects downwards and due to compressive membrane action, reaches its ultimate enhanced load at B. The slab behaves elastically during the initial stages, followed by inelastic behaviour as the loads approach B. Compressive membrane action develops at small deflections, after cracking of the slab. The compressive forces form in the slab due to jamming of the slab segments into the boundaries, causing the slab strips to arch from boundary to boundary, which enhance the flexural strength of the slab sections.

As the load is increased beyond point B, the load carried by the slab decreases very rapidly due to the reduction of the compressive membrane force. For a two-way slab, it can still carry loads beyond point B when the membrane forces in the central region change from compression to tension between point B and C. This transition from compressive membrane action to tensile membrane action can result in violent snap-through of the slab, due to the sudden drop of axial forces. In a one-way slab, the snap-through would lead to catenary mode with axial tensile forces generated in the slab. If the tensile forces cannot be resisted at the supports, the slab would collapse. For a two-way slab, the load is resisted beyond point C by the reinforcement acting as a plastic tensile membrane with full-depth cracking of the concrete over the central region due to the large stretch of the slab surface. Tensile membrane

action does not alter the collapse mechanism of the slab and the slab can carry further load with an increase in deflection until D, when the reinforcement fractures. The limiting point when fracture occurs at D depends on the ductility of the steel.

3.3.1. Compressive membrane action

The application of compressive membrane action in normal civil engineering design has not matured even though it has been known for more than three decades (Wood, 1961; Park et al., 2000). However, if compressive membrane forces exist in floor systems, they can be used to provide a 'silent' safety factor (Woodson et al., 1999). Tests of compressive membrane action in slabs have been described by Park (1964a, 1964b), Guice et al. (1989) and Vecchio et al. (1990b). Park (1964a, 1964b) has used plastic theory to determine the load-deflection behaviour at and after the ultimate load for a slab with compressive membrane forces. The capacity of the slabs is associated with the midspan deflection to thickness (δ/h) ratio. The peak capacity of a slab with a slenderness ratio of 20 occurs when δ/h is 0.5 (Park et al., 2000). Stockier slabs will reach their peak capacities at lower values of δ/h. Park et al. (2000) have shown that compressive membrane action can be mobilised when the support stiffness is at least $S = 2E_c/(L/h)$, where E_c is the modulus of elasticity of the concrete and L/h is the span to depth ratio.

3.3.2. Tensile membrane action

Park (1964c) has proposed a theory to determine the load carried at large deflections by tensile membrane action. The theory was derived based on tests of concrete slabs with full horizontal restraint by Park (1964c). Significant tensile membrane action in slabs can occur only if there is stiff edge restraint to prevent movement of the edges (Park et al., 2000). Park (1964c) has recommended a safe value of $0.1L_x$ (Short span/10) for the maximum central deflection after tensile membrane has developed.

Tests by Wood (1961), Sawczuk et al. (1965), Taylor (1965) and Hayes (1968) have shown that some tensile membrane behaviour can form in unrestrained two-way slabs. The membrane forces form in the slab as a result of the geometry of deformations as the slab deflects. Figure 3-5 shows a laterally unrestrained uniformly loaded square slab under large vertical deflections with a yield line pattern in the slab. Membrane forces form in the slab when the slab regions at the edges tend to move inwards but are prevented by the adjacent

outer edges. The segments of the slabs act as shells, with the lower central region of the slab in tension, and the upper outer region in compression (Taylor, 1965). Considering equilibrium of a segment (segment *A* in Figure 3-5), the total tension forces of the reinforcement are equal to the compression forces in the concrete. The forces are not in balance, when considering specific lengths of the yield line, as is normally assumed in yield line theory. However, the forces are in balance when considering the yield line overall (Taylor, 1965).

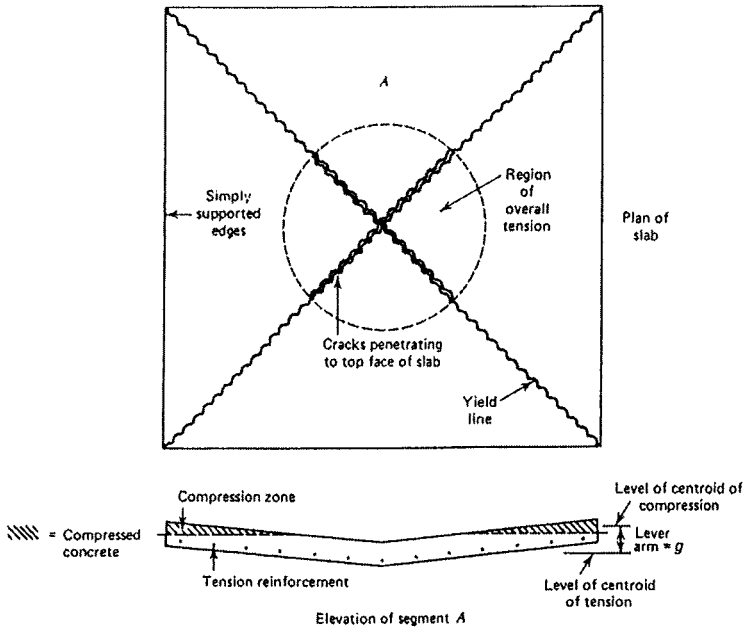

Figure 3-5: Tensile membrane action in an unrestrained, uniformly loaded slab (Taylor, 1965).

Increasing deflections occur in the slab due to rotations between the segments of the slab at the yield lines, which have formed earlier. The effect of the change in geometry, due to the increasing vertical deflections, increases the effective lever arm of the internal forces (Taylor, 1965). This increases the tensile membrane enhancement and the load carrying capacity of the slab. In two-way slabs, the ultimate capacity of the slabs can be increased from 1.5 to 2 times above the yield line capacity (Woodson et al., 1999).

Sawczuk et al. (1965) and Hayes (1968) have developed analytical methods for considering membrane action in unrestrained slabs. Their design methods assumed that the critical mode of failure was by cracks forming across the short span of the slabs, intersecting the yield lines as shown in Figure 3-6. The method by Sawczuk et al. (1965) was based on an energy method while Hayes (1968) developed an equilibrium method based on the failure mode proposed by Sawczuk et al. (1965). The Building Research Establishment (BRE) has recently tested a

trapezoidal profiled slab to investigate the effects of tensile membrane action in slabs (Bailey et al., 2000). This will be described in further detail in section 3.8.2.

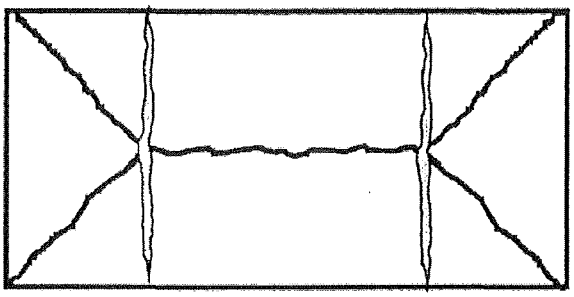

Figure 3-6: Critical mode of failure in the slabs assumed by Sawczuk et al (1965) and Hayes (1968).

Unlike compressive membrane action, tensile membrane action does not depend on the surrounding members in a structure and can develop in a slab with simply supported conditions. Tensile membrane behaviour can be an important factor to limit catastrophic collapse under fire conditions. This will be discussed further in section 3.8. The reserve capacity due to tensile membrane action is also an important consideration in the design of blast-resistance structures where large deflections are indicative of very large energy absorbing capabilities (Woodson et al., 1999).

3.4. Simply supported one-way slabs under fire conditions

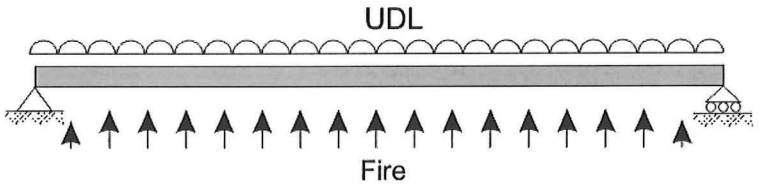

Figure 3-7: A simply supported slab exposed to a fire from below.

When a simply supported one-way concrete slab is exposed to a fire from below as shown in Figure 3-7, a non-linear temperature gradient will form across the depth of the slab. The temperature gradient will cause the concrete slab to expand outwards and deflect downwards. The vertical deflection is mainly due to thermal bowing of the slab which is a result of the non-linear thermal expansion across the depth of the slab. The high temperatures at the bottom surface will cause the bottom reinforcing steel to lose its flexural strength and stiffness, resulting in additional deflections of the slab. When the flexural strength at a section of the slab falls below the level of the applied bending moment, a plastic hinge will form and the slab will fail.

3.5. Axial restraint of fire exposed one-way concrete floor systems

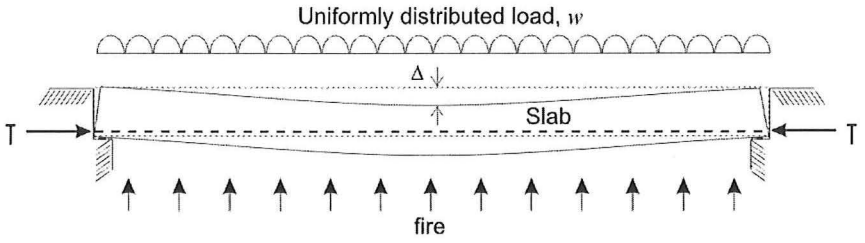

Figure 3-8: A restrained simply supported one-way slab exposed to a fire from below.

Figure 3-8 shows a simply supported one-way slab exposed to a fire from below. If the horizontal movement from the thermal expansion is restrained by a rigid surrounding structure (Figure 3-7), compressive axial forces will develop in the slab.

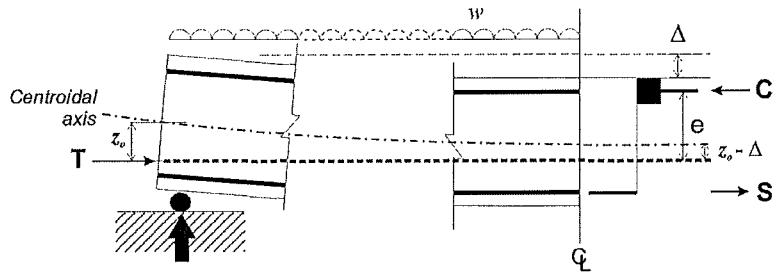

Figure 3-9: Free body diagram of a restrained simply supported slab.

Figure 3-9 shows the free body diagram of half of a restrained reinforced concrete slab exposed to a fire on the underside. The equilibrium of the forces require the compression stress block to have a force, C, equal to the sum of the tensile forces in the reinforcing steel, S, and the external thrust force, T, i.e.: C = S + T. The equilibrium between the applied and resisting moments at midspan at failure is:

$$R^{+}_{fire} = wL^2/8 - T(z_o - \Delta) \qquad \textbf{Equation 3-1}$$

Where R^{+}_{fire} = Positive flexural capacity of the slab at elevated temperatures

z_o = Distance between the position of thrust force and the centroidal axis of slab at the supports

Δ = Midspan vertical deflection

w = Uniformly distributed load

L = Clear span of the slab

Equation 3-1 is based on the derivation presented by Harmathy (1993). The PCI (Gustaferro et al., 1989) and Buchanan (2001) have presented a similar equation expressed by Equation 3-2. The only difference is the term 'e' which is defined as the distance between the line of thrust at the supports and the centre of the concrete compressive block at midspan (Refer to Figure 3-10).

$$R^{+}_{fire} = wL^2/8 - T.e \qquad \textbf{Equation 3-2}$$

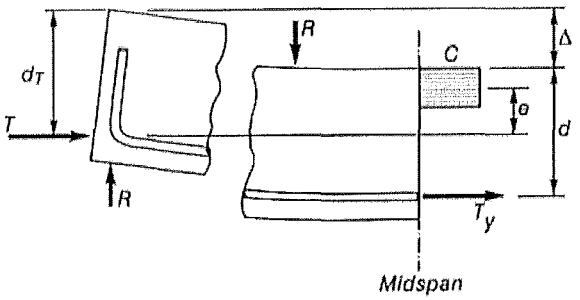

Figure 3-10: Definition of 'e' in the free body diagram of a restrained slab (Buchanan, 2001).

The following discussion on axial restraint will be based on Figure 3-9 and Equation 3-1 as it has been shown to be more consistent with the analyses presented in section 5.8, rather than that presented by Equation 3-2.

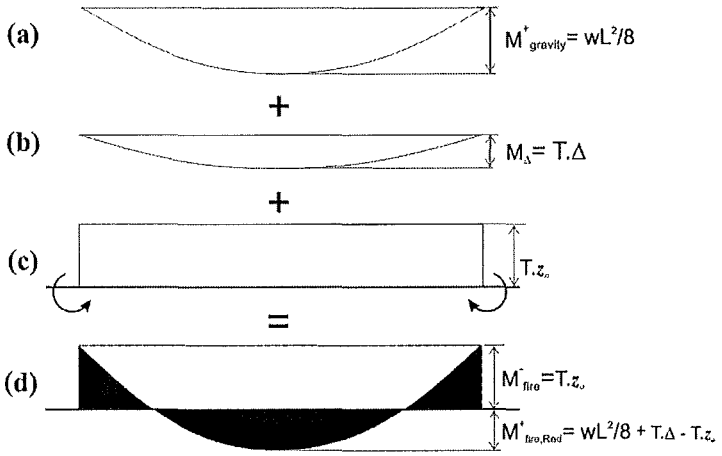

Figure 3-11: Components of moments in a restrained slab with its line of thrust at the slab soffit.

The effectiveness of the restraint is dependent on the distance of the thrust force to the centroidal axis of the slab at the end supports, z_o (refer to Figure 3-9). Figure 3-11 shows the moments that act on a restrained slab when the line of thrust is located close to the soffit of the slab. Figure 3-11a shows the bending moment diagram due to the gravity loads. Figure 3-11b shows the moments due to the downward deflection of the slab, coupled with the restraint force, T, and Figure 3-11c shows a uniform negative moment due to the restraint force, T, acting at a distance, z_o, below the centroidal axis at the supports of the slab. The combined bending moment diagram due to the external thrust and the gravity load is shown in Figure 3-11d. The moment due to the gravity loads, $M^+_{gravity}$, remains constant during the fire but the moments due to M_Δ and $T.z_o$ can change during the course of the fire, which will also change the shape of the combined bending moment diagram. The equation of the midspan moments is given by Equation 3-1.

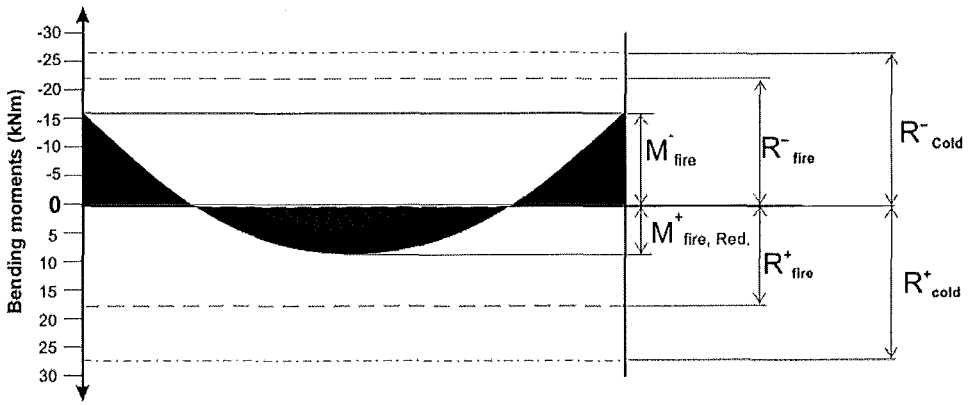

Figure 3-12: Applied and resisting moments of a restrained slab.

Figure 3-12 shows the same bending moment diagram from Figure 3-11d, with typical positive (R^+_{cold}) and negative flexural capacities (R^-_{cold}) added. As the temperatures increase during the fire, the flexural capacities will steadily reduce, shown by the lines marked R^+_{fire} and R^-_{fire}. The shape of the bending moment diagram can only change within the limits of the reduced positive and negative flexural capacities. If the reduced positive flexural capacity, R^+_{fire}, falls below the applied bending moment, $M^+_{fire,Red}$, a plastic hinge will form at a section of the slab and the slab will collapse. However, the negative moment, M^-_{fire}, which is due to the thrust force acting below the centroidal axis can reduce the applied positive moments, $M^+_{fire,Red}$, which will require the positive flexural capacity to be further reduced before it is exceeded by the positive moments, thus allowing the slab to be exposed to the fire for a longer time. If the negative moment is sufficiently large, it can reduce the positive moments at midspan to zero. In this case, the positive flexural capacity can drop to zero without collapse of the slab. However, the negative moments at the slab supports can increase only up to the limit of the negative flexural capacity, R^-_{fire}, which depends on the compressive strength of the bottom reinforcing bars at the end span. The negative moments cannot be further increased if the bottom reinforcing bars yield in compression.

Even with the reduction of the positive moments by the $T.z_o$ moment, a plastic hinge can still form at midspan, causing failure, if the applied positive moment, $M^+_{fire,\ Red}$, increases sufficiently and exceeds the slab's positive flexural resistance, R^+_{fire}. This increase of the positive moment during the fire is attributed to the M_Δ moment, which is the product of the deflections and the thrust force. If the slab deflects downwards excessively until the midspan deflections, Δ, equal z_o, the terms $T.\Delta$ and $T.z_o$ in Equation 3-1 will cancel out and become

zero. Thus, the flexural enhancement due to restraint will be lost and only the flexural capacity of the slab can be relied on to resist any additional positive moments. Compressive axial restraint can be detrimental if the deflections, Δ, are larger than z_o, as the compressive restraint force, T, coupled with the large deflections will increase the applied midspan moment and reduce the time to the formation of a plastic hinge.

The thrust force from the rigid supports can increase the flexural stiffness of the slab, to prevent large downward deflections. Paradoxically, the rigid supports will form large compressive forces in the slab, which will also increase the M_Δ moments, even for small deflections. Therefore, the flexural resistance at midspan can also be exceeded for a rigidly restrained slab with small vertical deflections. This will result in a sudden collapse when a plastic hinge suddenly forms at midspan.

3.5.1. Effect of line of thrust at different support conditions

The effectiveness of restraint of a fire exposed slab is sensitive to the position of the line of thrust and the amount of restraint provided by the surrounding structure. The compressive forces in the slab will form a shallow arch in the slab to resist the applied loads. For the compressive forces to enhance the flexural resistance of the slab, the line of thrust has to remain below the centroid axis of the slab. Greater flexural enhancement can be mobilised if its line of thrust at the supports is located further below the centroidal axis (Figure 3-13a).

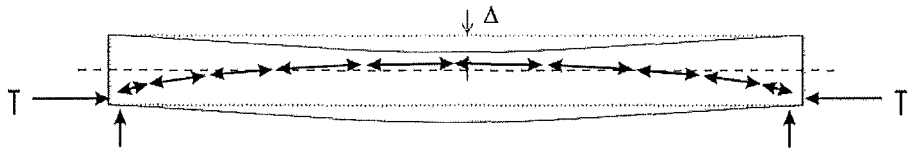

(a) Line of thrust close to soffit of slab

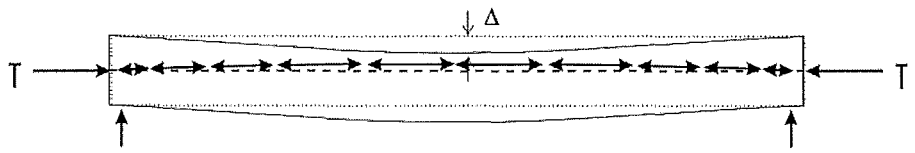

(b) Line of thrust far from soffit of slab

Figure 3-13: Compressive membrane action for different positions of line of thrust

When the position of line of thrust at the supports is located close to or above the centroidal axis (Figure 3-13b), the compressive forces cannot sufficiently enhance the flexural resistance

of the slab and can be detrimental to the slab. An example of such an application would be in double-tee slabs which have their webs cut out (refer to Figure 3-14a). In this case, the line of thrust will be too close to the centroidal axis to produce any enhancement. If the thrust force acts above the centroidal axis of the slab, it can produce a sagging moment, which will accelerate the development of the applied positive moments, and reduce the time to forming a plastic hinge, and failure.

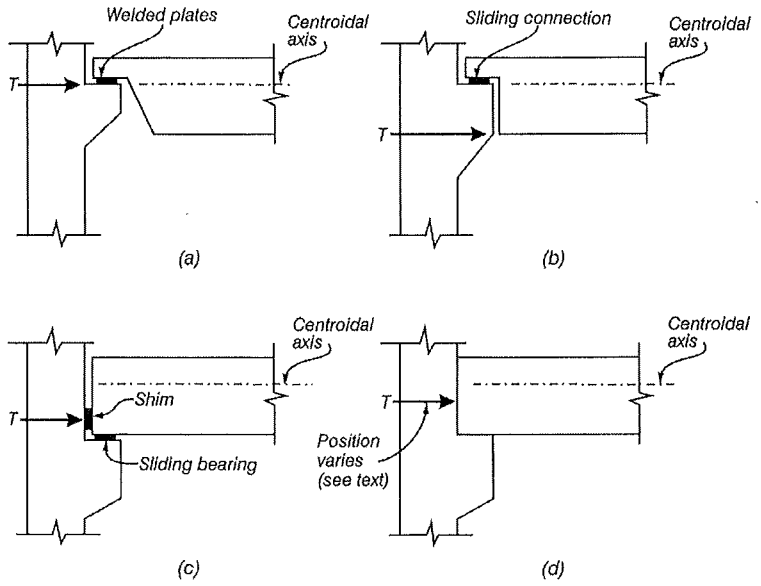

Figure 3-14: Location of point of action for different support conditions (Carlson et al., 1965).

The height of the line of thrust can only be located accurately for specific support conditions where the line of thrust is well defined due to the method of construction. An example of such an application would be in precast construction where metal shims are placed between the vertical faces of the ends of slabs and the restraining structure (Figure 3-14a, b and c).

For cast in-situ or continuous slabs (Figure 3-14d), the height of the line of thrust at the supports changes during the course of the fire. Fire tests of restrained floor slabs at the PCA furnace (Issen et al., 1970 and Lin et al., 1983) have shown that for highly restrained slabs, the line of thrust moves from below the depth of the slab towards the centroidal axis during the fire. For normal weight concrete, the line of thrust will reach the centroidal axis in less than 2 hours. For lightly restrained slabs, the Concrete Reinforcing Steel Institute (CRSI, 1980) has provided recommendations shown in Table 3-1 for determining the line of thrust for solid slabs.

Fire exposure (hours)	Location of line of thrust at supports
2	25mm (1 in.)
3	32mm (1¼ in.)
4	38mm (1½ in.)

Table 3-1: Position of line of thrust in cast-in-situ slabs recommended by CRSI (1980).

3.5.2. Experimental and theoretical analyses of restrained fire exposed floor systems.

The investigation of the effects of restraint on fire exposed concrete floor systems was pioneered by the Portland Cement Association (PCA) (Selvaggio et al., 1963). The tested specimens consisted mainly of double-tee floor systems. The specimens were fire tested with different amounts of allowable expansion and were subjected to the ASTM E119 standard fire. The slabs in the PCA tests were allowed a certain amount of free elongation ΔL, followed by complete restraint. Anderberg et al. (1982) have questioned whether this sort of support condition occurs in real construction and have recommended simulating different degrees of restraint by different axial stiffnesses. The PCA tests showed that almost any amount of restraint greatly enhanced the fire resistance of the slabs as they were able to support their loads considerably longer than for the simply supported condition (Issen et al., 1970). Based on these results, a step-by-step method incorporating several nomograms was developed by the Prestressed Concrete Institute, PCI (Gustaferro et al., 1989) which was described in section 2.4.2.

Lin et al. (1983) have also conducted a large number of fire tests on restrained concrete floor slabs exposed to the ASTM E119 fire. Their test results showed that the performance of the floor slabs was not greatly affected by the degree of restraint, except near the 0% and 100% restraint conditions. Under zero restraint, the slab will behave as a simply supported member and will result in a lower fire resistance. At full restraint (100%), the high restraining forces could result in a compressive failure.

Anderberg et al. (1982) have used a non-linear finite element program, CONFIRE, to investigate the structural behaviour and fire resistance of concrete members exposed to fire. Their analysis was on simply supported concrete slabs with different amounts of allowable horizontal expansion of the slabs. Their analyses showed that the fire resistance of the floor slabs did not increase with increasing axial restraint and that the PCI method cannot be

universally applied to all types of floor systems. They also argued that the maximum thrust that formed in the slabs analysed cannot be used to determine its fire resistance based on the PCI method and concluded that the PCI method over-predicts the thermal strains, particularly at strains in excess of 0.15%.

Cooke (1993) has conducted a series of fire tests on restrained concrete flat slabs. The tests showed that when the line of thrust at the supports is located at the exposed face of the slab, the fire resistance of the slabs is significantly better than slabs with their line of thrust located at mid-depth. The tests also showed that an axial load applied at mid-depth of the slab end supports produced significantly shorter times to failure than a slab with no axial restraint.

3.6. Effect of continuity on the fire resistance of one-way and two-way slabs

Slabs which are continuous over several supports are subjected to some level of horizontal restraint when exposed to fires and are only unrestrained on rare occasions (Harmathy, 1993). For this reason, the effect of horizontal restraint on slabs with rotational restraint at the supports, such as continuous slabs will be discussed. Continuous slabs have better structural fire resistance than pin-supported slabs due to their higher level of redundancy against failure (CRSI, 1980; Gustaferro et el., 1989; Harmathy, 1993; Buchanan, 2001; Fleischmann et al., 2002). Their better performance in fires is attributed to moment redistribution which allows the loads to be resisted by alternative means after the first plastic hinge forms. However, FIP (1986) have presented a different view about the fire resistance of continuous structures, that precast slabs with limited flexural continuity have better performance under fire conditions than continuous slabs.

Anderberg (1978) has performed analytical studies of the behaviour of continuous concrete slabs under fire conditions. The numerical analyses were based on experimental fire tests (Anderberg, 1973) and were performed with a finite element computer program which was a modified version of "FIRES-RC" (Becker et al., 1974). In the experimental tests, the rotations of the slabs were fixed but the end supports were free to move horizontally. The slabs were subjected to various heating conditions to simulate realistic fire conditions. Their numerical analyses showed good agreement with the test results and demonstrated the effects of moment redistribution at the end supports. Their numerical analysis was extended to investigate

continuous slabs with axial restraint which showed that large positive moments formed at the supports after significant moment redistribution during the initial stages.

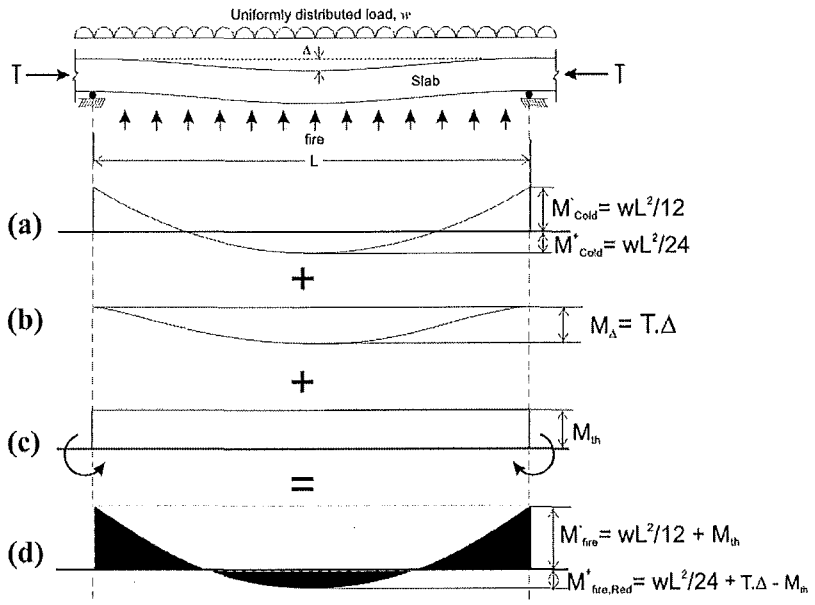

Figure 3-15: Components of moments in a restrained continuous slab.

Figure 3-15 shows the bending moments of an interior span of a continuous slab, subjected to a fire from the underside. The heated span is assumed to be uniformly loaded and horizontally restrained. The bending moment diagram due to the gravity loads is shown in Figure 3-15a. The vertical deflections and thermal thrust also produce a moment, M_Δ (Figure 3-15b). A uniform hogging moment, M_{th}, (Figure 3-15c) along the length of slab is formed, due to the rotational restraint against the curvature induced by the thermal gradient. This hogging moment increases the negative moments at the supports and reduces the positive moments along the span. The combined bending moment diagram due to the gravity loads and the thermal effects is shown in Figure 3-15d. The shape of the bending moment diagram will change during the fire, due to the M_{th} and M_Δ moments, but only within the limits of the reduced positive and negative flexural capacities. Unlike the pin-supported slab, the continuous slab will not fail until the flexural capacity is exceeded at three plastic hinge locations.

In a continuous slab, the position of the line of thrust at the supports can be determined from the bending moments at the supports. Figure 3-15 shows that M^-_{fire} consists of the moments imposed due to the gravity loads, $wL^2/12$, and the moments due to restraint against thermal curvature, M_{th}. By definition, the bending moment at the supports is defined as the couple of

the axial force in the slab, T, and the eccentricity, z_o (refer to Equation 3-3). This eccentricity is the position where the axial force is acting across the depth of the slab at the supports, relative to the centroidal axis of the slab.

$$M^-_{fire} = T.z_o \qquad \textbf{Equation 3-3}$$

where T = Axial force in the slab

z_o = Position of line of thrust relative to the centroidal axis

Therefore, the eccentricity of the axial force relative to the centroidal axis of the slab is:

$$z_o = \frac{M^-_{fire}}{T} \qquad \textbf{Equation 3-4}$$

3.7. Catenary action in one-way slabs

Large deflections can occur in one-way slabs after significant periods of fire exposure. For simply supported slabs, rapidly increasing deflection indicates the onset of failure. If the slabs have the capacity for horizontal tensile restraint at the supports, the large deflections can result in the loads being carried by catenary action, with tensile forces in the slabs. This requires the supports to have sufficient anchorage and tensile capacity to resist these forces. The magnitude of the tensile forces at the end supports, T, when the slab deforms into a catenary with a midspan deflection, Δ, is shown by Equation 3-5.

$$T = \frac{wL^2}{8.\Delta} \qquad \textbf{Equation 3-5}$$

3.8. Tensile membrane behaviour in fire exposed two-way slabs

The Broadgate building fire showed that the composite floor slabs of a steel framed building played an important load bearing role when the unprotected secondary steel beams lost significant strength and stiffness. At ambient temperatures, composite slabs with steel decking are designed and assumed to behave as one-way systems, resisting the loads through bending and shear. Under fire conditions, the unprotected composite slabs undergo very large vertical deflections due to thermal bowing and loss of strength of the steel deck and the supporting beams. The slabs behave as a two-way membrane and are supported by the colder perimeter beams and columns. As the beams weaken in the fire, the load resistance progressively transfers to the slabs, resisting the loads by tensile membrane action. The compression ring forms at the edges of the heated slab in addition to a tension field in the middle of the heated slab. The tensile stresses are resisted by the mesh in the slab. This mechanism will enable the slab to resist the loads provided the vertical supports at the edges can be maintained and provided the steel in the tension zone does not fracture.

3.8.1. Cardington fire tests

Following the Broadgate building fire, a series of full-scale fire tests was conducted in the 8 storey steel framed test building at the Cardington Large Building Test Facility in 1995/1996 (Figure 3-16). The tests showed that unprotected reinforced concrete floor slabs on steel decking do not collapse after a compartment burnout, in spite of very high measured steel temperatures and suffering considerable deformations (Bailey et al., 1999). The fire tests were conducted by British Steel and the Building Research Establishment (BRE), involving different compartment sizes and test configurations at different locations in the building. In the tests, the soffit of the trapezoidal composite deck and all the steel beams were unprotected. The columns were fully protected up to the soffit of the slabs. The maximum fire temperatures in the tests exceeded 1000°C. The composite floors suffered large deflections (~L/20) but there was no structural collapse (Figure 3-17). The beams showed signs of local buckling and the connections showed signs of being subjected to high tensile forces which resulted in plate and web fractures.

Figure 3-16: Fire tests at the Cardington steel building (Newman et al., 2000).

Figure 3-17: Large deflections of the composite slabs following the fire tests at the Cardington steel building (Newman et al., 2000).

3.8.2. BRE ambient temperature test

A test was conducted at the BRE to investigate tensile membrane action in slabs exposed to fire conditions. The test was conducted at ambient conditions on a slab which measured 9.5m x 6.5m. Although the test was conducted at ambient conditions, the test was intended to simulate tensile membrane behaviour in a slab that would be exposed to fire conditions. The slab was simply supported at the perimeter on beams and columns but it was horizontally unrestrained. The slab was subjected to an increasing load with a series of point loads to represent a uniformly distributed load over the slab. The slab was built on a trapezoidal-shaped composite steel deck which was later removed from beneath after the concrete was cast, leaving the concrete slab reinforced only with the A142 mesh. The absence of the steel decking represented the minimal contribution of strength and stiffness to the slab during a real fire.

Failure of the slab occurred under a uniformly distributed load of 4.81kPa, which was more than double the load carrying capacity determined from classical yield line analysis (2.3kPa). The slab failed when a large full depth crack formed in the middle of the short span of the slab, followed by a full depth crack forming across the diagonal of the slab. The test showed that a composite slab simply supported on four edges could carry loads considerably in excess of those predicted by conventional yield line design principles (Bailey et al., 2000).

3.8.3. Design methods incorporating tensile membrane action

Following the tests conducted at the BRE, Bailey et al. (2000a, 2000b) and Bailey (2001) have developed a method for determining the ultimate load carrying capacity of two-way slabs incorporating the effects of tensile membrane enhancement under elevated temperatures. The design method estimates the load capacity of a two-way slab at a given displacement, based on the membrane forces in the slab. The design method calculates an enhancement factor, due to effects of the membrane forces on the flexural strength, for the yield line load capacity. The method considers the failure mode shown in Figure 3-18 and differs from the failure mode (refer to Figure 3-6) presented by earlier researchers (Sawczuk et al, 1965; Hayes, 1968). This method has shown agreement with published data of the fire tests at the Cardington Large Building Test Facility (Bailey et al, 2000). The design method also includes a check on the ultimate failure of the system based on the maximum permissible deflections due to the mechanical strains of the reinforcement and the thermal bowing deflections.

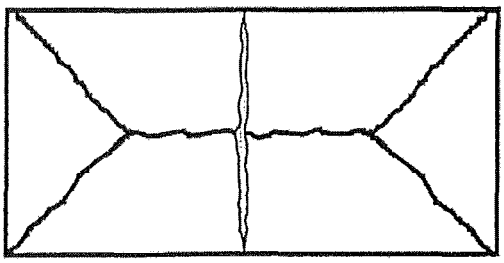

Figure 3-18: Assumed failure mode of the slab by Bailey (2001).

The postulated membrane behaviour is not yet fully understood, especially at elevated temperatures. Newman et al. (2000) have applied this procedure to a limited range of conditions involving low to moderate fire severity, in which the influence of elevated temperatures on the components is expected to be minor.

Clifton et al. (2003) have extended this design method for application in New Zealand. This method considers higher fire severities compared to those specified for the UK application given by Newman et al. (2000). This design method takes account of the effects of elevated temperatures on the load resisting components and the strength contributions of the secondary beams to the slabs. This design method also checks the shear capacity of the slab at elevated temperatures and provides detailing provisions for the slab reinforcement. Clifton et al. (2003) have recommended the use of steel with high ductility, equivalent to hot-rolled reinforcing, at

the regions with negative moments such as the supports where the steel may be required to accommodate high tensile strains without fracture.

Comparison of the simple design method with the VULCAN finite element program has shown that the simple design method may predict higher tensile membrane enhancement, hence greater fire resistances, than predicted with finite element analysis (Huang et al., 2002). The differences of the results were particularly significant for highly reinforced square slabs, where the simple method predicted much greater enhancement due to tensile membrane action.

3.8.4. Numerical analysis by other researchers

The fire at the Broadgate building and the tests at the Cardington building led to intensive 3D computer modelling with sophisticated computer programs to understand the behaviour of steel framed structures in fire and tensile membrane action in composite slabs. Huang et al. (1999b, 2000b, 2001a) have modelled the fire tests at the Cardington building (Figure 3-19) with the VULCAN program and have shown good agreement with the test results. Their analyses supported the theory and experimental observations that the floor slabs resisted the loads by tensile membrane action and formed a tensile zone in the middle of the fire exposed slab, surrounded by a compression ring (Figure 3-20). Their analyses showed that membrane action played a very important role in supporting the loads on the slabs and highlighted the importance of the ability of the fire exposed slab to deform into double curvature and behave as a two-way slab. Slabs with high aspect ratios would tend to deform into a catenary which may lead to runaway failure, rather than develop tensile membrane action (Huang et al., 2002).

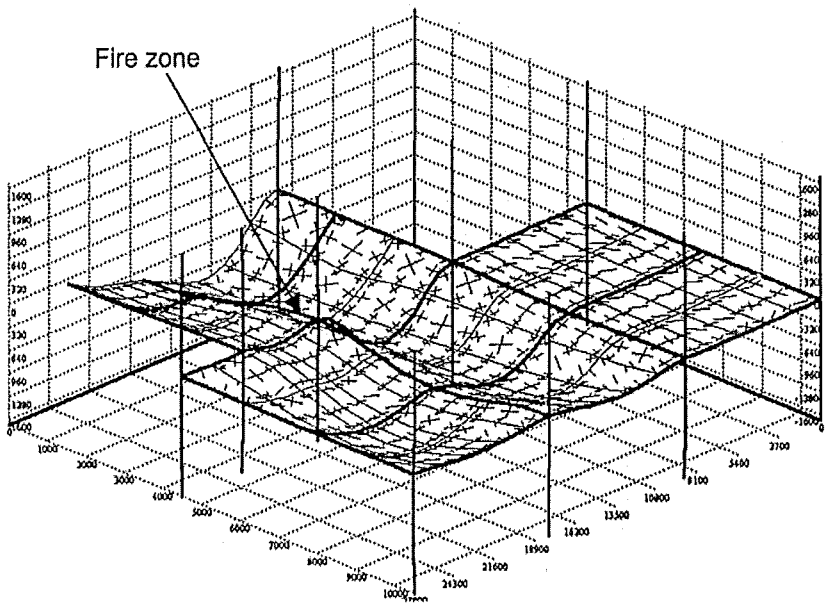

Figure 3-19: Deflected shape of the BRE large compartment fire test analysed with VULCAN (Huang et al., 2000b).

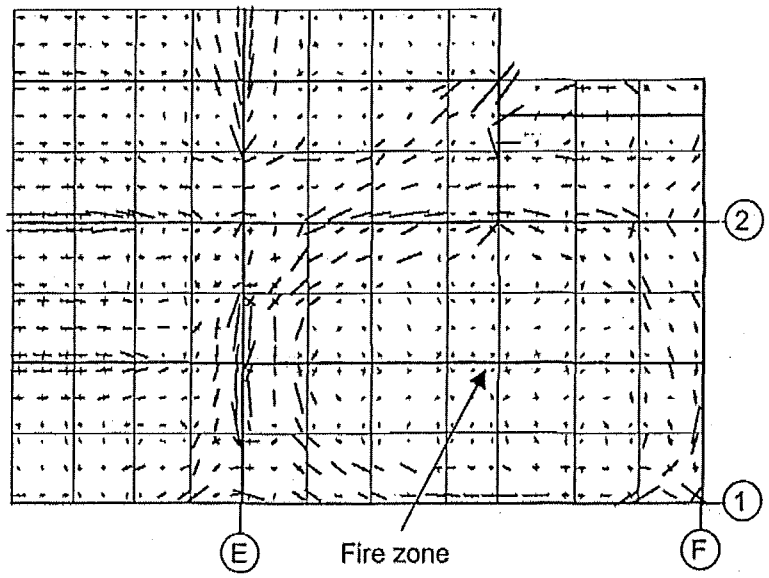

Figure 3-20: Distribution of the principal membrane tractions obtained from VULCAN analyses for the British Steel Corner Fire Test (Huang et al., 2000b).

Gillie et al. (2001) have also successfully modelled the Cardington fire tests with the ABAQUS program, combined with the FEAST package. Gillie et al. (2002) have suggested placing larger amounts of reinforcing mesh lower in the slabs than in normal design practice. Although the mesh would have less cover and be exposed to higher temperatures, it would gain more ductility due to the high temperature effects. The greater steel content would compensate for the lower strength of the steel and provide greater crack control to prevent integrity failure. The higher ductility of the mesh would enable it to continue to resist the

tensile strains in the middle of the slab under large deflections. Conversely, if the steel had greater cover, it would remain cooler and might rupture due to the lower ductility at lower temperatures.

O'Callaghan et al. (2000) have also used ABAQUS to model the Cardington building. Three different models were used, which were a grillage model, a beam/shell model and a full shell model. Their analyses found that the grillage model underestimated the experimental deflections but showed good agreement with the magnitude of the forces in the beam/shell model. However, the grillage model cannot account for the effects of in-plane and transverse shear forces. The beam/shell model and the full shell models can be used to accurately predict the true structural behaviour. The full shell model can be used to capture the local buckling effects in the beams. However, capturing this phenomenon was not important as its global response was similar to the beam/shell model (O'Callaghan et al., 2000).

4. THE SAFIR FINITE ELEMENT PROGRAM

4.1. General

This chapter describes the SAFIR computer program which is used for the numerical analysis of this research. SAFIR is a special purpose, non-linear finite element program for analysing steel and composite structures exposed to fire. It was developed by J.M. Franssen at the University of Liege, Belgium. SAFIR is based on an earlier program called CEFICOSS (*C*omputer *E*ngineering of the *FI*re resistance of *CO*mposite and *S*teel *S*tructures) which was developed in the 1980's.

This chapter describes some of the characteristics of SAFIR and are based on the contents of the *User's Manual for SAFIR2001free* (Franssen et al., 2002a). The full details of the program can be found in the *User's Manual* and *Elements of Theory for Safir 2001 Free* (Franssen et al., 2002b).

4.2. Capabilities of SAFIR

SAFIR was developed for 2D and 3D thermal and structural analysis of structures exposed to fires. Its analysis can account for geometrical non-linearity due to large displacements and material non-linearity in the thermal and mechanical properties. It utilises various types of elements, calculation procedures and incorporates various types of material models for thermal and structural analysis. Although it was developed specifically for analysing structures under fire conditions, SAFIR can also perform structural analysis at ambient temperatures.

4.3. Analysis procedure

SAFIR consists of two analysis components, which are the thermal analysis and structural analysis. The behaviour of the structure is simulated as a function of time using the temperature distributions in the structural elements evaluated from the thermal analysis. Torsional analysis of 3D beam elements can also be performed, whereby a beam section may be subjected to warping.

Step 1: Thermal analysis

The thermal analysis is performed independently of the structural analysis and needs to be carried out before the structural analysis of fire exposed structures. 2D sections and 3D elements can be analysed with the thermal analysis program.

To perform the thermal analysis, the geometry of the cross-section and its material properties are first defined. This is done with a pre-processor, *Wizard XP,* written by D.I. Pintea and J-M. Franssen (Figure 4-1). Alternatively, a text editor can be used to manually discretise the cross section. Plane sections are discretized by triangular or 4-noded isoparametric elements. For 3D analysis, the members are discretised by six or eight noded solid elements (prismatic or non-prismatic). The materials in the section can vary from element to element and their properties are temperature dependent. The materials such as steel, reinforced concrete and composite steel-concrete sections can be utilised to define the section.

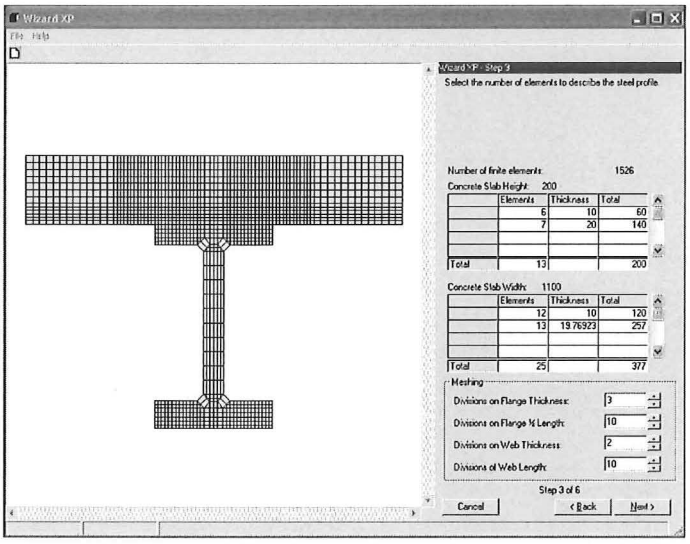

Figure 4-1: SAFIR Pre-Processor WizardXP interface.

The two-dimensional solid elements are used to define the cross section of beam, shell or truss elements in the thermal analysis. These solid elements are also referred to as 'fibres' in the beam cross section. The output of the thermal calculations performed on 3D solid elements cannot be utilised to perform three-dimensional structural analysis.

Having discretised the cross section, it is then subjected to a time-temperature profile and analysed with SAFIR to determine the thermal distribution across the cross section. The time-temperature profile applied to the thermal analysis can utilise either fire curves built into the

program or user-defined fire curves defined with data points. The results of the thermal analysis are stored in a data file and can be viewed with a post-processor, *Diamond XP,* written by D.I. Pintea and J-M. Franssen.

In the thermal analysis, heat transfer in the plane section or solid is by conduction. The evaporation of moisture in the material can be modelled by modifying the thermal properties of the materials. Radiation in internal cavities of the section can also be considered in the thermal analysis such as in hollow core concrete members (Figure 4-2).

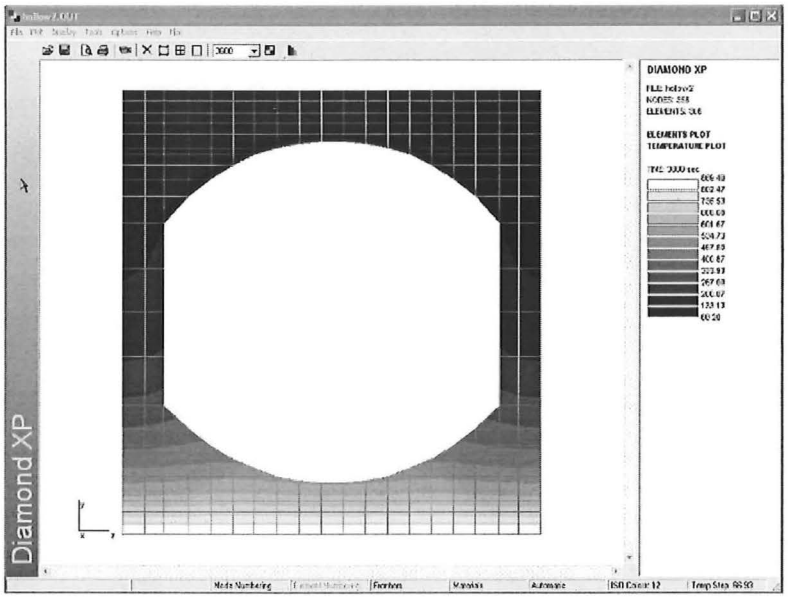

Figure 4-2: Thermal analysis of a hollow core concrete slab with an internal cavity, viewed with the DiamondXP Post-processor.

Step 2: Structural analysis

The structural analysis can be performed in the 2D or 3D domain for structures in ambient and fire conditions. The structural analysis in fire conditions is performed after the temperature histories in the elements have been defined. The analysis is performed as a function of time in the fire using the temperature distributions in the elements which were obtained from the thermal analysis output. For 3D analysis with beam elements, torsional analysis of the beams must be performed prior to the structural analysis to determine the torsional stiffness of the beam elements. Truss, beam and shell elements are available for discretising the structure. Some of these elements will be further described in section 4.4.

SAFIR uses an incremental-iterative solver for the structural analysis. An iterative technique is used to find the equilibrium between the external load and the internal stress at every time step. For each iteration, the tangent stiffness matrix is evaluated and the system of equations is solved using the Newton-Raphson method (Figure 4-3).

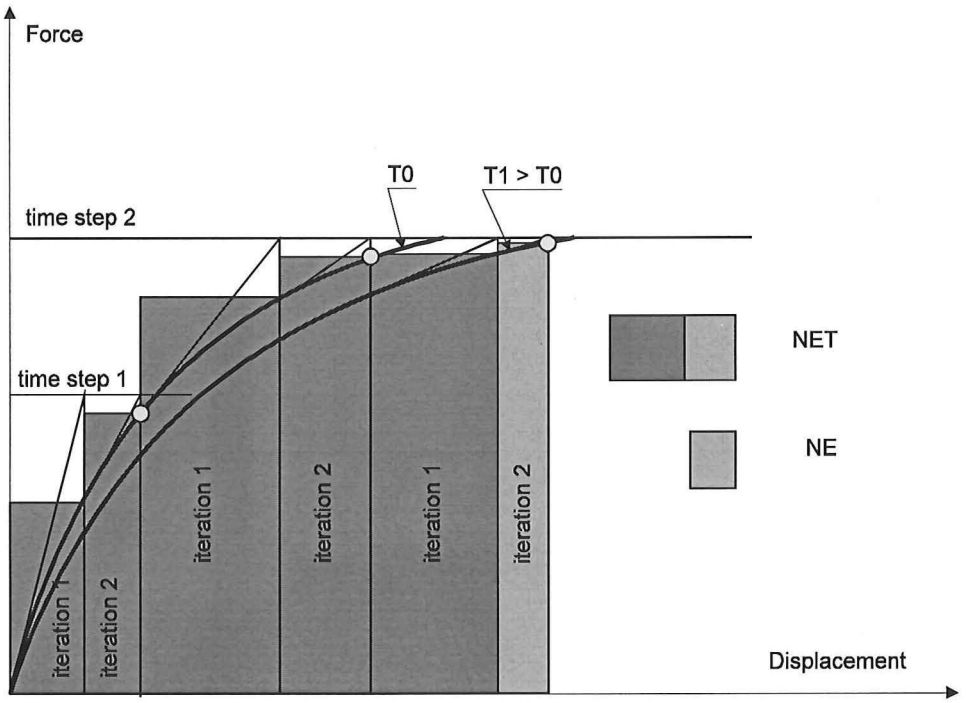

where : NE Norm of the Energy, calculated at each iteration

NET Norm of the Total Energy, calculated as the summation of all the previous NE

Figure 4-3: Convergence iterations for the SAFIR structural analysis (Franssen et al., 2002b)

The iterations are repeated for every time step until convergence is achieved. When convergence is achieved, the following data are computed:

i) Displacements of the structure at each node;

ii) Axial and bending moments at each integration point in each element;

iii) Stresses, strains and the tangent modulus of each element in each fibre and each longitudinal integration point of the beam element;

iv) Stresses, strains, bending and membrane stiffnesses of the shell elements.

The procedure repeats successive time steps and halts when the specified final time is reached or when the structure fails. Local failure of a structural member does not lead to overall structural failure. This is dealt with by the arclength technique. The arclength technique in SAFIR is similar to the method described by Crisfield (1981) and can be used to

accommodate failure of a single column in a redundant framed structure and snap-through behaviour of slabs. Automatic adaptation of the time step increment is possible and the structural calculation continues until failure. This means that the failure point is not affected by any deflection criterion.

In the analysis, large displacements, thermal strain effects and temperature dependant non-linear materials are taken into account. SAFIR uses a total corrotational method to solve for the large displacements. The unloading of the stresses in a material, such as during the decay phase of a fire, is parallel to the elastic-loading branch (Franssen, 1990). The program also allows imposed displacements and residual stresses by means of initial strains.

4.4. Structural elements

This section describes the beam and shell elements that will be used in the analysis of this research project.

4.4.1. The SAFIR Beam Element

The 2D beam element is defined by three nodes (Figure 4-4). N1 and N2 represent the end nodes and define the position of the beam in space. A third node, N3, lies between the two end nodes and supports the non-linear component of the longitudinal displacement. The longitudinal displacement of the node line is a second order power function of the longitudinal co-ordinate, while the transverse displacement of the node line is described by a third order power function of the longitudinal co-ordinate. The end nodes of the 2D beam element, N1 and N2, have three degrees of freedom comprising two displacements and one rotation.

The 3D beam element has an additional node, N4, to define the position of the local y-axis of the beam. The end nodes of the 3D beam have seven degrees of freedom, three displacements, three rotations and a warping degree of freedom.

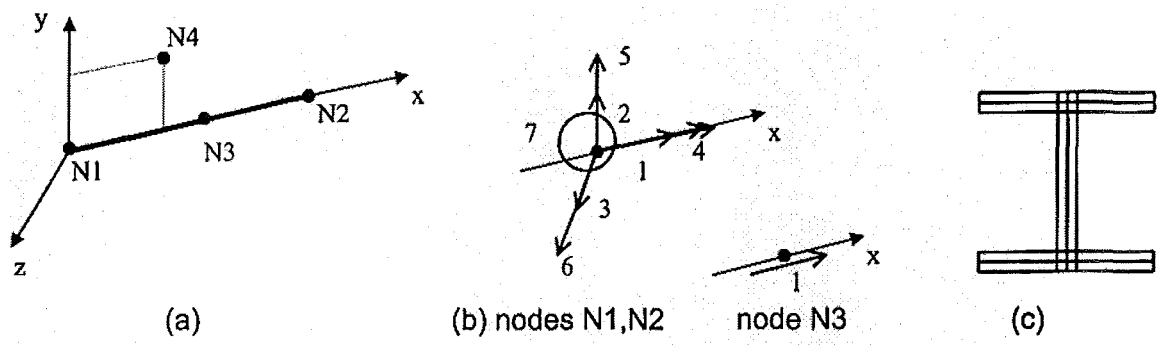

Figure 4-4: Beam element (a) Local axes (b) Degrees of freedom at nodes (c) Cross section (Franssen et al, 2002b).

The cross-section of the beam element is discretized by the fibre model, consisting of quadrilateral and/or triangular shaped elements. The integration along the length of the beam is performed with Gauss integration. The number of Gauss integration points along the length of each beam varies from one to three. Typically, two integration points are used. At every longitudinal point of integration, all the variables such as temperature, strain and stress are uniform in each fibre. Each fibre in the beam can have its own material, allowing composite sections to be made and analysed.

There are several assumptions made in the beam element that were incorporated in the program:

1. Plane sections remain plane under bending.
2. Shear energy is not considered as per Bernoulli's hypothesis.
3. In the case of strain unloading, the material behaviour is elastic with the elastic modulus equal to the Young's modulus at the origin of the stress-strain curve.
4. The plastic strain is not affected by the increase in temperature.
5. Plastifications are only considered in the longitudinal direction of the member; i.e.: uniaxial constitutive models.
6. The non-linear portion of the strain is averaged on the length of the elements to avoid locking.
7. Non-uniform torsion is considered in the beam element.
8. Local buckling of steel fibres in the beam element cannot be accounted for.

4.4.2. The SAFIR shell element

Shell geometry

The SAFIR shell element is a 4 node quadrilateral element. The shell element (Figure 4-5) is defined by four corner nodes in the order of nodes 1, 2, 3 and 4, and has a constant thickness, *h*. The middle points of the edges of the elements are a, b, c and d while the centre of the local system of coordinates lies at the intersection, o, between a-c and b-d. The *z* axis is perpendicular to the d-b and a-c plane.

There are 4 Gauss integration points on the surface of the shell element. There are also integration points distributed across the depth of the shell at the positions of the surface integration points. The number of Gauss integration points across the thickness is defined by the user, ranging from 2 to 10.

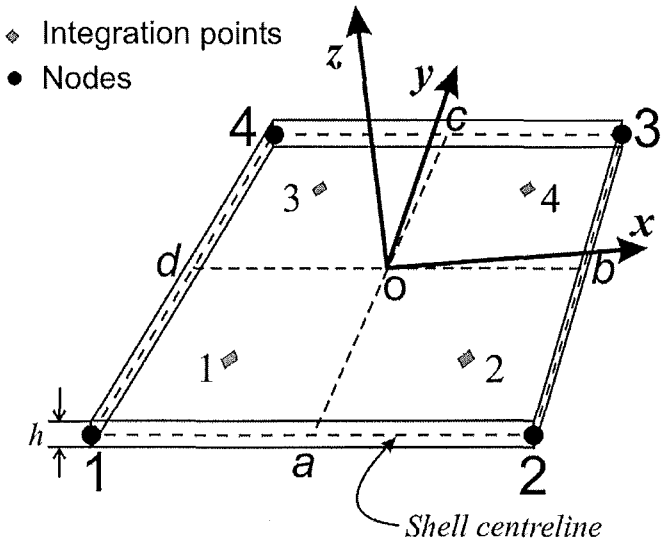

Figure 4-5: Geometry of the shell element (Franssen, 2002b)

Shell formulation

The shell element combines the membrane properties of a membrane element and flexural properties of a plate element. Talamona et al. (2000) has presented more details of the shell element formulation and has successfully used the shell element to model steel members. The properties of the plate element are based on the Discrete Kirchhoff Quadrilateral (DKQ) which was originally formulated by Batoz et al. (1982). Some of the properties of the DKQ plate element are:

- The out-of-plane displacements and rotations are parabolic along each side.
- The contribution of the shear strain energy is neglected.

- The transverse shear strain is zero at a finite number of points in the element, rather than at every point as in classical thin plate theory. The shear strains at the Gauss points are set to zero.
- The rotations along the edges vary linearly.

Some of the membrane properties of the shell element are:

- The element has a cubic membrane displacement field.
- The shear strains over the element are assumed to be constant.

Reinforcing bars

The steel of the reinforcing bars in the shell element is modelled based on a smeared model (i.e.: The unit area of the reinforcing steel is assumed as a thin sheet of steel in each shell element.) The reinforcing layers in the shell elements lie parallel to the local x-y plane. Each layer is defined by its local vertical coordinate in the shell and the orientation of the reinforcing relative to the local x axis. Multiple layers of reinforcing bars can be defined in the shell element. Several assumptions of the reinforcing steel are:

- The cross section of the rebar is not subtracted from the plane section of the element. This means that, in a reinforced concrete slab, steel and concrete are simultaneously present at the location of the bars.
- The bars resist actions parallel to the directions of the reinforcement. The reinforcing bars cannot directly resist shear forces.

4.5. Material properties

Numerous material models are available in the SAFIR program subroutines for analysis at elevated and ambient temperatures. The strength of SAFIR lies in its ability to perform 2D and 3D thermal and structural analysis of fire exposed members with various thermal and mechanical material models.

The available models for thermal analysis of concrete include calcareous and siliceous concrete based on EC2 (1995). Reinforcing, prestressing and structural steel models based on EC3 (1995) are available to model various types of steel. The Eurocode material properties for concrete and steel have been defined in sections 2.5 and 2.6, respectively. Insulation

materials such as gypsum and user defined material properties can also be specified for the thermal analysis.

Several different uniaxial and plane stress analysis models are available for structural analysis at elevated temperatures. These material models are available for different types of steel and concrete. Their mechanical properties are based on the Eurocodes (Refer to sections 2.7 and 2.8). The steel and concrete mechanical models can also be used for analysis at ambient conditions. The stress-strain relations for steel are linear-elliptic models, while the relations are non-linear for concrete. In structures exposed to fire loads, the materials are subjected to initial strains (ε_i), thermal strains (ε_{th}) and stress related strains (ε_σ). The difference between the total strain (ε_{total}) (obtained from nodal displacements and the initial and thermal strains) yield the stresses.

Some of the assumptions of the material models in SAFIR include:

1. Cracking and crushing of concrete can be included in the structural analysis.
2. SAFIR assumes perfect bond between two materials and cannot account for slippage between concrete and the steel.
3. SAFIR cannot account for spalling of concrete or ablation of materials such as gypsum.
4. Shear failure of the beam elements and the shell elements slab cannot be considered in the analysis.

4.6. Common features in all analyses

There are a few common features in the computations of the different analyses.

1. The matrix bandwidth is optimised to reduce the computer storage and calculation time. This is done by using an internal re-numbering of the system equations, which is transparent to the user.
2. Mater-slave relations can be used to impose the same temperature or displacement at two different nodes.
3. Graphical post-processing capabilities can be done by the post processor, DIAMONDXP.

4.7. Sign conventions

4.7.1. Global and local axes

The Cartesian co-ordinate system is used to define the global axes for the structural analysis. For 2D problems, the global axes are labelled as G1 and G2, while the local axes are labelled L1 and L2 (Refer to Figure 4-6). The applied force and displacements are positive in the direction of G1 and G2. The applied moments and rotations are positive in the counter-clockwise direction, based on the '*right-hand rule*'.

For three-dimensional problems, the global axes are labelled G1, G2 and G3 and the local axes are labelled L1, L2 and L3. The movement is dextrosum; the applied force and moments, displacements and rotations are all positive in the G1, G2 and G3 directions.

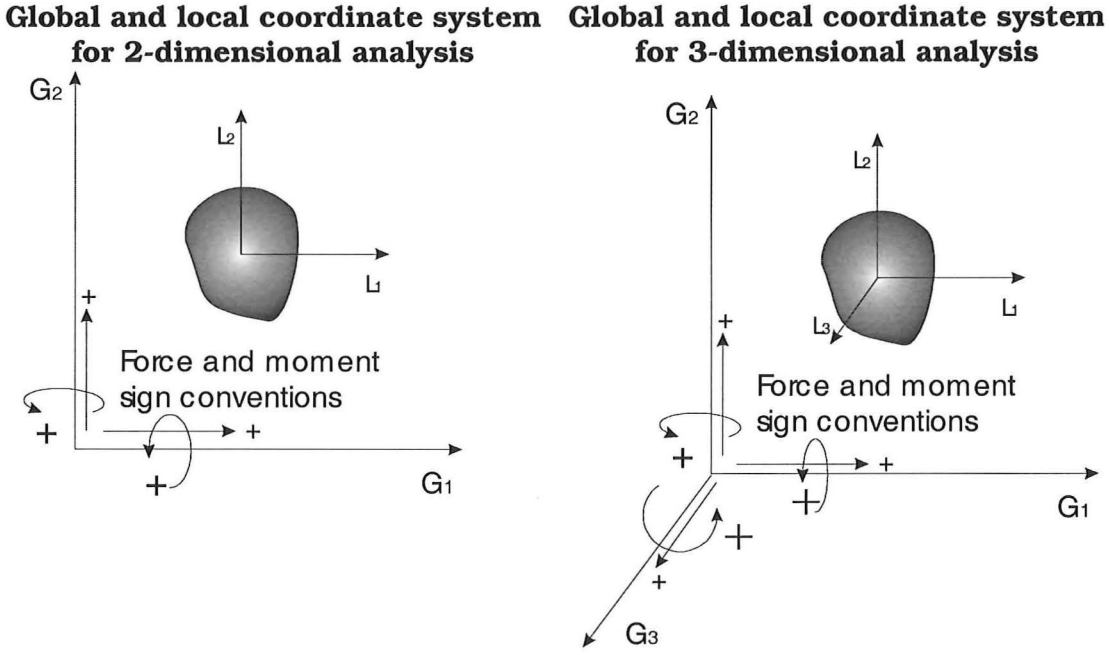

Figure 4-6: Global and local co-ordinate axes and positive sign conventions used in SAFIR.

4.7.2. Stresses

The stresses are positive in tension. The axial forces are obtained as a summation of all the stresses, which are also positive in tension. The bending moments in the beam elements are obtained as the summation of $y_i\sigma_i$, with y_i measured on the local axis, L1. The moments are positive when the fibres in tension have a positive local co-ordinate.

5. COMPRESSIVE MEMBRANE ACTION IN ONE-WAY SLABS UNDER FIRE EXPOSURE

5.1. Introduction

This chapter describes the numerical analysis of restrained one-way reinforced concrete flat slabs exposed to fire. The purpose of the analysis is to investigate the influence of compressive axial restraint in fire-exposed reinforced concrete slabs. The analysis will be performed as a 2D analysis using SAFIR and will cover various types of end support conditions with different amounts of axial and rotational restraint. For pin-supported slabs, the effect of different positions of line of thrust will be analysed to model various types of slab construction. Previous analytical work on restrained pin-supported slabs under fire conditions by Anderberg et al. (1982) did not consider the effect of the position of line of thrust and assumed it remained at mid-depth.

5.2. Analysis

5.2.1. Scope of analysis

The different analyses are summarised in Table 5-1. The scope of the analysis covers different support conditions, different fire exposures, positions of line of thrust and restraint stiffnesses. The details of the different parameters are explained in the following sections. All analyses are run for four hours of exposure to the ISO fire (or until failure if less than four hours).

Section	Support condition	Position of line of thrust	Restraint stiffness, k
5.3	Pin supports	Fixed, -25mm$\leq x_o \leq$125mm	Full restraint
5.4	Pin supports	Fixed, x_o = 50mm	$0 \leq k \leq$ full restraint
5.5	Pin supports (ISO fire with decay phase)	Fixed, x_o = 50mm	$0 \leq k \leq$ full restraint
5.6	Rotationally restrained	Moveable	$0 \leq k \leq$ full restraint
5.7	Rotationally restrained (Curtailed top steel)	Moveable	$0 \leq k \leq$ full restraint
5.8	Pin supports	Moveable	$0 \leq k \leq$ 1000%
5.9	Pin supports (Effect of top steel at supports)	Moveable	1%, 10%, 100%

Table 5-1: Cases analysed in this chapter.

Support conditions

The support conditions shown in Table 5-1 consists of three basic types:

1. *Pin supports*: Free to rotate at the supports and fixed position of line of thrust.
2. *Rotationally restrained*: The rotations at the supports are fully restrained, as in continuous slabs.
3. Pin supports with moveable line of thrust: Rotational restraint depends on the axial restraint stiffness and the line of thrust at the supports may move, as in cast-in-situ slabs.

The support conditions are shown in further detail in Figure 5-1 and Figure 5-2.

1) Pin supports

a) Unrestrained against horizontal movement (*pin-roller*)

b) Fully restrained against horizontal movement (*pin-pin*)

c) Horizontally restrained by a spring

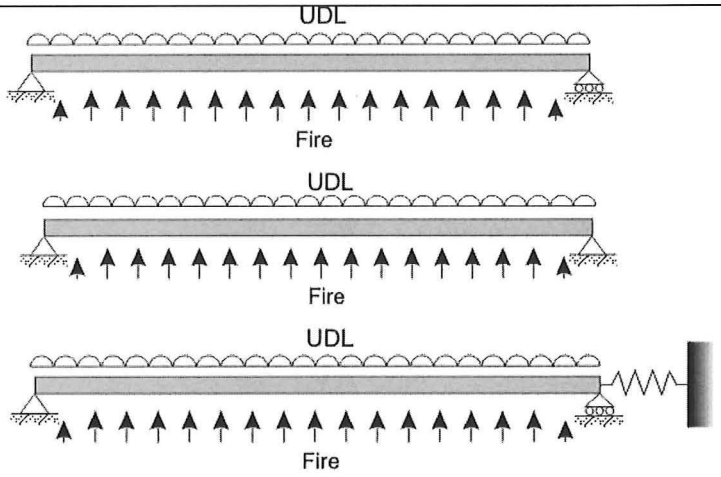

Figure 5-1: SAFIR models of pin-supported slabs.

2) Rotationally restrained

a) Unrestrained against horizontal movement (*fix-slide*)

b) Fully fixed on both supports (*fix-fix*)

c) Rotationally and vertically fixed on both supports, horizontally restrained by a spring

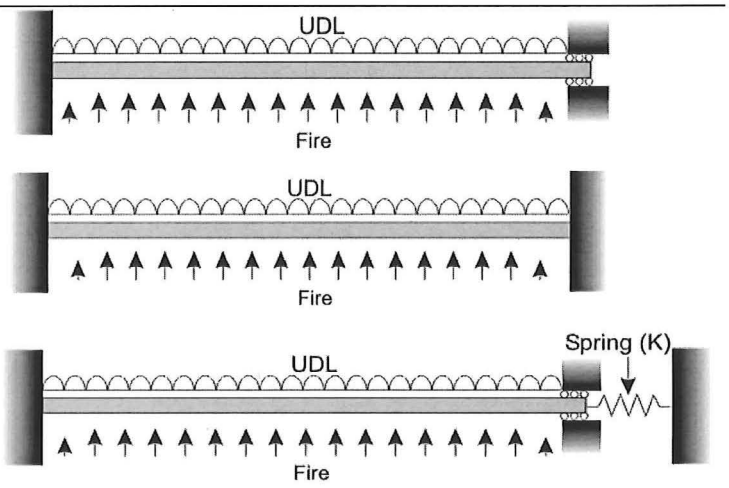

Figure 5-2: SAFIR models of rotationally restrained slabs.

3) Pin supports with moveable line of thrust

Horizontally restrained by a spring, position of line of thrust not fixed.

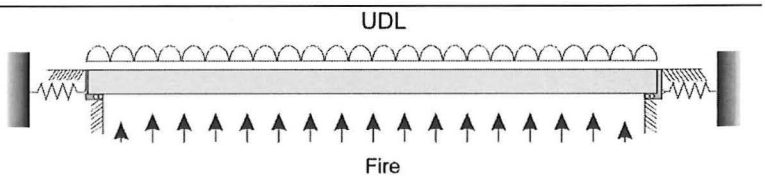

Figure 5-3: SAFIR model of pin-supported slab with moveable line of thrust.

In both Figure 5-1 and Figure 5-2, cases (a) represent slabs with no horizontal restraint and are free to move horizontally. Cases (b) represent the opposite extreme of case (a) with full horizontal restraint and cases (c) represent slabs with some horizontal restraint, restrained by an axial spring. The stiffness of the spring varies, depending on the stiffness of the support conditions, from being very low similar to cases (a), to full horizontal restraint, as in cases (b).

Position of line of thrust

For pin supported slabs shown in Figure 5-1, the line of thrust can be defined in the program by incorporating vertical rigid elements at the ends of the slab to introduce the eccentricity relative to the centroidal axis of the slab. This line of thrust is assumed to be fixed throughout the course of the fire. For the purposes of discussion, the position of the line of the thrust is measured as a distance, x_o, from the fire-exposed face (soffit) of the slab, as shown in Figure 5-4. For the analysis of the pin-supported slab, the position of the line of thrust at the supports will be varied from -25mm (25mm below the soffit of the slab) to 125mm above the soffit of the slab (refer to Figure 5-4). The purpose of analysing the different fixed positions of line of thrust is to model the behaviour of slabs with different support conditions and lines of thrust, as seen in Figure 3-14.

For the slab with full rotational restraint (Figure 5-2) and the pin supported slab with its line of thrust not fixed (Figure 5-3), the position of line of thrust is not fixed and moves across the depth of the slab during the course of the fire.

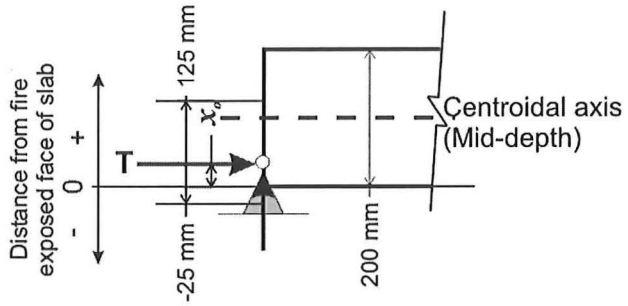

Figure 5-4: Range of different positions of line of thrust considered for pin-supported slabs.

Restraint stiffness

The slabs are modelled with different axial spring stiffnesses. The axial stiffnesses of the springs range from zero to fully restrained. The axial stiffness, k, is measured relative to the axial stiffness of the slab, such that 100% stiffness is equivalent to an identical additional slab at one end support (Equation 5-1).

$$\text{Axial restraint stiffness}, k = \frac{\text{Axial stiffness of supporting structure}}{\text{Axial stiffness of slab}} \times 100\% \qquad \textbf{Equation 5-1}$$

5.2.2. Properties of the slab

The slabs that are analysed in this chapter span 5 metres and have a depth of 200mm. The cross section of the slab that will be analysed is shown in Figure 5-5. For the purposes of discussion, a metre width of the slab is considered but in the computer analyses, only a 125mm wide strip with a single reinforcing bar at the top and bottom is modelled. This is to reduce the computational effort of the analysis.

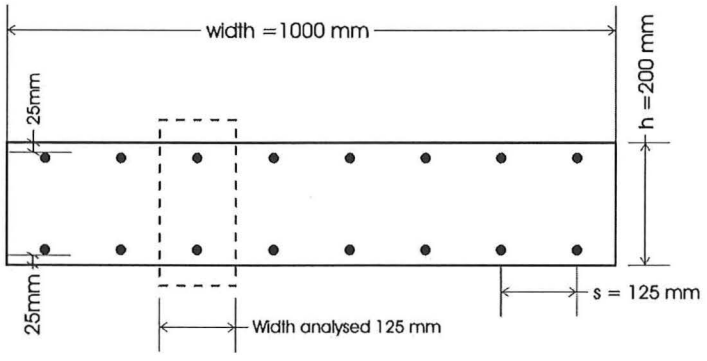

Figure 5-5: Cross section of the slab modelled with SAFIR.

The properties of the slab are as follows:

Slab geometry

Span, L:	5.0m
Depth, h:	200mm
Width, b:	1.0m
Aspect ratio, L/h:	25

Concrete properties

Compressive strength (ambient temperature) f'c:	30 MPa
Elastic modulus (ambient temperature), $E_{c,o}$:	18 GPa
Tensile strength, f'_t:	Zero
Concrete model (thermal and mechanical):	Siliceous aggregate (EC2, 1995)
Concrete cover, c_c:	25mm

Reinforcing steel properties

Yield strength (ambient temperature), $f_{y,o}$:	430 MPa
Elastic modulus (ambient temperature), $E_{s,o}$:	210 GPa
Steel model (thermal and mechanical):	Hot-rolled steel (EC2, 1995)
Bar diameter, d_b:	12mm
Bar spacing, s:	125mm (top and bottom)
Bar lengths	Continuous (top and bottom)

Loads

Self weight + Superimposed dead load, G	5.30 kN/m
Live load, Q	4.0 kN/m
Ultimate load, 1.2G + 1.6Q	12.8 kN/m
Fire load, 1.0G + 0.4Q	6.9 kN/m
Load ratio at fire conditions, r_{load}	0.34
Fire exposure	ISO 834 standard fire (4 hour duration)

5.2.3. Method of analysis

The analysis of the floor slabs was performed with SAFIR. The thermal analysis of the cross section is first performed to determine the temperatures across the slab. The variation of the temperature distributions in the slab with time are then used for the structural analysis.

Thermal analysis

Figure 5-6 (a) shows the finite element discretisation of the cross section of the slab. It shows a 125mm wide section of the slab. The thermal gradient of the slab, when exposed to the ISO standard fire from below, is shown in Figure 5-6 (b). Figure 5-7 shows the variation of the temperatures at the exposed surface, mid-depth and unexposed surface when the bottom surface was exposed to the ISO fire. The temperatures on the exposed face increase very rapidly during the initial stages but temperatures on the unheated surface do not rise until after the first hour. As the fire progresses, the rate of temperature rise on the heated surface decreased while the temperatures at mid-depth and on the unheated side slowly increase.

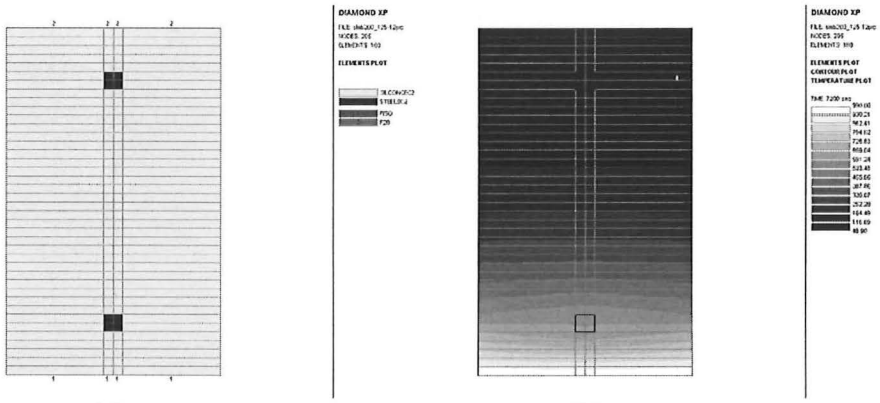

(a) (b)

Figure 5-6: Thermal analysis of a 125mm wide strip: (a) SAFIR discretisation of the slab, (b) Temperature distribution after a 2 hour exposure to the ISO fire.

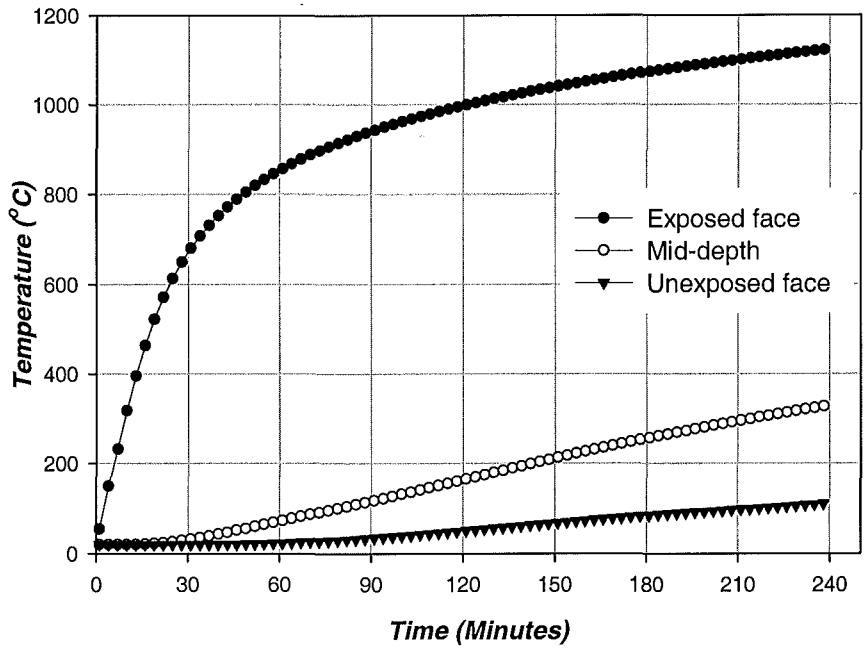

Figure 5-7: Temperature variation at the exposed face, mid-depth and unexposed face of the slab.

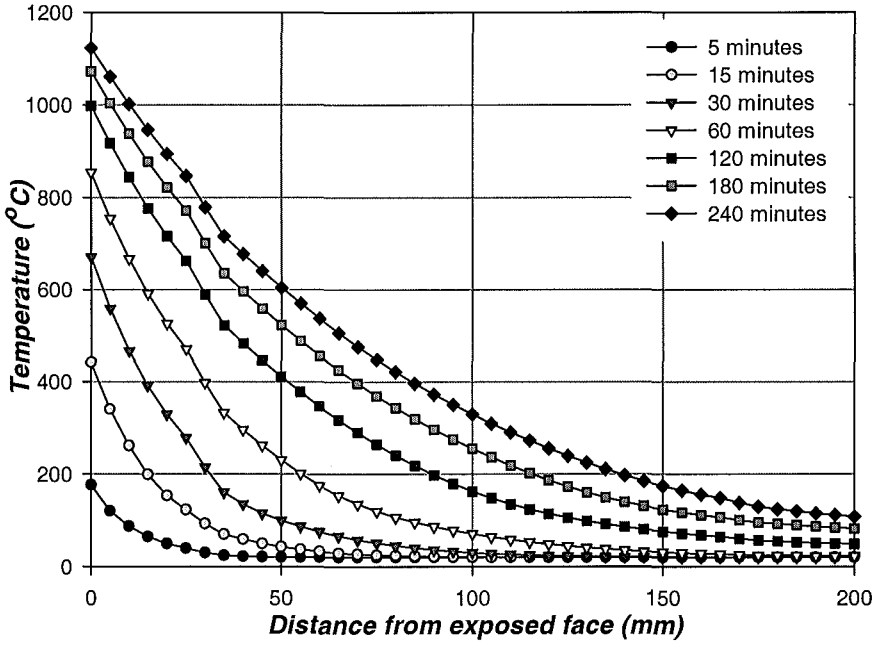

Figure 5-8: Temperatures across the 200mm thick slab during the 4 hour ISO fire exposure.

Figure 5-8 shows the temperatures across the 200mm thick slab during the 4 hour ISO fire. The graph shows very steep temperature gradients across the slab during the first 30 minutes of the fire. At 30 minutes, the temperature on the heated surface is 670°C but the unheated side still remains at ambient temperature. After 4 hours, the temperature gradient across the slab remained relatively steep even though the temperatures in the central region had already started to rise.

Structural model

The structural model used to analyse the slabs with the different configurations will be described in detail in each of the sub-sections. In all the analyses, the vertical deflections of the slabs are measured at the centroid of the slab section.

5.2.4. Assumptions

In addition to the assumptions described in sections 4.4.1 and 4.5, the following assumptions are also made during the analyses of the one-way slabs:

- The slabs behave purely as one-way slabs. Two-way action in the slabs is not considered.
- The fire exposure along the length of the slab is uniform.
- The centroidal axis of the slab remains constant and does not move during the fire.
- Localised shear failure of the slab is not considered in the analysis.

5.3. Pin-supported with full horizontal restraint

The behaviour of pin-supported slabs with full axial restraint is discussed here. The purpose of this analysis is to model precast slabs with fixed positions of line of thrust at the supports such as those seen in Figure 3-14. The analysis in this section serves to investigate the effect of different positions of line of thrust even though full axial restraint may not exist in real construction. Separate analyses will be conducted for different positions of line of thrust at the end supports, ranging from -25mm (25mm below the exposed face) to 125mm into the depth of the slab (refer to Figure 5-4). The position of the line of thrust is fixed for each analysis and does not change during the fire. The Concrete Structures Standard (SNZ, 1995) recommends a fire resistance rating for stability of 105 minutes for a simply supported one-way slab with 25mm cover.

5.3.1. Structural model

The slab is analysed with 2D analysis and is modelled as a beam, using 20 2D beam finite elements (Figure 5-9). The cross section of the slab is shown in Figure 5-6 and the slab is loaded with a uniformly distributed load. The different positions of line of thrust at the supports are modelled by imposing an eccentricity, z_o, relative to the centroidal axis of the slab elements, with vertical rigid elements (Figure 5-10). The slab is horizontally and vertically restrained at the end of the rigid element, as shown in Figure 5-10. Figure 5-10 also shows that only the bottom reinforcement was anchored into the end supports. The axial spring is modelled with a truss element with elastic material properties and is not exposed to the fire.

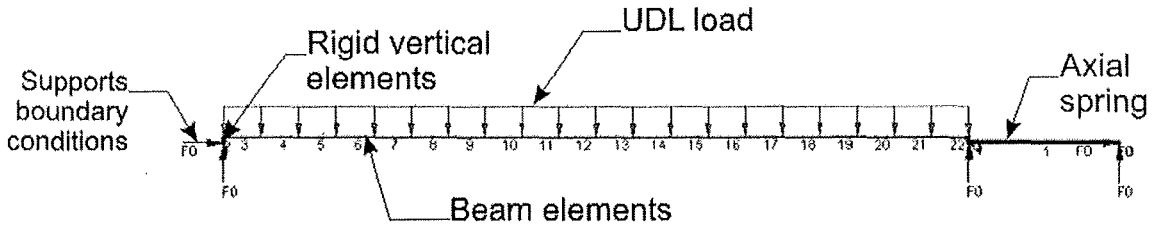

Figure 5-9: Discretisation of the slab with SAFIR for the structural analysis.

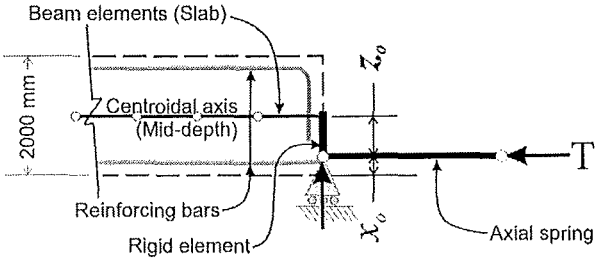

Figure 5-10: Detail of the end support for a pin-supported slab.

5.3.2. Midspan deflections and axial forces

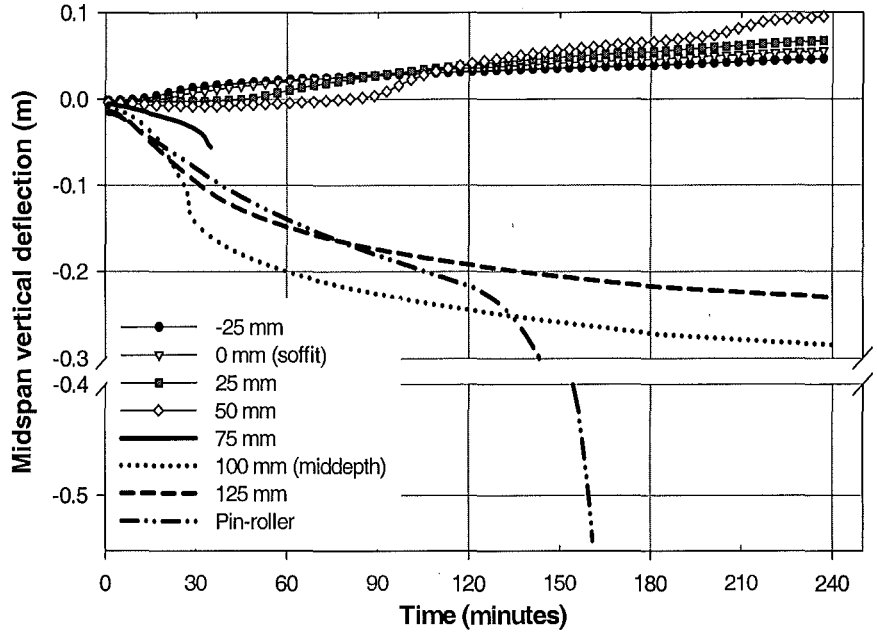

Figure 5-11: Midspan vertical deflection versus time.

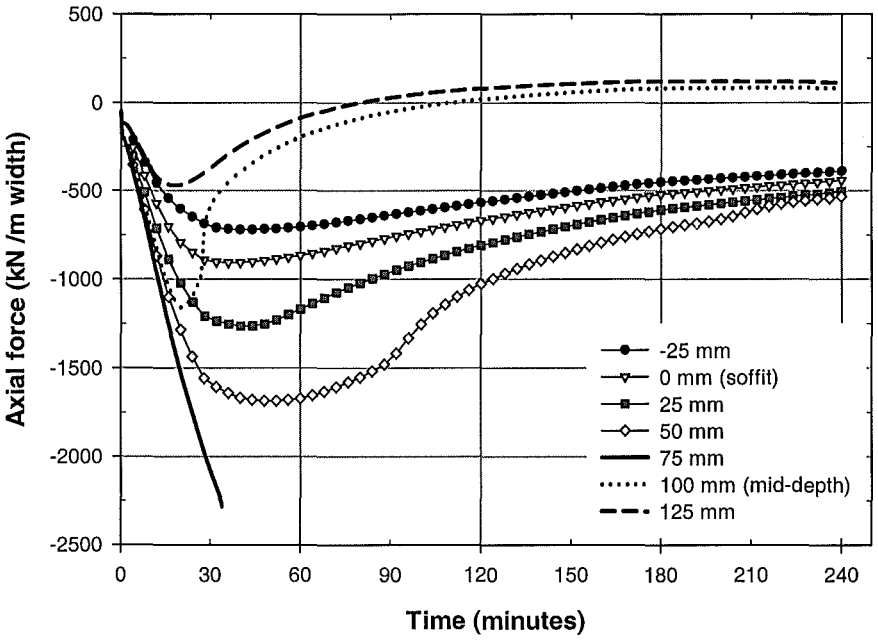

Figure 5-12: Axial force in the slabs versus time.

Figure 5-11 shows the variation of the midspan deflections of the slabs during the exposure to the ISO fire. Note that the slab deflections in the analyses are measured at the centroidal axis of the slab. Negative deflection is downward deflection and positive is upward. Figure 5-12 shows the variation of the axial forces in the slabs. Negative axial forces are compression

forces and positive are tension forces. The behaviour of the slab will be discussed in different sections.

Pin-roller slab

Figure 5-11 shows that an unrestrained simply supported slab on pin-roller supports gradually deflected downwards during the initial stages of the fire. At approximately 120 minutes, the deflection rate increased, leading to runaway failure. The initial deflection of the slab is due to the steep temperature gradient across the slab (refer to Figure 5-8). The steep temperature gradient produced non-uniform thermal expansion of the concrete across the depth of the slab, which resulted in the thermal bowing deflection. The large deflections at runaway failure were associated with the loss of strength and stiffness of the reinforcing steel at midspan, resulting in plastic hinge formation. There were no axial forces in the pin-roller slab because there is no horizontal end reaction.

Position of line of thrust, -25mm ≤ x_o ≤ 50mm

When x_o is located between -25mm (outside the depth of the slab) and +50mm, the slab showed very small sagging deflections during the initial stages of the fire. As the fire progressed, the sagging deflection of the slab changed to a hogging deflection shown by the upward deflection at midspan (Figure 5-11). These slabs remain in a hogging deflected shape (Figure 5-13), similar to an arch, until the end of the fire without collapse.

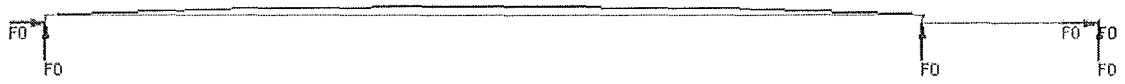

Figure 5-13: Final hogging deflected shape superimposed over the initial shape of the slab (x_o = 0mm).

Position of line of thrust, 75mm ≤ x_o ≤ 125mm

When x_o is located close to the centroidal axis, between 75mm and 125mm, the slabs behaved differently to the other slabs discussed previously. Figure 5-11 shows that these slabs sagged downwards and formed large vertical deflections. The analysis of a slab with x_o at 75mm stopped prematurely at 32 minutes. This is due to the program failing to converge to a solution when the slab snapped-through, immediately after a plastic hinge had formed at midspan.

When x_o is at 100mm (mid-depth) and 125mm, the behaviour of the slabs during the initial stages resembled the simply supported slab and deflected downwards at a much higher rate than the other slabs. Unlike the pin-roller slab, these two slabs did not exhibit a runaway failure and survived the fire for the entire duration of four hours. The slab with x_o at 100mm showed a sudden increase in the deflection rate after 28 minutes due to snap-through of the slab. The snap-through was accompanied by a sudden drop of the axial forces (see Figure 5-12) which resulted in the compression forces changing to tension. If the slab supports could not resist these tensile forces, the slabs would collapse and fail earlier than the pin-supported slabs after they had snapped through. Had the supports been unable to resist the tension forces, the slabs with x_o at 100mm and 125mm would have failed at 110 minutes and 80 minutes, respectively. However, the analyses assumed that the bottom reinforcing steel was anchored into the supports and the slabs could resist the tension forces. The poorer performance of the slab with the line of thrust acting at mid-depth (x_o =100mm) compared with the pin-roller slab is consistent with observations in the fire tests by Cooke (1993) (See section 3.5.2).

When the line of thrust at the supports is located just below the centroidal axis, the small eccentricity from the centroidal axis could not increase the flexural strength and stiffness of the slabs. When the line of thrust is located 25mm below the centroidal axis (x_o= 75mm), the behaviour of the slab lies in a bifurcation region where it could either pop-up and form a hogging deflected shape, or snap-through and form large sagging deflections. The graph shows substantially higher compression forces in this slab than the other slabs at the time the analysis stopped.

5.3.3. Bending moments

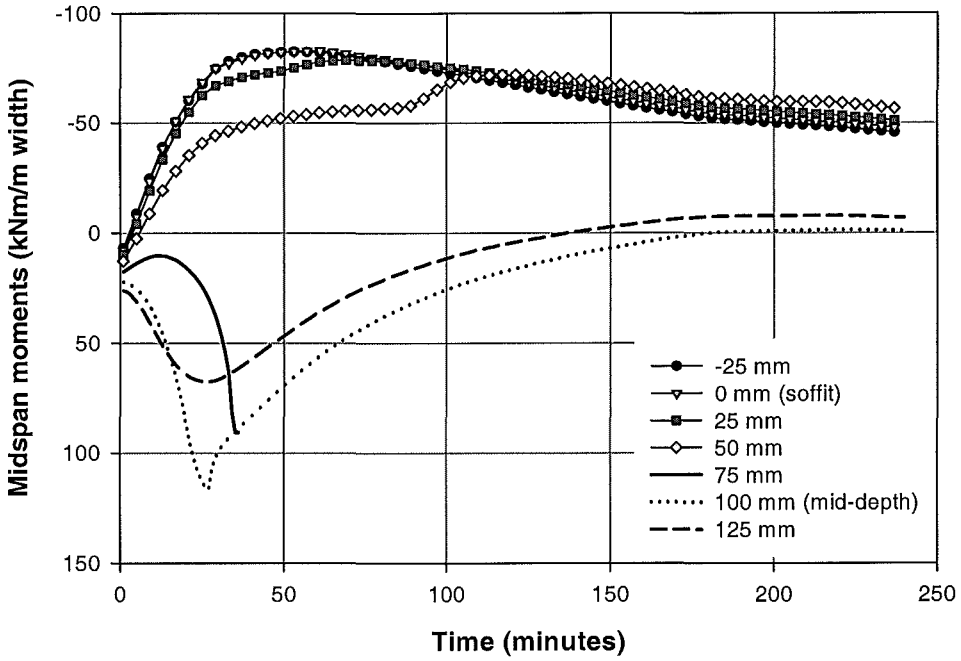

Figure 5-14: Midspan bending moments versus time.

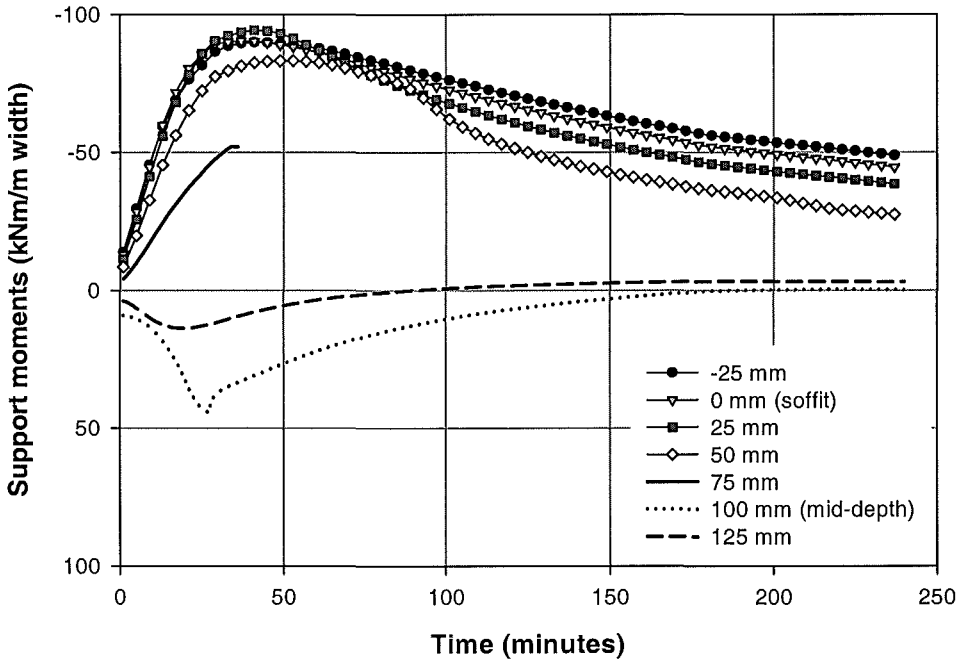

Figure 5-15: Support bending moments versus time.

Position of line of thrust, -25mm ≤ x_o ≤ 50mm

Figure 5-14 and Figure 5-15 show the variation of the bending moments at midspan and the supports, respectively. The hogging moments are negative and the sagging moments are positive. When x_o lies between -25mm and +50mm, the hogging moments at the supports and

midspan increased very rapidly during the initial stages and reached a peak after approximately 40 minutes. The hogging moments decreased gradually until the end of the fire. The moments in the slabs are internal moments which are caused by the axial forces acting about the eccentricity relative to the centroidal axis.

The hogging moments reached their peak when the bottom steel at the supports yielded in compression, thus preventing further increase of the hogging moments. The bottom steel at the supports yielded in compression rather than the top steel yielding in tension, due to the high temperatures at the bottom surface which decreased the compressive strength of the steel. The top steel remained cool and did not suffer significant strength degradation. After the hogging moments had reached their peaks, the moments started to decrease because of the decreasing compressive strength of the steel and concrete at the fire exposed face.

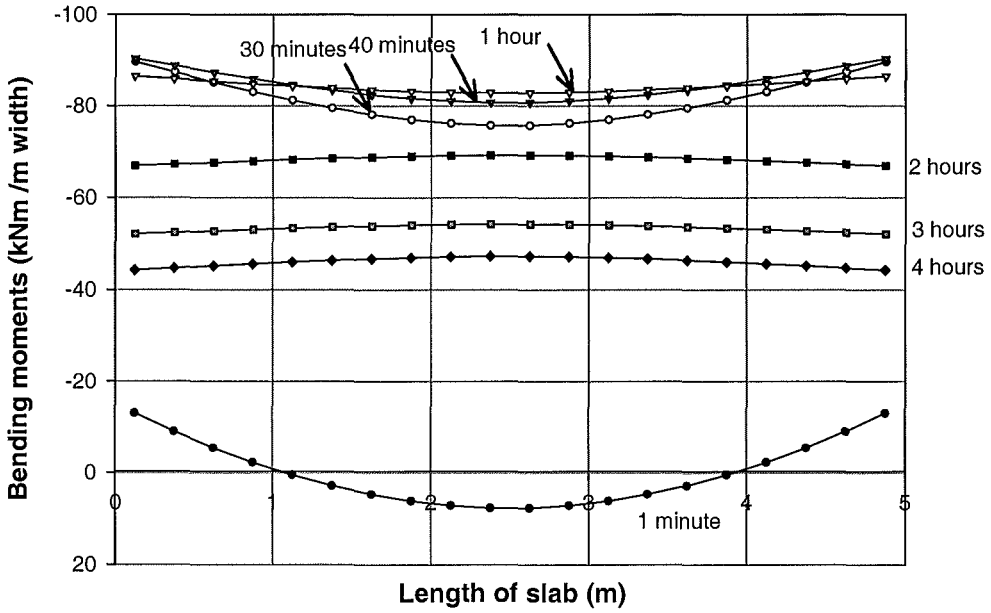

Figure 5-16: Bending moment diagram at different times (Line of thrust, x_o=0mm and full horizontal restraint).

Figure 5-16 shows the bending moment diagram of the slab during the fire with the line of thrust located at the soffit of the slab, i.e.: $x_o = 0$. During the initial stages (1 minute), negative moments have formed near the end supports. The negative moments, which were due to the thrust force T acting at a distance z_o below the centroidal axis, reduced the positive moments which were imposed by the gravity loads. As the fire progressed, the shape of the bending moment diagram changed very rapidly. By 30 minutes, the moments along the slab had become negative hogging moments. Between 40 minutes and 1 hour, the negative moments at

midspan had progressively decreased as a result of the slab deflecting into the shape of an arch. After two hours, larger negative moments formed at midspan than at the support due to the M_Δ moments, caused by the hogging deflection of the slab coupled with the external thrust force. The moments along the entire length of the slab remained negative until the end of the fire with positive flexural strength unutilised to resist the gravity loads.

Position of line of thrust, 75mm ≤ x_o ≤ 125mm

When x_o is located at 100mm (mid-depth), Figure 5-14 shows that the positive moments at midspan increased very rapidly during the initial stages until it reached a peak at 25 minutes. After reaching the peak, the positive moments decreased very suddenly and gradually reduced to zero at the advanced stages of the fire. The peak corresponded to a positive plastic hinge forming at midspan. When the plastic hinge formed, the deflections increased very suddenly and the slab sagged into a catenary. The loads were then resisted by tensile action, rather than by bending action. Although the theoretical flexural strength at ambient conditions was 60kNm/m, the calculated peak moment at midspan when the plastic hinge formed was in excess of 100kNm /m. The increase of the positive flexural strength of the slab was due to the strength enhancement by the compressive restraint forces.

When x_o is at 75mm, a positive plastic hinge formed at midspan due to the large positive moments at midspan. The positive plastic hinge formed in spite of the presence of substantial negative moments at the supports (Figure 5-15) which would have reduced the positive moments. However, large positive moments due to the compressive forces (T) coupled with the deflections (Δ) exceeded the flexural capacity at midspan, resulting in a plastic hinge forming at the time the analysis stopped.

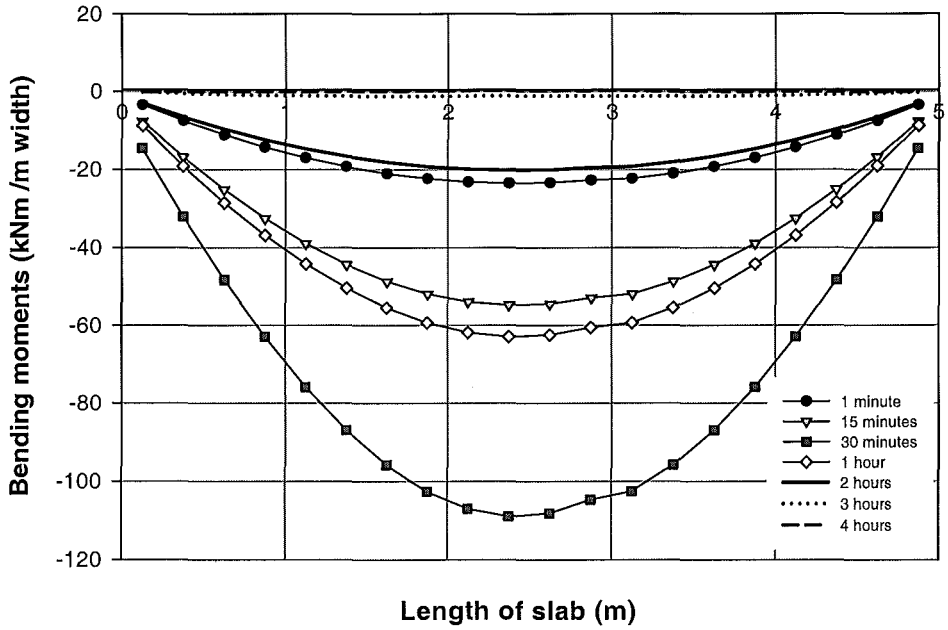

Figure 5-17: Bending moment diagram at different times (Line of thrust, x_0=100mm and full horizontal restraint).

Figure 5-17 shows the variation of the bending moment diagram for the slab with x_o at 100mm (mid-depth). The bending moment increased very rapidly and reached its peak at 30 minutes. After that, it gradually diminished as the slab deformed into a catenary. The shape of the bending moment diagram remained positive throughout the fire because the line of thrust of this slab coincided with the centroidal axis of the slab. Thus, there was no eccentricity which formed negative moments in the slab.

When x_o is at 125mm, the positive moment reached a maximum of 60kNm/m when a plastic hinge formed. This is equal to its theoretical unrestrained flexural strength. In this case, the compressive axial forces in this slab were not large enough to increase the flexural strength of the slab.

5.3.4. Conclusions

The analyses of the pin-pin slabs with full horizontal restraint have shown that:

- The behaviour of the slabs is very sensitive to the position of line of thrust relative to the centroidal axis of the slab.
- Compressive axial restraint is beneficial to the slab if the line of thrust is located well below the centroidal axis. Compressive restraint in these slabs will result in small and upward deflections during the fire exposure.
- Compressive axial restraint is not beneficial to the fire resistance of the slab if the line of thrust is located close to the centroidal axis. This will produce large sagging deflections (L/20) during the fire exposure, with axial tensile forces generated late in the fire. Under large vertical deflections, the high compressive restraint will increase the deflections of the slab and decrease the time to plastic hinge formation.

5.4. Pin-supported with varying axial restraint

This section investigates the behaviour of a pin-supported slab with different levels of horizontal restraint. The position of the line of thrust at the supports, x_o, is held constant, at 50mm above the exposed face of the slab. The stiffness of the spring is varied from 1% to full horizontal restraint. A pin-roller slab is plotted for comparison. The structural model is based on the model shown in Figure 5-9 of section 5.3.1.

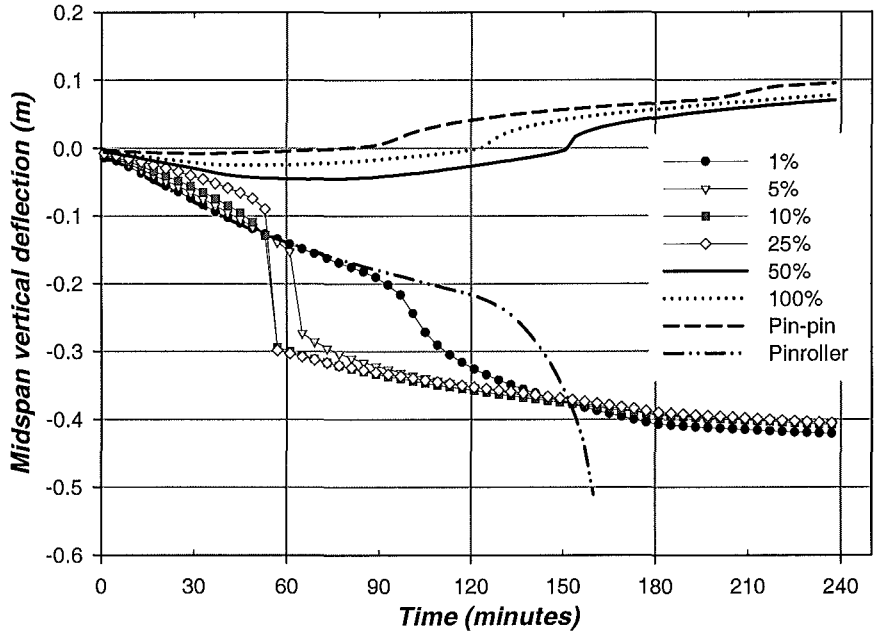

Figure 5-18: Midspan vertical deflection versus time, pin-supported x_0=50mm.

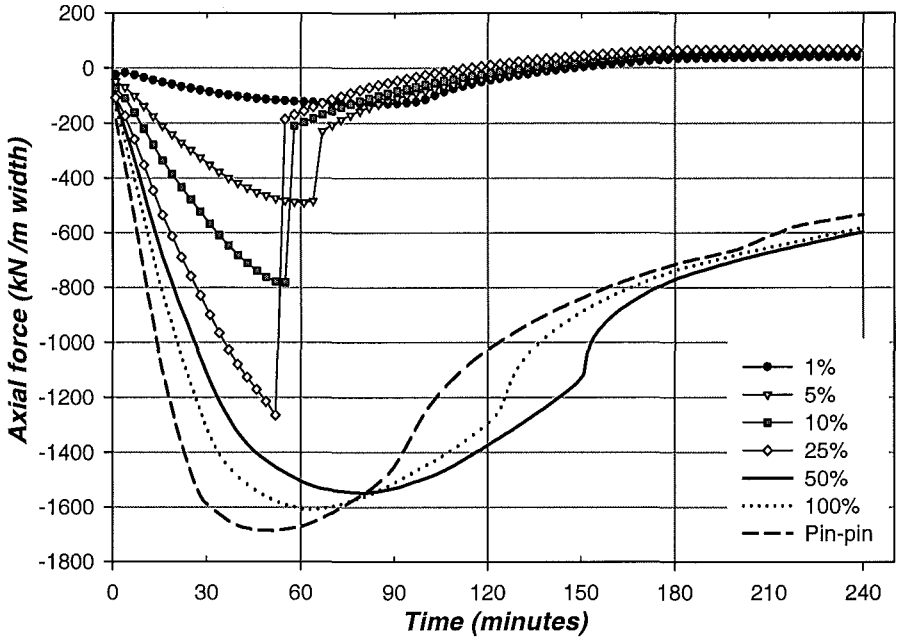

Figure 5-19: Axial force versus time, pin-supported x_0=50mm.

Figure 5-18 shows the behaviour of the pin-supported slab with different levels of spring stiffness. The behaviour of the slabs with different levels of restraint can be classified into two groups: $k \leq 25\%$ and $k > 25\%$.

5.4.1. Spring stiffness, $1\% \leq k \leq 25\%$

Figure 5-18 shows that with 1% spring stiffness (k), the slab behaved very similarly to the pin-roller slab during the initial stages. Just after 90 minutes, the deflections increased very suddenly due to a minor snap through of the slab. Figure 5-19 shows that the axial force of the slab increased very slowly and dropped off when the deflection rate increased at 90 minutes.

When the spring stiffness ranges from 5% to 25%, the drop of the midspan deflections due to snap through became increasingly more violent. The rate of rise of the compressive axial forces increased proportionately with spring stiffness, resulting in large compressive axial forces in the slabs. When snap-through occurred, the large deflections relieved the compressive restraint forces shown by the marked decrease of the compressive forces in Figure 5-19. The slabs subsequently deformed into a catenary which led to tensile forces forming in the slabs. The slabs will collapse if the supports are unable to resist the tensile forces.

5.4.2. Spring stiffness, $50\% \leq k \leq$ fully restrained

When the stiffness of the spring is increased above 50%, the slabs exhibit a different nature. They showed an initial downward deflection during the first hour. After this, the sagging deflections decreased and the slab eventually deflected upwards, forming a shape of an arch. None of these slabs collapsed and remained in hogging deflection until the end of the simulation. A bifurcation region lies between 25% and 50% representing a transition of behaviour where the slab would form large vertical deflections when the stiffness is less than 25% or upward hogging deflections when the stiffness is greater than 50%.

5.4.3. Discussion

Under small deflections, compressive forces have a significant role of increasing the flexural stiffness and strength of the slab. If the slab continues to deflect, as a result of thermal bowing and loss of stiffness, a sudden 'snap-through' of the slab may occur. The snap-through causes the compressive forces to drop very significantly into tension and changes the load resistance of the slab from bending action to catenary action. In some cases, SAFIR terminated its analysis as it was unable to accommodate the sudden drop of the axial forces.

Snap-through of a fire-exposed slab occurs only if the slab is sufficiently rigidly restrained. It also depends on the position of the line of thrust. If the slab is highly restrained and the line of thrust is close to the exposed face of the slab, it will pop-upwards. If its line of thrust at the supports is close to the centre of gravity, the high axial forces will cause a violent downward snap-through. If the slab is lightly restrained, the axial forces in the slab may not be sufficient to cause snap-through, so the slab will deflect in a gradual trend, as a pin-roller slab.

5.4.4. Conclusions

The analyses of the pin-supported slabs with its line of thrust located 50mm from the bottom exposed face have shown that:

- The axial restraint force generated during the fire is dependent on the axial stiffness of the support system. High axial stiffness produces high axial forces.
- For pin-supported slabs with their line of thrust fixed and located close to the soffit (less than 50mm above the soffit), high axial restraint ($k \geq 50\%$) produces good behaviour and high fire resistance.
- With intermediate or low axial restraint stiffness ($k \leq 25\%$), the slab will deform into a catenary resulting in axial tensile forces being generated. If the slab does not have sufficient axial tensile capacity at the supports to resist the tensile forces, it will collapse.

5.5. Pin-supported with varying axial restraint and decaying fire

This section investigates the behaviour of a restrained pin-supported slab subjected to the ISO fire with a decay phase. The slab is subjected to varying restraint stiffnesses and the line of thrust at the supports is fixed at 50mm above the soffit. The decay phase occurred 60 minutes after the initial growth phase and is defined as a linear reduction of the fire temperature. The rate of the temperature reduction is shown by Equation 5-2 (Feasey et al., 2002):

$$\frac{dT}{dt} = \left(\frac{dT}{dt}\right)_{ref} \sqrt{\frac{F_v / 0.04}{b/1900}} \qquad \textbf{Equation 5-2}$$

The reference decay rate, $(dT/dt)_{ref}$, is based on the Eurocode and is equal to 625°C/hour for fires less than 30 minutes, and decreases linearly to 250°C/hour for fires burning greater than 2 hours. The variables F_v and b are the ventilation factor and square root of the thermal inertia of the compartment linings, respectively. Assuming that the ventilation factor F_v is 0.04 and b is 1900 $Ws^{0.5}/m^2K$ for a concrete compartment lining, Equation 5-2 would give a decay rate equal to the reference decay rate, shown in Equation 5-3. For a 60 minute fire exposure, the decay rate would be 500°C/hour.

$$\frac{dT}{dt} = \left(\frac{dT}{dt}\right)_{ref} = 500°C \qquad \textbf{Equation 5-3}$$

5.5.1. Slab temperatures

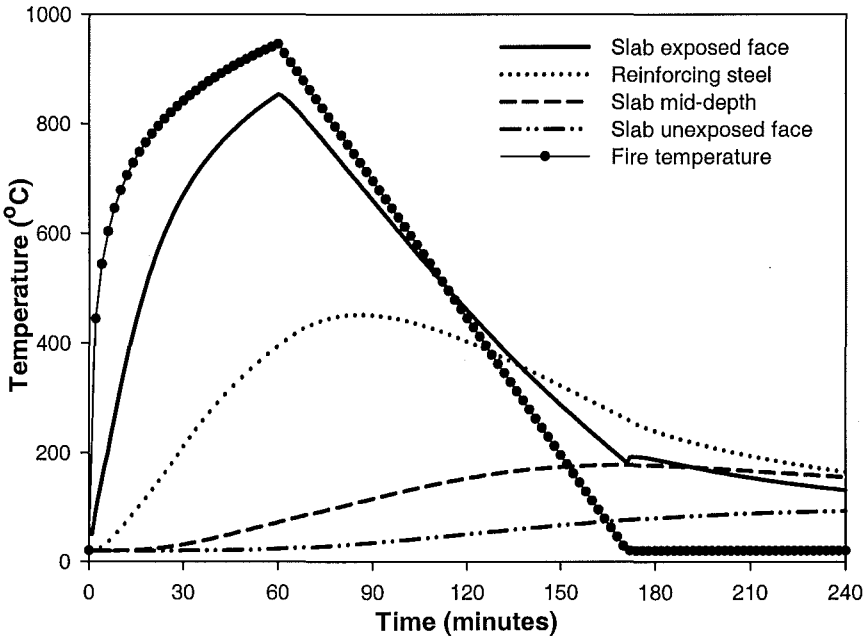

Figure 5-20: Temperatures in the slab exposed to the ISO fire with a decay phase.

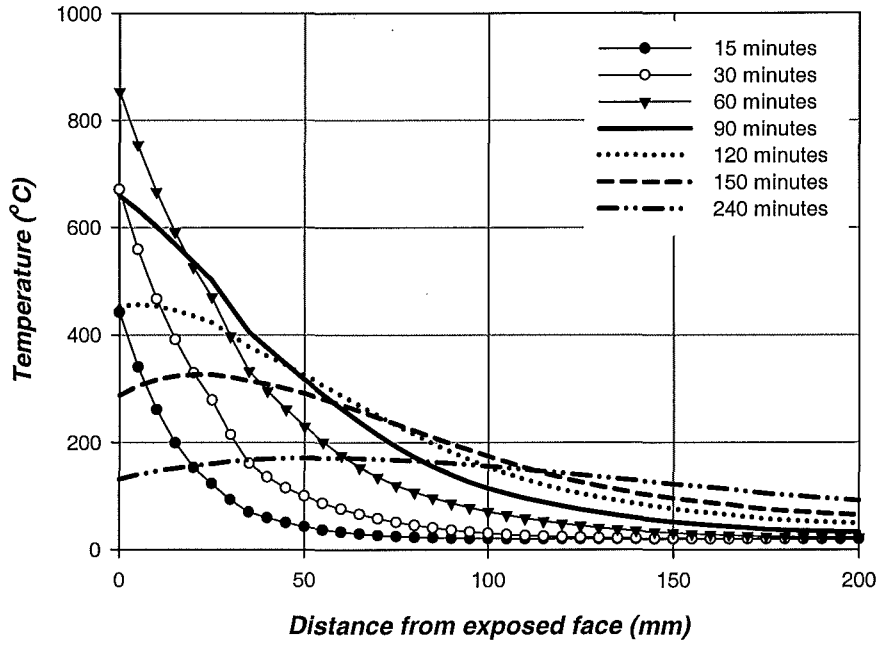

Figure 5-21: Temperature distribution in the slab under the decaying fire.

Figure 5-20 shows the temperatures of the ISO fire with a decay phase occurring 60 minutes after the burning phase and the temperatures at various locations in the 200mm concrete slab. The graph shows that the temperature at the exposed face increased in a similar trend to the fire temperatures while the temperatures further from the exposed face lagged behind. Beyond 2 hours, the temperatures across the entire depth of the slab were higher than the fire temperatures, even though the fire had already decayed. Figure 5-21 shows the distribution of the temperatures in the slab during the decaying fire. The figure shows that during the decay phase, the temperatures at the exposed face dropped off while the temperatures further from the exposed face still showed a slight increase. After 4 hours, the temperature distribution in the slab was almost constant.

5.5.2. Midspan vertical deflections

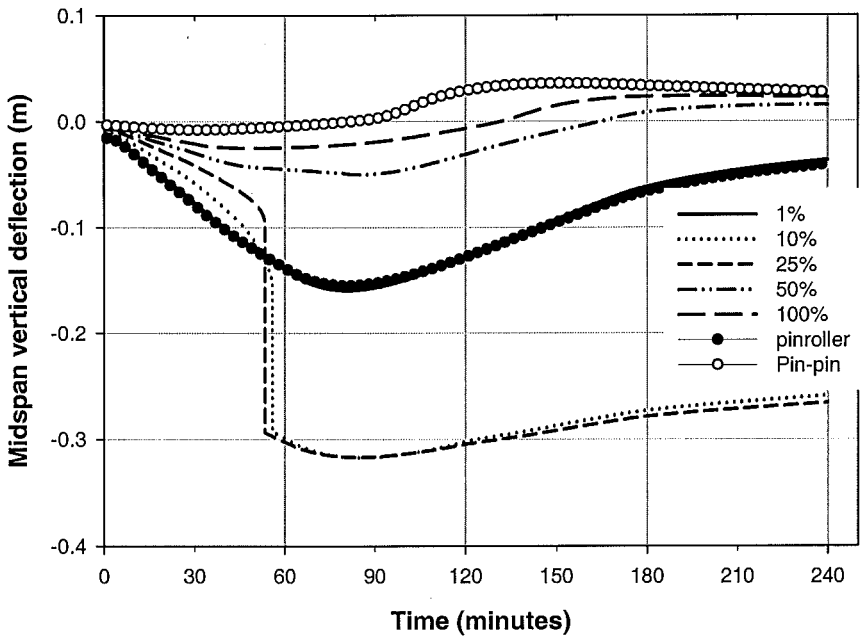

Figure 5-22: Vertical deflection of pin-supported slabs after exposure to the ISO fire with a decay phase.

Figure 5-22 shows the midspan vertical deflections of slabs subjected to the decaying fire. The graph shows that the fully restrained slab (pin-pin) briefly deflected downwards during the initial stages of the fire. After 30 minutes it gradually deflected upwards and formed a hogging deflected shape. The slab reached its peak hogging deflection of +30mm at 150 minutes. After that, it deflected downwards again in a linear trend as the slab started to cool. The reduction of the hogging deflections was due to the reduction of the thermal strains in the slab and the thermal thrust force at the supports.

This similar behaviour was also observed in the slabs with restraint stiffnesses as low as 50%. At 50% axial stiffness, the slab deflected downwards at a faster rate during the initial stages, forming larger deflections than the fully restrained slab. This trend is similar to the slabs analysed without the decay phase (See section 5.4). This slab continued to deflect downwards even when the fire had already decayed after 60 minutes. It eventually deflected upwards after approximately 90 minutes and formed a hogging shape after 165 minutes.

When the restraint stiffness was reduced to 25% and 10%, the deflection trend of the slabs started to diverge, and resulted in snap-through before the decay phase started. This behaviour is identical to that seen in section 5.4 since snap-through occurs before the fire started to

decay. The slabs formed large vertical deflections as they deformed into catenary mode. The downward deflection continued after snap through until approximately 85 minutes. The slab started to deflect upwards slightly, reducing the sagging deflections, due to the decreasing temperatures.

With 1% spring stiffness, the slab behaved in an identical manner to the *pin-roller* slab. The differences between the two slabs cannot be seen on the plot. During the initial stages, both slabs deflected linearly at a faster rate than the other slabs. Due to the lower axial restraint stiffness, the two slabs were able to deflect more freely resulting in higher rates of vertical deflection. After approximately 80 minutes, the slabs started to deflect upwards due to the decreasing temperatures and thermal strains in the slab. After 4 hours, the cooling of the slab had reduced the midspan deflections to 40mm.

5.5.3. Axial forces

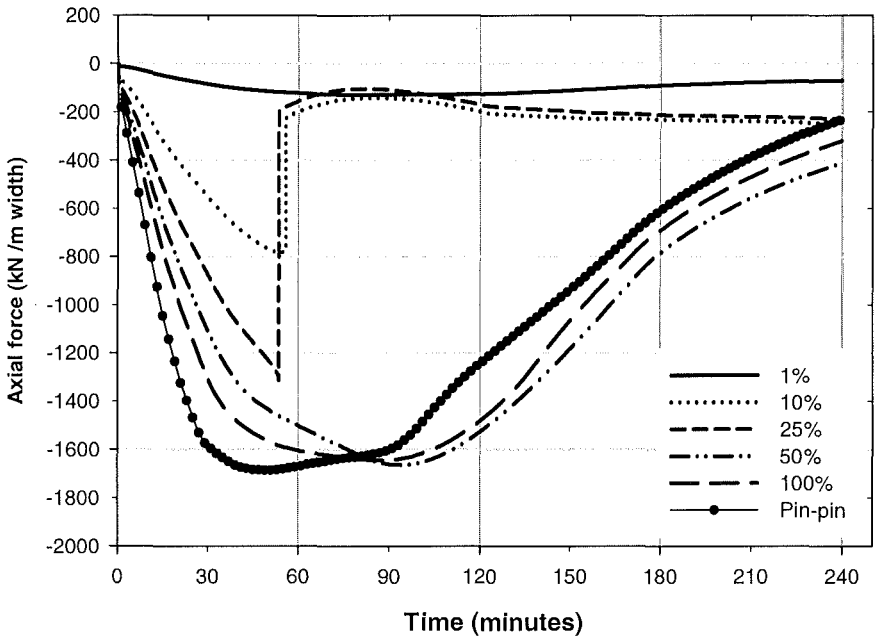

Figure 5-23: Axial forces in slab after exposure to the ISO fire with a decay phase.

Figure 5-23 shows the axial forces in the slabs exposed to the ISO fire with the decay phase. The graph shows that the axial forces in the slabs with high levels of restraint (*Pin-pin*, 100% and 50%) increased linearly during the initial stages of the fire and approached a plateau in a non-linear trend. The peaks of the axial forces corresponded to compressive yielding of the bottom steel and due to the slabs deflecting upwards. In the *pin-pin* slab, the axial forces

decreased very gradually between 30 minutes and 90 minutes due to the slab deflecting upwards into hogging deflection. After 90 minutes, the axial forces decreased at a higher rate in a similar trend to the slabs with 50% and 100% restraint stiffness. The higher decreasing rate was caused by contraction of the slabs at the supports when the temperatures decreased.

The compressive axial forces in the slabs with 25% and 10% restraint stiffness increased rapidly as the slabs deflect downwards during the initial stages of the fire. When snap through occurs, the compressive forces decreased very suddenly as the slabs deformed into a catenary. Even after the slabs had deformed into a catenary, low compressive forces were still present in the slab rather than tension forces as seen in section 5.4.

5.5.4. Conclusions

The analyses in this section have shown that the behaviour of the pin-supported slab in a real fire is no worse than in a long ISO fire. In many cases, better slab behaviour was observed in the decaying fire compared with the long ISO fire.

5.6. Rotationally restrained slabs with varying axial restraint

The behaviour of a single span slab with full rotational restraint at both end supports and various amounts of horizontal restraint is discussed in this section. The purpose of this is to simulate continuous slabs with various amounts of axial restraint. The axial restraint stiffnesses range from zero horizontal restraint (*fix-slide*, see Figure 5-2a) to full horizontal restraint (*fix-fix*, see Figure 5-2b). A slab with rotational restraint at both end supports and 25mm concrete cover has a fire resistance rating of 180 minutes, based on the Concrete Structures Standard (SNZ, 1995). The top and bottom reinforcing bars are assumed to be continuous in the slab and are connected to the end supports. The effect of curtailment of the top reinforcing bars will be discussed in section 5.7. Previous analytical work on fire exposed continuous slabs has been reported by Anderberg (1978).

5.6.1. Structural model

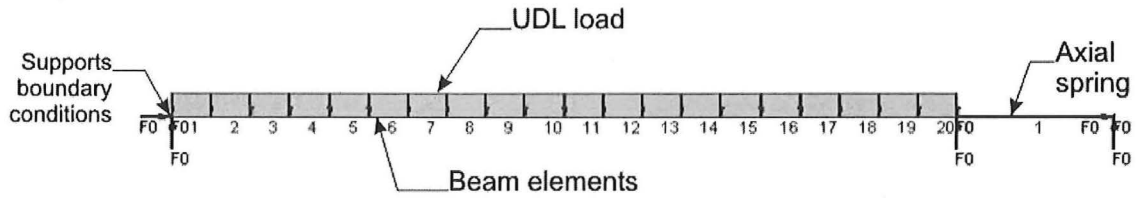

Figure 5-24: SAFIR structural model of the slab with full rotational restraint at both end supports.

Figure 5-24 shows the structural model of the slab with full rotational restraint at both end supports. The model is similar to that of the pin-supported slabs, utilising beam elements to represent the slab and an axial spring to model the axial restraint of the supporting structure. Unlike the pin-supported slabs, the rotations at the end supports of this slab are fixed and the node-line of the axial spring coincides with the node-line of the beam elements, as shown in Figure 5-25. To model flexural continuity of the slab, the reinforcing bars are assumed to be connected to the supports as shown in Figure 5-25.

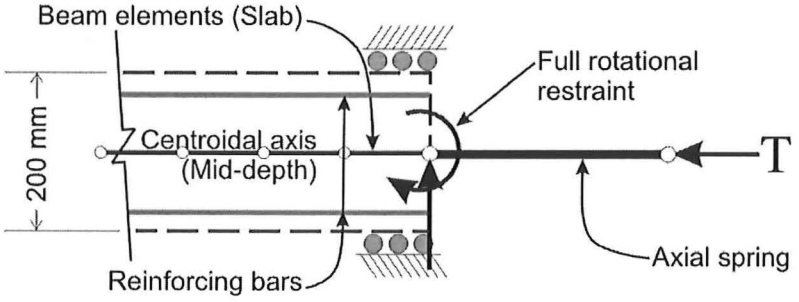

Figure 5-25: Detail of end support for the slab with rotationally fixed supports.

5.6.2. Midspan vertical deflections

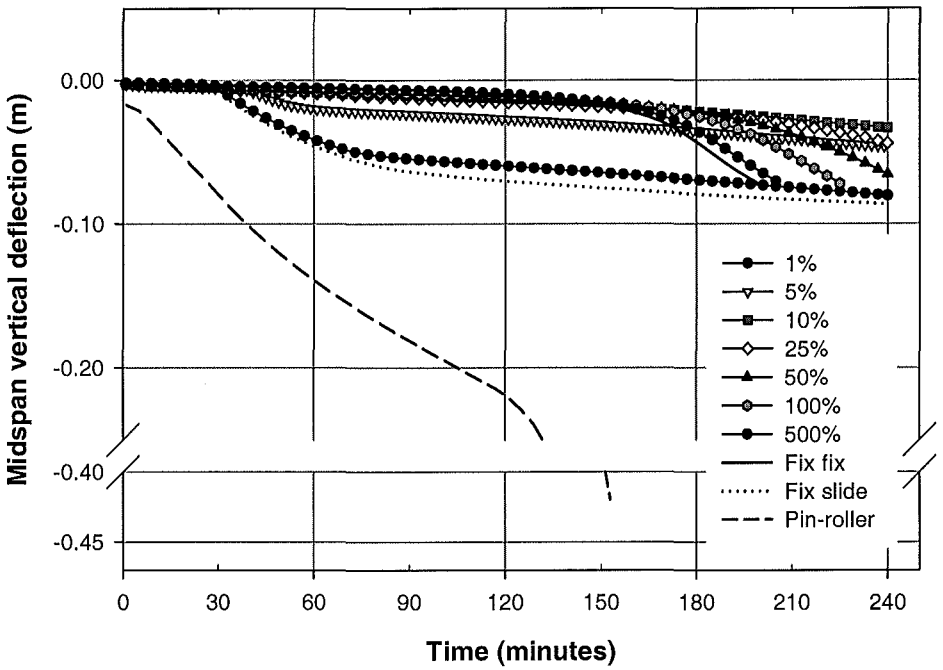

Figure 5-26: Midspan vertical deflection versus time.

Figure 5-26 shows the midspan vertical deflections of the slabs with full rotational restraint at the supports with various amounts of horizontal restraint. Also plotted on the same graph is the vertical deflection of a pin-roller slab. The graph shows that slabs with rotational restraint at the end supports have much better performance under fire conditions compared with the pin-roller slab. This behaviour is consistent with those reported by other researchers (CRSI, 1980; Gustaferro et el., 1989; Buchanan, 2001; Fleischmann et al., 2002) but is different to that presented by FIP (1986).

Spring stiffness, 0% (fix-slide) ≤ k≤ 5%

Figure 5-26 shows that slabs with low axial restraint (*fix slide*, 1% and 5%) initially showed very small midspan deflections until about 30 minutes when the deflection rate showed a sudden increase. The increase of the deflection rate in the 5% slab was not as obvious as the *fix-slide* and 1% slabs. After this, the slabs continued to deflect at a gradual and linear rate until the end of the fire and did not suffer collapse. The final deflections of the slabs were below 100mm.

Spring stiffness, 10% ≤ k≤ full horizontal restraint (fix-fix)

When the spring stiffnesses ranged from 10% to full horizontal restraint, the slabs showed very small deflections during the early stages of the fire until 165 minutes, when the deflection rates of the slabs started to increase. When the spring stiffness ranged from 10% to 50%, the slabs lasted the entire 4 hour fire exposure without collapse. However, when the spring stiffness was increased beyond 50%, structural failure of the slabs occurred at the advanced stages. The time to collapse of the slab decreased with increasing spring stiffness. The discussion of the failure mechanism will be presented in section 5.6.5.

5.6.3. Axial forces

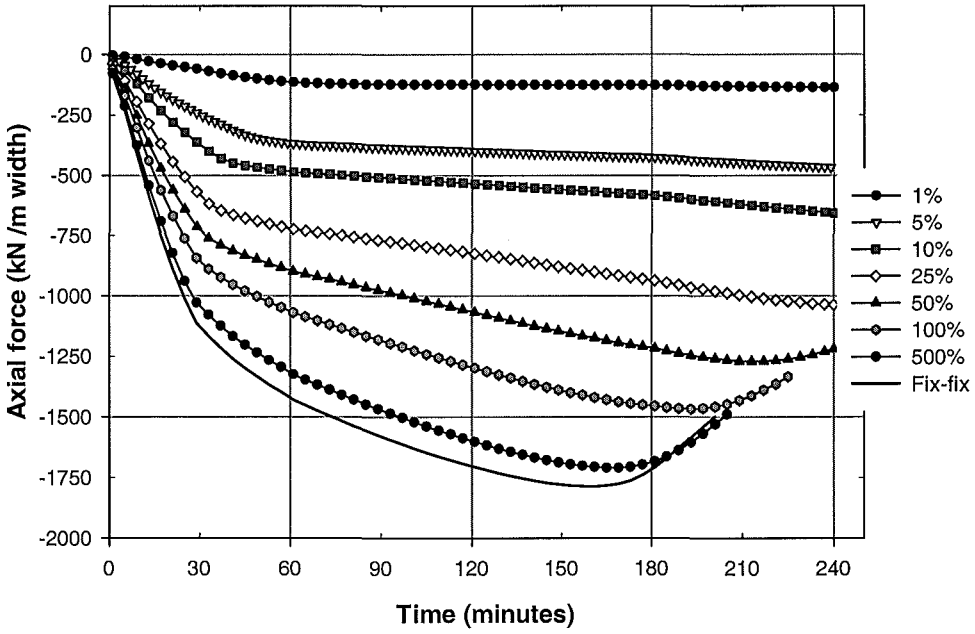

Figure 5-27: Axial force in slabs versus time.

Figure 5-27 shows the variation of the axial forces in the slabs. All the slabs remained in compression throughout the entire duration of the fire. The compressive axial forces in all the slabs showed a bilinear increase with time. The slabs with spring stiffnesses above 50% showed a decrease at the later stage of the fire, but still remained in the compression region. The decrease of the axial forces in the slabs with spring stiffness higher than 50% was due to the increase of the deflections at the advanced stages, prior to failure.

5.6.4. Bending moments

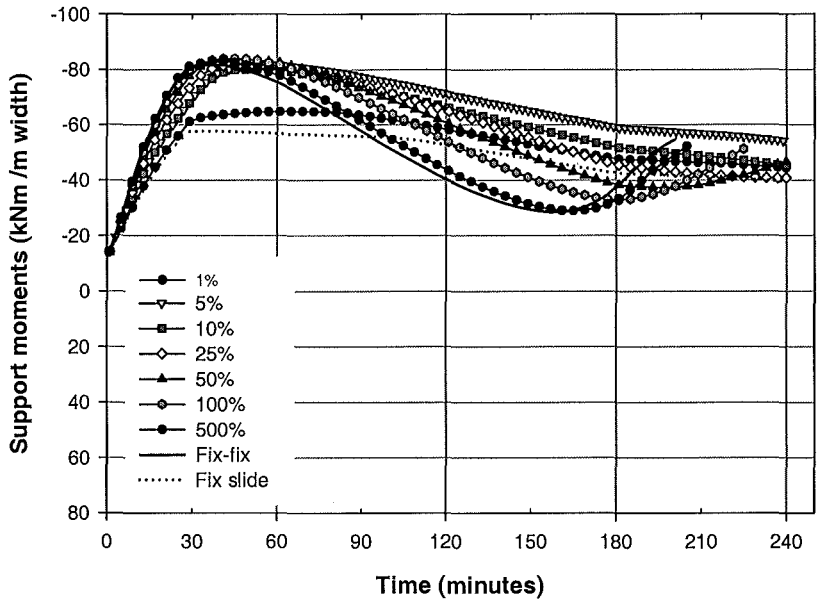

Figure 5-28: Support bending moments versus time.

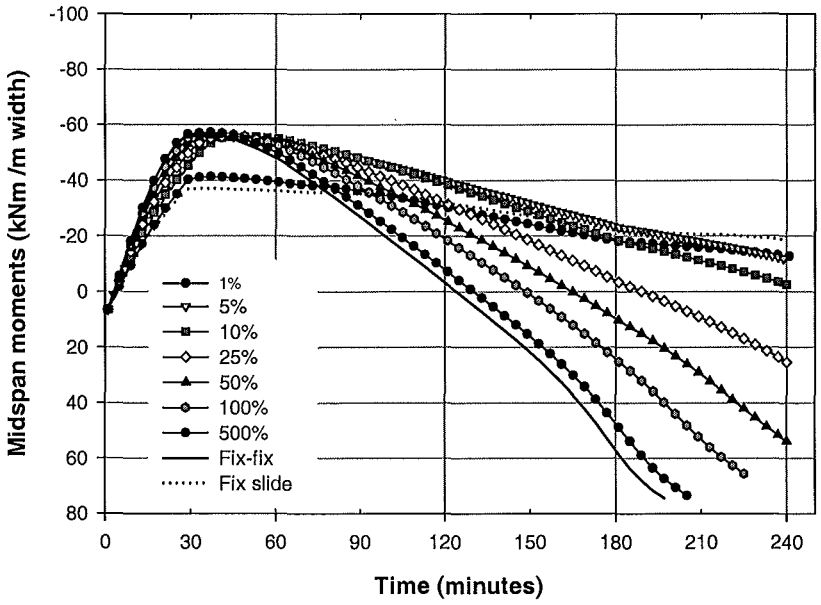

Figure 5-29: Midspan bending moments versus time.

Figure 5-28 and Figure 5-29 show the variation of the bending moments at the supports and midspan of the slab, respectively.

Spring stiffness, k = 0% (fix-slide) and 1%

The graphs showed that during the initial stages of the fire, the bending moments at the supports and midspan increased very rapidly in a linear trend until they reached a plateau. After that, the moments levelled off and slowly decreased. The peak of the negative moments was due to a negative plastic hinge forming at the supports. The positive moments were fully redistributed which prevented a plastic hinge forming at midspan and subsequent collapse due to a mechanism in the slab.

Spring stiffness, 5% $\leq$ k $\leq$ full horizontal restraint (fix-fix)

With spring stiffness ranging from 5% to full restraint, the negative moments at the supports and midspan initially increased rapidly until they reached a peak and then dropped off. The peak was due to compressive yielding of the bottom steel at the supports, which prevented further increase of the negative moments. The support moments of the slabs with stiffnesses greater than 50% increased again at the later stage of the fire (after 150 minutes) while the midspan moments continued to decrease. The increase of the negative moments at the supports at the final stages was due to moment redistribution initiated by a plastic hinge forming at midspan. This caused the slab to behave as two slabs which cantilevered from the end supports. The increase of the deflections, coupled with the compressive axial forces, increased the M_{Δ} moments and caused the positive moments to increase.

5.6.5. Reinforcing steel stresses

This section describes the variation of the reinforcing steel stresses in the rotationally restrained slabs. The discussion will be focussed on the slabs horizontally restrained with 1% spring stiffness and the fully fixed slab. In the graphs, the tension stresses are positive and compression stresses are negative. The stresses of the top (unexposed face) and bottom (exposed face) reinforcing steel at the supports and midspan of the slab are plotted, along with their respective proportional (f_p) and yield (f_y) limits. These limits change with time and temperature according to the material properties of the Eurocode (EC2, 1995). The limits for the top and bottom steel are plotted separately because they decrease at different rates during the fire due to the faster heating of the steel strength at the exposed face.

Spring stiffness, k=1%

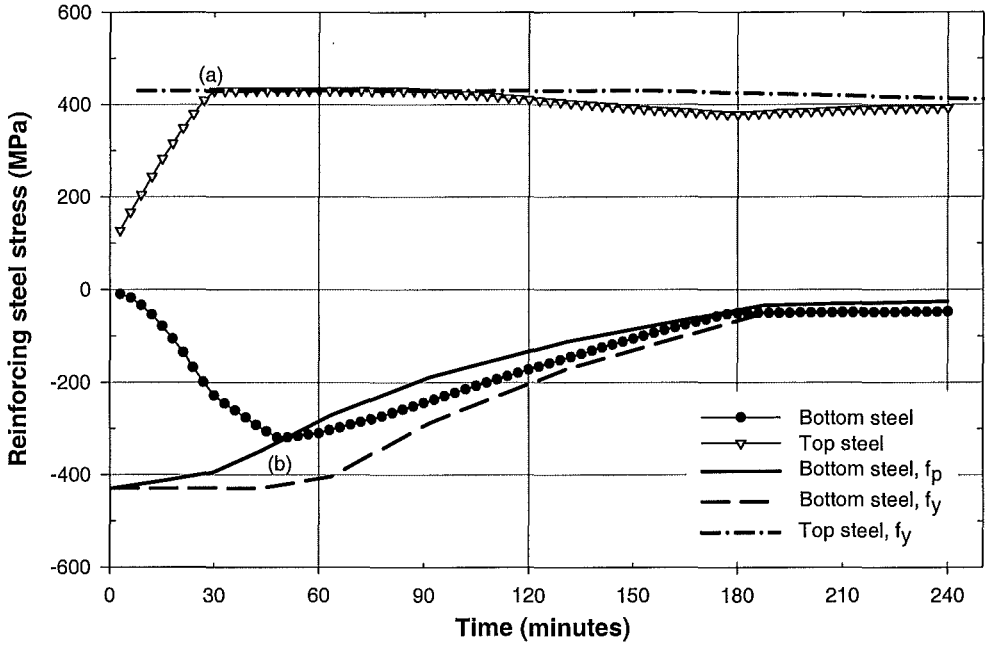

Figure 5-30: Stresses of reinforcing bars at supports of the slab with spring stiffness, k=1%.

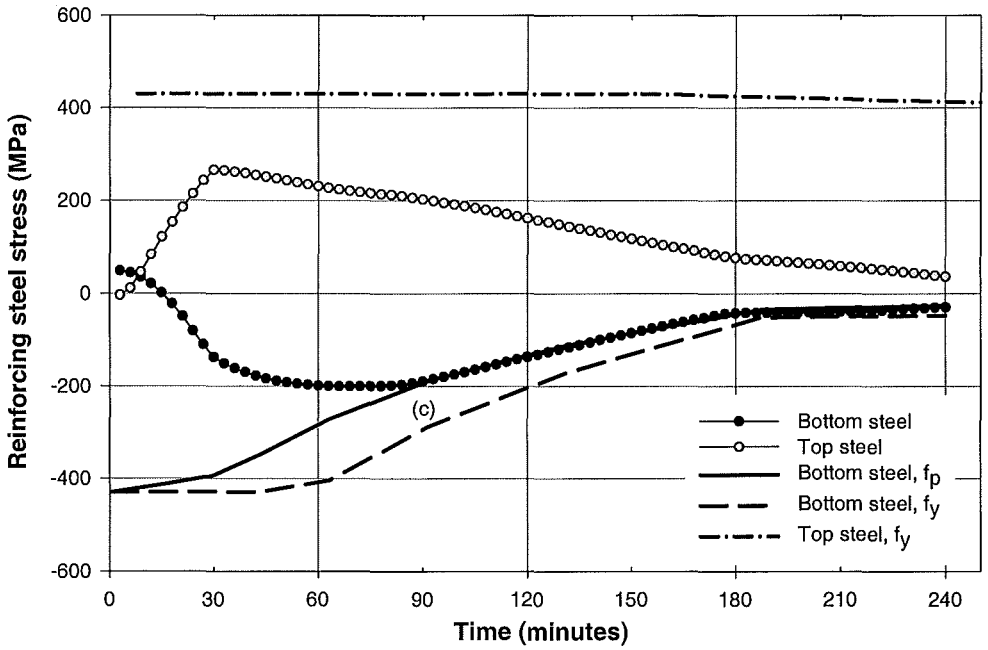

Figure 5-31: Stresses of reinforcing bars at midspan of the slab with spring stiffness, k=1%.

Figure 5-30 and Figure 5-31 show the variation of the steel stresses in the slab with 1% spring stiffness. During the initial stage of the fire, the top steel stresses at the supports and midspan increased rapidly in a linear trend until the steel at the supports yielded in tension (Point *a* of Figure 5-30). At the same time, the compressive stresses at the bottom of the slab also started

to increase. The increase of the tensile stresses of the top steel and the compressive stresses of the bottom steel was due to the negative moments induced by restraint against thermal bowing. The yielding of the top steel at the supports resulted in plastic hinges forming at the supports and caused the slab to lose its rotational restraint. This enabled the slabs to bow freely, indicated by the sudden increase in the deflection trend at 30 minutes (Figure 5-26). The bottom steel at the supports and midspan reached their compression proportional limits at 50 (Point *b* of Figure 5-30) and 80 minutes (Point *c* of Figure 5-31), respectively, but this did not have any effect on the behaviour of the slab as it continued to deflect in a linear trend until the end of the fire.

Full horizontal restraint

Figure 5-32 and Figure 5-33 show the variation of the stresses in the reinforcing steel for the slabs that were fully fixed at both end supports. The compressive stresses of the bottom steel at both the supports and midspan increased very rapidly during the initial stages of the fire, reaching their compressive proportional limits at 27 minutes and 30 minutes, respectively. This caused the negative moments in the slabs to reach a peak, as shown in Figure 5-28 and Figure 5-29. In contrast to the lightly restrained slab (k=1%), the top steel stresses of this slab remained relatively low during the initial stages of the fire, with the top steel at midspan being in compression and the steel at the supports being in tension. The reason for the relatively low tensile stresses throughout most of the fire was due to the high compressive forces imposed by the rigid horizontal restraint.

At failure, the steel stresses at midspan started to change from compression to tension. At this stage, the positive flexural strength of the slab had been severely depleted. This resulted in a rapid redistribution of the moments to the supports, shown by increase of the negative moments at the supports (Figure 5-28) along with the tensile stresses of the top steel at the supports (Figure 5-32). Final failure occurred when the tensile stresses of the top steel at the supports reached their yield limit and caused a plastic hinge to form at each support. This produced a mechanism in the slab and resulted in collapse.

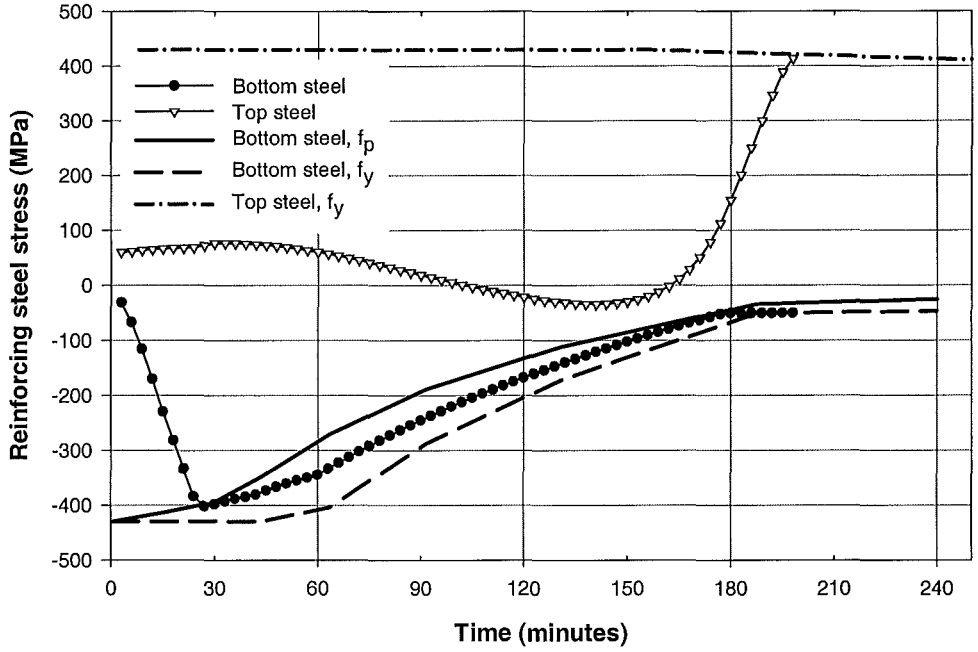

Figure 5-32: Stresses of reinforcing bars at supports of the slab with full horizontal restraint.

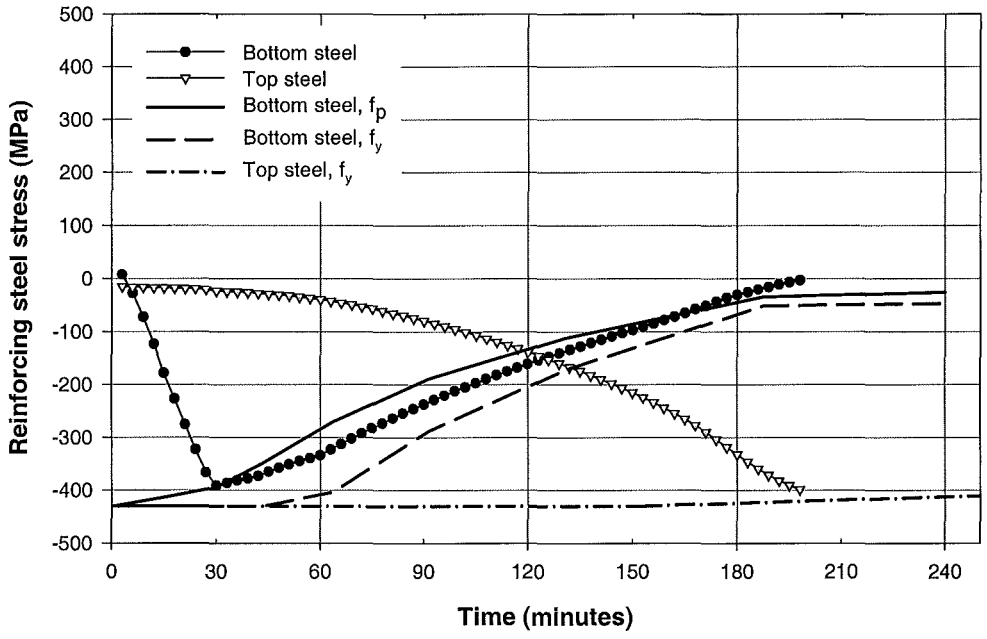

Figure 5-33: Stresses of reinforcing bars at midspan of the slab with full horizontal restraint.

5.6.6. Position of line of thrust at the supports

This section will determine the variation of the height of the line of thrust across the depth of the slab at the supports of the rotationally restrained slabs during the fire exposure fire.

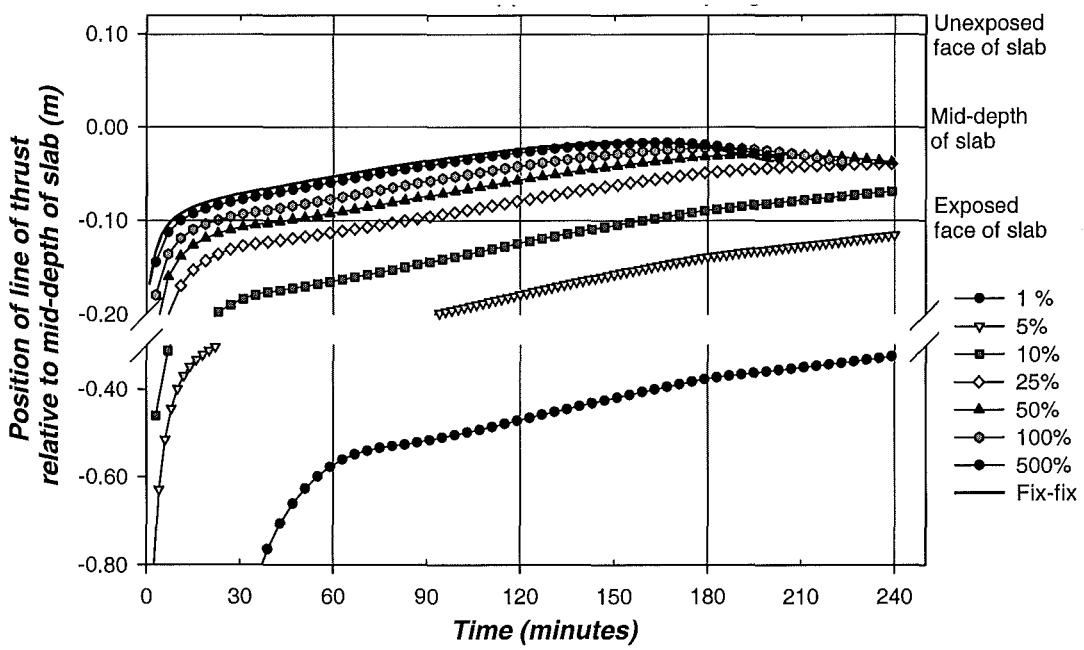

Figure 5-34: Variation of the position of the line of thrust at end supports.

Figure 5-34 shows the variation of the position of the line of thrust at the supports. The position of the line of thrust, which is an eccentricity, z_o, measured relative to the centroidal axis of the slab, is calculated from Equation 3-4. Figure 5-34 shows that at the start of the fire, the line of thrust of most of the slabs lies outside the depth of the slab. During the initial stage of the fire, the position of the thrust force rapidly moved upwards followed by a more gradual and linear rise into the depth of the slab. At the advanced stages of the fire, the line of thrust dropped off slightly in some cases. The movement of the line of thrust into the depth of the slab was attributed to the depletion of the concrete and reinforcing strength from the soffit towards the unheated side.

5.6.7. Conclusions

The analyses of the slabs with rotationally restrained supports have shown that:

- Slabs with flexural continuity have excellent behaviour under fire conditions.
- Slabs with rotationally fixed supports had better fire resistance than simply supported slabs (pin-roller) and had smaller deflections than the equivalent pin-supported slabs.
- The calculated height of the axial restraint force at the supports moves upwards from the heated face to the centroidal axis during the fire exposure.

5.7. Rotationally restrained slabs with curtailed top reinforcement

The slabs with full rotational restraint in the previous section (section 5.6) were analysed with continuous top and bottom reinforcement in the slab. In this section, the rotationally restrained slabs are analysed with its top steel at the supports curtailed to as this is done in typical construction for economy of the reinforcing. The slabs are analysed with different axial restraint stiffnesses.

5.7.1. Structural model

The structural model of the slab that is used in the following analyses is identical to that shown in section 5.6.1. Figure 5-35 shows the reinforcing steel layout for a metre width of the slab, curtailed according to the Concrete Structures Standard (SNZ, 1995). Only the top steel was curtailed while the bottom steel content was not altered and was assumed to span continuously between the two end supports.

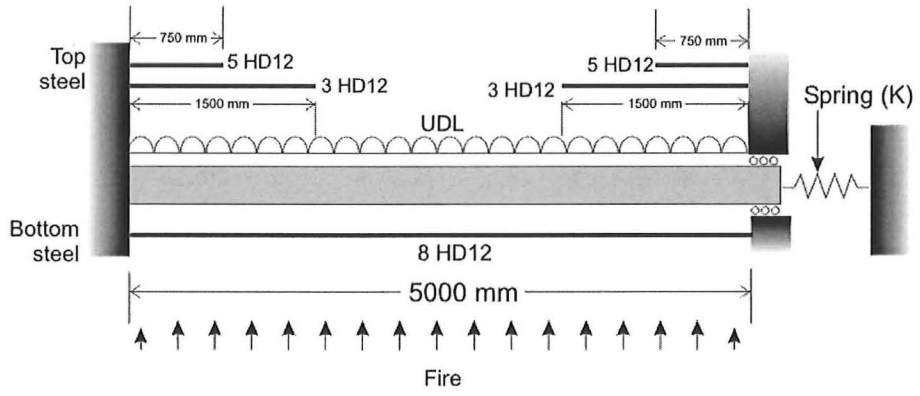

Figure 5-35: Layout of the curtailed reinforcement in the slab with rotationally restrained supports.

The curtailed top reinforcement according to the code, shown in Figure 5-35, includes the development lengths, L_d, which is the length of the reinforcing bar required for it to reach its full strength. The development length for the reinforcement is calculated with Equation 5-4 which is obtained from NZS 3101 (SNZ, 1995).

$$L_d = \frac{0.5\alpha_a f_y}{\sqrt{f'_c}} d_b = 471\text{mm} \approx 500\text{mm} \qquad \textbf{Equation 5-4}$$

Where d_b = 12mm

α_a = 1.0

f_y = 430 MPa

f'_c = 30 MPa

In SAFIR, the reinforcing bars can reach their full strength at the point where the bars are terminated. Therefore, the SAFIR analysis is performed using the reinforcing layout shown in Figure 5-35 but without the development length as it would give the slab additional negative flexural capacity than in the actual curtailed slab. The lengths of the reinforcement, without the development lengths, used in the SAFIR analysis are shown in Figure 5-36.

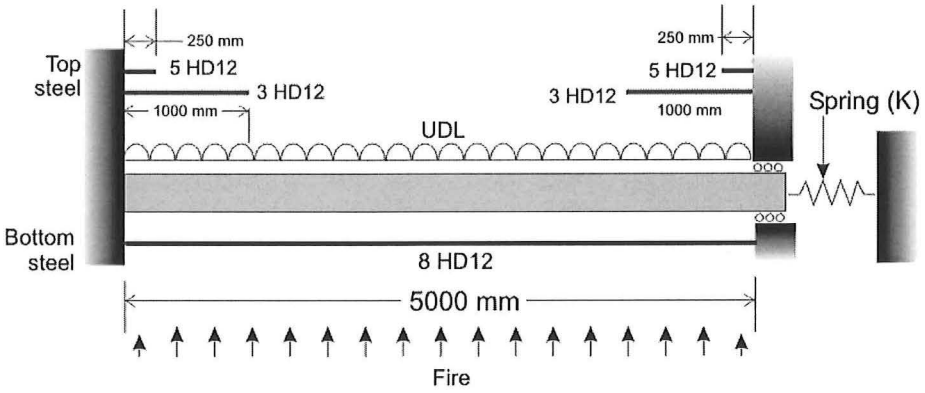

Figure 5-36: Layout of the curtailed reinforcement used in the SAFIR analysis.

5.7.2. Midspan vertical deflections

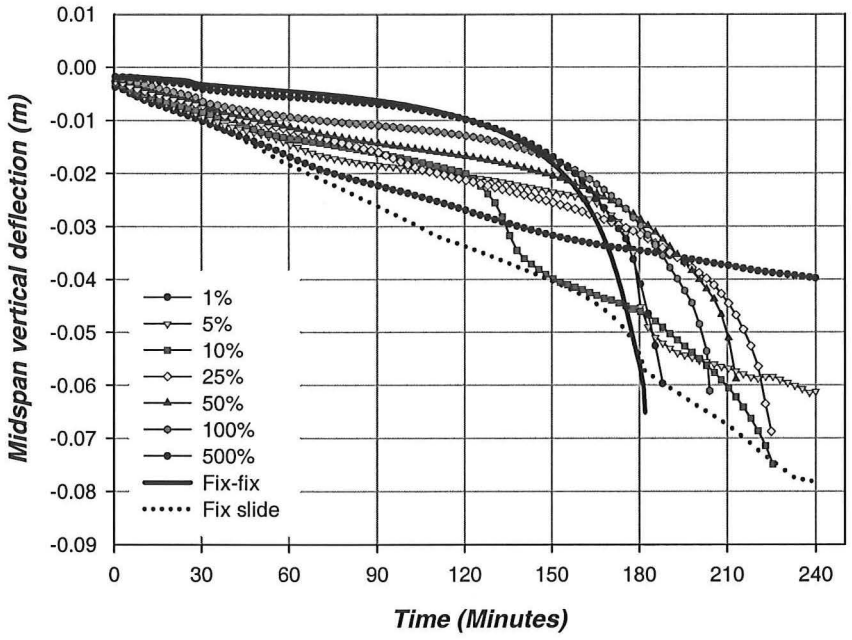

Figure 5-37: Midspan vertical deflections of the slabs with rotational restraint and with curtailed top steel.

Figure 5-37 shows the variation of the midspan vertical deflections of the slabs with curtailed top reinforcement at the supports. The graph shows that the behaviour of the slabs was very similar to the slabs analysed in section 5.6 which had continuous top steel in the slab. Figure 5-37 shows that the *fix-slide* slab and the slab with 1% axial restraint stiffness showed similar

deflection trends during the initial stages, but they started to diverge after 70 minutes when the deflection rate of the *fix-slide* slab increased.

The slabs with axial restraint stiffness of 5% and 10% initially deflected at a lower rate than the 1% and *fix-slide* slabs. At the advanced stages of the fire, the deflection rates of the 5% and 10% slabs increased suddenly and levelled off again. The 10% slab failed at 226 minutes but the 5% slab lasted the entire fire duration. The slabs with axial restraint stiffness equal or greater than 25%, the slabs failed earlier as the axial restraint stiffness increased. This trend is similar to the slabs which had continuous top steel (See section 5.6); although the curtailed slabs failed slightly earlier than the slabs which were not curtailed for the same stiffness.

Figure 5-38 shows the typical deflected shape of the *fix-slide* and 1% slabs during the advanced stages of the fire. Even though the slab deflected downwards at midspan, the slab had deflected upwards at 1.0m inwards from each end. This deflected shape was caused by thermal bowing and two plastic hinges forming at the sections of the slab where the top steel was terminated (designated P.H.). The two plastic hinges formed when the negative moments exceeded the negative flexural strength at the regions where the top steel was terminated. The sections of the slab at the supports behaved as two short cantilevers and supported the central span which hung between the two cantilevers.

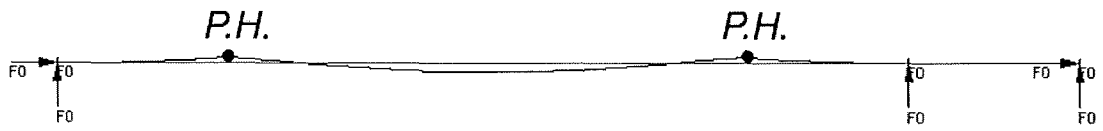

Figure 5-38: Deflected shape of the slab with 1% axial restraint after 2 hours exposure to the fire (Deflections magnified two times).

5.7.3. Conclusions

The analyses of the slabs in this section have shown that rotationally restrained slabs with top steel curtailed according to code recommendations (SNZ, 1995) showed excellent behaviour, similar to those with continuous top steel.

5.8. Pin-supported slabs with moveable line of thrust

5.8.1. Introduction

This section investigates the behaviour of pin-supported slabs with moveable line of thrust at the end supports. The purpose of this analysis is to simulate cast-in-situ slabs without flexural continuity or precast slabs with infill between the vertical faces at the ends of the slab and the supporting structure (Figure 5-39). For these slabs, the line of thrust is moveable during the fire and its position depends on the axial restraint stiffness and the stiffness of the slab during the fire. These slabs are assumed to have no flexural continuity and will be modelled without top or bottom reinforcing bars anchored to the supports. The effect of top reinforcing bars at the supports of these slabs is discussed in section 5.9.

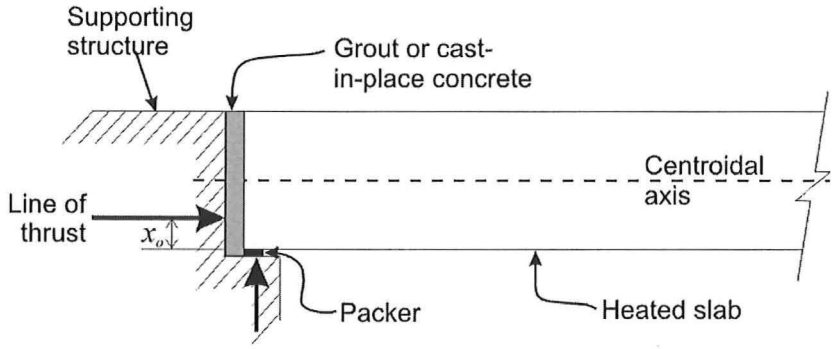

Figure 5-39: Precast slab with in-fill between the slab and the supports.

5.8.2. Structural model

In a similar fashion to the slabs in the previous sections, the slab is modelled as a one-way slab using plane frame analysis. The geometric properties, material properties and loading conditions of the slab are similar to those described in section 5.2.2. The only difference in this case is that the top steel of the slabs will not be modelled, as shown in Figure 5-41.

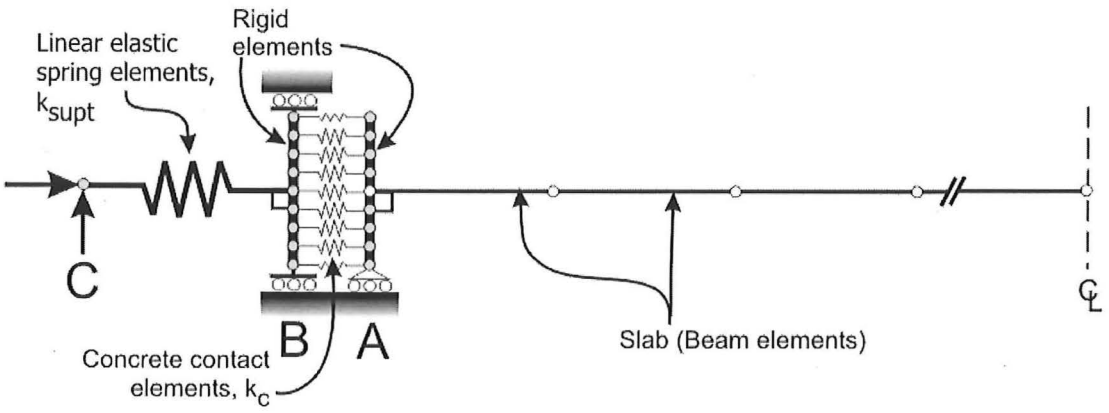

Figure 5-40: SAFIR structural model.

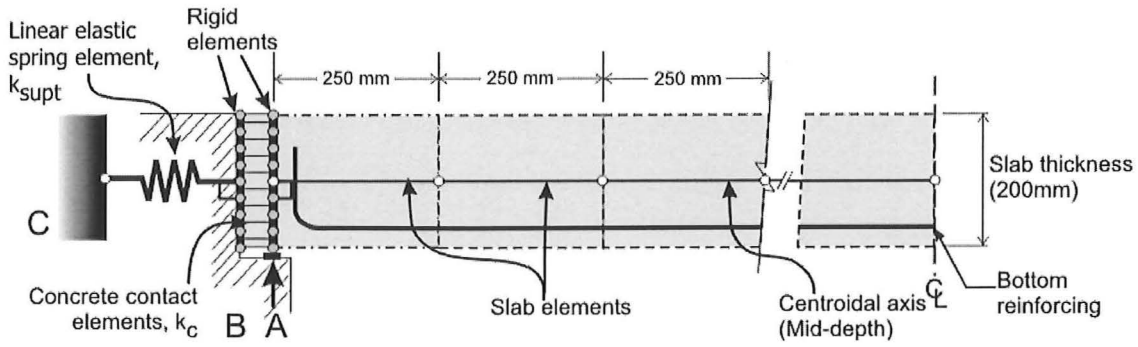

Figure 5-41: Physical representation of the structural model.

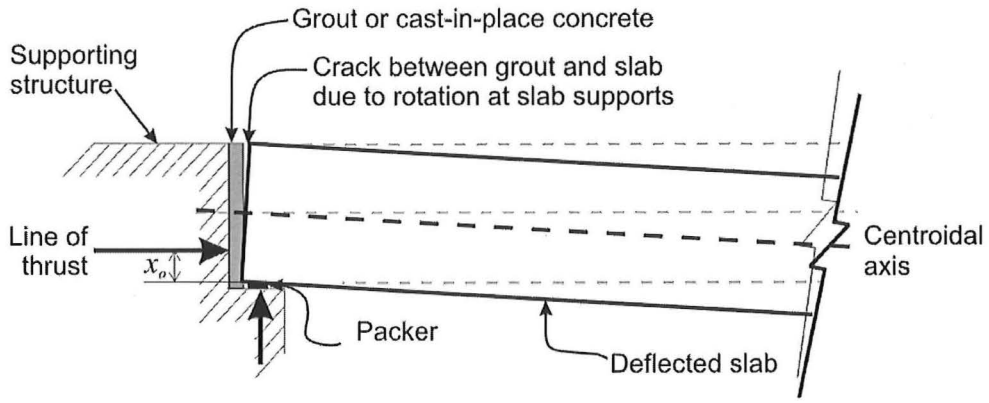

Figure 5-42: Cracking of the in-fill due to deflection of the slab.

Figure 5-40 shows the SAFIR structural discretisation of the slab and its support conditions and Figure 5-41 shows the physical representation of the structural model. Due to the symmetric support and loading conditions, only half of the slab was modelled. The slab is represented by beam finite elements which are connected to a series of vertical rigid elements, at the end supports at *A*. These rigid elements represent the vertical face of the end of the slab as shown in Figure 5-41, and enforce plane sections at the end supports. The height of the vertical rigid elements is equivalent to the thickness of the slab. The slab is vertically supported at the bottom of the rigid elements and is free to rotate at the supports.

The rigid elements at *A* are connected to another series of vertical rigid elements at *B* by contact elements with concrete properties. These contact elements represent the concrete infill between the slab and the supporting structure. They can resist compression forces but do not have tension resistance. Under tension strain, the elements will crack and will not be able to support any tensile stress. For instance, when the slab deflects and rotates at the supports, as shown in Figure 5-42, the elements at the top will crack.

The second set of rigid elements at *B* is connected to a spring. This second set of rigid elements is free to move horizontally but is rotationally and vertically restrained, as shown in Figure 5-40. The main spring represents the axial stiffness (k_{supt}) of the surrounding structure. The horizontal and vertical degrees of freedom at the end of the axial spring are fixed at *C*. The concrete contact elements enable the slab and its supporting system to choose the position of the line of thrust during the fire, unlike the pin-supported slabs in the previous sections which had their line of thrust fixed throughout the entire fire duration.

The analyses of the previous cases have assumed that the reinforcing bars were anchored to the supports. In this case, the reinforcing bars at the ends of the slabs are terminated at the ends of the slabs and are not connected to the support. Therefore, the supports cannot resist any tensile forces when the slabs deform into a catenary.

The analysis of the slab is conducted with different values of stiffness of the supporting structure. The stiffness of the supporting structure is changed by varying the stiffness of the main axial spring. The axial stiffness of the supporting structure range from 1% of the slab's axial stiffness to 1000% (i.e.: 10 times greater than the slab's axial stiffness).

5.8.3. Midspan vertical deflections

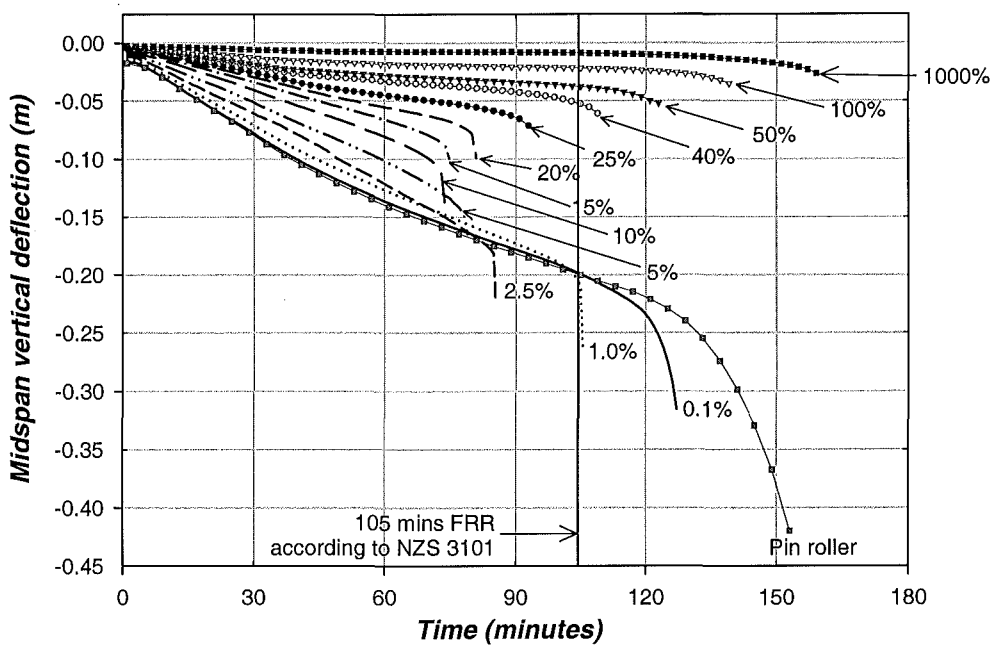

Figure 5-43: Variation of the midspan vertical deflections of the slab for different axial restraint stiffnesses during the ISO fire.

Figure 5-43 shows the variation of the midspan vertical deflections of the slab with various axial restraint stiffnesses. The graph shows the code recommended fire resistance (NZS, 1995) of 105 minutes for the slab, based on the concrete cover. The code recommended value is used to define the limits when compressive restraint has a beneficial effect on the slab behaviour. The graph shows that slabs with axial restraint stiffnesses greater than 40% and less than 1% had better fire resistances than the code recommendations. Slabs with axial restraint stiffnesses between 2.5% and 25% had lower fire resistances than the code recommendations.

The graph shows that the slab with the lowest deflections was the slab with 1000% spring stiffness and the slab with the largest deflections was the pin-roller slab. The slab with 1000% restraint stiffness failed at very small deflections at 160 minutes. Despite the relatively small deflection at the point of failure (-30mm), the program could not further iterate to obtain a solution. The reason for the failure will be explained in the following sections.

The pin-roller slab suffered very large deflections during the fire and failed with very large deflections due a plastic hinge forming at midspan. The graph shows that when the spring stiffness was increased from the unrestrained condition (pin-roller) to 10% stiffness, the fire

resistance of the slab decreased. At 10% stiffness, collapse occurred at 74 minutes, which is half the failure time of the pin-roller condition. As the spring stiffness was further increased from 10% to 100%, the fire resistance of the slab increased very markedly. However, increasing the spring stiffness ten times from 100% to 1000% showed only a slight increase in fire resistance.

The slabs with spring stiffnesses between 0.1% and 2.5% failed due to runaway failure. Between 2.5% and 20%, the slabs failed at large deflections due to snap-through. For slabs with spring stiffnesses greater than 20%, the reason for the "failure" was not obvious because the deflections at failure were small and did not suggest a runaway failure.

5.8.4. Horizontal deflections and axial forces

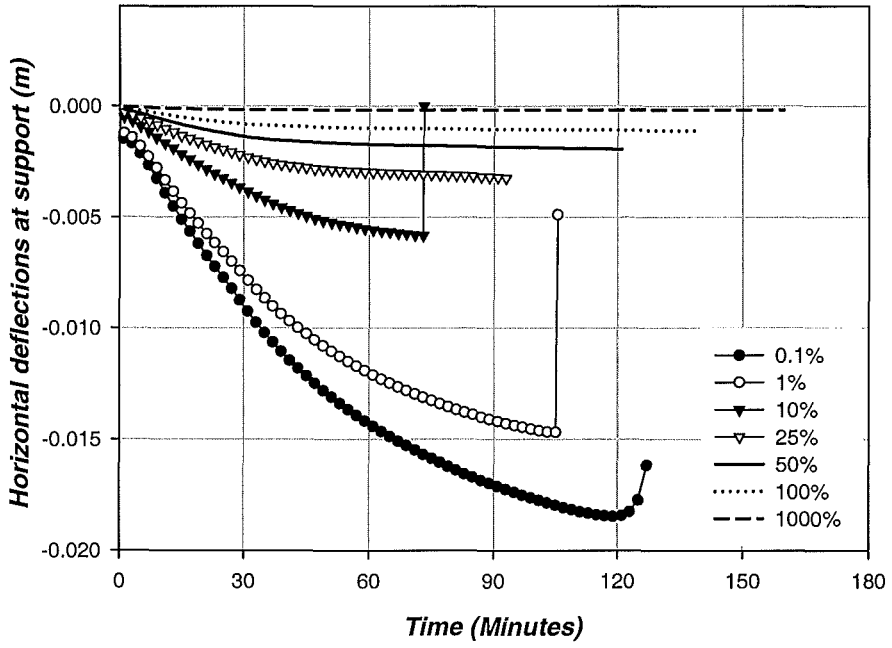

Figure 5-44: Variation of horizontal deflections at supports.

Figure 5-44 shows the variation of the horizontal deflections at the supports. The horizontal deflections of the bottom corner of the slab, where the slab is vertically supported on the roller, are plotted. Negative displacement is outward expansion while positive displacement represents inward contraction. The graph shows that slabs with low axial restraint produced large horizontal deflections while slabs with high axial restraint have small horizontal deflections. Not all the slabs that were shown in Figure 5-43 are presented here.

With 0.1% axial stiffness, the slab deflected outward in a non-linear trend with a higher expansion rate followed by a lower rate. When runaway occurred, the supports pulled inwards at the final stages. With 10% spring stiffness, a similar deflection trend was observed but with smaller horizontal deflections. At failure, the horizontal deflections dropped very markedly when the end supports of the slabs suddenly pulled inwards due to snap-through. The graph shows that the maximum horizontal deflections of the slabs at each end support ranged from 0.2mm at 1000%, to 18.5mm at 0.1%.

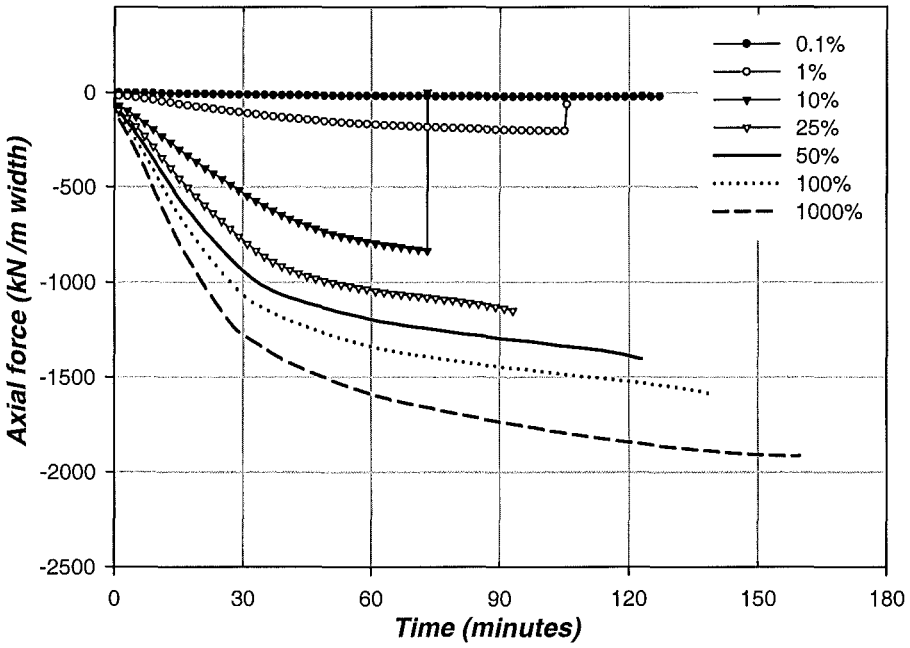

Figure 5-45: Variation of axial forces in the slabs with moveable lines of thrust.

Figure 5-45 shows the variation of the axial forces in the slab with different amounts of axial restraint. The graph shows that high axial restraint produced high compressive forces in the slab and that the axial forces were inversely proportional to the amount of permitted expansion. All the slabs with different amounts of axial restraint showed a similar bilinear increase of axial force. The decrease of the rate of rise of the axial forces was due to compressive yielding of the bottom reinforcing steel.

5.8.5. Reinforcing steel stresses

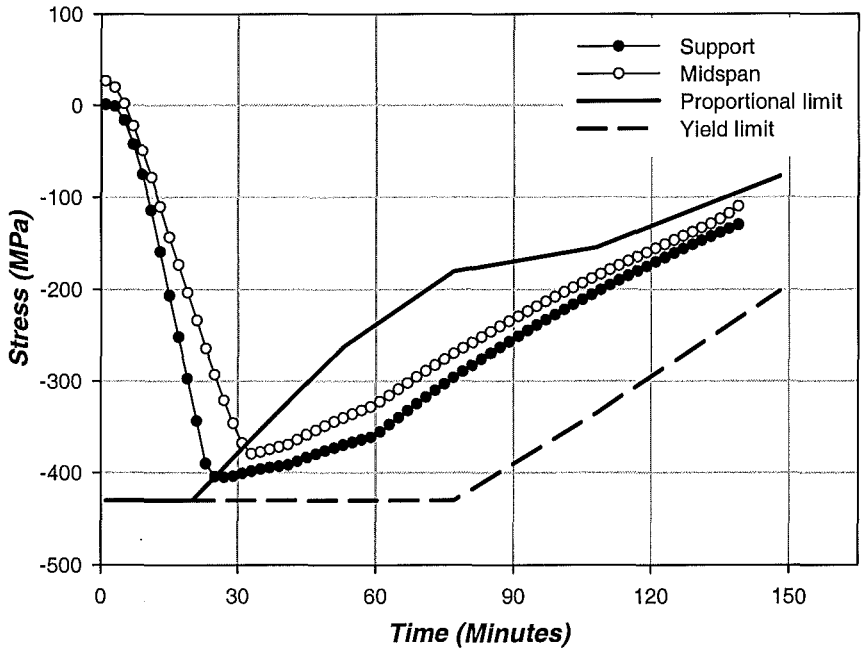

Figure 5-46: Variation of stresses in the bottom reinforcing steel for k=100%.

Figure 5-46 shows the variation of the stresses in the bottom reinforcing steel for the slab with 100% spring stiffness. During the initial stages, the compressive stresses increased linearly due to the high axial restraint forces. The compressive stresses at midspan were slightly lower than those at the support due to the higher tensile bending stresses imposed by the gravity loads at midspan. The support steel reached its linear-elastic proportional limit at 28 minutes followed by the midspan steel at 33 minutes. When the bottom steel at the supports reached the proportional limit and spread to the midspan region, the axial stiffness dropped very significantly and caused the rate of rise of the axial forces to decrease, as shown in Figure 5-45.

5.8.6. Bending moments

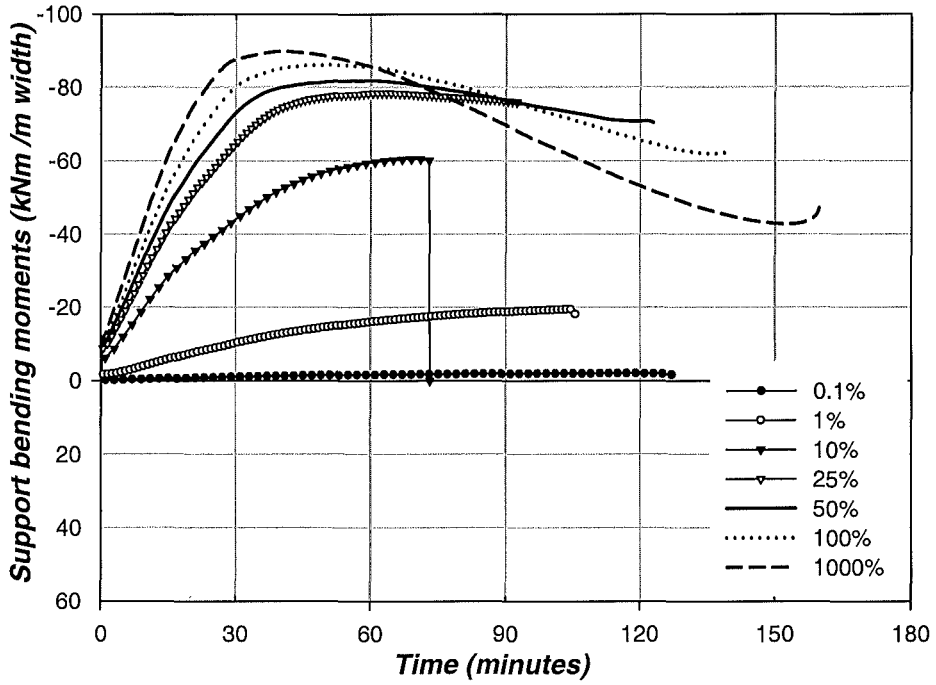

Figure 5-47: Variation of the bending moments at the supports.

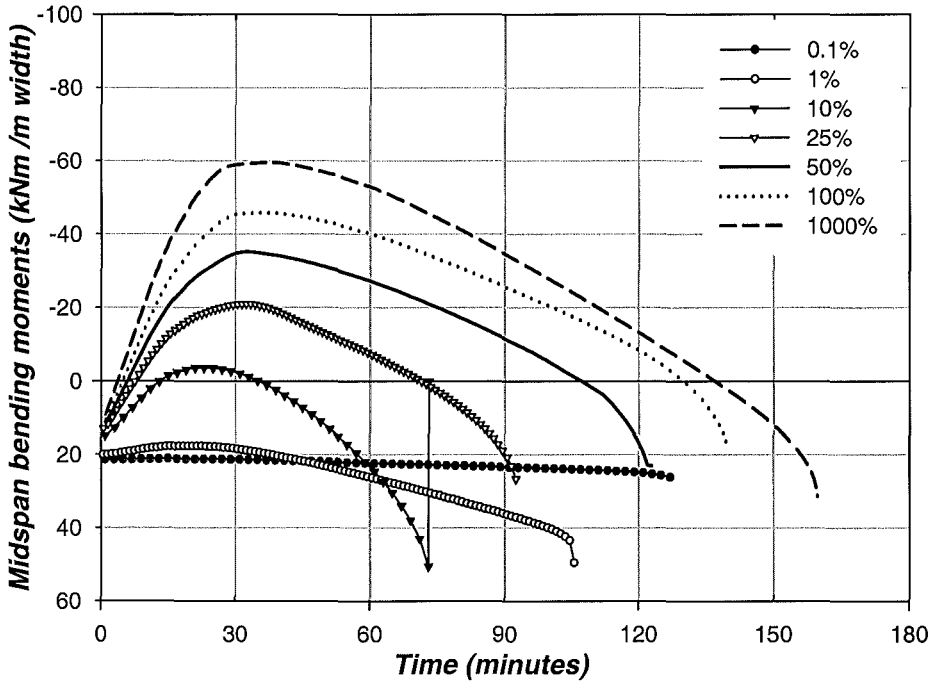

Figure 5-48: Variation of the midspan bending moments.

Figure 5-47 and Figure 5-48 show the variation of the bending moments at the supports and midspan, respectively. The graphs show a very significant variation of the moments at the supports and midspan during the fire. The negative moments at the supports, produced by the compressive axial force acting below the centroidal axis of the slab, redistributed the midspan

moments, causing the positive moments at midspan to change to negative moments (Figure 5-48). High restraint stiffnesses produced higher rates of redistribution and higher maximum moments. The difference between the negative and positive moments was due to the moments induced by the gravity loads and the M_Δ moments.

With 1% spring stiffness, the graph shows that the positive moments at midspan increased only slightly at the end of the analysis, due to the small M_Δ moments at midspan. The slab with 0.1% spring stiffness showed almost constant bending moments at midspan and at the supports.

5.8.7. Variation of the line of thrust at the supports

This section presents the variation of the line of thrust at the supports during the fire.

Spring stiffness, 25% ≤ k ≤ 1000%

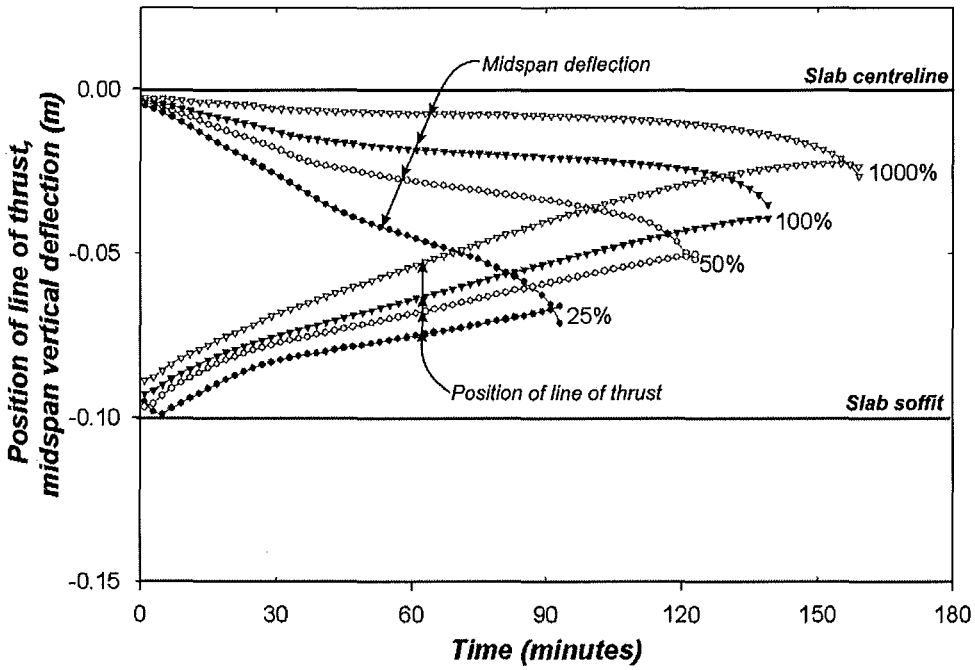

Figure 5-49: Variation of the line of thrust at the supports for spring stiffness between 25% and 1000%.

Figure 5-49 shows the variation of the line of thrust of the slabs with spring stiffnesses ranging from 25% to 1000%. The midspan deflections of the slabs are also plotted on the same graph. The position of the line of thrust, which is the eccentricity measured relative to the centroidal axis of the slab, z_o, is calculated from Equation 3-4.

$$z_o = \frac{M^-_{fire}}{T}$$

Where M^-_{fire} = Moment at the supports

T = Axial force in the slab

z_o = Eccentricity of the line of thrust relative to the centroidal axis

Figure 5-49 shows that during the initial stages of the fire, the thrust force at the slab supports lies just above the soffit of the slab. As the fire developed, the line of thrust moved upwards towards the centreline of the slab. This observation is consistent with that seen in the tests on slabs with high restraint conducted at the PCA furnace (Issen et al., 1970). The graph shows that the rate of rise of the thrust force increased with increasing restraint stiffness. The graph also shows that the slabs failed when the midspan deflections, which are measured at the centroidal axis of the slab, dropped below the position of line of thrust at the supports.

Figure 5-50 shows the slab when the line of thrust is close to the soffit and the deflections are small enough so that the centroidal axis at midspan lies above the line of thrust. At this stage, the compressive force, T, due to the external restraint has a beneficial effect on increasing the stiffness of the slab. When the midspan centroidal axis drops below the line of thrust, due to the line of thrust moving upwards and the slab deflecting downwards (Figure 5-51), the external thrust force ceases to provide flexural enhancement to the slab. At this point, any external thrust would produce a detrimental effect on the slab as it increases the deflections and midspan moments, leading to snap-through and failure.

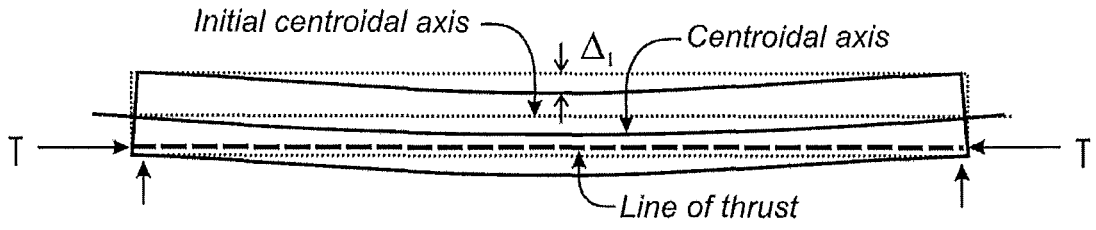

Figure 5-50: Midspan centroidal axis above line of thrust.

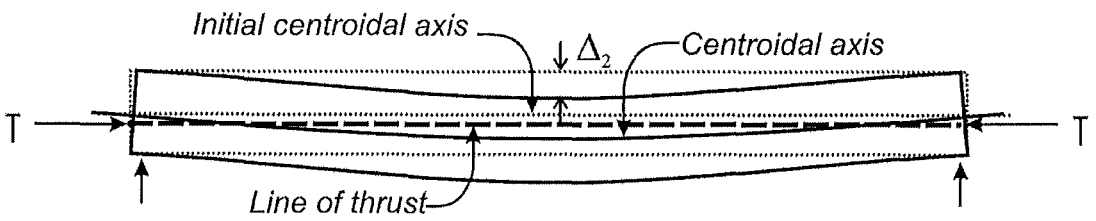

Figure 5-51: Midspan centroidal axis below line of thrust.

Spring stiffness, 0.1% ≤ k ≤ 20%

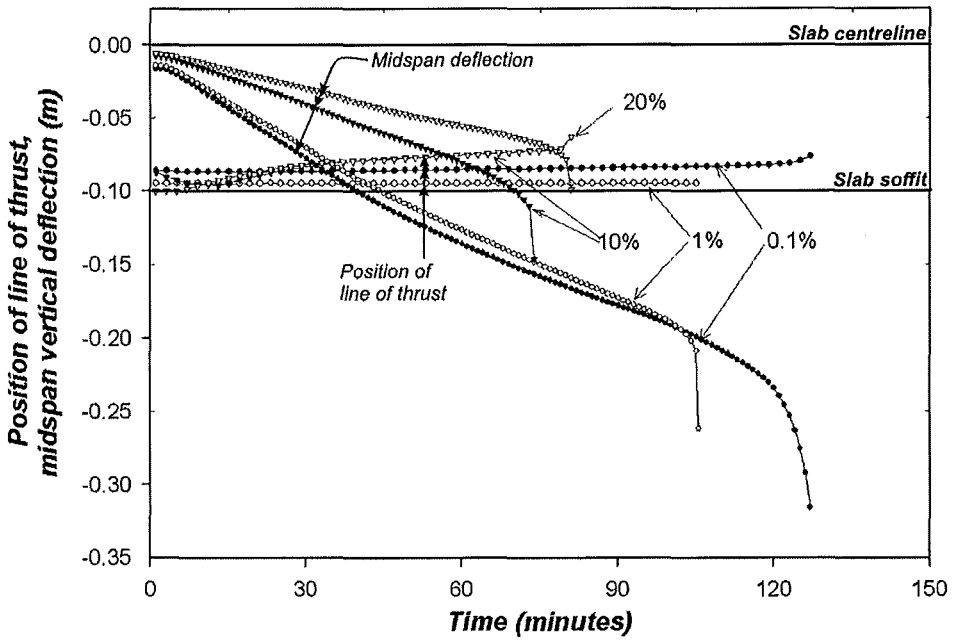

Figure 5-52: Variation of the line of thrust at the supports for restraint stiffness between 0.1% and 20%.

Figure 5-52 shows the results of the slab with restraint stiffnesses ranging from 0.1% to 20%. For the slabs with restraint stiffnesses of 10% and 20%, the graph shows that the position of line of thrust was located at the bottom of the slab during the start of the fire and moved upwards towards the centre of the slab. For the slabs with 0.1% and 1% restraint, the position of the line of thrust remained almost constant and within the bottom 25mm of the slab throughout the entire fire. This observation is consistent with the experimental results of the PCA fire tests (Issen et al., 1970) and the recommendations made by CRSI (1980) which showed that the line of thrust acts near the bottom of slabs when the thrust force is low (See section 3.5.1).

The slab with 20% restraint stiffness showed similar behaviour to the slabs of the previous figure; which failed when the centroidal axis deflection dropped below the line of thrust. Figure 5-52 shows that the slabs with 0.1%, 1% and 10% restraint did not collapse even when the centroidal axis at midspan dropped below the line of thrust at the supports. The graph shows that the slabs with low axial restraint were not sensitive to the centroidal axis dropping below the position of line of thrust.

5.8.8. Comparison of thrust-expansion results from SAFIR with PCA tests

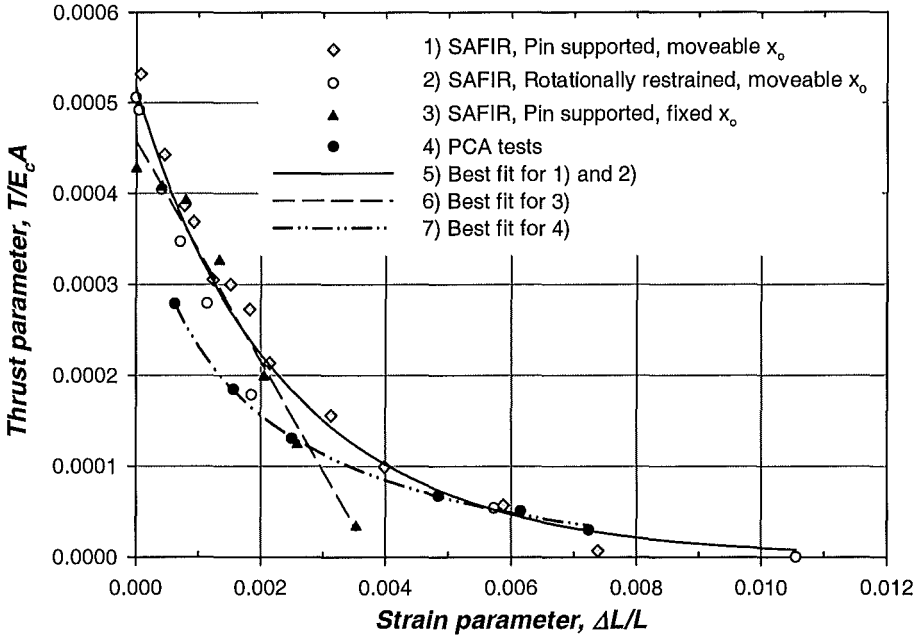

Figure 5-53: Thrust parameter versus strain parameter.

Figure 5-53 compares the maximum thrust force and expansion of the slabs analysed using SAFIR with the tests conducted at the PCA furnace (Issen et al., 1970). The maximum thrust force and their corresponding axial expansion are plotted for the slabs analysed with different spring stiffnesses. The results for the pin-supported slabs with fixed lines of thrust (x_o) (Section 5.4) and moveable (Section 5.8) lines of thrust are plotted, along with the rotationally restrained slabs (Section 5.7).

The thrust parameter (T/E_cA) consists of the maximum axial force in the slab, T, calculated with SAFIR, the elastic modulus of the concrete at ambient conditions, E_c, and the cross sectional area of the slab, A. The strain parameter ($\Delta L/L$) is the expansion of the slab, ΔL, at the maximum axial force, relative to the initial length of the slab, L. The dimensionless parameters from the SAFIR analyses are compared with the results of the fire tests of restrained double-tee specimens conducted at the PCA furnace (Issen et al., 1970). The PCA double-tee specimens were constructed with normal-weight calcareous aggregate concrete and reinforced with reinforcing bars. A best fit curve for the slabs with moveable line of thrust (pin supports and rotationally restrained supports) (Line 5) is plotted. The best fit curves for the pin-supported slabs with fixed line of thrust (Line 6) and the PCA tests (Line 7) are also shown.

The analyses of the slabs with moveable line of thrust analysed with SAFIR showed good overall agreement with the PCA tests as they both showed exponential decrease of axial force with increasing strain. Curve 5 shows that SAFIR predicted higher axial forces than the PCA tests for strain levels below 0.0055. At strain levels above 0.0055, the thrust force obtained from the SAFIR analyses and the PCA tests showed good agreement.

For the pin-supported slabs with fixed line of thrust, SAFIR shows a linear decrease of the axial force with increasing strain. For strains less than 0.0028, SAFIR predicted higher axial forces than the PCA tests. However, for strains greater than 0.0028, the axial forces predicted using SAFIR were lower than the PCA tests and the SAFIR slabs with moveable line of thrust. This linear variation of axial force is similar to the results predicted by earlier researchers.

Finite element analyses by Anderberg et al. (1982) on restrained pin-supported slabs with fixed position of line of thrust also showed that the maximum axial force decreased linearly with increasing strain. Their analyses showed significantly lower axial forces for strains larger than 0.0015, compared with the PCA tests. The analyses with SAFIR and by Anderberg et al. (1982) have shown that if the position of line of thrust is fixed, the maximum axial force decreases linearly with strain. If the slabs have a moveable line of thrust, the SAFIR analyses and the PCA tests show that the maximum axial force decreases exponentially.

The higher forces predicted by the SAFIR analyses at strains below 0.0055, compared with the PCA tests, can be attributed to the type of concrete used in the analyses. The SAFIR analyses were performed with siliceous aggregate concrete which has a higher coefficient of thermal expansion than the calcareous aggregate concrete used in the PCA tests. This would produce higher thermal expansion which would lead to higher maximum compressive restraint forces.

5.8.9. Comparison of the SAFIR analyses with the PCI hand method for flat slabs

This section compares the PCI hand method with the findings of the SAFIR analyses for axially restrained pin-supported slabs. The comparison is summarised in Table 5-2 and is based on the SAFIR analyses of pin supported flat slabs in this section (section 5.8) with moveable line of thrust, and with fixed line of thrust (Section 5.3). The full details of the PCI recommendations are reported by Gustaferro et al. (1989).

Axial restraint stiffness	Findings of SAFIR analyses of pin-supported slabs	PCI hand method
Low	• Applies to slabs with maximum expansion of $\Delta L/L \geq 0.0055$ and $k \leq 1\%$ (e.g.:28mm/5000mm) • Large deflections occur early in the fire, followed by runaway failure. • FRR decreases, from the unrestrained condition (*pin-roller*), as the axial restraint increases. • For slabs with moveable line of thrust, the line of thrust is located near the bottom of the slab.	• Defined as slabs with "*minimal restraint*". • This method is not applicable for slabs with low axial restraint because it requires the deflections to be small enough so that the concrete compressive block at midspan is above the line of thrust at the supports, whereas SAFIR analyses showed large deflections in slabs with low restraint.
Intermediate	• $0.001 < \Delta L/L < 0.0055$ and $1\% < k < 40\%$ • Failure occurs much earlier than the unrestrained condition (*pin-roller*). • For slabs with moveable line of thrust, the line of thrust moves upwards towards the centroidal axis.	• Defined by the PCI method as slabs with "greater than minimal" axial restraint. • The method may be used if the line of thrust at the supports is known (e.g.: precast construction, see Figure 3-14). • For cast-in-situ construction, the method is difficult to use because the position line of thrust moves and its exact position is not known.
High	• $\Delta L/L \leq 0.001$ and $k \geq 40\%$ (e.g.: 5mm/5000mm) • Small vertical deflections. • FRR increases with increasing restraint. • Beneficial effects of compressive axial restraint are lost when the centroidal axis drops below the line of thrust, resulting in failure.	

ΔL = Amount of horizontal expansion of the slab; L = Clear span of the slab; FRR= Fire resistance rating

Table 5-2: Comparison of the PCI hand method with the SAFIR analyses for axially restrained flat slabs without flexural continuity (i.e.: Pin-supported slabs).

SAFIR analyses

The analyses with SAFIR in section 5.8 showed that flat slabs with low restraint have a permissible horizontal expansion, ΔL, greater than or equal to 0.0055L (i.e.: $\Delta L/L \geq 0.0055$) and axial restraint stiffness less than 1%. SAFIR analyses showed that these slabs behaved similarly to the *pin-roller* slab, with large deflections during the fire followed by runaway deflections at failure.

The SAFIR analyses showed that slabs which have maximum expansion between 0.001L and 0.0055L and axial restraint stiffness between 1% and 40% performed poorly. Early failure of the slabs was due to snap-through, causing the slabs to fail as early as 50% of the time to failure of the *pin-roller* slab. This poor behaviour occurs in pin-supported slabs with both fixed and moveable line of thrust. The analyses with SAFIR showed that the fire resistance of flat slabs with low and intermediate axial restraint progressively decreased from the *pin-roller* condition as the amount of axial restraint was increased.

Compressive restraint has a beneficial effect on the fire resistance of slabs and produces higher fire resistance than the code recommendations when the maximum permissible expansion is less than 0.001L and axial restraint stiffness greater than 40% (high restraint). With high axial restraint, the vertical deflections of the slabs are small and the line of thrust moves upwards towards the centroidal axis during the fire. When the centroidal axis drops below the line of thrust, the beneficial effects of compressive axial restraint are lost and the loads are resisted by the residual flexural strength of the slab.

The analyses in this section showed that increasing axial restraint stiffness does not always increase the fire resistance of pin-supported slabs.

PCI hand method

The PCI method would be difficult to use for flat slabs because:

- The method assumes that any level of restraint increases slab fire resistance whereas SAFIR shows that compressive restraint produces very poor behaviour for slabs with intermediate axial restraint stiffness. The SAFIR analyses showed that compressive restraint increased the fire resistances of slabs above the code recommendations only when $\Delta L/L \leq 0.001$ and $k \geq 40\%$ (i.e.: High restraint).

- For cast-in-situ slabs with high axial restraint, the line of thrust moves upwards during the fire, towards the centroidal axis and its position is not known. This makes the PCI method difficult to use for these slabs because the method requires knowledge of the position of line of thrust in the slab during the fire.
- To use the PCI method, it requires the user to distinguish between '*minimal restraint*' and '*greater than minimal*' restraint. However, the method does not provide any guidelines or limits to define the different levels of restraint.
- The tests at the PCA furnace, which the PCI method is based on, showed good results with high restraint because of the types of slabs that were tested and the way the slabs were supported. The tests were conducted mostly on double-tee precast slabs. The slabs were supported at the bottom of the webs of the slabs, far below the centroidal axis of the slab which is located near the top of the slab, in the flange of the slab. The line of thrust was initially located at the bottom of the slab and moved upwards during the fire. For flat slabs, the distance from the centroidal axis to the line of thrust is significantly less than in double-tees because the centroidal axis is located at mid-depth. Therefore, the increase of the fire resistance due to compressive restraint would be greater in double-tees than in flat slabs as it would take longer for the centroidal axis in the double-tee to drop below the line of thrust compared with the flat slabs.

5.8.10. Conclusions

This section presents the analyses of pin-supported slabs with moveable line of thrust modelled to simulate cast-in-situ slabs without flexural continuity. The results of the analyses have shown that:

- Compressive restraint increases the fire resistance of pin-supported slabs above the code recommended value when the axial restraint stiffness is high ($\Delta L/L \leq 0.001$ and $k \geq 40\%$).
- For slabs with high axial restraint, compressive restraint is beneficial to the slab behaviour when the vertical deflections are small and the line of thrust at the end supports is located below the centroidal axis. The beneficial effects of compressive restraint are lost when the centroidal axis of the slab drops below the line of thrust.
- For slabs with low and intermediate axial restraint ($\Delta L/L>0.001$ and $k<40\%$), compressive restraint produces worse behaviour than the *pin-roller* (unrestrained) condition.
- Compared with the rotationally restrained slabs, the time to failure of the slabs can be very low if there is no top steel anchored into the supports.
- The thrust-expansion results from the SAFIR analyses of slabs with moveable line of thrust showed a similar trend and good agreement with the results of the PCA tests.
- The PCI hand method is not recommended for assessing the required stiffness to enhance the fire resistance of pin-supported slabs, because it is an over-simplification of slab behaviour in fire.

5.9. Pin-supported slabs with moveable line of thrust with different amounts of top steel at supports

This section investigates the effect of different lengths of top steel at the supports of pin-supported slabs with moveable line of thrust. The purpose of this is to simulate cast-in-situ slabs with some flexural continuity or precast slabs with infill at the ends of the slab and starter bars from the supports lapped into cast-in-situ concrete topping, as shown in Figure 5-54. The latter description is a typical method of construction of simply supported precast slabs in New Zealand (NZCS-NZNSEE, 1999; Herlihy, 1999). The top steel provides some rotational restraint to the slab and also allows some redistribution of the bending moments in the slabs. The behaviour of the cast-in-situ slabs with top steel at the supports is compared with the pin-supported slabs with fixed position of line of thrust and the slabs with full rotational restraint. The comparison will be made for slabs with low (1%), intermediate (10%) and high (100%) axial restraint stiffness.

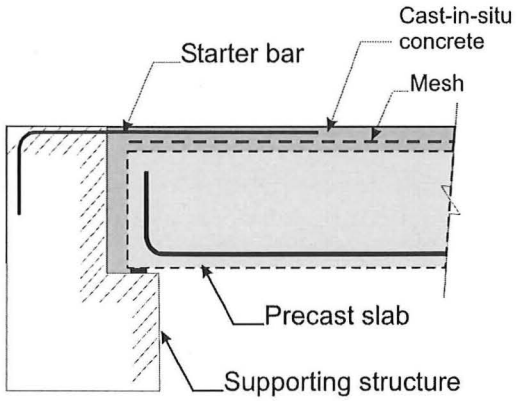

Figure 5-54: Typical support construction of simply supported precast slabs in New Zealand (NZCS-NZNSEE, 1999)

5.9.1. Structural model

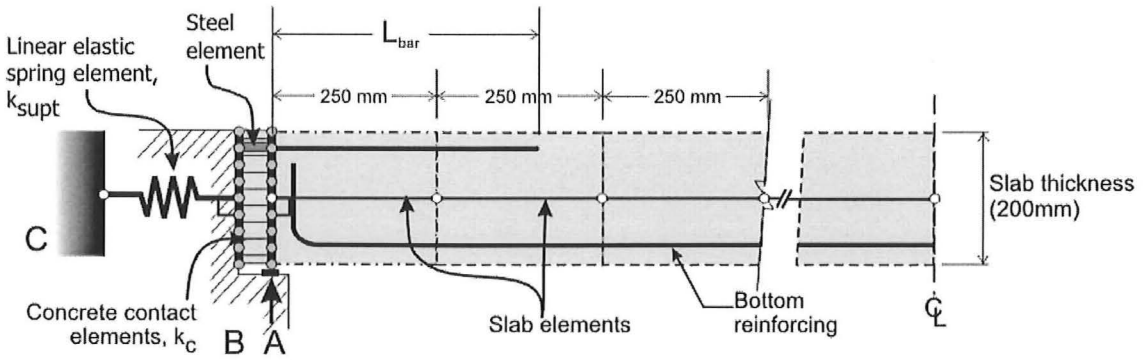

Figure 5-55: SAFIR model of cast-in-situ slab (pin-supported with moveable line of thrust) with top steel.

Figure 5-55 shows the SAFIR structural model of the cast-in-situ slab with some top steel at the supports. This model is similar to that shown in Figure 5-41 but it includes the top steel. A steel truss element was modelled between the vertical rigid elements, *A* and *B*, to represent the continuity of the top steel in the concrete infill from the slab to the support. A steel content of 380mm^2/m is used to model the top steel at the supports. This amount is based on typical starter bar configurations used in practice in New Zealand (i.e.: HD12 bars spaced at 300mm centres) (Herlihy, 1999). The lengths (L_{bar}) of the top steel that are modelled range from 0mm to 750mm. Note that L_{bar} is the length of the bar used in the SAFIR analysis and does not include the development length (L_d) required for the bars to reach full strength.

5.9.2. Cases analysed

The different cases that will be compared are shown in Table 5-3. Cases a), b), f) and g) have been analysed in the previous sections and are plotted for comparison. The different cases shown in Table 5-3 will be compared for 1%, 10% and 100% axial restraint stiffness.

Slab	End support	Top steel	See section
a)	Pin-supported, fixed line of thrust (x_o=50mm)	Not anchored to supports	5.4
b)	Pin-supported, moveable line of thrust	L_{bar} = 0mm	5.8
c)	Pin-supported, moveable line of thrust	L_{bar} = 250mm	-
d)	Pin-supported, moveable line of thrust	L_{bar} = 500mm	-
e)	Pin-supported, moveable line of thrust	L_{bar} = 750mm	-
f)	Rotationally restrained	Continuous	5.6
g)	Rotationally restrained	Curtailed[1]	5.7

Table 5-3: Cases compared in this section.

1 = Curtailed according to the Concrete Structures Standard (SNZ, 1995)

5.9.3. Vertical deflections of slabs with different support conditions (k=1%)

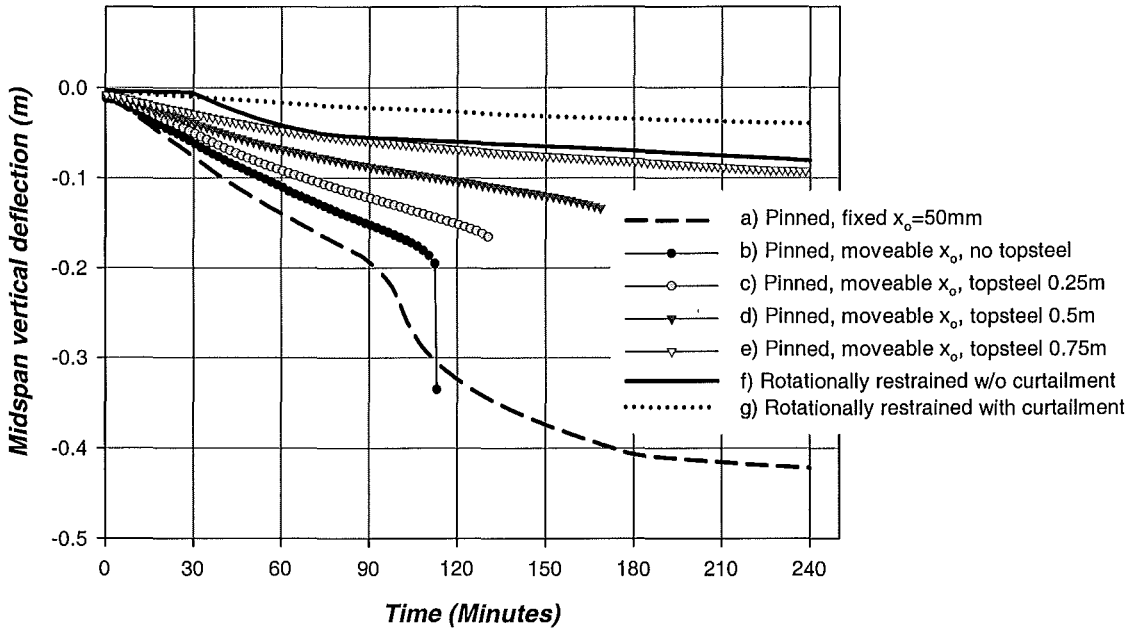

Figure 5-56: Midspan vertical deflections of the slabs with 1% axial restraint stiffness.

Figure 5-56 compares the midspan deflections of the slabs with different types of end conditions with 1% axial restraint stiffness. The graph shows that the slab with the largest deflections was the pin-supported slab with its line of thrust (x_o) fixed at 50mm above the soffit (slab *a*). The slab deflected downwards linearly in a gradual manner until just after 90 minutes when the deflection rate increased and the slab deformed into catenary mode and hung in tension.

The graph shows that the pin-supported slab with a moveable line of thrust but without top steel (slab *b*) had lower deflections and a higher fire resistance than slab *a*. As the length of the top steel in the pin-supported slabs increased (slabs *c, d* and *e*), the fire resistances of the slabs increased as they failed at later stages in the fire and their behaviour approached the slabs with full rotational restraint. Unlike slab *b*, SAFIR was unable to detect the deflections of the slab when runaway failure occurred in slabs *c* and *d*. With 0.75m top steel, the pin-supported slab (slab *e*) had a similar deflection curve to the slab with full rotational restraint (slab *f*). As the lengths of the top steel increased, the amount of rotational restraint at the end supports increased and the slab behaviour started to approach the slabs with full rotational restraint.

For the rotationally restrained slabs, the slab with the curtailed topsteel (slab *g*) had lower midspan deflections than the slab with continuous steel (slab *f*). This was because the midspan region of slab *g* was raised by the ends of the slab at the supports which acted as two cantilevers (See Figure 5-38).

5.9.4. Vertical deflections of slabs with different support conditions (k=10%)

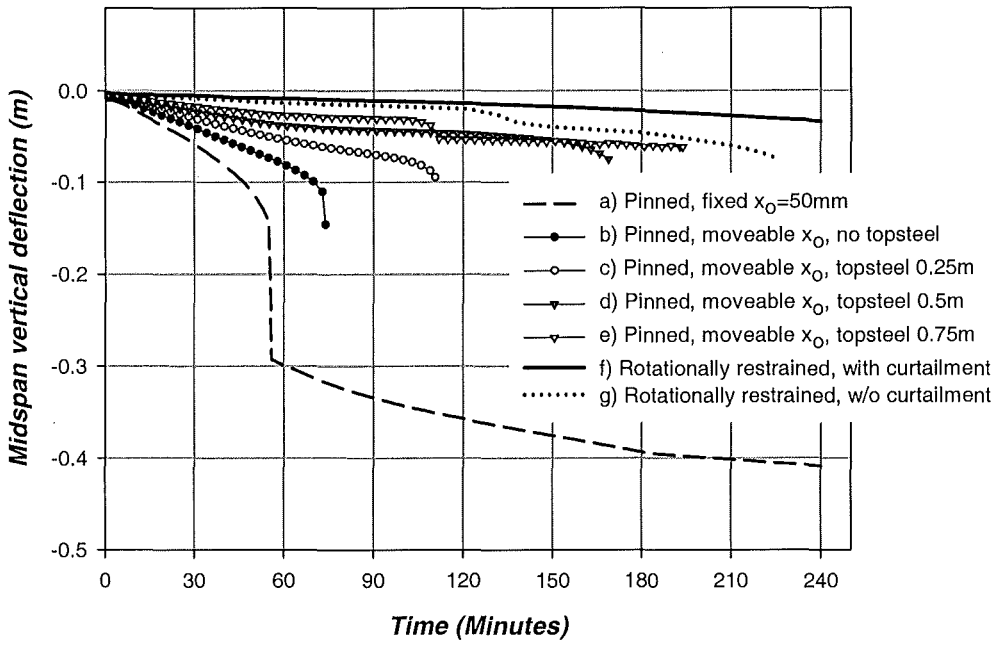

Figure 5-57: Midspan vertical deflections of the slabs with 10% axial restraint stiffness.

Figure 5-57 shows the variation of the midspan deflections of the slabs with different end supports, with 10% axial restraint stiffness. The graph shows that the slabs with 10% axial restraint behaved similarly to the slab with 1% axial restraint. Figure 5-57 shows that for each type of support condition, the slabs with 10% axial restraint had poorer behaviour compared with those with 1% axial restraint. The pin-supported slab with its line of thrust fixed (slab *a*) showed the largest deflections while the rotationally restrained slab with continuous top steel had the smallest deflections during the fire.

Comparing the slabs with 1% (Figure 5-56) and 10% restraint stiffness, runaway deflection occurred significantly earlier in slabs *a* and *b* when restrained with 10% stiffness than with 1% stiffness. However, Figure 5-57 shows that the fire resistance of the slabs increased significantly to 111 minutes with 0.25m top steel at the supports. The graph shows that the fire resistance of the slab increased to 169 minutes and 194 minutes with 0.5m and 0.75m top steel, respectively.

The graph shows that the effect of curtailment on the rotationally restrained slab was minimal. The slab with curtailed top steel (slab *f*) had slightly larger deflections at the advanced stages and a lower fire resistance of 225.5 minutes than the slab with continuous top steel.

5.9.5. Vertical deflections of slabs with different support conditions (k=100%)

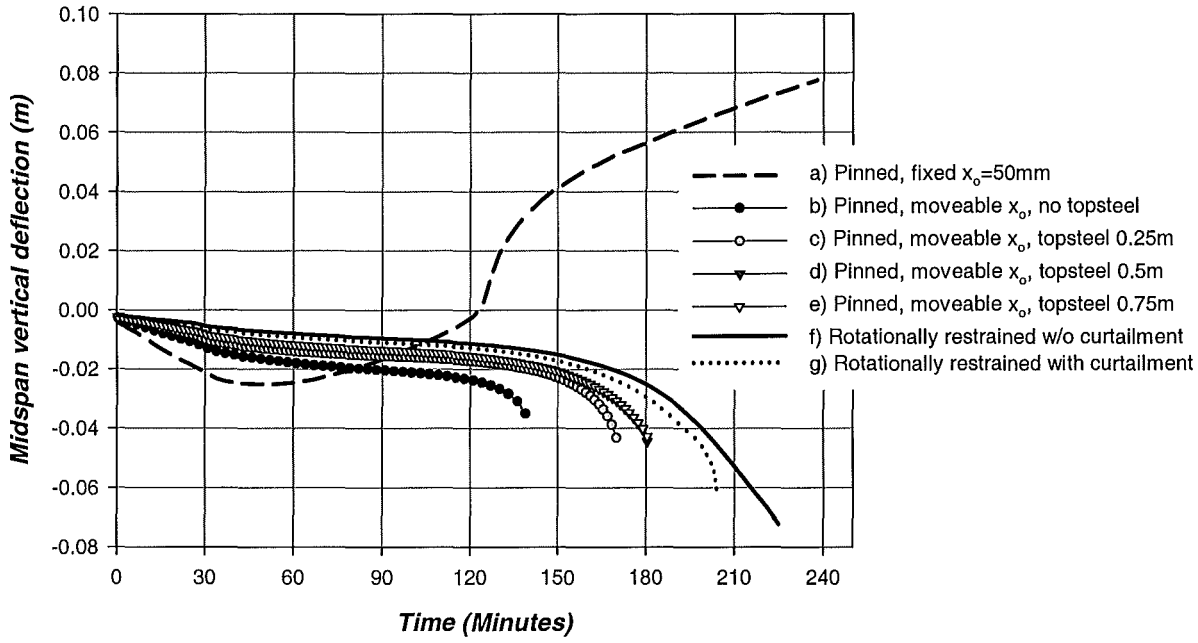

Figure 5-58: Midspan vertical deflections of the slabs with 100% axial restraint stiffness.

Figure 5-58 shows the variation of the midspan deflections of the slabs with 100% axial restraint stiffness with different types of supports. The graph shows that the pin-supported slab with its line of thrust (x_o) fixed at 50mm above the soffit deflected downwards very rapidly during the initial stages. After 50 minutes, the sagging deflections reduced and the slab deflected upwards and formed a hogging deflected shape until the end of the fire. The pin-supported slab with a fixed line of thrust had the highest fire resistance as the hogging deflected shape of the slab enabled it to resist the loads as a shallow arch.

If the position of line of thrust could move (slab *b*) the analyses show that the pin-supported slab had much lower fire resistance (140 minutes) than if it had its position of line of thrust was fixed. The fire resistance of the slab increased substantially when 0.25m topsteel was provided at the end supports, increasing the failure time from 140 minutes in slab *b* to 170 minutes in slab *c*. By increasing the length of the topsteel to 0.5m, the fire resistance of the slab increased only slightly to 180.5 minutes, but showed no increase when the length was further increased to 0.75m, shown by the identical deflection curves.

If full rotational fixity is provided at the end supports, the fire resistance of the slabs would be increased to 204 minutes for the slabs with curtailed topsteel, and 225 minutes for the slab with continuous top steel.

5.9.6. Conclusions

This section presents the analyses of pin-supported slabs with moveable line of thrust modelled to simulate cast-in-situ reinforced concrete slabs. The results of the analyses have shown that:

- The fire behaviour of cast-in-situ reinforced concrete slabs lies between the pin-supported slabs and rotationally restrained slabs.
- The fire resistance of cast-in-situ reinforced concrete slabs increased from the pin-supported condition to the rotationally restrained condition as the length of the top steel at the supports increased.
- The time to failure of cast-in-situ slabs can be very low if there is no top steel anchored into the supports.
- The fire behaviour of slabs with low (1%) and intermediate (10%) axial restraint stiffnesses was sensitive to the length of the top steel at the supports. The fire resistance of these slabs increased significantly as the length of the top steel increased.
- The fire behaviour of slabs with high axial restraint (100%) was less sensitive to the lengths of the top steel at the supports.

5.10. Conclusions

The main findings of the research on one-way slabs are follows:

i) The behaviour of one-way slabs under fire conditions is very sensitive to their end support conditions and the axial restraint stiffness.

ii) Slabs with rotational restraint at both end supports have much better behaviour and significantly higher fire resistance than pin-supported slabs.

iii) The behaviour of a slab under compressive restraint is not easy to quantify and model, even with a sophisticated finite element program. Computer modelling of restrained reinforced concrete floor systems is difficult because of poor information about the actual boundary conditions in real construction, especially the likely height of the axial restraint force, which may change in location during fire exposure.

5.10.1. Pin-supported slabs with fixed line of thrust

The analyses of pin-supported slabs with fixed line of thrust have shown that:

i) The behaviour of axially restrained pin-supported slabs under fire conditions is very sensitive to the position of the line of thrust at the supports and the stiffness of the axial restraint.

ii) High compressive axial restraint does not always increase the fire resistance of one-way pin-supported slabs. High compressive restraint is beneficial only if the line of thrust at the supports is located well below the centroidal axis and when the centroidal axis of the slab remains above the line of thrust during the fire exposure.

iii) High compressive axial restraint produces poor slab behaviour if the line of thrust at the supports is located close to the centroidal axis. In this case, high compressive restraint increases the vertical deflections of the slab and decreases the time to plastic hinge formation.

iv) For pin-supported slabs with the line of thrust fixed and located close to the soffit (up to 50mm above the soffit), high axial restraint ($\Delta L/L \leq 0.001$ and $k \geq 40\%$) produces good behaviour and high fire resistance. With intermediate or low axial restraint stiffness ($\Delta L/L > 0.001$ and $k < 40\%$), the slab deforms into a catenary, resulting in axial tensile forces being generated. If the slab does not have sufficient axial tensile capacity at the supports to resist the tensile forces, it will collapse.

v) The behaviour of a pin-supported slab in a real fire is no worse than in a long duration ISO fire. In many cases, better slab behaviour was observed in the decaying fire compared with a long duration ISO fire.

5.10.2. Rotationally restrained slabs

The analyses of rotationally restrained slabs have shown that:

i) Slabs with flexural continuity have excellent behaviour under fire conditions.

ii) Rotationally restrained slabs with low axial restraint have better fire resistance than simply supported slabs and have smaller deflections than equivalent pin-supported slabs.

iii) Rotationally restrained slabs with top steel curtailed according to code recommendations (SNZ, 1995) showed similar behaviour to those with top steel over the full length of the slab.

5.10.3. Pin-supported slabs with moveable line of thrust

Pin-supported slabs with moveable line of thrust refer to slabs modelled to simulate cast-in-situ reinforced concrete slabs (See Section 5.8 and 5.9 for details). The analyses have shown that:

i) Compressive restraint increases the fire resistance of pin-supported slabs with moveable line of thrust if the axial restraint stiffness is high ($\Delta L/L \leq 0.001$ and $k \geq 40\%$). For slabs with high axial restraint, compressive restraint is beneficial to the slab behaviour if the vertical deflections are small and if the line of thrust at the end supports is located below the centroidal axis. The beneficial effects of compressive restraint are lost if the centroidal axis of the slab drops below the line of thrust.

ii) For slabs with low and intermediate axial restraint stiffness ($\Delta L/L > 0.001$ and $k < 40\%$), compressive axial restraint produces worse behaviour than the *pin-roller* (unrestrained) condition.

iii) Compared with the rotationally restrained slabs, the time to failure of these slabs can be very low if there is no top steel anchored into the supports.

iv) The fire behaviour of these slabs with low and intermediate axial restraint stiffnesses is sensitive to the length of the top steel at the supports. The fire resistance of these slabs increases as the length of the top steel increase. Slabs with high axial restraint are less sensitive to the lengths of the top steel at the supports.

v) The thrust-expansion results from the SAFIR analyses of slabs with moveable line of thrust showed a similar trend to the results of the PCA tests.

vi) The PCI hand calculation method is not recommended for assessing the required stiffness to enhance the fire resistance of pin-supported slabs, because it is an over-simplification of slab behaviour in fire.

6. EXPERIMENTAL FIRE TESTS OF TWO-WAY SLABS

6.1. Introduction

The experimental fire tests of two-way concrete slabs at the BRANZ fire resistance furnace are presented in this chapter. The main objective of the fire tests is to investigate the behaviour of two-way concrete slabs in a controlled furnace environment. This chapter summarises the details of the fire tests and is based on the fire test report by Lim et al. (2002) where the full details and data can be obtained. The observations of the fire tests and some of the data recorded will be presented in this chapter. Comparison of the fire tests results with finite element modelling will be described in chapter 9.

6.1.1. Impetus

The impetus of the experimental fire tests comes from the full scale fire tests conducted at the Cardington Large Building Test Facility (Bailey et al., 1999; Newman et al., 2000) and another independent test conducted at the Building Research Establishment (BRE) (Bailey et al., 2000) to simulate the behaviour of simply supported two-way slabs under fire conditions. Those tests demonstrated the significant effects of tensile membrane action on increasing the fire resistance of composite slabs. Numerical simulations of the Cardington building by previous researchers (Huang et al., 1999, 2000, 2001; Sanad et al., 1999; Elghazouli et al., 2001) have shown good agreement with the test results. However, there are no published fire tests of two-way slabs in a controlled furnace environment which could be easily used to verify existing computer models. The ambient test at the BRE did not account for the thermal effects on the slab behaviour which include thermal bowing and expansion of the slab, and strength degradation of the steel and concrete. The need to determine the slab performance under a representative severe fire condition and to obtain data of fire tests in a controlled environment led to the fire tests at BRANZ Limited (Building Research Association of New Zealand).

6.1.2. Objectives

The objectives of the fire tests were:

- To investigate the behaviour of concrete and composite two-way floor slabs, in a controlled furnace test.
- To investigate the influence of tensile membrane action on the structural fire resistance of two-way slabs.
- To determine the amount of steel content required for crack control to prevent integrity failure and to assess the performance of hard-drawn reinforcing mesh at elevated temperatures.
- To verify the SAFIR finite element program (Franssen et al., 2002).
- To verify the current analytical design methods proposed by Bailey (2001) and Clifton et al (2003) for slabs under severe fire conditions.

6.1.3. Scope

Six concrete slabs were tested using the BRANZ fire resistance furnace. The floor slabs consisted of three reinforced concrete flat slabs and three different proprietary composite steel-concrete slabs. The slabs measured 3.3m wide by 4.3m long and were simply supported on all four sides above the furnace which had an opening of 3.0m by 4.0m. The slabs were horizontally unrestrained and were loaded with a constant uniformly distributed load. The slabs were all heated on the underside with the ISO 834 standard fire curve for three hours.

6.2. Organisation of the tests

The slabs were constructed between July and November 2001, at the Civil Engineering Laboratory of the University of Canterbury, Christchurch. After the slabs were constructed, they were stored in a warehouse to cure and dry. The slabs were shipped to Wellington where they were stored at the BRANZ Fire Laboratory until the scheduled date of the tests. The fire tests were conducted from 21st June 2002 to 5th July 2002.

6.3. Specimen Details

6.3.1. Slab configurations

Six slabs were tested at the BRANZ furnace. The slabs consisted of three flat slabs and three proprietary composite steel-concrete slabs. Each slab measured 3.3m wide by 4.3m long and the thicknesses ranged from 90mm to 130mm. The six configurations that were tested are shown in Table 6-1 and Table 6-2. The flat slabs were 100mm thick and differed from each other by the amount of reinforcing steel. The flat slabs may be considered to represent composite slabs with steel decking that have lost significant flexural strength and stiffness due to the effects of the fire exposure. The different quantities of reinforcing in the flat slabs were intended to investigate its effect on crack control in the slabs to prevent integrity failure.

The furnace represents a fire compartment with a two-way slab supported over it. The slabs are directly exposed to the fire, on the assumption that there is no fire protective ceiling in the compartment. The rigid vertical supports at the four edges of the slabs represent fire protected primary beams which do not deflect during the fire. The tests may be considered to simulate floor systems supported on unprotected secondary beams which do not retain any significant strength or stiffness during the fire.

	Slab	Slab thickness	Reinforcing mesh	Concrete cover to bottom bar
1.	661 flat slab	100mm	661 mesh	25mm
2.	HD12 flat slab	100mm	HD12 bars	25mm
3.	D147 flat slab	100mm	D147 mesh	25mm
4.	130mm Hi-bond slab	130mm	D147 mesh	20mm above steel ribs.
5.	130mm Traydec slab	130mm	D147 mesh	15mm above steel ribs.
6.	Speedfloor	90mm	661 mesh	25mm

Table 6-1: Configuration of slabs that were tested

100mm flat slabs	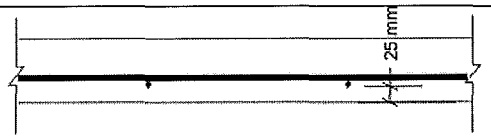
Dimond Hibond	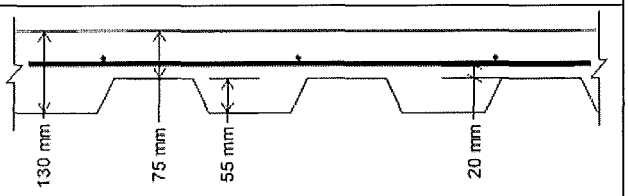
Traydec	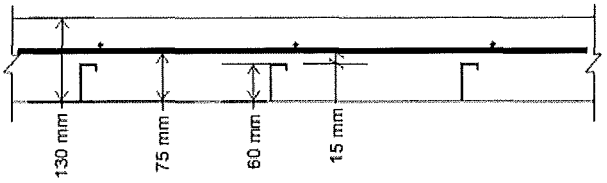
Speedfloor	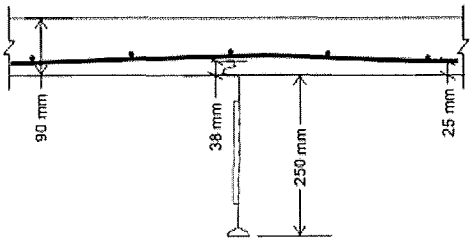

Table 6-2: Cross section of slabs that were tested

6.3.2. Reinforcement

Different types of reinforcing steel were used in the tests, which consisted of hard-drawn mesh and hot-rolled reinforcing bars (Table 6-3). The mechanical properties of the mesh and bars shown in Table 6-3 were determined from tensile tests on samples of the reinforcing steel at ambient conditions. Figure 6-1 shows the typical stress-strain curves of the three different types of mesh used in the slabs, determined from tensile tests of the samples.

Table 6-3 and Figure 6-1 show that the cold drawn D147 and 661 mesh had much higher strength than the hot-rolled HD12 bars but they had lower strain limits. The strain limit is the maximum strain on the stress-strain curve for each type of steel and is the point where the steel ruptures (Figure 6-1). The 25mm clear concrete cover to the bottom reinforcement in the flat slabs provided a two-hour fire resistance stability rating in accordance with the New Zealand Concrete Structures Standard (NZS, 1995). The reinforcement configurations for slabs 4 and 5 of Table 6-1 provided a uniform moment capacity for the two composite steel-concrete slabs, assuming the steel decking did not contribute to the bending strength during the fire.

The mesh in the slabs were arranged so that the bars that spanned the short direction were placed below the bars that spanned in the long direction. This increased the lever arm of the bars spanning in the short direction to allow larger moments to be carried across the short direction. The ribs of the *Dimond Hi-bond* and *Tray-dec* steel decking and the joists of the Speedfloor slab spanned in the long span of the furnace. The properties of the steel decking and joists are shown in Table 6-4 and were obtained from the manufacturer's listings.

Reinforcing steel	Description	Bar diameter	Grid spacing	Yield stress*	Steel content	Strain limit*
D147 mesh	Cold drawn deformed mesh	8.7mm	300mm	565 MPa	198mm^2/m	2.3 %
661 mesh	Cold drawn plain mesh	7.5mm	150mm	568 MPa	295mm^2/m	3.2 %
HD12 bars	Hot rolled deformed bars	12mm	200mm	468 MPa	565mm^2/m	21 %

*Average of three samples from tensile tests

Table 6-3: Properties of the reinforcing steel at ambient conditions.

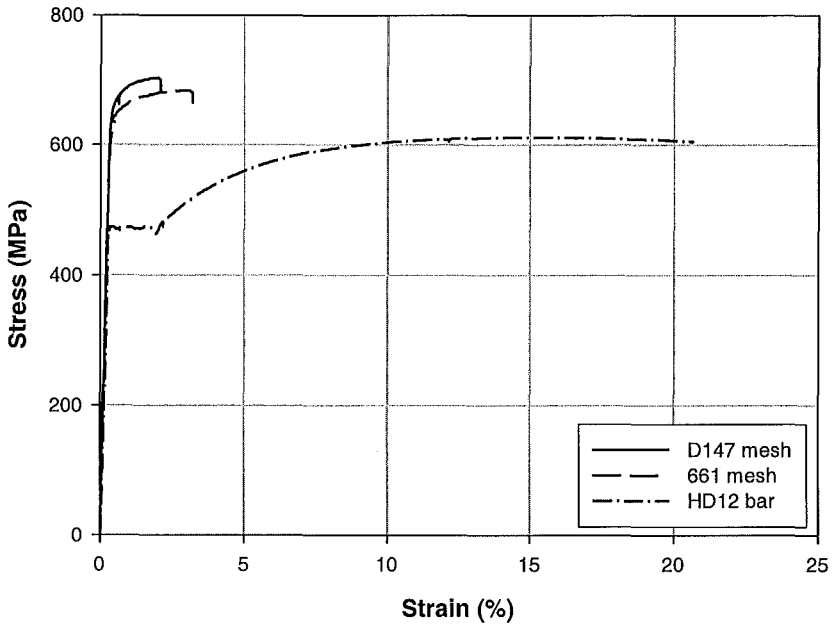

Figure 6-1: Typical stress strain curves of the reinforcing steel at ambient conditions from tensile tests.

Steel decking/ joists	Steel deck/joist thickness	Yield stress
Dimond Hibond	0.75mm[1]	550 MPa[1]
Traydec	0.75mm[2]	550 MPa[2]
Speedfloor	3mm[3]	350 MPa[3]

Table 6-4: Properties of the steel decking and joists of the composite slabs

1= Hibond Design Manual (Dimond Industries, 1997)

2= Traydec 300 Specification and Design Manual (Forgan Jones Structural Ltd, 1996)

3= Speedfloor Holdings Ltd.

6.3.3. Concrete

Normal weight concrete was used for the slabs and the specified compressive strength was 30MPa. The aggregates were 19mm greywacke (siliceous) aggregates. The compressive strengths of the concrete were determined by cylinder crushing tests conducted 7 days and 28 days after the concrete was cast. Crushing tests were also conducted a week after the fire tests to determine the strengths of the concrete during the fire tests. The results of the crushing tests are shown in Table 6-5.

Slab	28 day strength	Age of concrete during fire tests	Strength during fire tests
661 slab	32.8 MPa	287 days	36.6 MPa
HD12 slab	22.6 MPa	216 days	36.7 MPa
D147 slab	32.8 MPa	293 days	36.6 MPa
Hibond	30.2 MPa	308 days	32.1 MPa
Traydec	30.2 MPa	310 days	32.1 MPa
Speedfloor	31.5 MPa	214 days	37.6 MPa

Table 6-5: Compressive strengths of concrete.

6.3.4. Strain gauge and thermocouple layouts

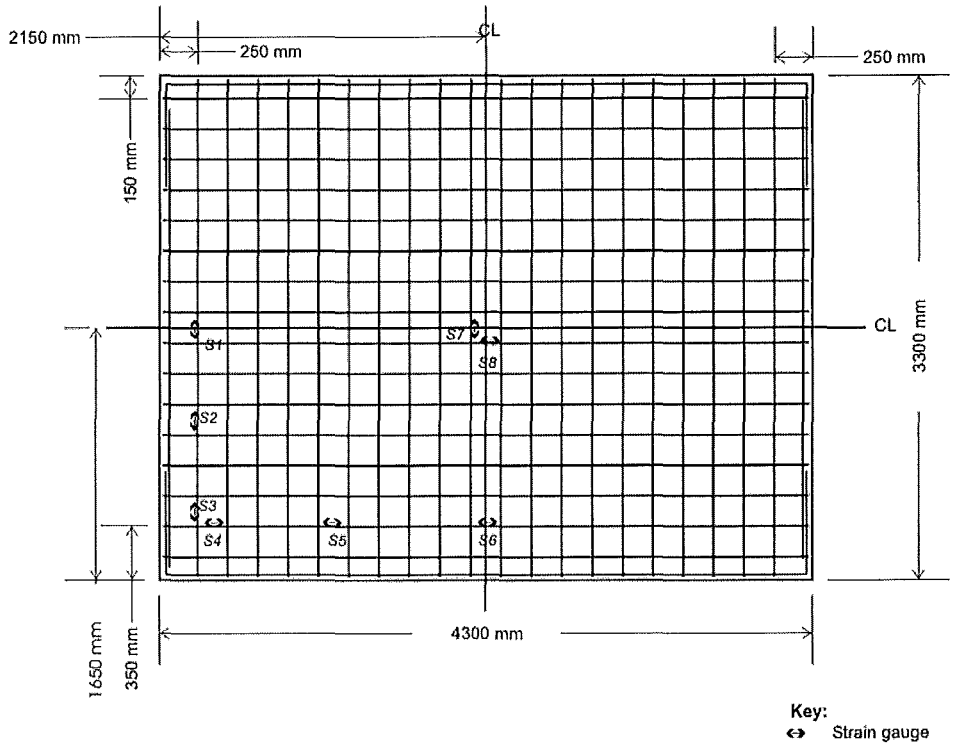

Figure 6-2: Typical layout of strain gauges in the slabs.

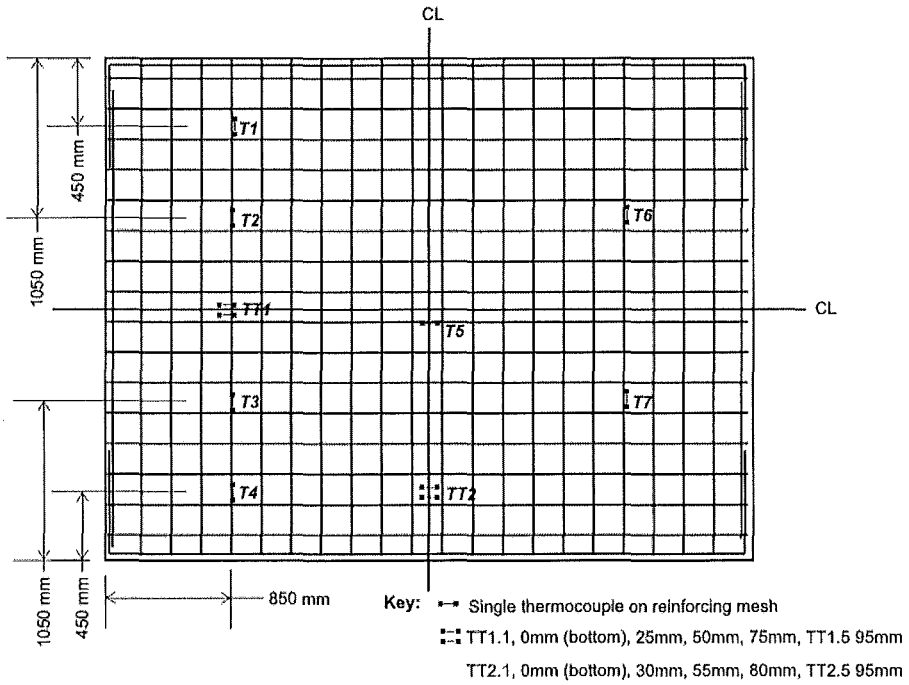

Figure 6-3: Typical layout of thermocouples in the slabs.

Figure 6-2 shows the typical strain gauge layout in the slabs. This figure shows a slab with 8 strain gauges, arranged to measure the strains of the reinforcing steel in the middle and the edges of the slab. Some of the slabs were more heavily instrumented to measure the strains at

other locations such as at the quarter spans of the slab or at the steel joists in the Speedfloor slab. The layouts of the strain gauges for each of the slabs can be found in the fire test report. The strains in the reinforcing bars of the slabs were measured with high-temperature resistant strain gauges. These strain gauges were only accurate up to 300°C and had a maximum strain limit of 1% strain. The strain gauges were attached with high temperature resistant glue, water-proof coating and wires in order for the gauge to function up to its maximum operational temperature.

Figure 6-3 shows the typical layout of thermocouples and thermocouple trees in a slab. The thermocouples were placed at mid-height of the reinforcing bars and are labelled as T1, T2, etc. The thermocouple trees are labelled as TT1 and TT2. Five key thermocouples were also attached to the unheated surface of each slab. Type-K thermocouples were used to measure the temperatures of the reinforcing steel and across the thickness of the slabs.

6.4. Test configuration

6.4.1. General

This section describes the slab loading, support conditions and the instrumentation used to measure the deflections.

6.4.2. Testing standard

The fire tests were conducted on an oil-fired furnace. The ISO 834 standard fire curve (ISO, 1975) was used to heat the slabs.

6.4.3. Fire testing sequence

The slabs were tested in the sequence shown in Table 6-1. The flat slabs with medium (661 mesh) and high (HD12) levels of reinforcing were tested first to determine whether or not the level of loading was appropriate for the weaker flat slab and composite slabs, and to detect problems with the data logging equipment for the subsequent slabs which had more instrumentation.

6.4.4. Support conditions

Vertical supports

Figure 6-4 shows the cross section of the slab and loading drums over the furnace. The slabs were simply supported on four edges and were unrestrained against horizontal movement. The slabs were supported over the furnace on a rectangular frame which was made of steel C-channels and had a reinforced concrete beam lining the internal perimeter.

The slabs were vertically supported at their four edges on cylindrical rollers on top of the concrete beam. The rollers were placed continuously around the perimeter of the supporting frame. The rollers represented simple support conditions which allowed the slab to freely rotate and roll horizontally at the supports. Due to the rough surface of the concrete beam, 5mm thick steel plates were welded over the concrete beam to the steel frame to form a smooth rolling surface for the rollers (Figure 6-5 and Figure 6-6).

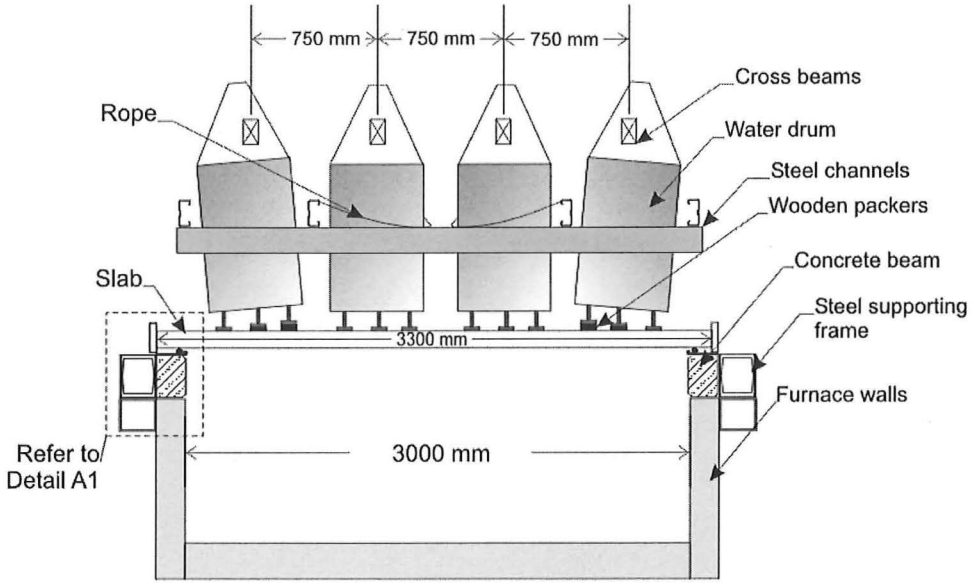

Figure 6-4: Section across the short span of the furnace.

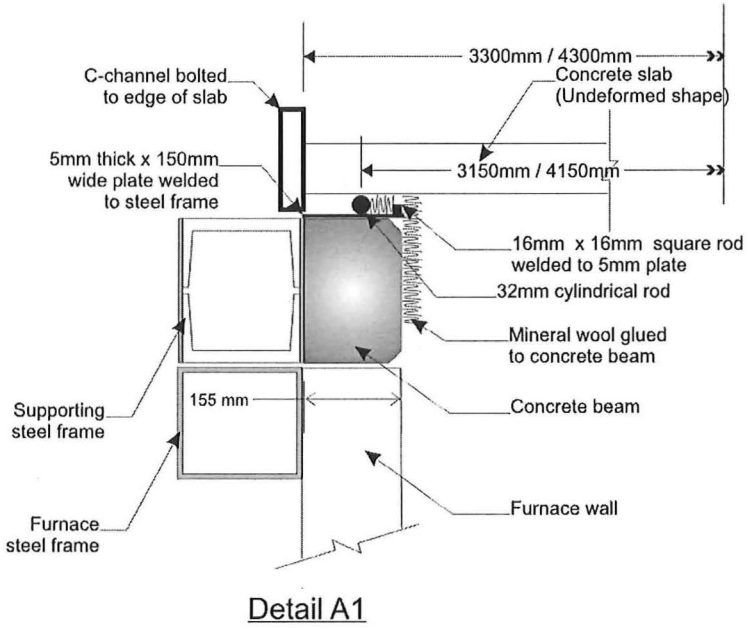

Figure 6-5: Detail A1 (Detail of slab support on the furnace)

A 16mm square rod was welded to the edge of the steel plates to stop the rollers from rolling into the furnace (Figure 6-5). Mineral wool was glued to the vertical faces of the concrete beam (Figure 6-5 and Figure 6-7) to prevent the rollers from being directly exposed to the flames and to prevent the flames from coming out of the gap between the rollers and the slab.

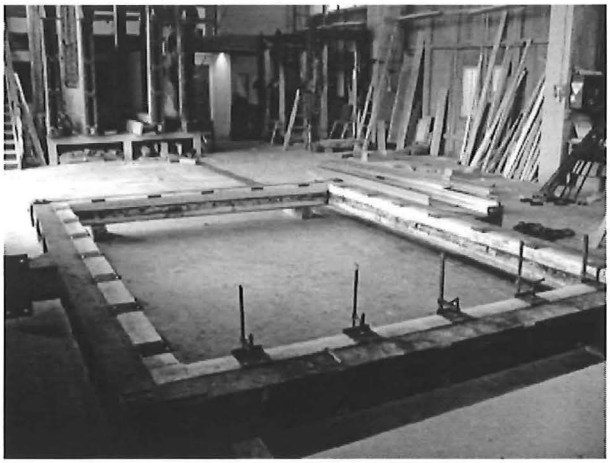

Figure 6-6: Rectangular frame used to support the slab over the furnace. Note the 150mm wide plates welded to the steel frame, over the concrete beam.

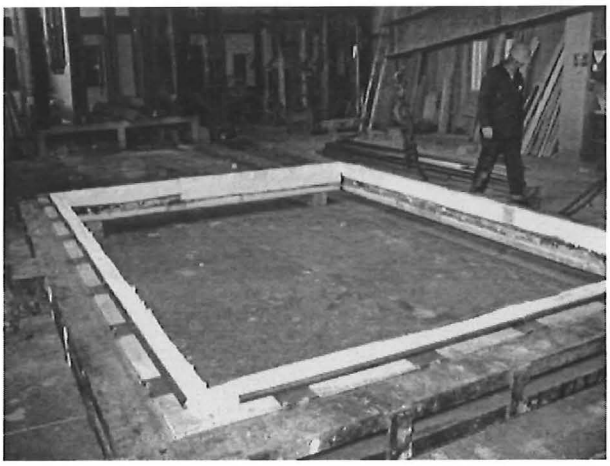

Figure 6-7: Steel rollers positioned on the frame with the mineral wool lining the internal perimeter.

A 150mm wide steel flashing was placed underneath each slab around the entire perimeter when they were constructed (Figure 6-8 and Figure 6-9). The steel flashing served to minimise the friction between the bottom surface of the concrete slab and the rollers. The steel flashing also prevented local crushing of the concrete when the slab was supported on the rollers. The slab was positioned onto the steel frame and both the frame and slab were lifted simultaneously onto the furnace.

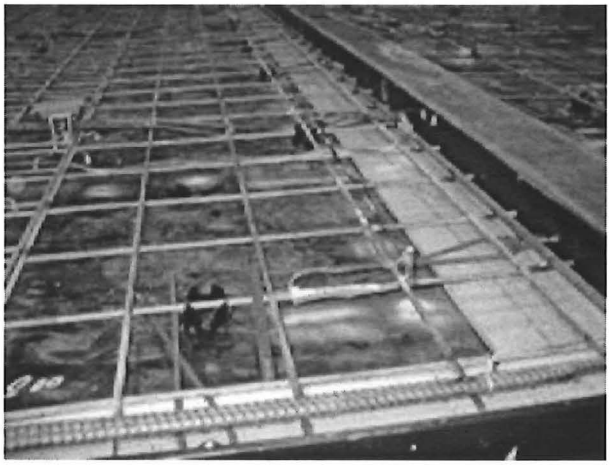

Figure 6-8: Steel flashing placed around the perimeter prior to pouring of the concrete.

Figure 6-9: Steel flashings at the bottom of the slab.

Corner clamps

The corners of the first two tests (661 and HD12 flat slabs) were not clamped down and were free to lift. However, the amount of curling of the corners during those two tests was very large and would not represent the behaviour of a slab under realistic support conditions found

in a typical building. Therefore, the corners were clamped down in the tests of the remaining four slabs. The corners were clamped down with steel angles placed diagonally across the corners which were welded or bolted to the supporting steel frame (Figure 6-10).

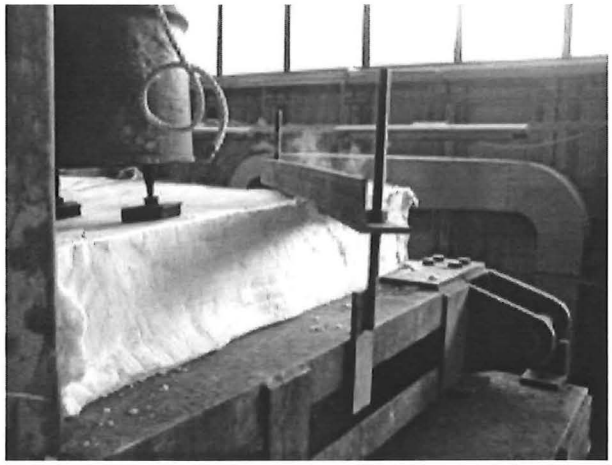

Figure 6-10: Steel angle bolted to the supporting steel frame to clamp down the corners.

6.4.5. Slab loading

In addition to the self weight of the slabs, a uniformly distributed load was applied on the slabs to simulate live loads. Twenty 200-litre water drums were placed on the slab to represent the uniformly distributed load. The combined weight of the water and the steel drums was 200kg per drum, equivalent to a uniformly distributed load of 3.0kPa. The drums were arranged in a uniform grid of four by five drums (Figure 6-11).

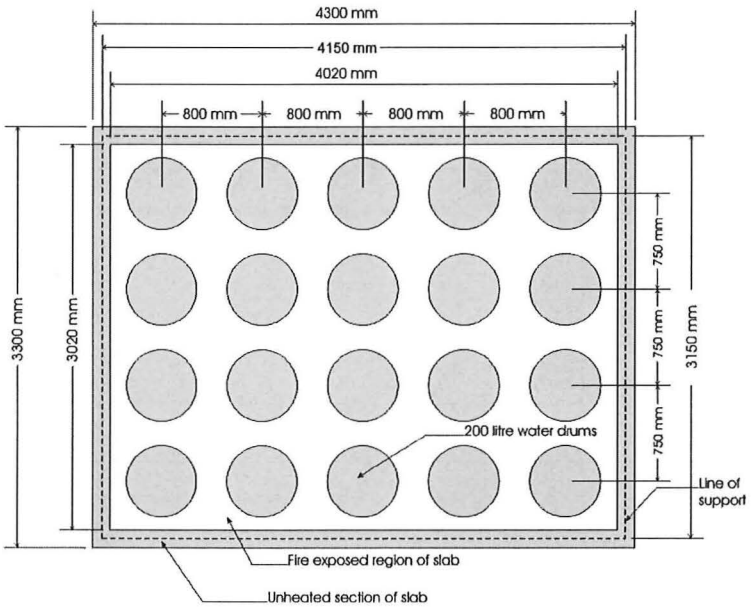

Figure 6-11: Position of the loading drums

The drums were lowered onto the slab by an overhead gantry crane (Figure 6-12). Each drum had a steel strap which allowed the drums to be hung off a series of parallel cross beams. The crane picked up the cross beams which in turn picked up the drums. The cross beams supported the drums to prevent them from falling into the furnace in the event of catastrophic collapse. Each drum had three swivel feet and each foot had a contact surface made of a 100mm square particle board. The slab specimens were loaded an least an hour before each test.

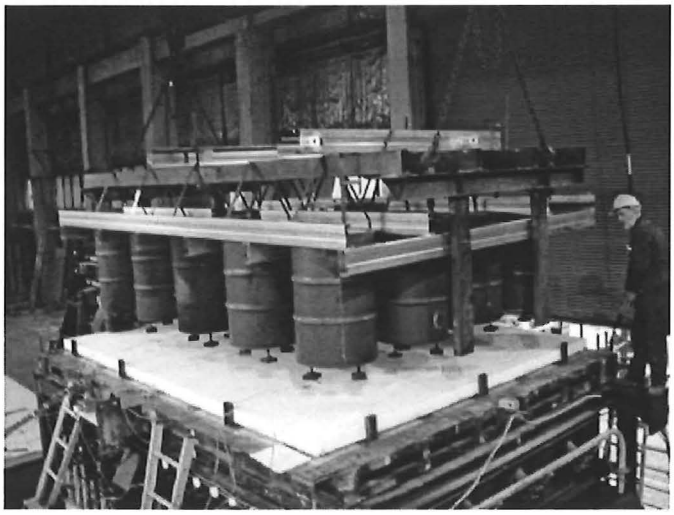

Figure 6-12: Lowering of the water drums onto the slabs.

	w_u (kPa)	Self weight, G (kPa)	Live load, Q (kPa)	Total load, G + Q (kPa)	Load ratio, r_{load}
Flat slab 661 mesh	21.9	2.31	3.0	5.31	0.24
Flat slab HD12 mesh	30.8	2.51	3.0	5.51	0.18
Flat slab D147 mesh	13.3	2.32	3.0	5.32	0.40
Hibond slab	69.1 (9.1)	2.43	3.0	5.43	0.08
Traydec slab	73.8 (9.1)	3.02	3.0	6.02	0.08
Speedfloor slab	55.1 (16.8)	2.32	3.0	5.32	0.10

Table 6-6: Applied loads on the slabs

Table 6-6 shows the applied loads on the slabs. The level of loads that was applied relative to the strength of the slabs is expressed by the load ratio, r_{load}. The load ratio is defined as the ratio of the applied loads on the structure, U^*_{fire}, to the loads that would cause collapse at ambient temperature, R_{cold} (Equation 6-1). The applied loads, U^*_{fire}, consisted of the self-weight of the slab (G) and the live loads from the water drums (Q). The slabs that were tested

had different levels of strength, R_{cold}, due to the different quantities of reinforcing and the types of steel decking resulting in the load ratios ranging from 0.080 to 0.406.

$$r_{load} = \frac{U^{*}_{fire}}{R_{cold}} = \frac{(G + Q)}{w_u} \qquad \textbf{Equation 6-1}$$

For the two-way slabs, the strengths of the slabs were determined by the ultimate load, w_u, which is the lowest load level that will form yield line cracks in the slabs. The ultimate loads were calculated from yield line theory (Park et al., 2000).

For the calculation of the ultimate loads of the composite slabs and the Speedfloor slab, the contributions of both the composite steel decking/joists and the steel mesh were included in the flexural strengths spanning in the longitudinal direction. In the transverse direction, only the contribution of the mesh was considered and the strength contribution of the steel decking was ignored. The numbers in the brackets are the ultimate loads of the slabs based on the reinforcing steel in the slab only, not including the strength contributions of the composite steel decks and joists.

6.4.6. Large differential vertical deflections

When the slabs undergo large vertical deflections, there was concern that the water drums would tilt onto each other and could interfere with the potentiometers which measured the vertical deflections. To address this problem, a steel grille was built around the drums (refer to Figure 6-12 and Figure 6-13) to prevent them from tilting and to ensure they remained vertical. The grille was made of cold-formed steel channels and was bolted to the legs of the frame which supported the cross beams above the drums.

6.4.7. Deflection measurements

The vertical deflections and horizontal movement of the slab edges were measured at the positions shown in Figure 6-13. The vertical deflections were measured across the centre of the slab in the long and short directions. The horizontal and vertical deflections were measured with rotary potentiometers. The rotary potentiometers were supported on steel purlins which were clamped onto the cross beams above the drums (Figure 6-14).

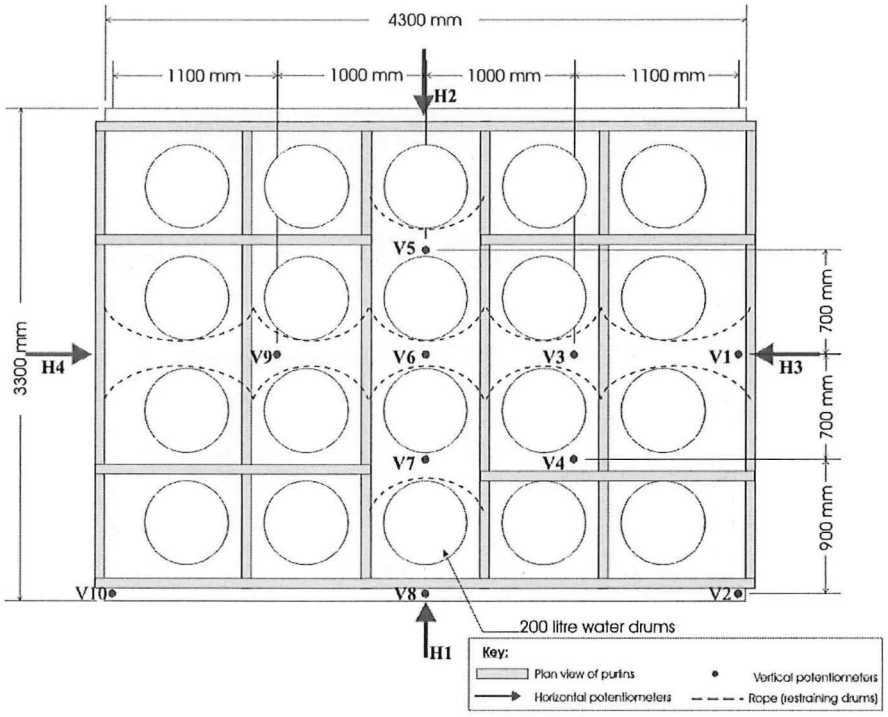

Figure 6-13: Plan view of the potentiometer layout and the steel grid.

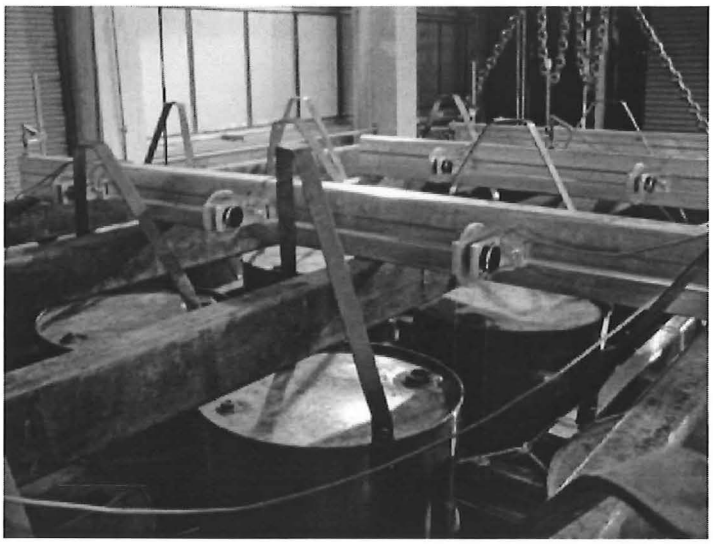

Figure 6-14: Potentiometers supported on the cross beams for measuring the vertical deflections.

6.4.8. Furnace details

Furnace temperatures

The temperature in the furnace was measured with 12 chromel-alumel thermocouples distributed evenly on a horizontal plane approximately 400mm below the soffit of each specimen.

Furnace pressure

The pressure in the furnace was controlled to 18 Pa at 300 mm below the underside of the slab for all the tests. The test standard followed was AS 1530 Part 4 (Standards Australia, 1997).

6.5. Construction and storage

The slabs were constructed at the Civil Engineering Laboratory at the University of Canterbury. The slabs were built and cast in pairs, starting with the Traydec and Hibond slabs with the steel decking of the composite slabs acting as formwork. The subsequent slabs were cast on top of the first two slabs. Polyethylene sheets were stretched over the previously cast slabs to act as bond-breakers to prevent the concrete of the slab above from sticking to the concrete on the slab below. The formwork of the slabs was built by bolting hot-rolled steel angles together. Steel flashings were laid around the perimeter of each slab, under the slabs, and served as a bearing surface for the slab on the rollers.

Figure 6-15 shows one of the four lifting anchors cast into each slab for lifting. Each of the inserts had a 2.3 tonne capacity. Additional reinforcing bars were tied to the anchors to prevent instantaneous failure by concrete rupture during lifting. The arrow in Figure 6-16 shows the strongbacks, attached with threaded inserts, placed over the formwork of the composite slabs. The strongbacks served as a template for positioning the threaded inserts during the casting of the slabs. The strongbacks were later attached to the threaded inserts and used for lifting the composite slabs.

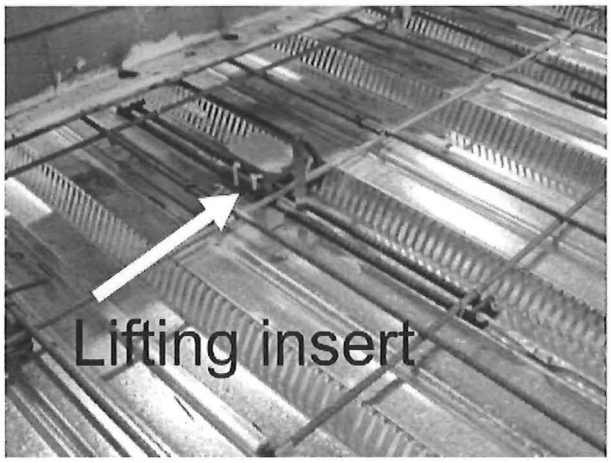

Figure 6-15: Lifting insert in one of the slabs.

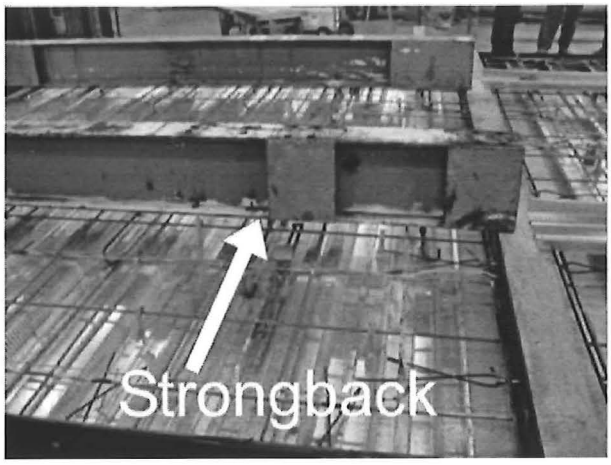

Figure 6-16: Hibond slab prior to casting, with strongbacks attached.

The concrete was supplied by mixer trucks to the Civil Engineering Laboratory. The concrete was poured with a skip (Figure 6-17) and vibrated with needle vibrators to prevent honey-combing. Concrete cylinder samples were made for each pour to be used for crushing tests. Wet gunny sacks were placed over the slabs after casting of the concrete for several days to allow the slabs to cure. The sacks were covered with a large polyethylene sheet to prevent moisture loss by evaporation (Figure 6-18).

Figure 6-17: Concrete being poured into the formwork and vibrated.

Figure 6-18: Slabs covered with wet gunny sacks and polyethylene sheets the day after being cast.

After all the slabs had been cast, they were transported out of the laboratory (Figure 6-19) and stored in another warehouse. They were stacked on an A-frame with three slabs on each side of the frame (Figure 6-20). Timber bearers were placed between the slabs to provide air

circulation between the slabs to allow them to dry and cure. A tent was constructed over the slabs with polyethylene sheets to form an air-tight condition and a dehumidifier was placed inside the tent to produce a dry condition in the tent to expedite the drying of the slabs. The concrete cylinders were also placed in the tent so that they would be exposed to the same conditions as the slabs.

Figure 6-19: Transporting of the slabs out of the Civil Engineering Laboratory.

Figure 6-20: Slabs being stacked on an A-frame in a warehouse.

6.6. Results

6.6.1. General overview

This section presents the results and observations of the fire tests. The deflections, temperatures and strains measured during the tests are presented. Only some of the results will be presented and the remainder of the results can be found in the test report by Lim et al. (2002).

The sign conventions of the graphs are similar to those used in the previous chapter. Negative vertical deflections are downward and positive deflections are upward. For the horizontal deflections, positive deflections indicate outward deflection (expansion) while negative deflections indicate inward deflection (contraction). Tensile strains are measured as positive strains, while compressive strains are negative. For the purposes of discussion, the long span of the slab is referred as the longitudinal direction and the short span is referred as the transverse direction.

6.6.2. Test 1: 661 flat slab

Furnace temperature

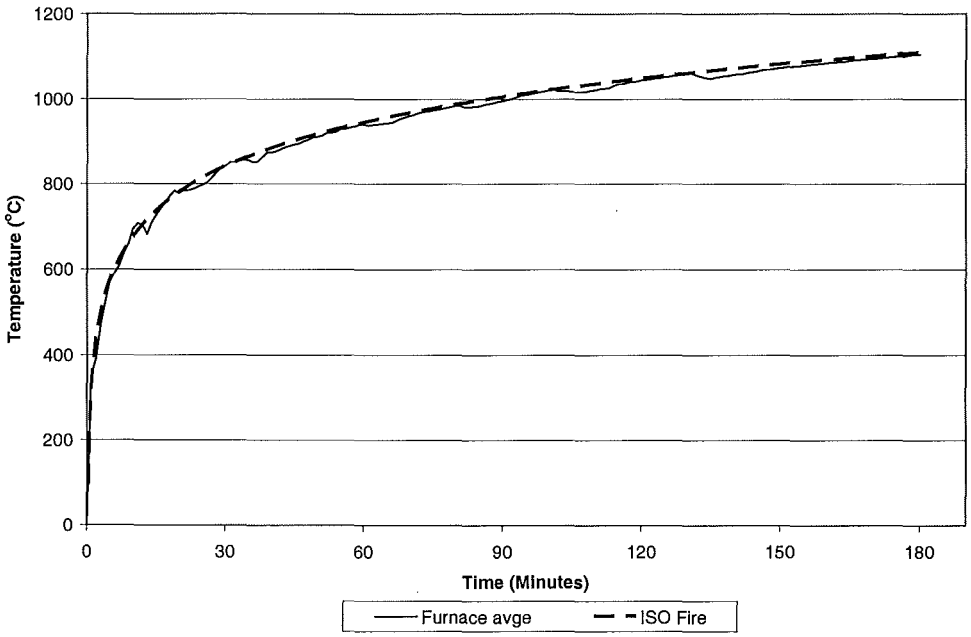

Figure 6-21: Furnace temperature during the 661 flat slab fire test.

Figure 6-21 shows the average temperature in the furnace during the fire test of the 661 flat slab. The temperature curve shown is the average of the twelve thermocouples in the furnace.

The furnace was driven so that the average temperature in the furnace followed the temperatures of the ISO 834 standard fire curve.

Observations

During the first 15 minutes of the fire test, the corners of the slabs started to curl upwards noticeably (Figure 6-22). Mineral wool was used to cover these openings to prevent the hot gases from escaping. Cracking at the top of the slab soon followed the curling of the corners. These cracks initiated from the middle of the slab and propagated outwards in the transverse direction to the edge supports. The cracks only formed on the surface and did not penetrate the full depth of the slab.

Water and steam then seeped through the cracks and formed a large puddle in the middle of the slab (Figure 6-23). During the later stages, the level of the puddle dropped as the water evaporated. There were no cracks visible on the bottom surface of the slab, seen through the viewing ports located on the east side of the furnace. After 2 hours, the corners of the slabs had lifted more than 100mm. The first set of surface cracks which appeared on the unheated surface across the transverse direction had opened up to approximately 5mm on the top surface. The cracks were superficial and did not allow flames to pass through the slab.

Figure 6-22: Curled corners of the slab.

Figure 6-23: Water puddle in the middle of the slab.

The bottom surface of the slab was smooth and did not show signs of cracking or spalling. The line indentations seen at the bottom surface were due to creases in the polyethylene sheets when the slab was cast and were not due to the effects of the fire (Figure 6-24). The most visible cracks on the top surface were in the middle of the slab, which formed across the

slab in the transverse direction at 300mm centres (Figure 6-25). Diagonal cracks also formed at the corners along with horizontal cracks running in the longitudinal direction, located approximately 600mm from the edges of the slab.

Figure 6-24: Underside of the slab after the fire test.

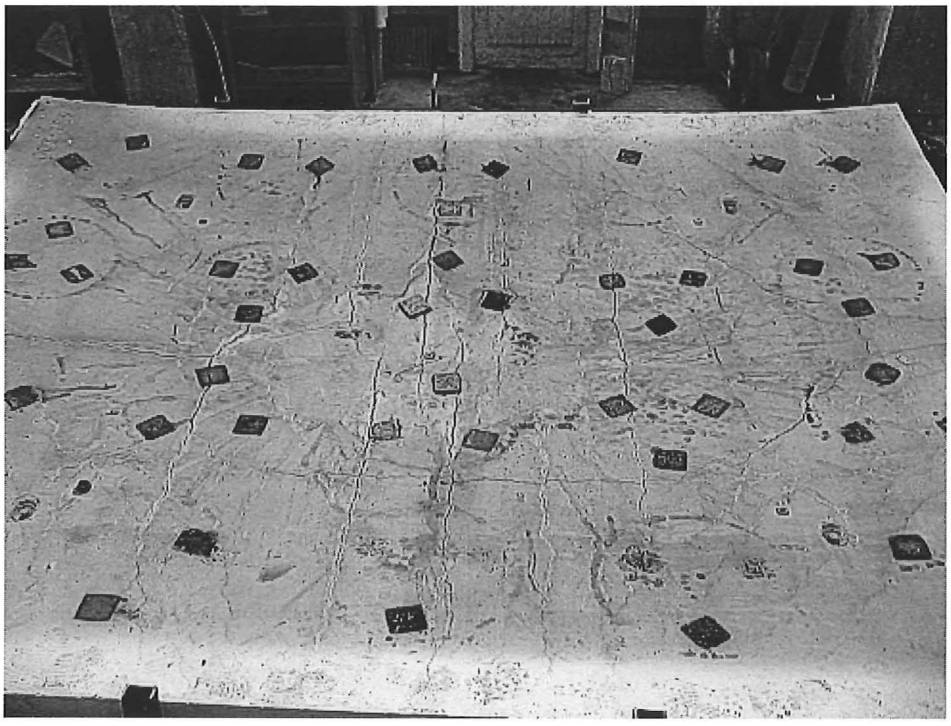

Figure 6-25: Top view of the slab after the test.

Deflections

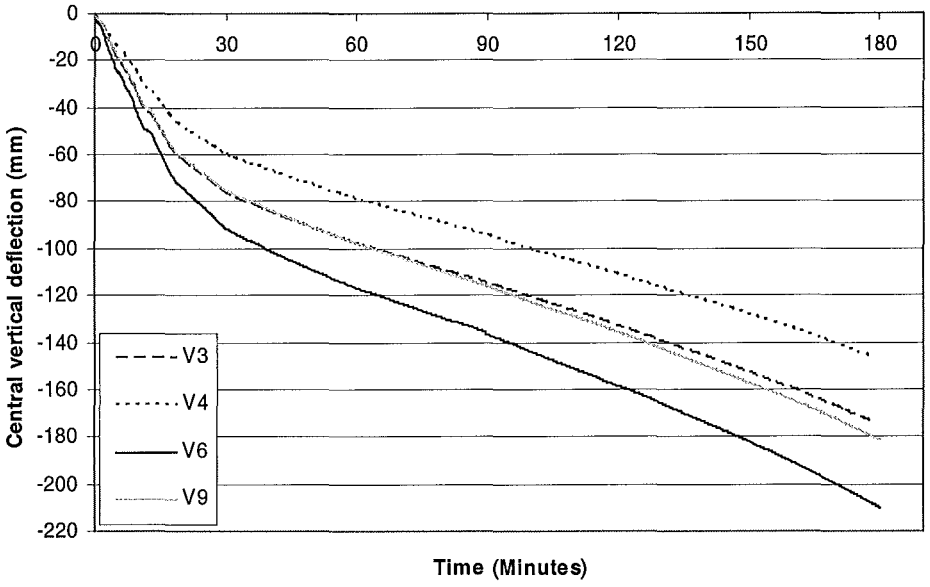

Figure 6-26: Central vertical deflections of the 661 flat slab.

Figure 6-26 shows the variation of the central vertical deflections of the slab during the fire. The slab deflected downwards very rapidly during the initial stage, reaching -74mm at midspan by 20 minutes, followed by a lower and constant rate of -0.8mm per minute for the remaining duration of the test. The deflections measured at quarter span of the slab showed similar trends but with lower deflections. The slab suffered very large midspan deflections (-210mm) at the end of the test.

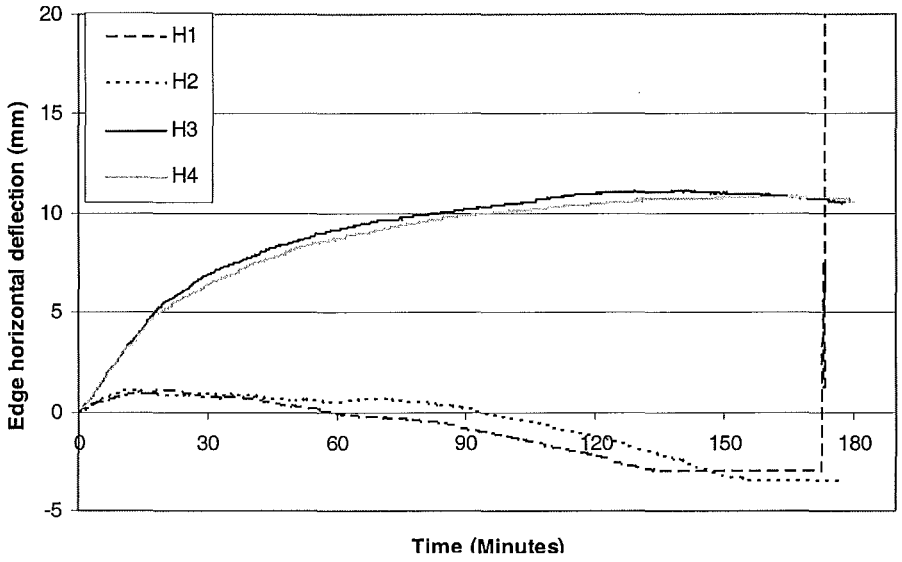

Figure 6-27: Edge horizontal deflections of the 661 flat slab.

Figure 6-27 shows the measured horizontal deflections of the slab. The horizontal deflections were due to a combination of expansion of the slab and downward deflection in the centre region. H1 and H2 measured the horizontal deflections in the transverse direction of the slab; while H3 and H4 measured the deflections in the longitudinal direction (refer to Figure 6-13). The graph shows very small transverse deflections during the initial stages, followed by contraction at the later stages when the middle of the long sides deflected inwards. The transverse horizontal deflections reached a plateau because the potentiometers ran out of travel. In the long direction, the slab showed a high linear expansion up to 19.3 minutes, followed by a slower non-linear increase.

Slab temperatures

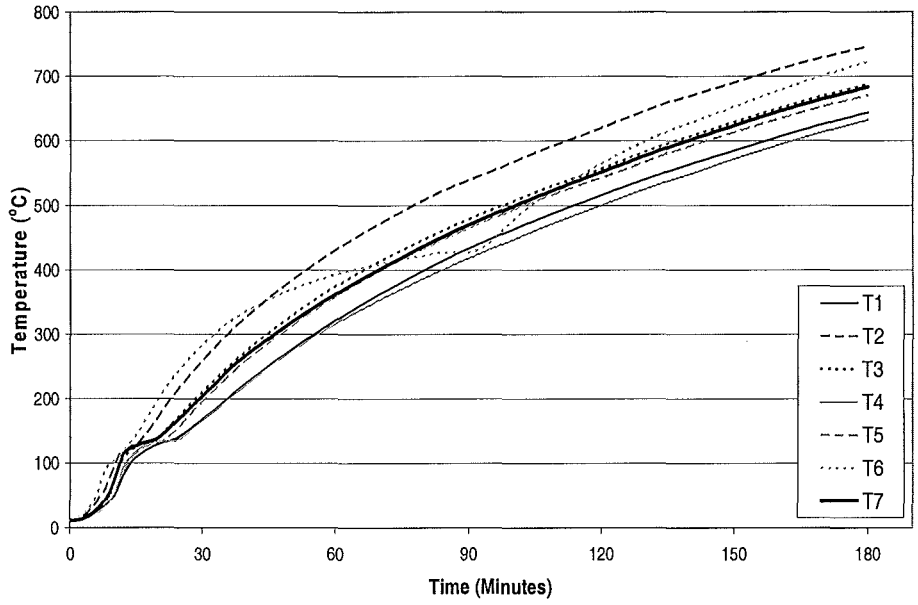

Figure 6-28: Temperatures of the reinforcing mesh in the 661 flat slab.

Figure 6-28 shows the temperatures of the reinforcing mesh. Apart from a slight variation between the thermocouples, the temperatures showed a consistent trend, rising from 12°C during the initial stage, up to a maximum of 746°C by the end of the test. The graph shows a plateau in the temperatures between 14 and 20 minutes. The temperature plateau was possibly due to the moisture increase at the level of the thermocouples caused by the moisture in the concrete being driven from the heated side to the unheated side.

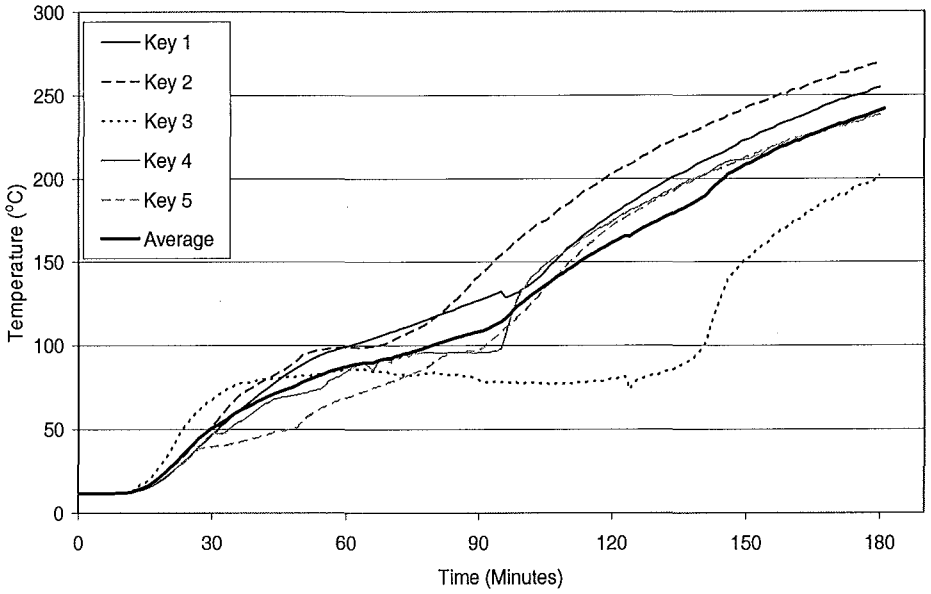

Figure 6-29: Temperatures of the unheated side of the 661 flat slab.

Figure 6-29 shows the temperature measurements of the five key thermocouples on the unexposed face of the slab. The temperatures started to increase 13 minutes after the fire started. Between 40 and 95 minutes, the rate of temperature rise decreased slightly, possibly due to the increased moisture on the top surface. When the water on the top surface evaporated, the temperatures increased once again at a faster rate. Thermocouple number 3, which was located in the middle of the slab, showed a temperature lag below the other thermocouple measurements and remained below 100°C until 140 minutes. This was due to the thermocouple being submerged in the puddle of water in the middle of the slab. After approximately 140 minutes, the puddle of water evaporated and the temperatures increased very rapidly. The average temperature rise measured by the five thermocouples exceeded the failure criterion of the 140°C temperature rise at 114 minutes (152°C). The local maximum temperature exceeded 180°C at 108 minutes.

Strain gauge measurements

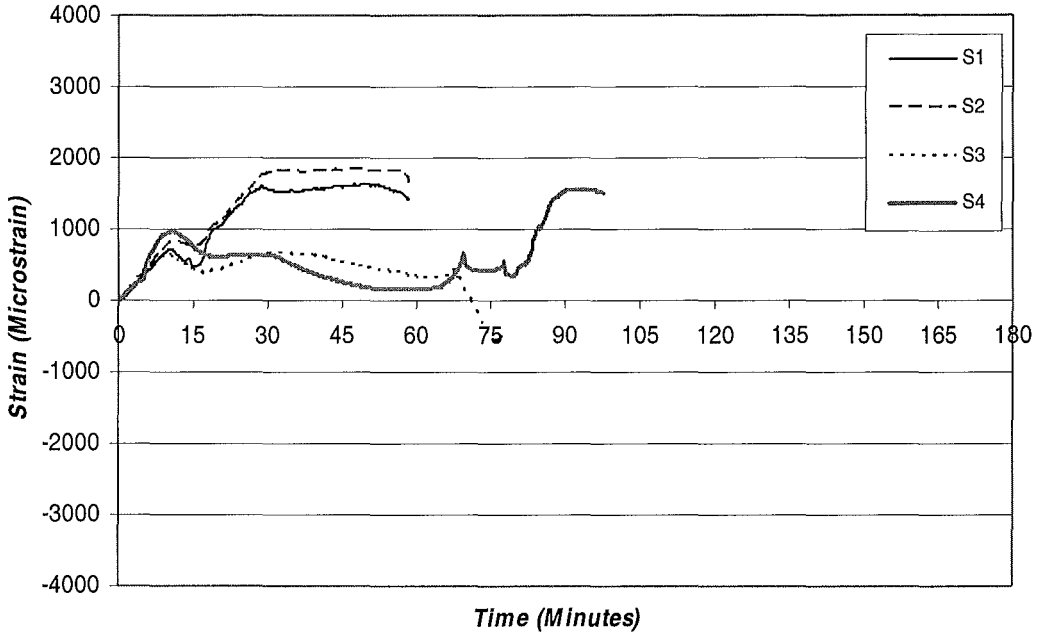

Figure 6-30: Strain gauge measurements in the 661 flat slab.

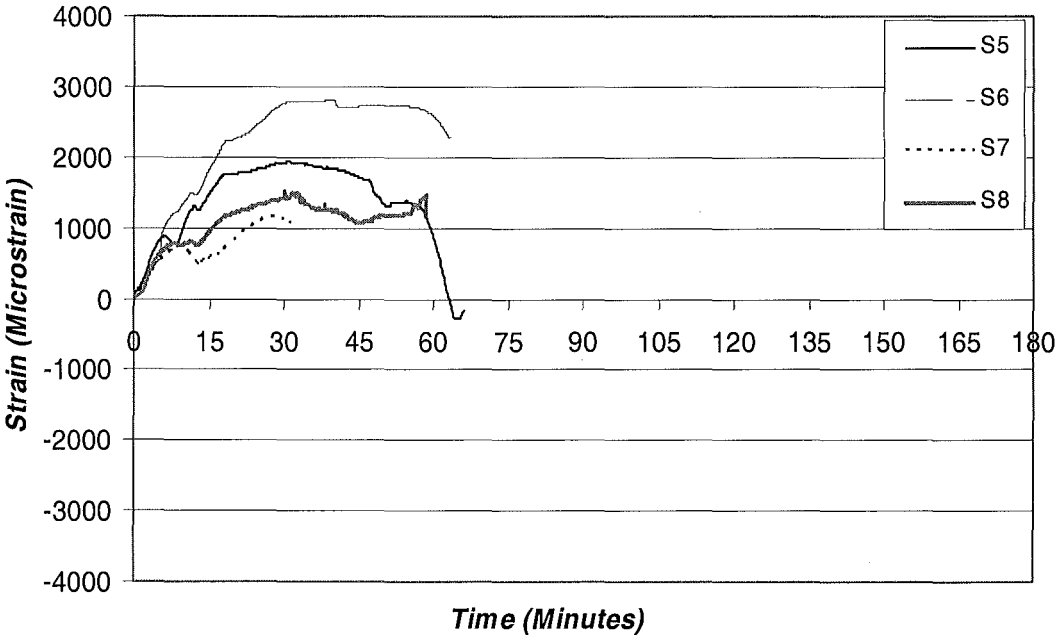

Figure 6-31: Strain gauge measurements in the 661 flat slab.

Figure 6-30 and Figure 6-31 shows the strains measured by strain gauges S1 to S8 in the slab. The positions of the strain gauges are shown in Figure 6-32. During the fire, most of the strain gauges showed a similar trend which showed that the tensile strains in the steel increased rapidly initially and levelled off. The graphs showed that the highest tensile strain of 2820 microstrain was measured at S6, which is located at the middle of the long edge. Relatively

high tensile strains were also measured at the edges, at strain gauges S1, S2 and S5. The strains measured at the corners S3 and S4 were significantly lower than those measured along the middle of the edges. The strains measured at midspan at gauges S7 and S8 were surprisingly lower than those measured at the edges. A possible reason for the high strains at the middle region of slab edges is that the expansion of the central part of the slab caused tensile stresses at the outer regions. After approximately 58 minutes, most of the strain gauges started to fail. By this stage, the recorded temperatures of the mesh had exceeded 300°C, indicating the strain gauges or their connections would have failed. The graphs showed that the strains measured in the steel were relatively low and well below the ambient rupture strain of the steel of 3.2% (32,000 microstrain).

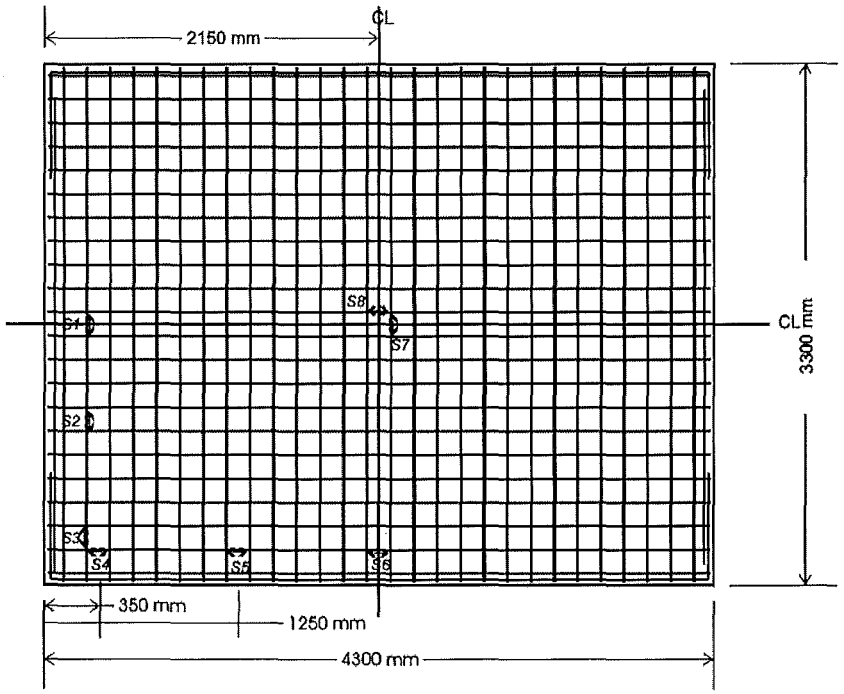

Figure 6-32: Strain gauge layout of the 661 slab.

6.6.3. Test 2: HD12 flat slab

Observations

Figure 6-33 shows the fire test of the HD12 slab underway. The behaviour of this slab was very similar to the 661 slab, but with smaller deflections. The test of this slab showed that the corners of the slab curled upwards very significantly but the deflections at the midspan region were lower compared with the previous slab. In a similar manner with the 661 slab, the bottom surface of the slab did not show visible cracks or signs of spalling. The number of surface cracks on the top of the slab was fewer and the sizes of the cracks were smaller than those seen in the first test due to the higher reinforcing steel content (Figure 6-34).

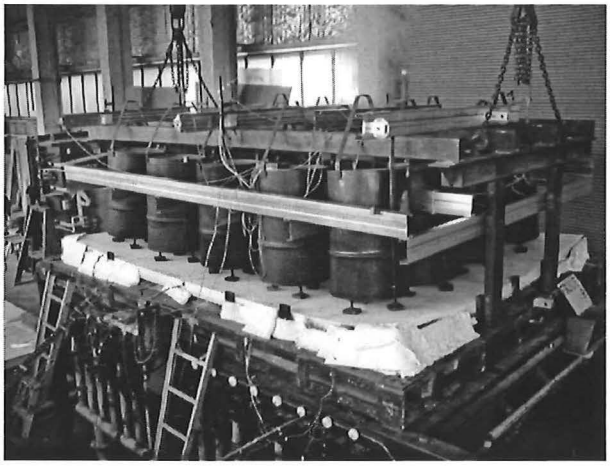

Figure 6-33: Fire test of the HD12 slab underway.

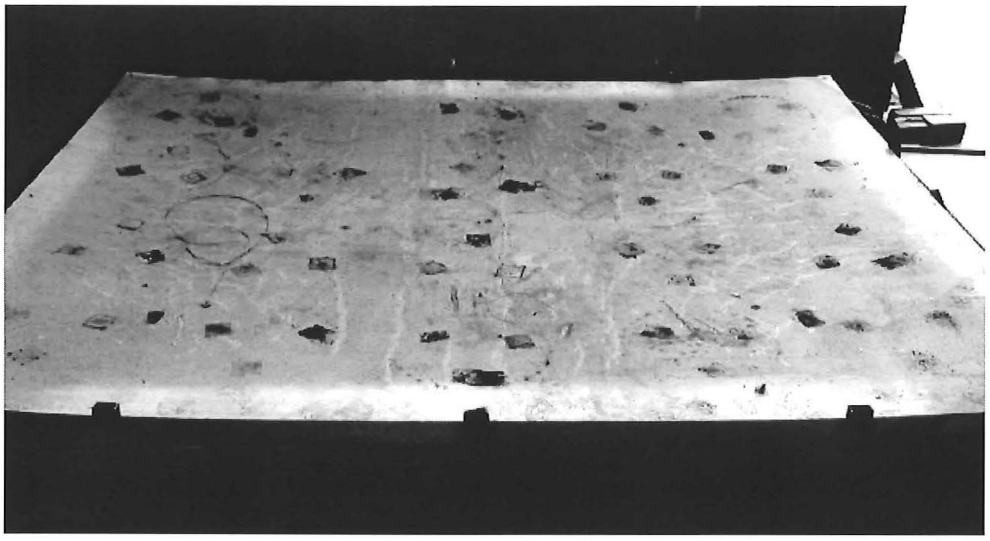

Figure 6-34: Top view of the slab after the test.

Deflections

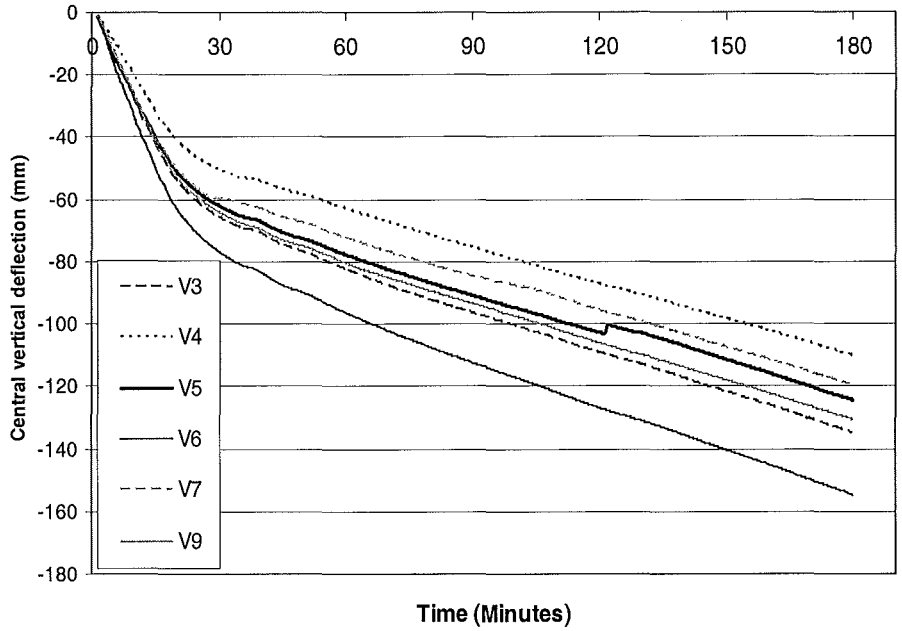

Figure 6-35: Central vertical deflections of the HD12 flat slab.

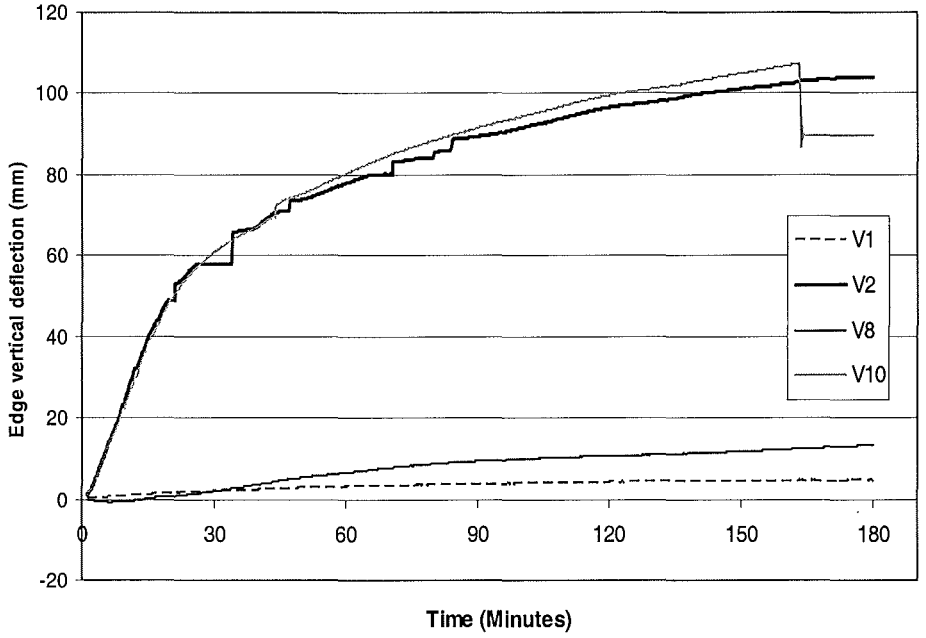

Figure 6-36: Edge vertical deflections of the HD12 flat slab.

Figure 6-35 shows the central vertical deflections of the slab. The deflection trend of the slab is similar to that of the first test. The slab deflected rapidly during the first 20 minutes, reaching -63mm at midspan by 20 minutes. After this, the deflection rate decreased and deflected at a linear rate until the end of the test. The final midspan deflection was -155mm.

The other measurement points of the slab showed similar deflection trends, but with lower deflections.

Figure 6-36 shows the vertical deflections at the edges of the slab. V1 and V8 measured the vertical deflections at the middle of the short and long spans of the slabs, respectively (refer to Figure 6-13). The vertical deflections of the corners of the slab measured with V2 and V10 showed that the corners deflected upwards in a similar trend as the central deflections of the slab, but in the opposite direction. At 163 minutes, the deflection measurements at position V10 dropped suddenly from 107mm to 90mm when the string attached to the potentiometer was severed by the flames which escaped through the corner of the slab.

Slab temperatures

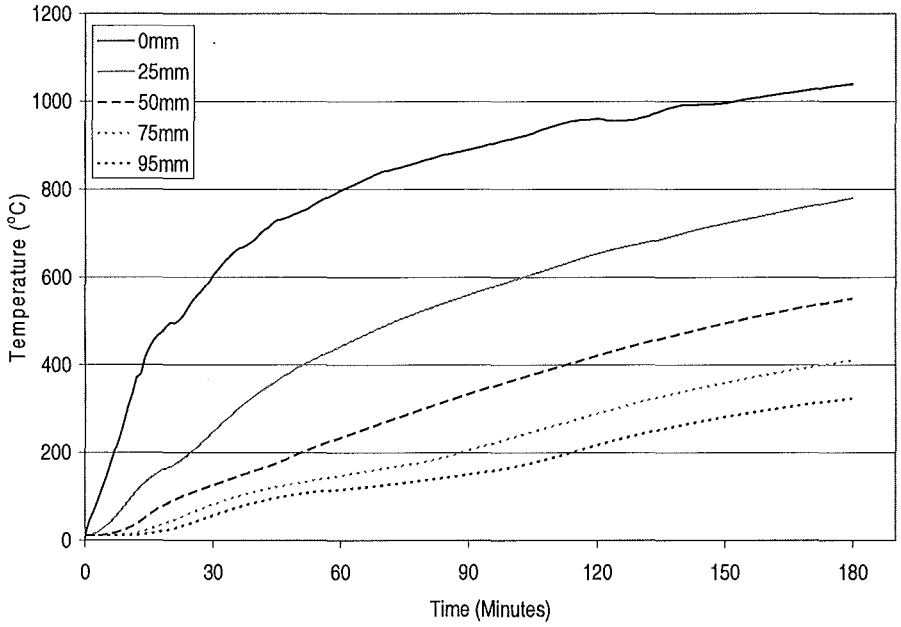

Figure 6-37: Temperatures in thermocouple tree 1 in the HD12 flat slab.

Figure 6-37 shows the temperatures of one of the thermocouple trees in the slab. The thermocouples measured the temperatures at various positions from the heated slab surface, ranging from 0mm (exposed face) to 95mm. The temperature difference across the slab was very significant during the initial stages of the fire but reduced at the later stages of the fire. The maximum temperature measured at the exposed face of the slab reached 1040°C at the end of the fire test. The temperatures of the reinforcing steel and at the unheated surface were similar to those measured in the 661 slab.

6.6.4. Test 3: D147 flat slab

Furnace temperature

Figure 6-38 shows the temperature in the furnace during the third fire test. During the initial stages of the test, the temperatures in the furnace were below the expected temperatures of the ISO fire. This was due to insufficient air flow into the furnace which caused incomplete combustion and resulted in a lot of black smoke pouring out of the furnace.

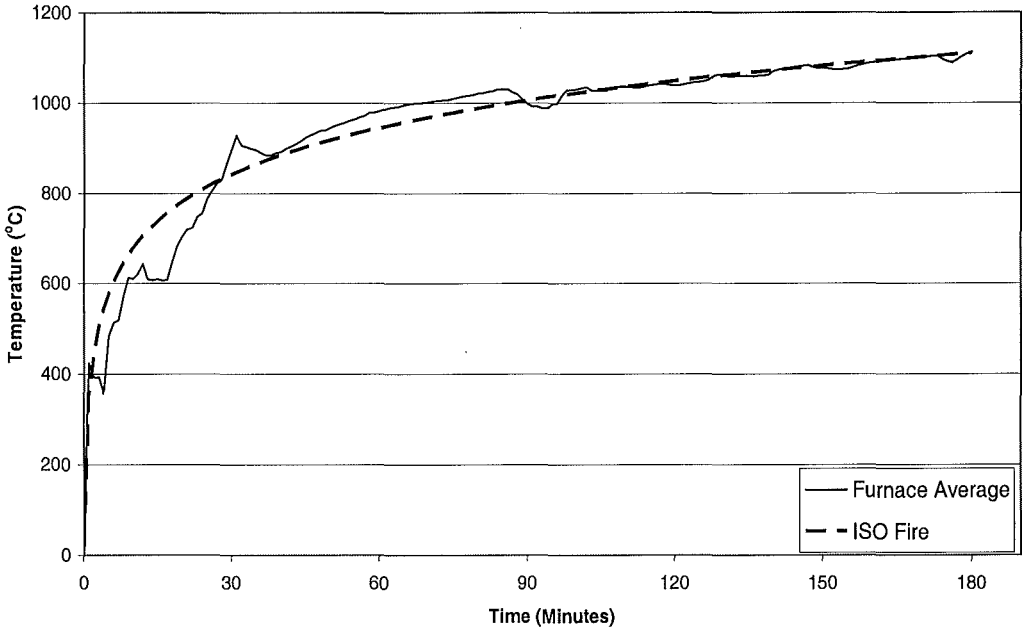

Figure 6-38: Furnace temperatures during the D147 flat slab fire test

Observations

In the test of this slab, the corners of the slab (and subsequent slabs) were clamped down to prevent them from curling upwards. During the early stages of the fire, diagonal cracks rapidly formed at the corners of the top surface. These cracks were due to restraint of the corners against curling. Three cracks also formed at an early stage of the fire in the middle of the slab, propagating in the transverse direction. The first crack formed 150mm off-centre in the transverse direction, with two more cracks running on each side, 600mm (2 bar spaces) parallel to the centre crack (Figure 6-39).

After 35 minutes, the diagonal cracks on the top surface had widened noticeably. Cracks had also appeared at the sides of the slabs. These cracks formed a 45 degree angle across the full depth to the top surface where it meets the surface diagonal cracks. The centre edges of the slab progressively deflected upwards, eventually reaching double curvature by two hours. The

cracks on top of the slab continued to widen as the test progressed, particularly the transverse cracks in the middle of the slab and the diagonal cracks at the corners. After approximatley 2 hours, hairline cracks started to form at the bottom surface of the slab (seen through the viewing ports of the furnace). A crack was clearly seen propagating in the transverse direction on the east side of the furnace. After 2 hours and 25 minutes, the midspan deflection readings reached the maximum limit of the potentiometer (V6) and further readings could not be recorded. The final midspan deflection was measured manually.

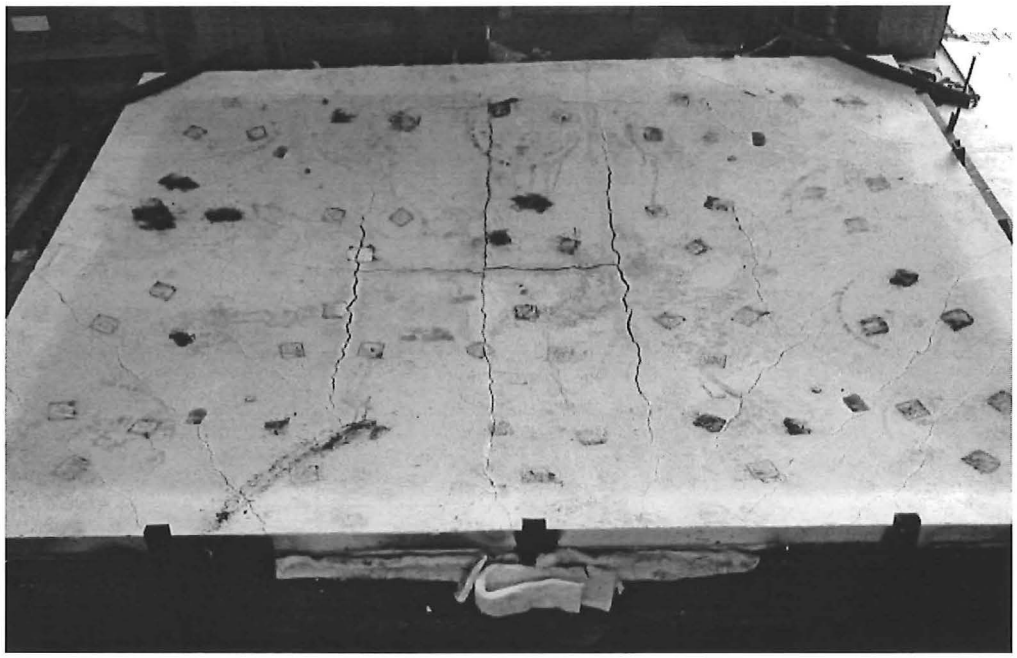

Figure 6-39: Crack pattern at the top surface of the slab.

Figure 6-39 shows the top surface of the slab immediately after the fire test. Three large cracks had formed in the transverse direction of the slab. These cracks were spaced at 600mm centres, equivalent to two grid spacings of the mesh. One full depth crack formed in the longitudinal direction at the centre of the slab. This full-depth crack was approximately 1200mm long. Surface cracks formed in a circular pattern around these large central cracks. Large cracks also formed in the longitudinal direction, located approximately 200mm from the edges of the slabs. In spite of the wide cracks on the top surface (up to 10mm), flames did not pass through the cracks, which would have caused integrity failure.

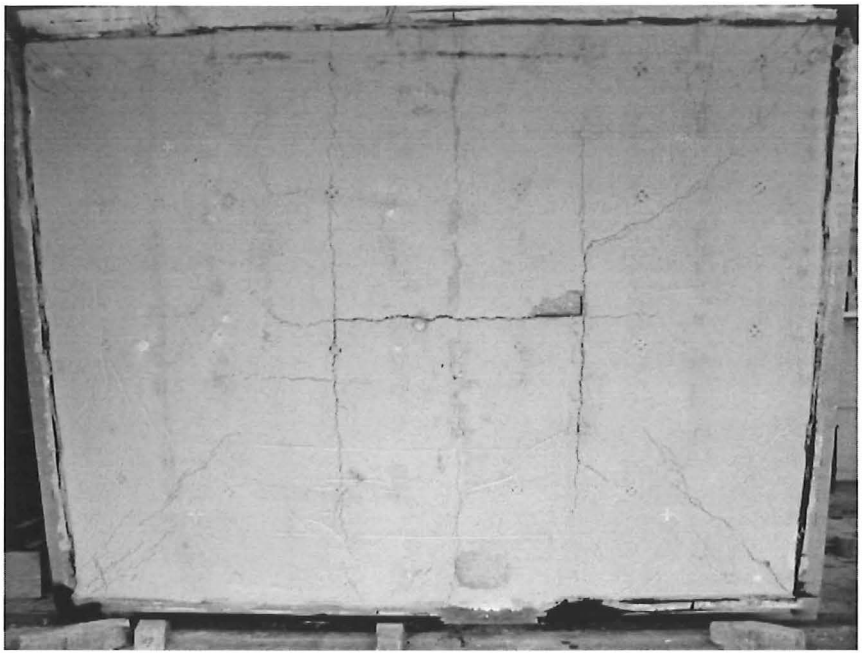

Figure 6-40: Crack pattern at the bottom surface of the slab.

Figure 6-40 shows the bottom surface of the slab one day after the fire test. Unlike the first two tests which showed a smooth and uncracked bottom surface, large cracks were clearly visible on the bottom surface of this slab. There were no signs of spalling on the underside of the slab. Figure 6-40 shows a small portion of the bottom surface cover near the centreline had fallen off. This occurred after the slab had cooled down and was not due to spalling. The middle longitudinal surface crack at the top had extended to its full depth and was clearly seen on the bottom surface of the slab. Two large full depth cracks which propagated in the short span could also be clearly seen at the bottom of the slab. A finer crack also formed in the middle of the slab, between the larger full depth cracks. This crack had closed up when it was examined the following day and corresponded to the centre transverse crack on the top surface. Fine diagonal cracks running at 45 degrees from the corners towards the centre region of the slab could also be seen. After the slab was broken up, examination of the reinforcing bars showed that none of the bars had ruptured during the fire.

Deflections

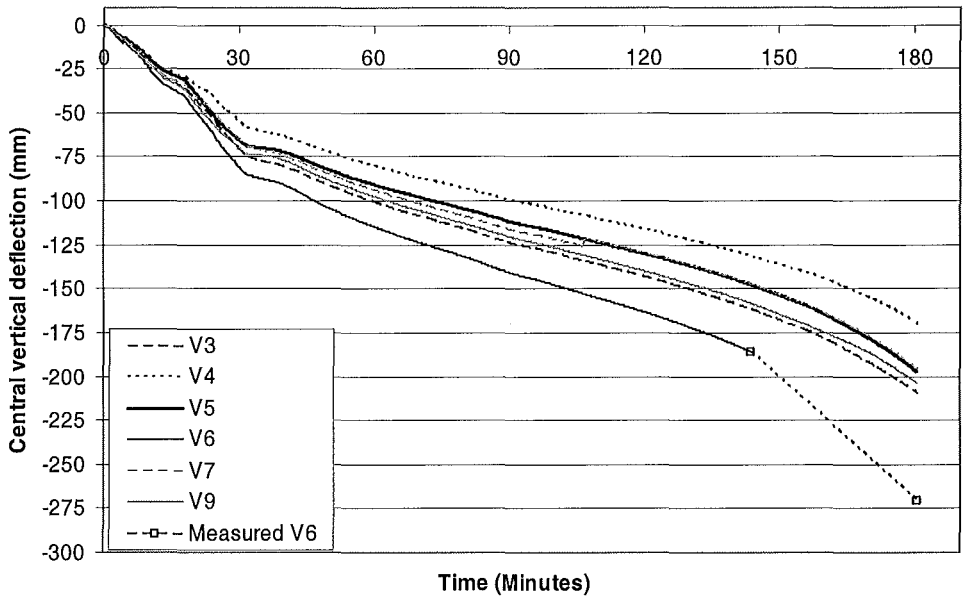

Figure 6-41: Central vertical deflections of the D147 flat slab.

Figure 6-59 shows the central vertical deflections of the slab. Unlike the first two tests, the vertical deflections did not show a smooth deflection trend during the first 45 minutes, due to the erratic furnace temperature. When the midspan vertical deflection reached -186mm, the central rotary potentiometer (V6) reached its limit of travel and could not measure further deflections. A manual measurement made at the end of the test showed that the slab had reached -271mm at midspan.

Slab temperatures

The temperatures measured across the slab and at the reinforcing bars were similar to those measured in the 661 and HD12 slabs.

6.6.5. Test 4: Dimond Hibond slab

Observations

During the first 5 minutes of the fire test, popping noises from the slab were heard. This was due to the steel decking at the bottom surface buckling (Figure 6-42) and debonding from the concrete. The concrete which was mechanically anchored to the decking was ripped from the slab when the decking debonded. The debonding of the steel deck from the concrete, possibly due to steam release at the bottom of the slab, created an air gap between the decking and the concrete. The steam release was possibly due to the high moisture content trapped on the bottom side of the slab. This phenomenon was also observed in the Broadgate and Churchill Plaza Building fires (Newman et al., 2000).

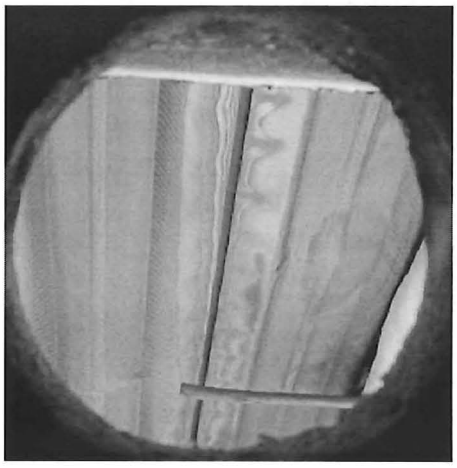

Figure 6-42: Buckling of the steel decking during the fire, seen through the east viewing port.

Figure 6-43: Debonding of the steel decking and diagonal cracks forming at the rib-slab intersection.

An initial crack across the slab in the transverse direction, caused by mishandling during the transportation of the slabs, had widened significantly. After 3 hours, just before the furnace was turned off, flames started to penetrate this crack. When the slab was lifted off the furnace, the steel decking was glowing pink, with severe blistering on the decking surface due to oxidisation of the steel (Figure 6-44).

Figure 6-44: Extensive blistering of the steel deck (shown by the black spots).

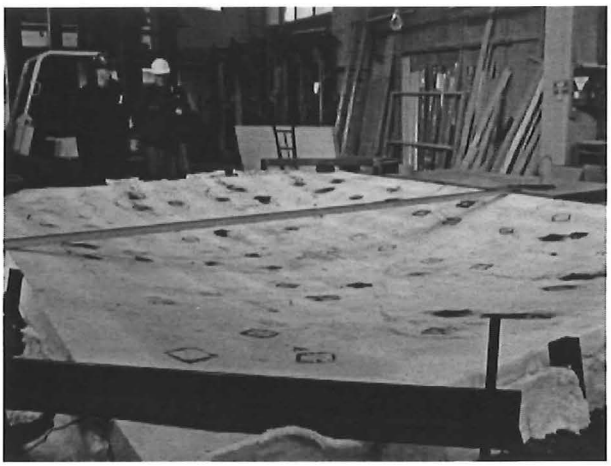

Figure 6-45: Deflected slab after the fire test.

Figure 6-45 shows the large deflections in the Hibond slab after the fire test. Figure 6-46 shows the crack pattern on the top surface of the slab. The cracks had been outlined with a marker to highlight the position of the cracks. A large crack (up to 9mm wide) had formed across the middle of the slab in the longitudinal direction. The slab also had a series of horizontal cracks running across the short span at regular spacing. The horizontal cracks formed at the position of the bars of the reinforcing mesh which were spaced at 300mm centres. The diagonal cracks which formed at the corners due to the corner clamps were also spaced at regular intervals.

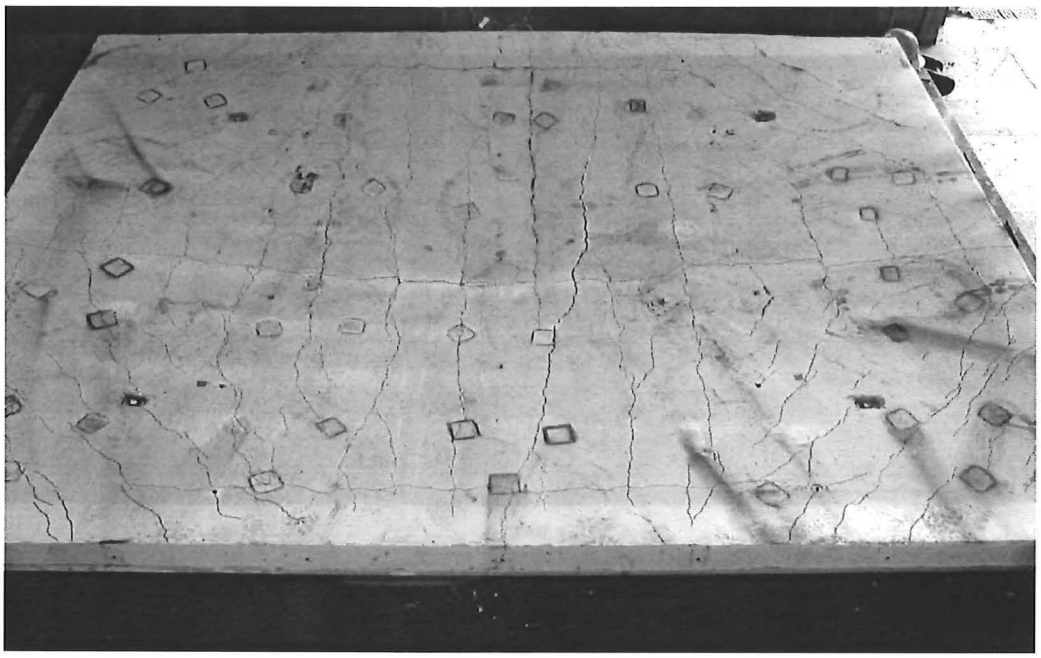

Figure 6-46: Top surface of the Hibond slab after the fire test.

Figure 6-47 shows that the centre of the long sides of the slab had deflected inwards, relative to the corners of the slabs. The large midspan deflections had caused the centre regions of the sides to contract and deflect inwards. Figure 6-48 shows that a large amount of concrete had spalled off the ribs of the slab when the steel decking was pried from the slab after the fire test. The steel decking held the concrete in place, preventing it from falling off the slab and exposing the reinforcing steel.

Figure 6-47: Inward deflection of the centre regions of the sides of the slab.

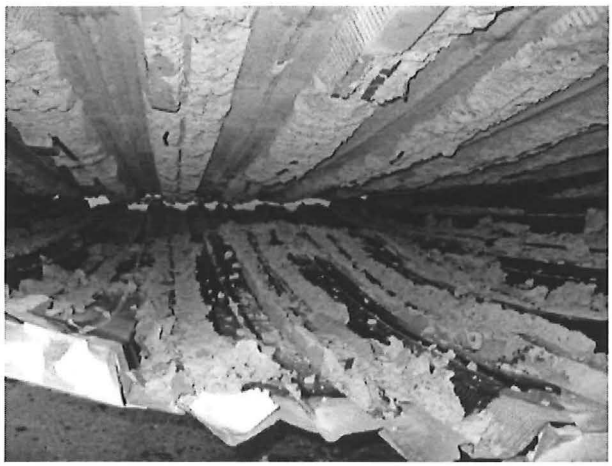

Figure 6-48: Bottom of the Hibond slab after the steel decking was pried from the slab.

Deflections

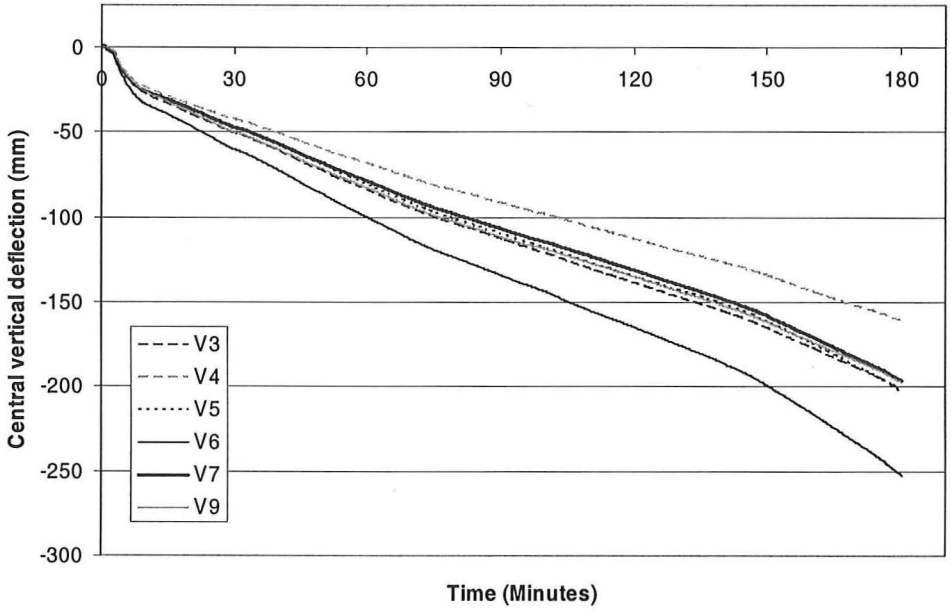

Figure 6-49: Central vertical deflections of the Hibond slab

Figure 6-49 shows the central vertical deflections of the HiBond slab. The slab deflected downwards very rapidly at a rate of approximately -3.7mm per minute during the first 8 minutes of the fire. After that, the slab deflected at a lower rate of -1.2mm per minute until 140 minutes and increased again slightly during the last 30 minutes. The final midspan deflection of the slab was -253mm.

Slab temperatures

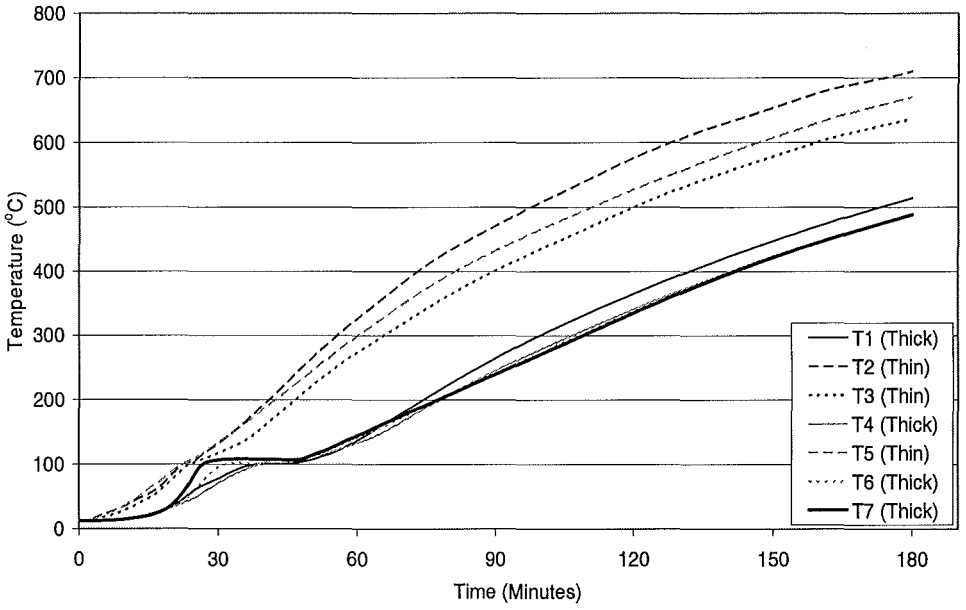

Figure 6-50: Temperatures of the reinforcing mesh of the Hibond slab.

Figure 6-50 shows the temperatures of the unexposed face of the slab. The initial temperature on the unexposed side was 13°C. Three of the thermocouples (T2, T3 and T5) showed higher temperatures than the other thermocouples. This was because they were mounted at the thin section of the slab while the other thermocouples were mounted on the thicker part of the slab which had the ribs as extra concrete cover. The thermocouples mounted over the ribs showed a distinct temperature plateau of 100°C between 26 and 48 minutes. This temperature plateau was due to the moisture accumulation at that level as it was progressively driven off from the heated side towards the cooler side.

6.6.6. Test 5: Traydec slab

Observations

Several minutes after the test started, popping noises similar to those during the Hibond test, were heard. The Traydec slab remained relatively flat and undeformed during the fire test compared with the previous slabs. When the test was stopped at 3 hours, the mid-span deflection had reached -126mm. The diagonal cracks at the sides of the slab had extended from the top of the ribs to the surface of the slab (Figure 6-51). A series of cracks formed in the transverse direction at the top of the slab (Figure 6-52). These transverse cracks were similar to those seen in the Hibond slab and occurred at the positions of the reinforcing bars. This slab had fewer diagonal cracks and the widths of its surface cracks were generally much smaller than those seen in the previous slabs.

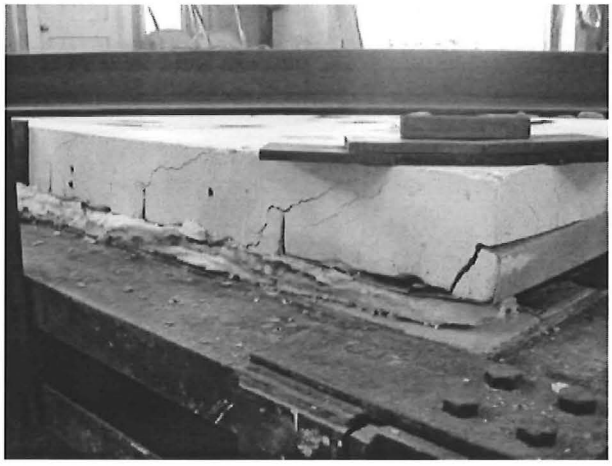

Figure 6-51: Diagonal cracks at the edges of the slab.

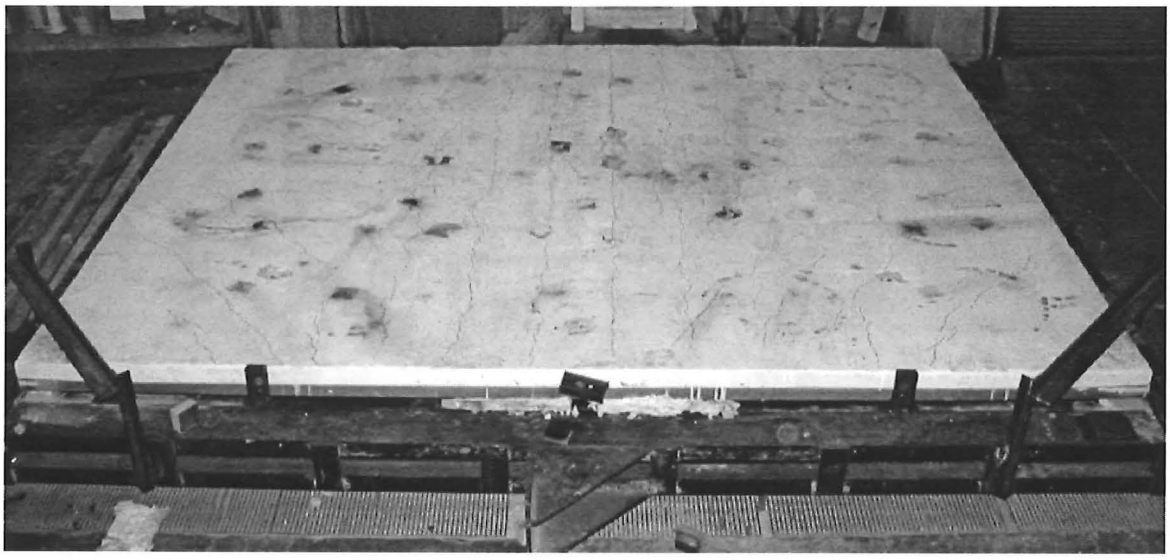

Figure 6-52: Top view of the Traydec slab.

The bottom surface of the steel decking did not oxidise as much as the Hibond slab (Figure 6-53). The flat surface of the decking had de-bonded from the concrete, but each individual sheet was locked into the concrete by the steel ribs, which prevented the whole sheet from separating from the concrete (Figure 6-54).

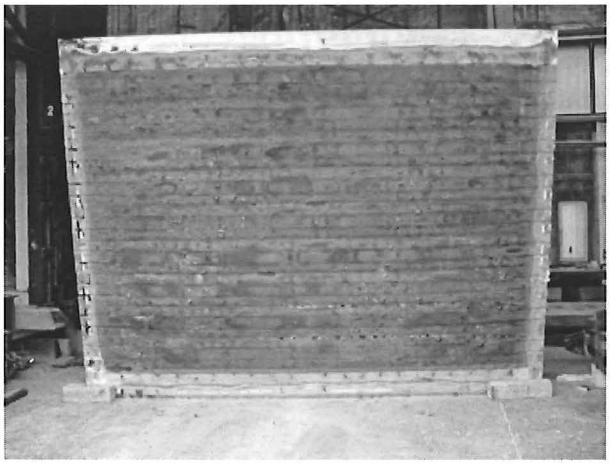

Figure 6-53: Underside of the Traydec slab after the test.

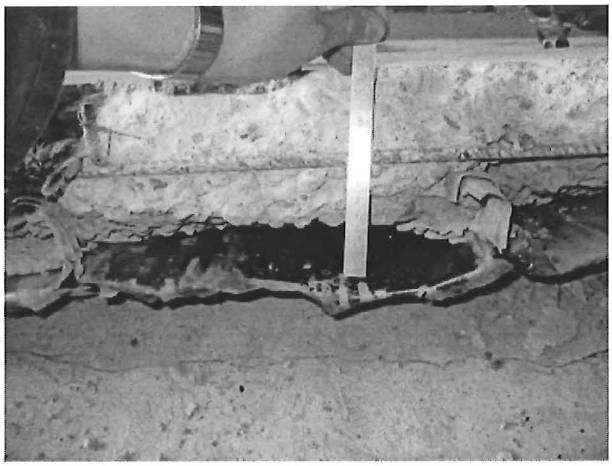

Figure 6-54: Section of the slab, showing the steel decking locked into the concrete by the ribs.

Deflections

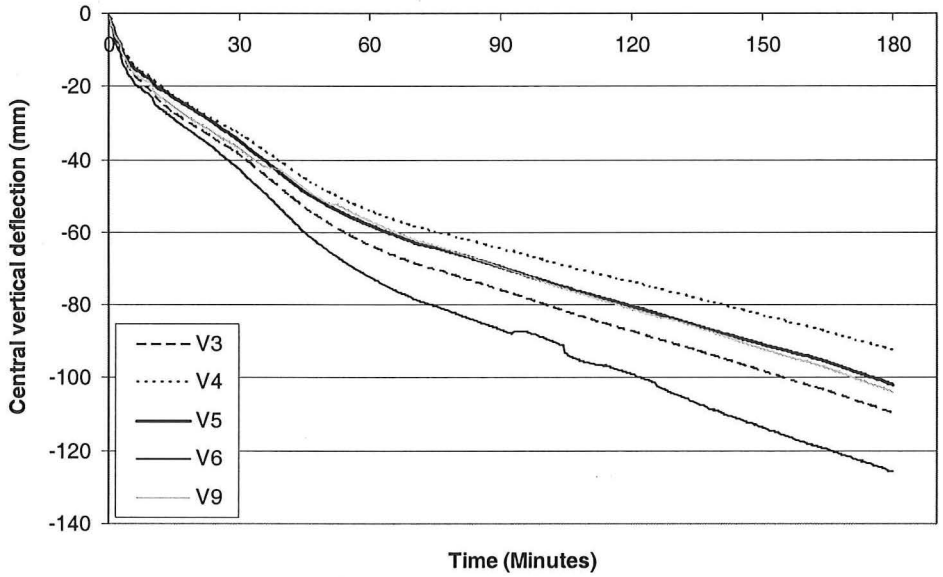

Figure 6-55: Central vertical deflections of the Traydec slab.

Figure 6-55 shows the central deflections of the slab. The graph shows that the slab deflected much quicker during the initial stages (6 minutes), followed by a slower deflection rate during the remainder of the test, which is a consistent trend with the results seen in the other tests. Compared to the previous slabs, the deflections of this slab were significantly lower, resulting in a final midspan deflection of -126mm at the end of the test. The smaller deflections of the slab were attributed to the thicker section of the slab. The thicker cover to the reinforcing steel and the embedment of the ribs of the steel decking in the concrete (Figure 6-54) kept the steel cool, preventing significant loss of stiffness which would result in large vertical deflections.

Slab temperatures

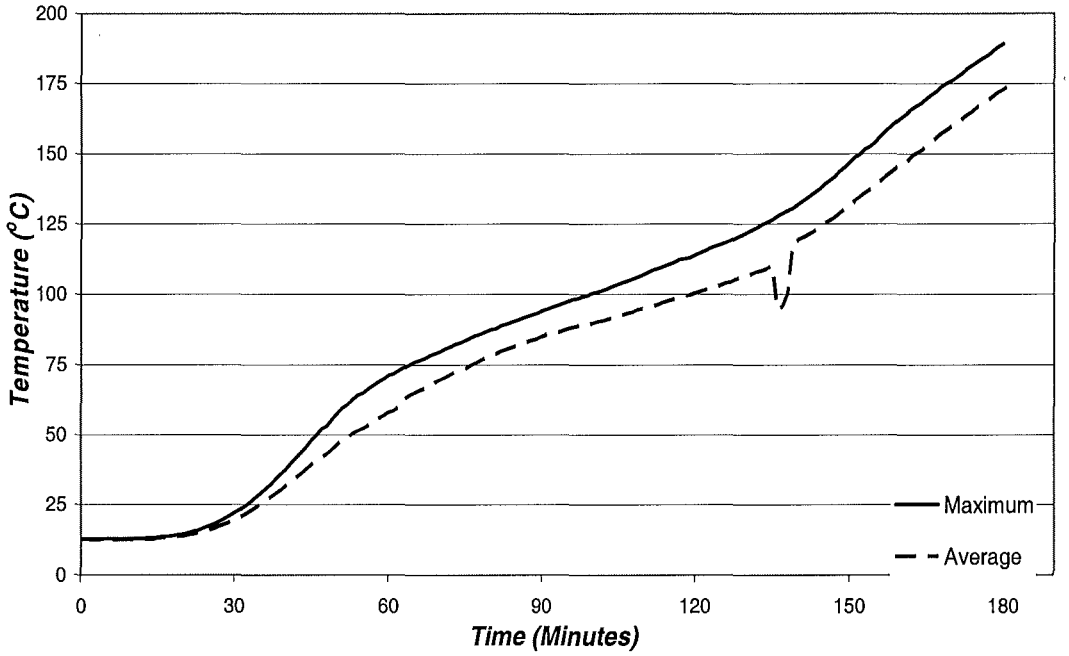

Figure 6-56: Temperatures at unheated side of the Traydec slab.

Figure 6-56 shows the temperatures of the unexposed face of the slab. The average temperature rise measured by the five thermocouples exceeded the failure criterion of the 140°C temperature rise (151°C) at 166 minutes. The local temperature rise exceeded 180°C on the unheated surface at 173 minutes. The average of the maximum temperatures on the unheated side was 173°C, compared with 242°C and 278°C in the flat slabs and Hibond slabs, respectively. The lower temperatures on the unheated side were due to the thicker section of the Traydec slab.

6.6.7. Test 6: Speedfloor slab

Observations

Figure 6-57 shows the Speedfloor slab prior to the fire test with the three steel joists spanning across in the long direction of the slab. During the first half hour, the steel joists had buckled and were glowing red due to direct exposure to the flames (Figure 6-58).

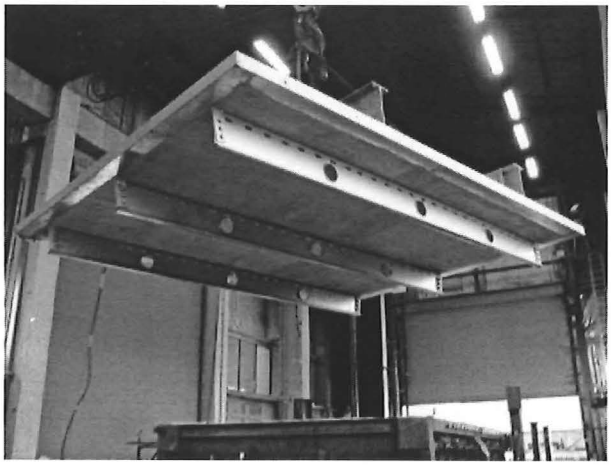

Figure 6-57: Speedfloor slab, before the test.

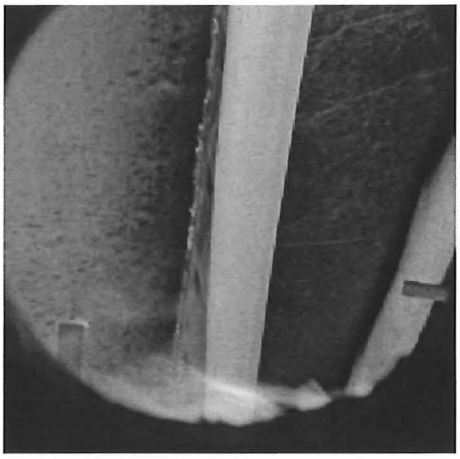

Figure 6-58: Buckling of the joist during the fire test.

At the end of the test (3 hours), the slab had deflected to -180mm at midspan. When the slab was lifted from the furnace, the steel joists were glowing pink and the surface of the joists suffered extensive oxidisation. The centre joist had buckled very severely while the joists at the sides showed less deformation (Figure 6-59). Figure 6-60 shows the ends of the joists near the face of the concrete beam. The bottom flanges of the joists did not butt up against the concrete beam, as there was a 10mm gap between the bottom flange of the joist and the vertical face of the concrete beam.

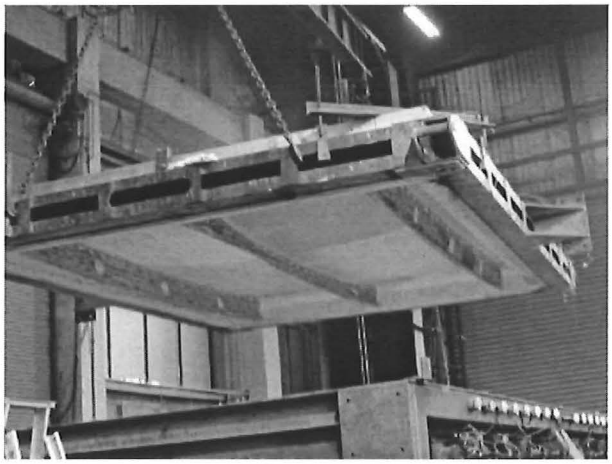

Figure 6-59: The Speedfloor slab being lifted off the furnace after the fire test.

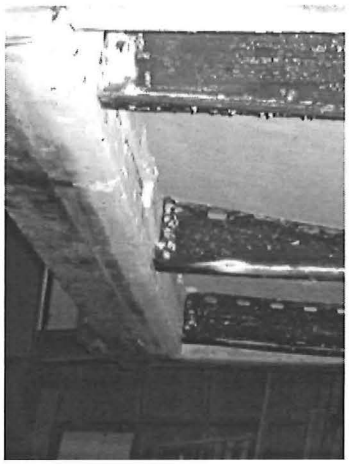

Figure 6-60: Extensive oxidization of the steel joists.

Figure 6-61 shows the crack pattern at the top of the Speedfloor slab. The cracks had been highlighted with a marker so that they would show up more clearly in the photos. The top surface of the slab showed extensive cracking in the transverse direction and diagonally at the corners. The widths of the cracks were narrow (up to 3mm) and did not crack the full depth of the slab. The transverse cracks in the middle of the slab were spaced at 150mm apart, and were located at the positions of the reinforcing bars. The largest crack on the top surface formed across the longitudinal direction, in the middle of the slab. This crack position corresponded to the location of the centre joist. The bottom surface of the slab showed a few hairline cracks propagating diagonally from the corners of the slab towards the centre region but there was no sign of full depth cracks. These hairline cracks were possibly due to yield lines forming.

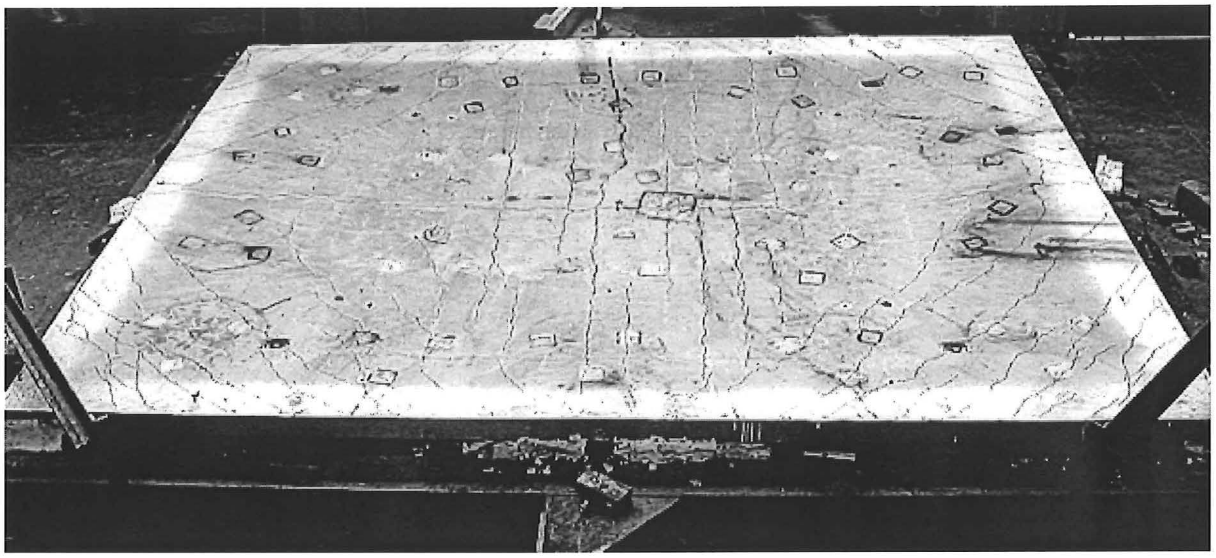

Figure 6-61: Top view of the Speedfloor slab.

Deflections

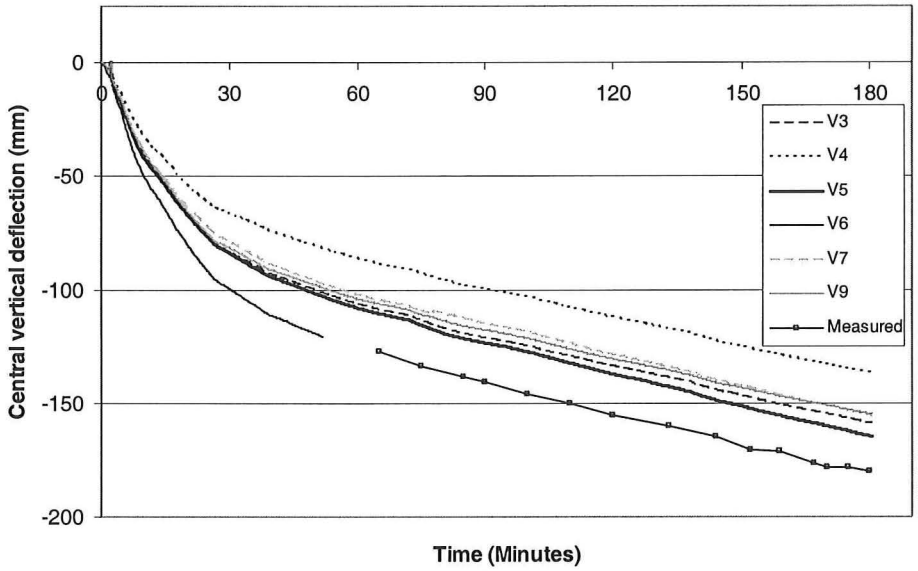

Figure 6-62: Central vertical deflections of the Speedfloor slab.

Figure 6-62 shows the central vertical deflections of the Speedfloor slab. The graph shows that the slab deflected downwards very rapidly during the initial stages, reaching 100mm by 30 minutes. The deflection rate of the slab decreased after the initial stage and continued in a linear trend. At 55 minutes, potentiometer V6 started to malfunction as it measured very erratic deflection readings. The potentiometer could not be replaced and the midspan deflections were measured by hand.

Slab temperatures

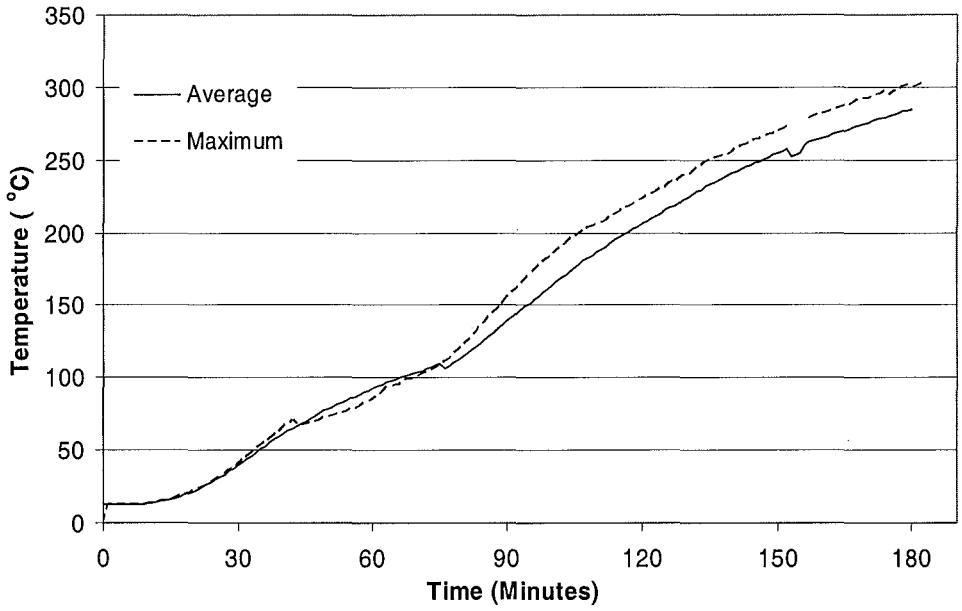

Figure 6-63: Temperatures at unheated side of Speedfloor slab

Figure 6-63 shows the temperatures of the unexposed face of the Speedfloor slab. The initial temperature on the unexposed side was 13°C. Insulation failure occurred when the local temperatures exceeded 180°C at 97 minutes. Integrity failure did not occur in this slab.

6.7. Discussion

6.7.1. Midspan deflections

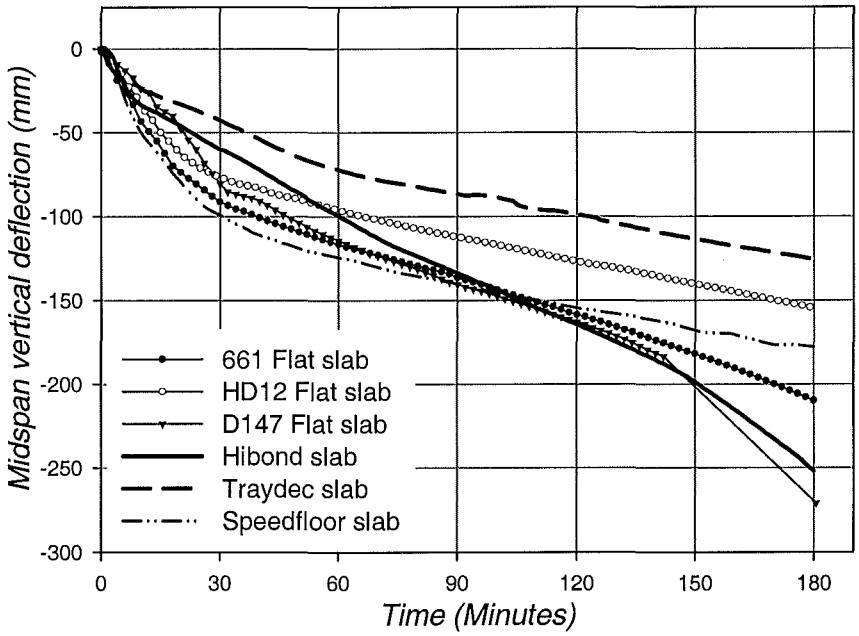

Figure 6-64: Comparison of the midspan vertical deflections in the six slabs tested at BRANZ

Figure 6-64 compares the midspan vertical deflections of the six different slabs during the fire tests. The graph shows that all the slabs had similar deflection trends during the fire. The slabs showed a high deflection rate initially followed by a lower deflection rate. The initial high deflection rate was due to thermal bowing of the slabs. The slabs with the steel decking showed a distinct bilinear deflection trend, with a rapid deflection rate during the initial stages, followed by a lower deflection rate during the remainder of the fire test. The transition to the lower deflection rate was possibly due to the steel deck buckling and debonding from the concrete, creating an insulating layer of air between the decking and the bottom surface of the concrete. The insulating layer of air reduced the rates of heating on the bottom surface of the concrete and led to a lower rate of thermal bowing deflection.

The deflection rates of the other slabs showed a gradual reduction after 20 minutes into a steady and constant rate for the remainder of the fire. The maximum deflections of the flat slabs with 198mm^2/m, 295mm^2/m and 565mm^2/m were -271mm, -210mm and -154mm, respectively. During the initial stages, the different steel contents had negligible effect on the deflection of the slabs as the deflections were caused by the non-linear thermal expansion of the concrete. However, during the later stages, the deflections of the slab were dependent on the steel content of the slab.

6.7.2. Test results versus code recommendations

Stability criteria

Slab	Expected fire resistance rating	Test result
100mm flat slab	120 minutes[1]	180 minutes (No failure)
Hibond slab	30 minutes[2]	180 minutes (No failure)
Traydec slab	240 minutes[1]	180 minutes (No failure)
Speedfloor slab	120 minutes[1]	180 minutes (No failure)

1 = NZS 3101 (SNZ, 1995) (Two-way slab, simply supported)

2 = Hibond Design Manual (Dimond Industries, 1997) (One-way, simply supported)

Table 6-7: Comparison of test results with design recommendations for stability criteria.

Table 6-7 compares the expected fire resistance stability ratings with the test results. The fire resistances recommended by NZS 3101 (SNZ, 1995) were based on the concrete cover to the reinforcement. With the exception of the Traydec slab, the other slabs achieved higher stability rating in the fire tests than those recommended by codes and design manuals. The stability ratings recommended by the codes were based only on the concrete cover to the reinforcing steel. The recommended fire resistance rating of the Hibond slab was significantly lower than that achieved in the test because its recommended rating was based on a one way slab. Fire resistance ratings for a two-way simply supported Hibond slab were unavailable because these slabs are normally designed as one-way slabs.

Insulation criteria

	Expected fire resistance rating	Test result
100mm flat slab	100 minutes[1]	108 minutes[4]
Hibond slab	105 minutes[2]	97 minutes
Traydec slab	160 minutes[3]	166 minutes
Speedfloor slab	83 minutes[1]	97 minutes

1 = NZS 3101: Part 1 (SNZ, 1995), Type A aggregate

2 = Hibond Design Manual (Dimond Industries, 1997)

3 = Traydec 300 Specification and Design Manual (Forgan Jones Structural Ltd, 1996)

4 = Average of three flat slabs

Table 6-8: Comparison of test results with existing design recommendations for insulation criteria.

Table 6-8 compares the insulation ratings recommended by the codes with the test results. The fire resistance ratings from the tests were similar to the test results and in most cases, the times to insulation failure in the tests were slightly greater than the recommended ratings.

Integrity criteria

The only slab that had an integrity failure was the Hibond slab. The integrity failure was minor and occurred just before the furnace was turned off at 180 minutes when small flames passed through one of the full depth cracks in the middle of the slab. This full depth crack was initiated by a crack which formed prior to the fire test due to mishandling of the slab. The other slabs did not suffer integrity failures.

6.7.3. Comparison with other tests

The D147 slab, which suffered the most visible cracking, had a similar crack pattern to that observed in the ambient temperature tests by Bailey et al. (2000). The D147 slab had three full depth cracks in the transverse direction in the midspan region, along with a single full depth crack in the longitudinal direction, and yield line cracks on the bottom surface. The tests by Bailey et al. (2000) only had one full depth crack in the transverse direction in addition to the yield-line cracks.

The slabs tested at Cardington were continuous over the supports (Newman et al., 2000). Large rotations at the edges of the slabs led to cracking of the concrete over the supports.

Large rotations were also observed at the slab edges in the BRANZ tests as expected because the edges were free to rotate.

For designing continuous slabs, the slabs must be detailed to withstand the large rotations over the supports without rupture of the reinforcing steel. Ductile reinforcing bars should be placed at the top over the supports rather than cold-formed mesh because the steel would not be exposed to high temperatures and have sufficient ductility to accommodate the high tensile strains associated with the large rotations.

6.7.4. Reinforcing steel properties

A week after the fire tests were completed, tensile tests were conducted on samples of the D147 mesh taken from the fire tested slabs. The purpose of this was to measure the strength and ductility of the steel after they had been exposed to elevated temperatures. Table 6-9 shows the properties of the steel in the Hibond and Traydec slabs after they were exposed to different maximum temperatures. The steel specimens were obtained from the bottom reinforcing bars. The maximum temperatures of the reinforcing steel of the Hibond and Traydec slabs measured at the end of the tests were 672°C and 351°C, respectively. The yield strength of the Hibond mesh had dropped from 565MPa to 396MPa. The strength of the mesh would have decreased very significantly during the fire but recovered to 396MPa at the time of the tensile tests, when the steel had cooled. At 672°C, the strength would have decreased to approximately 13% of its ambient yield strength (73MPa), based on the EC2 (1995) tables. For the Traydec mesh, the yield strength of the slab had increased from 565MPa to 592MPa when the steel was tested after the fire test.

Slab	Reinforcing steel	Max measured steel temperature*	Yield stress	Strain Limit
Hibond	**D147 mesh**	672 °C	396 MPa	26.7%
Traydec	**D147 mesh**	351 °C	592 MPa	8.7%

* Average of three thermocouples

Table 6-9: D147 mesh properties after the fire test

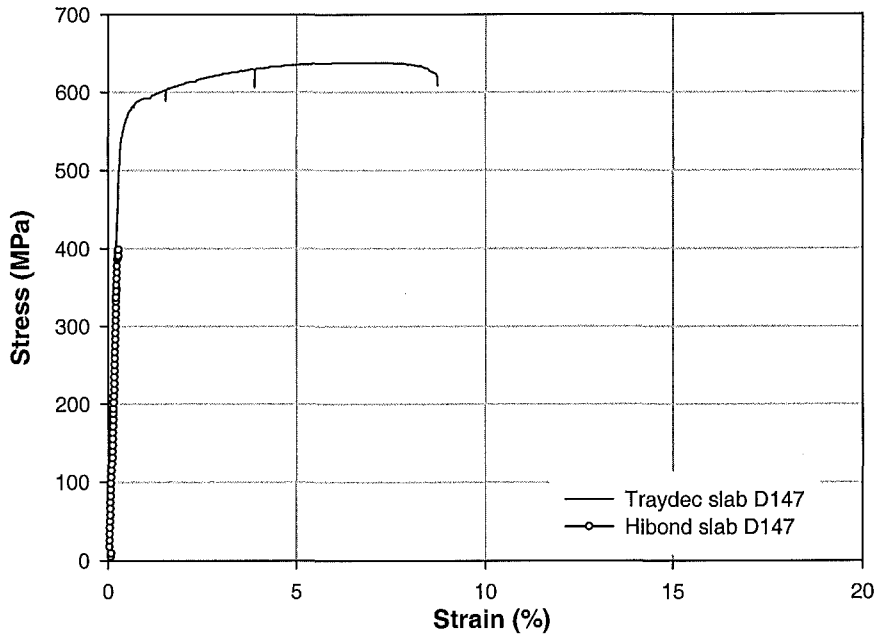

Figure 6-65: Stress-strain curves of D147 mesh after the tests

Figure 6-65 shows the stress-strain curves of the 147 mesh in the Hibond and Traydec slabs after they were exposed to various levels of heating. The graph shows that the strain limit (strain at rupture) in the Traydec mesh had increased to 8.7%. Despite being heated up to only 351°C, the steel showed a substantial increase in ductility from its initial value of 2.25%. The stress-strain curve of the Hibond mesh in Figure 6-65 did not show a yield plateau because the steel ruptured outside the measured gauge length and was not detected by the gauge. The strain limit of the Hibond mesh of 26.7% was determined by measuring the steel sample manually. This high strain limit indicated that the ductility of the cold-drawn mesh had increased significantly after being exposed to high temperatures. The high ductility of the heated reinforcing steel enabled the steel to accommodate the high tensile strains, preventing rupture of the reinforcing steel. If the steel had remained cool and the ductility low, it may have ruptured when subjected to high mechanical strains.

Tensile tests could not be performed on the 661 mesh because the available samples taken from the slabs after the fire tests were too short and could not fit into the testing machine.

6.7.5. Concrete moisture content

Slab		Slab weight		Water content	
		Before (kN)	After (kN)	Volume (litres)	Percent
1	661 slab	33.4*	31.2	225	6.5%
2	HD12 slab	35.7	33.8	188	5.2%
3	D147 slab	32.9	31.4	147	4.4%
4	Hibond slab	34.5	32.6	196	5.6%
5	Traydec slab	42.8	40.7	221	5.1%
6	Speedfloor	32.9	31.0	192	5.7%

*Estimated weight based on concrete density of 2400kg/m^3

Table 6-10: Moisture content of slabs

Table 6-10 shows the moisture content of the slabs which were measured by weighing the slabs before and after the tests. The difference of the weight was assumed to be entirely due to the moisture driven from the concrete during the heating of the slabs. The measured moisture content of the slabs ranged from 4.4% to 6.5%, and the average of moisture content of the six slabs was 5.4%. The low moisture content of the slabs and the absence of concrete spalling during the tests indicated that the slabs had been well cured and dried before the tests.

6.7.6. Instrumentation problems

Several instrumentation problems arose during the fire tests.

- The strain gauges only managed to record data during the initial stages of most of the fire tests. With the exception of the Traydec slab, the gauges and connections in most of the slabs burnt out by the first half of the tests and did not record any data during the final stages when the deflections of the slabs were significant.
- The rotary potentiometers malfunctioned in some of the tests as a result of prolonged exposure to the steam and high air temperatures rising from the top surface of the slabs.

6.8. Load capacity predictions of the tested slabs using theoretical methods

6.8.1. Load capacity predictions with yield line theory

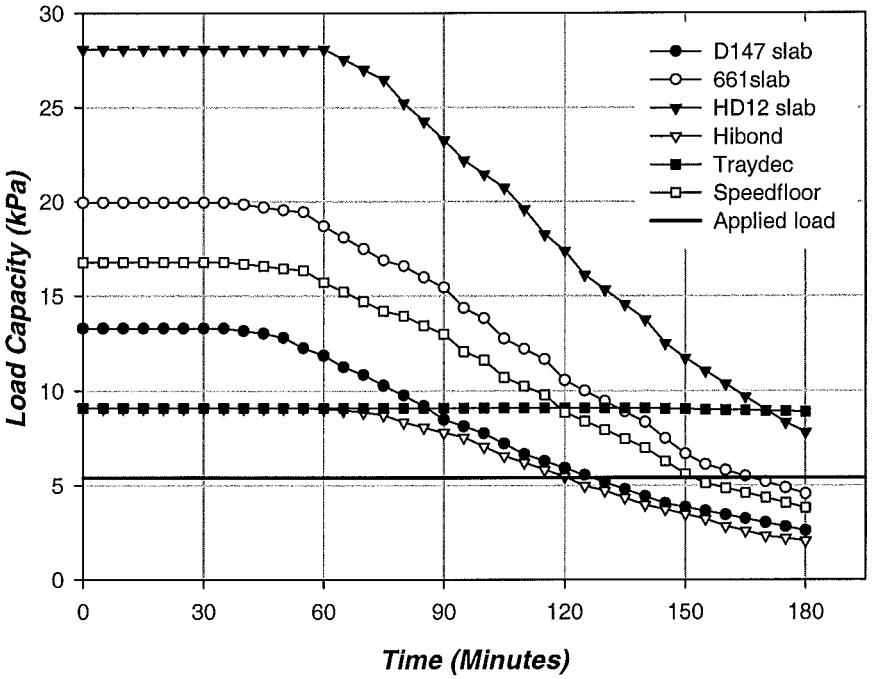

Figure 6-66: Variation of the load capacitiesduring the fire, $w_{u,fire}$.

Figure 6-66 shows the variation of the theoretical ultimate load capacities for the slabs during the ISO fire. The theoretical load capacities, $w_{u,fire}$, were calculated by yield line theory and with the reduced strengths of the reinforcing steel at elevated temperatures. The temperatures of the reinforcing steel were obtained from the measured temperatures of the reinforcing during the fire tests while the reduced strengths of the hot-rolled and cold-drawn reinforcing steel were determined from the strength reduction factors from the Eurocode (EC2, 1995).

The load capacities of the composite slabs were calculated with the assumption that the steel decking and joists had zero strength during the fire and did not contribute to the flexural strength of the slab. Therefore, the load capacities of these slabs were calculated based only on the reinforcing mesh. The load capacities of the composite slabs during the start of the fire would be much higher than shown. However, in the fire tests, the exposed steel deck and joists would lose their strength very rapidly and be dependant on the strength contribution by the reinforcing mesh. Hence, the assumption that the steel decking does not contribute to the flexural strength would provide a reasonably accurate estimate of the strength of the slabs during the fire.

With the exception of the Traydec slab, Figure 6-66 shows that the load capacities of the slabs varied similarly during the fire. The graph shows that the predicted strengths of the other slabs remained constant during the initial stage of the fire and started to decrease after 30 to 60 minutes fire exposure.

The load capacities of four of the six tested slabs had dropped below the level of the applied load by the end of the test. At the end of the fire test, the slab with the lowest predicted load capacity was the Hibond slab, due to the lowest concrete cover and smallest internal lever arm to the mesh. The D147 slab dropped below the applied load at 130 minutes soon after the Hibond slab and was followed by the Speedfloor slab (158 minutes) and the 661 slab (169 minutes) which both had a higher steel content.

The load capacity of the Traydec slab remained unchanged for most of the fire duration because of the large cover to the reinforcing. The ribs of the steel deck which were embedded in the concrete remained relatively cool and acted as fire emergency reinforcement. This enabled the slab to retain its flexural strength and stiffness; hence its relatively low deflections compared with the other slabs. The strength of the HD12 slab remained above the applied load at the end of the fire exposure even though it had suffered strength degradation because of its high steel content.

Although the predicted load capacities of the slabs had dropped below the level of the applied loads, the slabs did not collapse and possibly resisted the loads by tensile membrane action. The predicted load capacities based on yield line theory does not take account of tensile membrane enhancement; hence they predicted lower fire resistances.

6.8.2. Comparison between the Simple Design Method (Bailey, 2001) and test results

This section presents the calculations using the simple design method proposed by Bailey (2001) for two of the tested slabs. The simple design method predicts the load capacity of a slab due to tensile membrane enhancement during a fire.

The method assumes that the slab forms the yield-line crack pattern shown in Figure 3-18 and that the loads are resisted by tensile membrane action after the predicted yield line capacity drops below the applied load level. The method calculates the deflection that is required to provide the tensile membrane enhancement factor in order to resist the applied loads. The enhanced load capacity is calculated by applying the enhancement factor to the reduced yield-line load capacity.

The simple design method is applied to the D147 flat slab and the Hibond composite slab, whose predicted yield-line capacities had dropped below the applied load level by the end of the fire test (Figure 6-66). The method was applied after approximately 120 minutes when the yield-line capacities dropped below the applied load (5.4kPa) and that tensile membrane action was mobilised to resist the loads at that time.

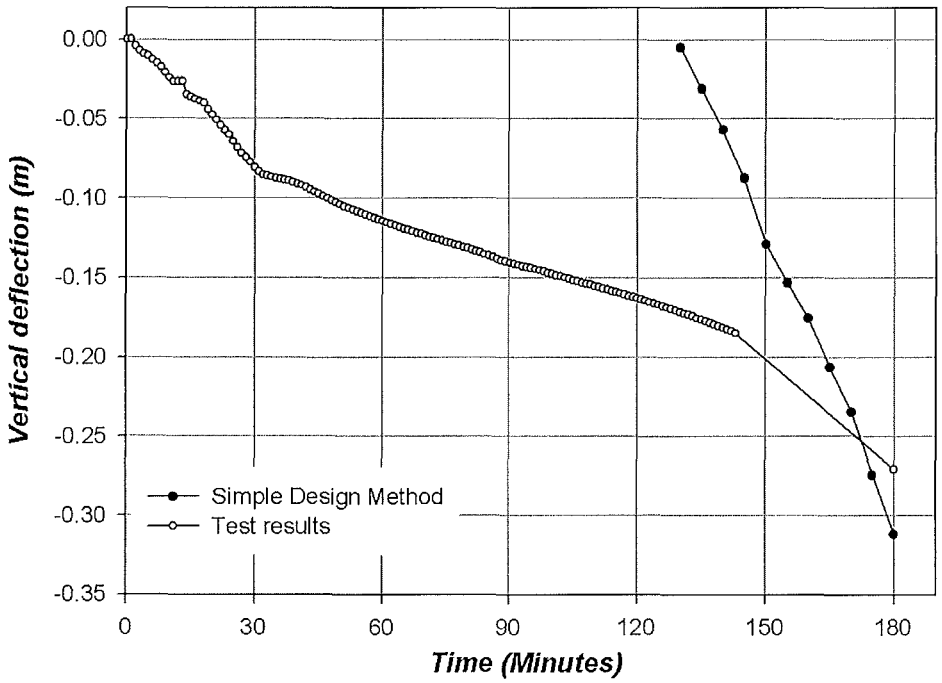

Figure 6-67: Comparison of the Simple Design Method with the D147 slab test results.

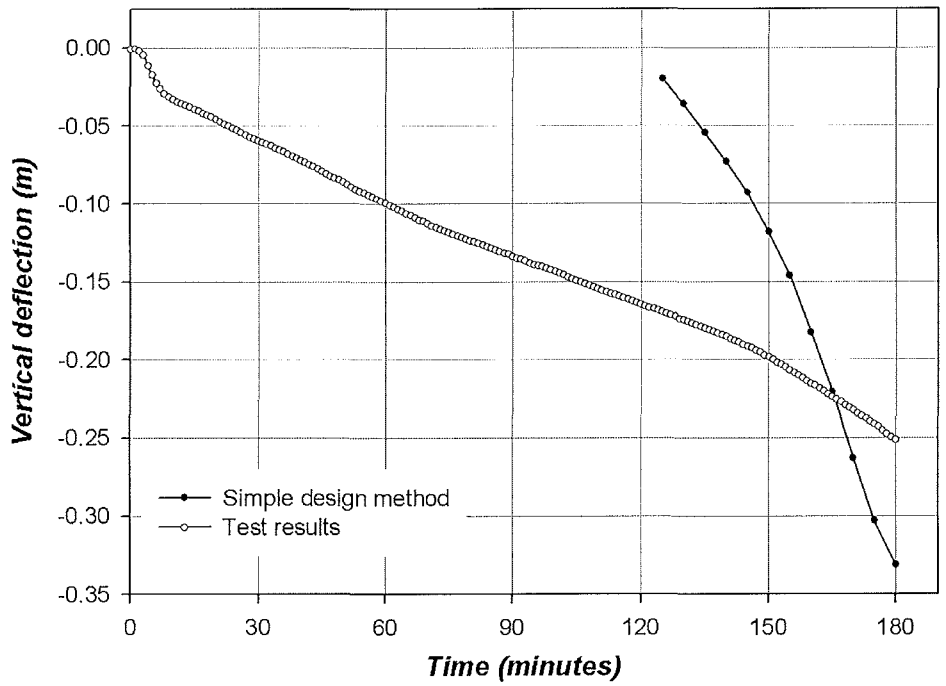

Figure 6-68: Comparison of the Simple Design Method with the Hibond slab test results.

Figure 6-67 and Figure 6-68 compare the predictions of the deflections required to provide the enhancement factors to resist the loads by tensile membrane action for the D147 and Hibond slabs, respectively. Figure 6-67 shows that for the D147 slab, up to 172 minutes, the method required lower deflections than the test deflections to provide the necessary tensile membrane resistance. This means that the method predicted higher strength capacity. The method predicted the required deflection exactly just after 172 minutes. Beyond that time, the method required a higher deflection to provide the necessary tensile membrane resistance. This trend is also observed when the method was applied to the Hibond slab. The method predicted the required deflection exactly at 166 minutes.

6.8.3. Conclusions

The comparison of the test results with the theoretical methods have shown that:

- Two-way slabs have much greater fire resistance than predicted with yield-line theory. The increased fire resistance is due to tensile membrane action which is not accounted for in yield-line theory.
- The simple design method proposed by Bailey (2001) shows agreement with the experimental test results and can be used to predict the required deflections to mobilise tensile membrane action to resist the applied loads.

6.9. Conclusions

Six fire tests of two-way concrete and composite slabs were conducted at the BRANZ furnace. The slabs were simply supported and horizontally unrestrained. The slabs were loaded with a live load of 3.0kPa and were exposed to the ISO standard fire for three hours. The tests showed that:

- The slabs supported the full design loads for the entire duration of the fire without collapse despite the large deflections (up to 270mm) sustained by some of the slabs. The temperatures of the reinforcing steel in some of the slabs exceeded 700°C after 3 hours along with very high temperatures in the slabs.
- The slabs showed extensive superficial cracking at the top surface. The tests showed that large full depth cracks did not form in slabs with steel content equal or greater than 300mm^2/m and with bar spacings of up to 200mm. Some of the slabs with light reinforcement contents of 200mm^2/m and with bar spacings of 300mm showed large full-depth cracks.
- The steel decking served as a good barrier to prevent integrity failure. However, the test of the Hibond slab showed that the steel decking could oxidise under prolonged fire exposure, leading to integrity failure.
- The slabs had much greater fire resistances than predicted with yield-line theory.
- The fire tests showed that the slabs formed double curvature and resisted the loads by tensile membrane action.
- Comparison of the simple design method with the test results showed that the method could be used to predict the load capacities of two-way slabs in fire.

7. THE ANALYSIS OF SLABS AT AMBIENT CONDITIONS USING THE SAFIR SHELL ELEMENT

7.1. Introduction

This chapter presents the analysis of two-way flat slabs at ambient conditions with the SAFIR shell element. The purpose of this is to assess the capability of the SAFIR shell element in predicting the ultimate load of two-way concrete slabs. This chapter also covers the modelling of a one-way composite slab at ambient conditions. The modelling of two-way slabs in fire conditions will be presented in chapters 8 to 10.

7.2. Two-way flat slab behaviour at ambient conditions

7.2.1. Introduction

In this section, the behaviour of a two-way simply supported slab at ambient conditions is modelled. The purpose of this is to assess the capability of the SAFIR shell element in predicting the ultimate load of two-way concrete slabs taking account the effect of membrane forces. The slab is simply supported at all four edges and is loaded to failure with a uniformly distributed load. The outer edges of the slab (beyond the supports) will not be considered in this section and will be analysed in section 7.3. The slab material and geometric properties are based on the D147 slab which was used in fire tests, described in chapter 6. In the following analyses, the cold drawn mesh used in the actual tested slabs was modelled as hot-rolled reinforcing steel because the material model for cold-drawn steel for 3D analysis was not available in SAFIR.

Previous experimental research on tensile membrane action on unrestrained simply supported two-way slabs has shown a significant increase in load capacity due to tensile membrane enhancement (Taylor, 1965; Sawczuk et al., 1965; Hayes, 1968). Recent 3D modelling of slabs at ambient temperatures has been presented by Huang et al. (2001a), who have used the VULCAN program to predict the ultimate load of two-way composite slabs at ambient conditions. Their analyses showed significant membrane forces in the slab as it approached failure, with a compression ring on the outer edges and a tension field in the middle region. The membrane forces produced a higher load carrying capacity than predicted with yield line theory.

7.2.2. Slab properties

The properties of the slab are shown below.

Slab geometry	
Length, L_y	4.16m
Width, L_x	3.16m
Thickness, h	100mm

Concrete properties	
Compressive strength, f'_c:	36 MPa
Elastic modulus, $E_{c,o}$:	21.6 GPa
Concrete cover, c_c	25mm to bottom-most bar
Concrete model	Eurocode 2 (EC2, 1995)

Reinforcing steel properties	
Yield strength (ambient temperature), $f_{y,o}$:	565 MPa
Reinforcing mesh, A_s	198mm^2/m
Reinforcing steel model	Hot-rolled steel (EC2, 1995)

7.2.3. SAFIR structural model

Figure 7-1 shows a typical finite element mesh used to model the slab. The mesh consists of 64 shell finite elements in an 8 by 8 grid of shell elements. Only a quarter of the full slab was modelled due to the symmetric load and support conditions. This also saves computational effort and time. The effect of varying the number of shell elements on the analyses will be discussed in section 7.2.4. The horizontal, rotational and drilling degrees of freedom were fixed at the axes of symmetry. The long span (X-direction) is referred as the *longitudinal* direction and the short span (Y direction) is referred as the *transverse* direction.

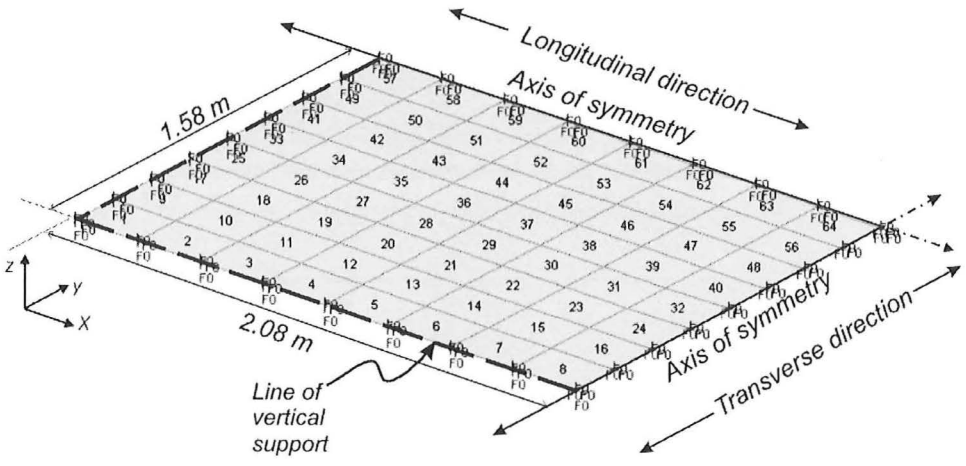

Figure 7-1: Finite element mesh of 64 shell elements.

7.2.4. Effect of the number of shell elements

This section discusses the modelling of the slab at ambient conditions with different number of shell elements. The purpose of this is to investigate the effect of the different mesh resolutions in predicting the behaviour and ultimate load of the slab. Theoretically, the finite element solution should approach the exact solution as the mesh resolution is refined (i.e.: the number of elements is increased) but it has the disadvantage of demanding larger computational resources and time.

Three different grid sizes are used in the analyses (Figure 7-2 to Figure 7-4). The number of shell elements range from 16 elements in the 4 x 4 grid, to 144 elements in the 12 x 12 grid. The analyses are conducted with zero concrete tensile strength and with a precision for convergence of 0.01. The effects of different levels of precision for convergence are discussed in section 7.2.5.

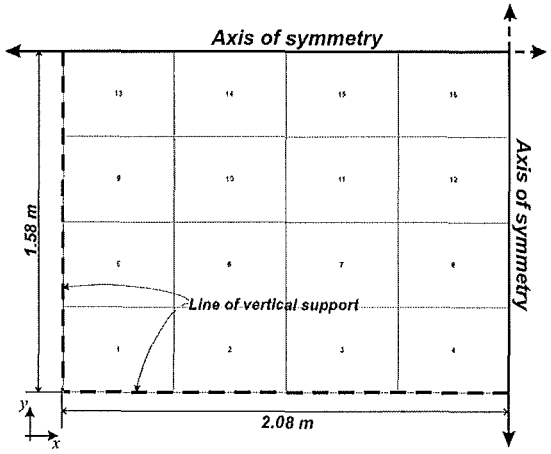

Figure 7-2: Coarse mesh, 4 x 4 grid, 16 elements

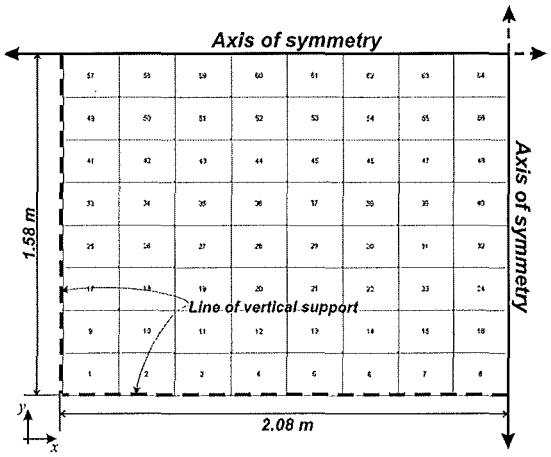

Figure 7-3: Medium mesh, 8 x 8 grid, 64 elements

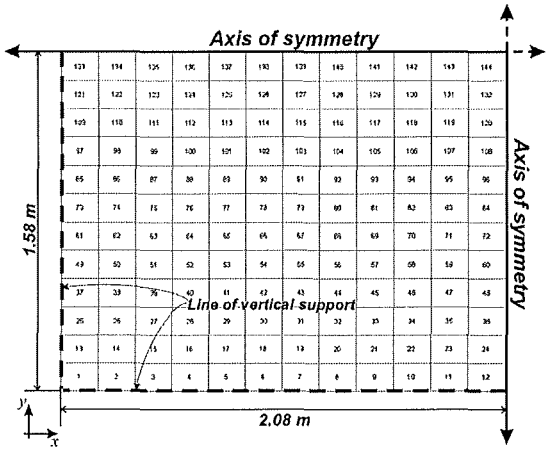

Figure 7-4: Fine mesh, 12 x 12 grid, 144 elements

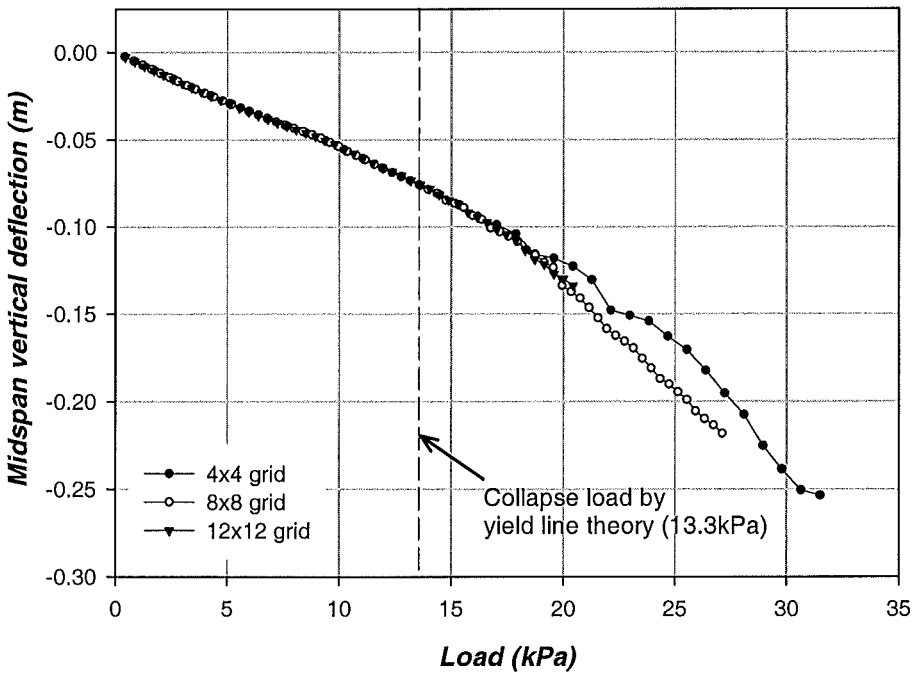

Figure 7-5: Midspan vertical deflection of the slab with different mesh resolutions.

Figure 7-5 shows the variation of the midspan vertical deflections of the slab under increasing load, for the different finite element meshes. The ultimate loads predicted with SAFIR are compared with the theoretical collapse load of 13.3kPa, calculated using yield-line theory. The graph shows that the slabs deflected immediately in a linear trend when the loads were applied. The different finite element meshes predicted identical linear deflection curves up to and beyond the theoretical ultimate load. At approximately 18kPa, the deflection trend of the slab with the 4x4 grid started to digress from the deflection path of the slabs with the finer mesh, leading to an erratic deflection trend. With a 12x12 grid, the slab failed at 20.4kPa, which equals to 1.54 times greater than the theoretical yield-line load capacity, w_u, of 13.3kPa. The deflected shape of the slab is shown in Figure 7-6. The slab with the 8x8 grid continued beyond 20.4kPa at a linear rate until it failed at 27.1kPa ($2.04w_u$). The slab with the 4x4 grid predicted a collapse load of 31.5 kPa ($2.37w_u$).

Tests by Hayes (1968) of unrestrained two-way slabs have shown that a slab with an aspect ratio of unity has a load capacity of 2 times greater than the predicted yield-line capacity. The tests have also shown that as the aspect ratio was increased to 2, the increase over the yield-line load capacity reduced to 1.5. The increased load capacity of $1.54w_u$ predicted by SAFIR with the 12x12 grid for the slab with an aspect ratio of 1.32 lies between the load capacities reported by Hayes (1968) for slabs with aspect ratios of 1.5 and 2.0.

Figure 7-5 shows that as the number of elements in the mesh increased, the predicted load capacity of the slab decreased. The analyses with the different mesh sizes stopped when the program failed to converge to a solution. Failure of the slab was most likely to be due to fracture of the reinforcing steel in the middle region of the slab. With a higher number of elements, the program detected failure more accurately at the integration points, due to crushing of the concrete or fracture of the reinforcement. With fewer elements, the program detected failure at a much higher load due to the sparser distribution of the integration points and has shown to be more susceptible to diverge from the actual solution.

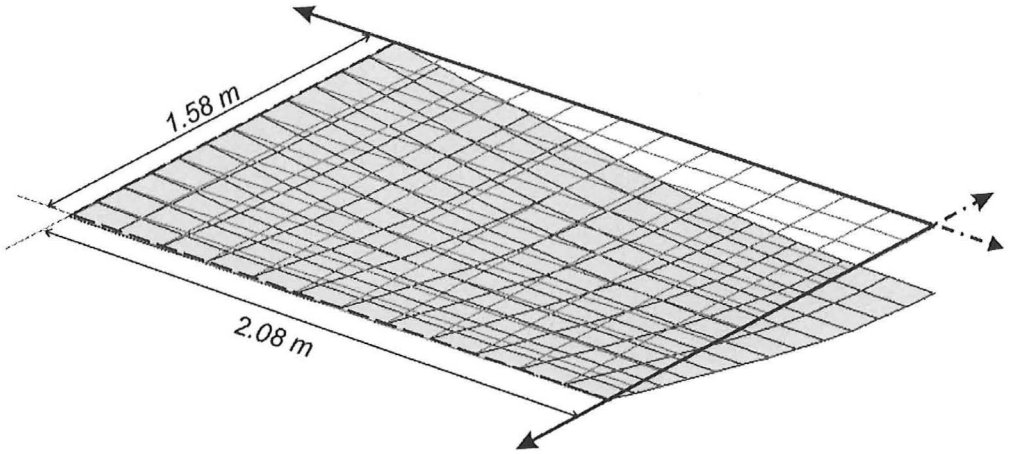

Figure 7-6: Deflected shape of the slab with the 12x12 grid at collapse (Deflections magnified 1.5 times).

In both the 4x4 and the 8x8 grids, large tensile stresses formed at the top surface at midspan when the loads were increased beyond 22kPa. These spurious tensile stresses were in the order of 10 to 30 MPa and were most likely to be numerical error, because tensile stresses cannot form on the top surface at midspan of the slab because the top surface is in compression. In addition, tensile stresses cannot form in the concrete because the analysis was performed without concrete tensile strength.

7.2.5. Effect of the precision required for convergence

The effect of the precision required to achieve convergence is discussed in this section. The convergence precision is the minimum precision which is required in order to obtain a converged solution, at a particular load increment. The analysis of the slab with different grid sizes in the previous section is repeated in this section, with a higher precision of 0.002. A precision higher than 0.002 could not be used because the program would terminate its analysis prematurely due to failure to achieve convergence. The results of the analyses will be compared with the results obtained with the precision of 0.010. With a lower precision, convergence to a solution can be easily achieved with fewer iterations than with a higher precision, but it is susceptible to divergence from the actual solution. The actual solution can be achieved with a higher precision, but may suffer convergence problems which leads to the analysis terminating prematurely.

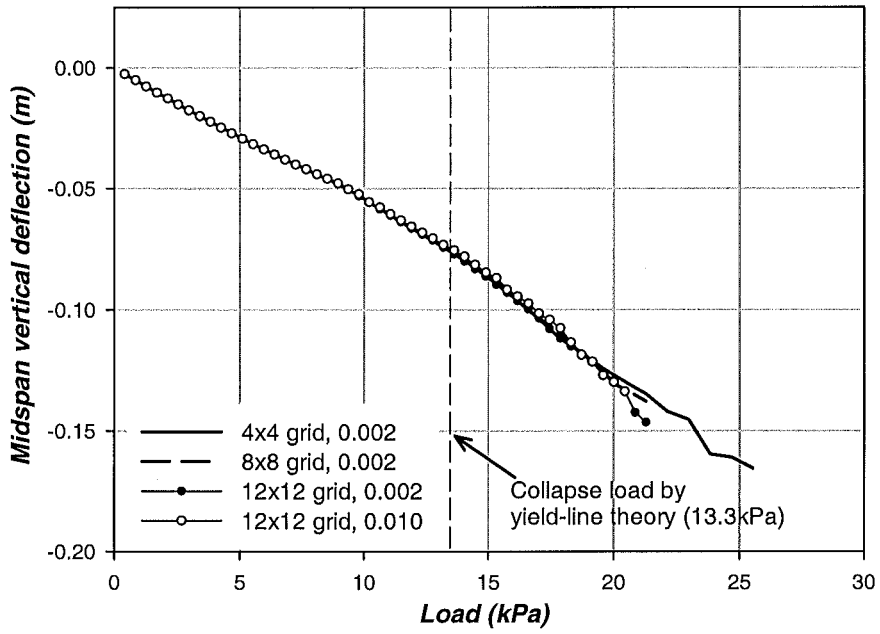

Figure 7-7: Midspan vertical deflection of the slab with 0.002 precision for convergence.

Figure 7-7 shows the variation of the midspan deflections of the slab with a precision of 0.002. The graph shows a similar deflection trend during the initial stages to that seen in the previous section (Section 7.2.4), where a lower precision was used. However, with the higher precision, the analyses with the 4x4 and 8x8 grids predicted lower load capacities. With the 4x4 grid, the deflection of the slab started to fluctuate at the final stages as it reached it calculated collapse load.

Table 7-1 compares the predicted ultimate loads of the slabs analysed with the two different precisions. The ultimate loads of the slabs with the 4x4 and 8x8 grids calculated with the precision of 0.002 were significantly lower than those calculated with the lower precision of 0.010. With the 12x12 grid, the higher precision did not cause a substantial difference in the ultimate load. The actual solution is assumed to be 21.3kPa, since it was determined with the highest number of elements and the highest convergence precision.

Finite element mesh	Precision = 0.010	Precision = 0.002
4 x 4 grid (Coarse mesh)	31.5 kPa ($2.37w_u$)	25.5 kPa ($1.92w_u$)
8 x 8 grid (Medium mesh)	27.1 kPa ($2.04w_u$)	21.3 kPa ($1.60w_u$)
12 x 12 grid (Fine mesh)	20.4 kPa ($1.53w_u$)	21.3 kPa ($1.60w_u$)

Table 7-1: Comparison of ultimate loads with different levels of precision for convergence.

With the coarse and medium grids, the solution converged to the actual solution when the precision level was increased. Table 7-1 shows that with a precision of 0.002, the 8x8 grid also predicted the same ultimate load as the 12x12 grid. The analyses show that the higher degree of precision should be used when a coarser finite element mesh was used. With the 12x12 grid, using a precision of 0.010 or 0.002 did not have a significant difference on the behaviour and ultimate load of the slab. The analyses also showed that an accurate solution can be obtained using an 8x8 grid and a precision of 0.002.

7.2.6. Effect of concrete tensile strength

This section investigates the behaviour of the slab with different values of concrete tensile strength. Concrete tensile strength is not normally included in typical structural design because real structures undergo cycles of loading and expansion and shrinkage, resulting in the structural members being cracked. However, for unloaded slabs, such as those tested in the fire resistance tests at BRANZ (Chapter 6), the slabs would not be loaded until the fire tests and would not have suffered much cracking. Hence, the concrete tensile strength should be considered in the modelling of the slab behaviour.

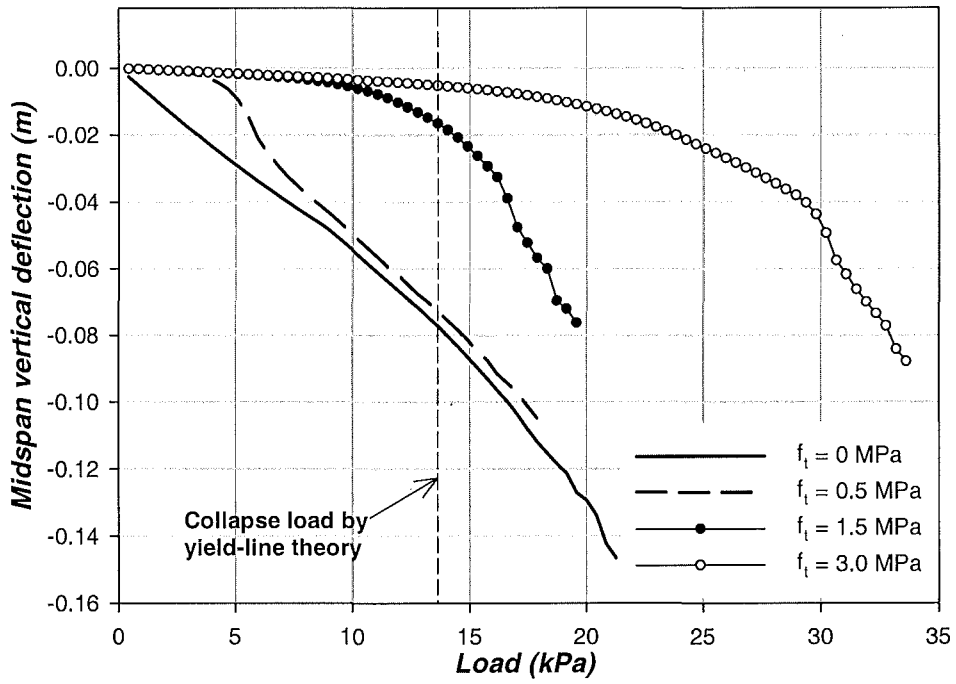

Figure 7-8: Midspan deflections of the D147 flat slab with different values of concrete tensile strength.

Figure 7-8 shows the variation of the midspan vertical deflections of the flat slab modelled with different values of concrete tensile strength, ranging from zero to 3.0MPa. 3.0MPa is assumed to be the full tensile strength and is obtained from the equation $0.5\sqrt{f'_c}$. Recommended concrete tensile strengths range from $0.33\sqrt{f'_c}$, recommended by (Bazant et al., 1982) to $0.62\sqrt{f'_c}$ recommended by the ACI (Mindess et el., 1981). Therefore, a value of $0.5\sqrt{f'_c}$ was used as an intermediate maximum strength between the two recommended values. The fully cracked section of the slab has much lower flexural stiffness compared with the slabs which have some concrete tensile strength, resulting in the larger deflections. In the fully cracked slab, only the reinforcing steel is available to resist the tensile forces. The anlaysis is carried out using the 12 x 12 grid and with a precision of 0.01.

With f_t equal to 0.5MPa, the slab sustained very small deflections during the initial stages. The midspan deflection is 1mm under its self weight (2.4kPa). As the load was increased, the concrete progressively cracked, transferring the tensile bending stresses from the concrete to the reinforcing steel. Cracking of the concrete occurred when the stresses at the Gauss integration points exceeded the tensile strength of the concrete. The cracking reduced the flexural rigidity of the slab and caused a sudden increase in the deflection rate between 5kPa to 6kPa. Beyond 6kPa, the slab deflection asymptotes towards the deflection curve of the fully cracked slab (f_t = 0 MPa) as cracking propagated through the slab. Failure of the slab occurred at a load of 17.9kPa, which is 1.34 times greater than the calculated ultimate load. The analysis with 0.5MPa concrete tensile strength predicted a lower load capacity than the fully cracked slab.

The analysis shows that when the tensile strength was increased to 1.5MPa, the slab deflections were initially very small. The deflections increased noticeably only when the applied load exceeded 10kPa. At the theoretical ultimate load capacity of 13.3kPa, the deflection had only reached -15mm. The analysis stopped at 19.6kPa, when the midspan deflection reached -76mm. With full concrete tensile strength (3MPa), the slab showed significantly smaller deflections compared with the other slabs. The ultimate load of this slab was 33.6kPa, which is 2.53 times greater than the theoretical load capacity.

Discussion

Figure 7-9 shows the stress-strain curve of concrete in tension. The stress-stain diagram, described more precisely as the hardening curve, gives the equivalent uniaxial strength as a function of the hardening parameter, i.e. the equivalent uniaxial plastic strain. The concrete stress increases linearly up to $0.8 f_t$, followed by a further non-linear increase up to $1.0 f_t$ which corresponds to an equivalent strain of $\varepsilon_{t,1}$. Beyond this, the stresses decrease to zero, with an equivalent strain of $\varepsilon_{t,u}$.

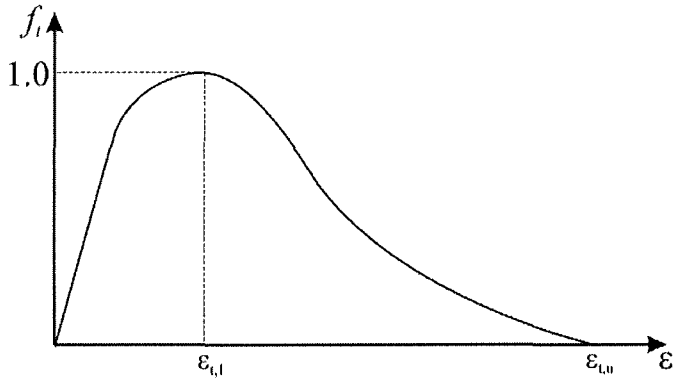

Figure 7-9 : Concrete hardening curve in tension.

During the analysis, when a point of the structure (an integration point) is on the decreasing branch of the stress-strain curve, the stiffness of the material is negative. This can be counterbalanced by the positive stiffness of the other points, such as the reinforcing bars, to maintain a positive stiffness matrix for the element. Unfortunately, in typical slabs, the reinforcement ratio is very low and the steel has limited capacity to accommodate the negative stiffness.

If the concrete tensile strength is low, the absolute value of the negative stiffness remains low and the stiffness matrix does not become negative. However, the value of the negative stiffness increases with increasing tension strength and positive stiffness cannot be maintained without increasing the value of $\varepsilon_{t,u}$ (J.M. Franssen, pers. comm.). At high levels of concrete tensile strength, the concrete becomes very ductile and does not undergo the expected amount of cracking. This causes the flexural rigidity of the slab to remain high and the deflections to remain low.

The modelling results have shown that the concrete model is very ductile in tension (particularly under high values of tensile strength) and the concrete in the tension region of the slab resists a significant tension force compared to the tension force resisted by the bars. This problem can be solved by ignoring tensile strength in the concrete, i.e.: using zero or low concrete tensile strength. The program can accommodate the numerical problems linked to the sudden cracking during the first step when there is zero or very low concrete tensile strength. Using this approach, there will be fewer problems during the rest of the analysis because further cracking, even if due to thermal stresses, will not generate negative stiffness. The only

drawback is that the program might overestimate the deflections, especially during the initial stages of an experimental test in which the concrete may be uncracked.

7.2.7. Stresses in reinforcing bars

This section looks at the stresses of the reinforcing steel at different locations in the slab. The discussion is based on the analysis with a 12x12 grid with a precision of 0.002 and f_t of 0.5MPa. The analysis with f_t of 0.5MPa is considered to be a good representation of the behaviour of the slab even though it slightly underestimated the ultimate load capacity. The element numbers and the locations of the steel which will be referred to are shown in Figure 7-10. The stresses across the middle of the slab in the longitudinal (X) and transverse (Y) directions are plotted.

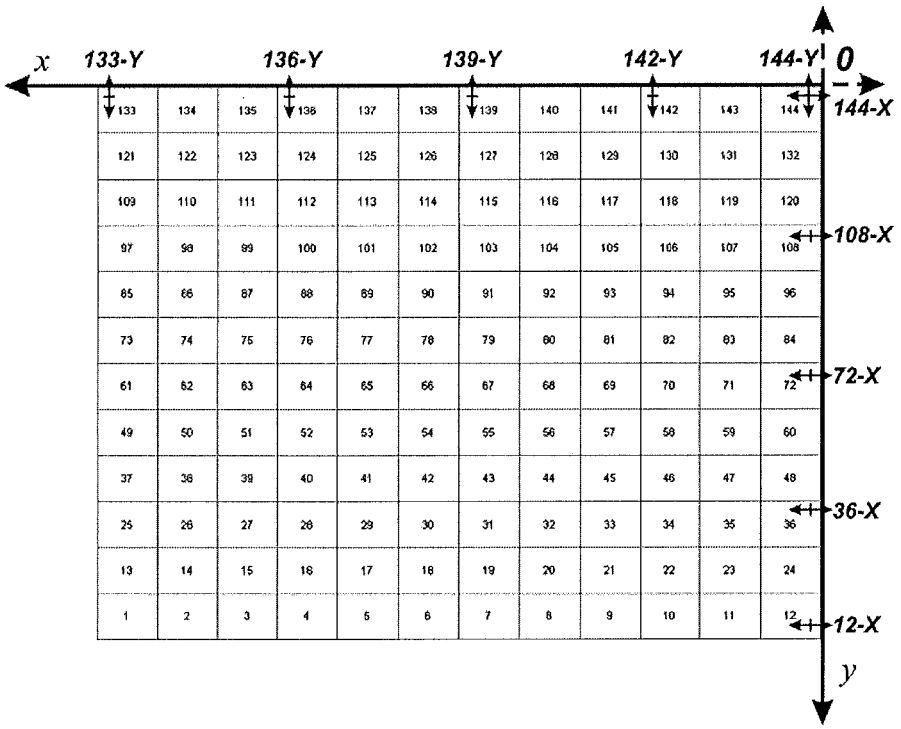

Figure 7-10: Positions where the reinforcing stresses are plotted with time.

Y-direction stresses

Figure 7-11 shows the variation of the stresses in the reinforcing steel across the short span of the slab (Y-direction). The stresses of the steel at elements 133, 136, 139, 142 and 144 were plotted (See Figure 7-10). The numbers next to the legends represent the distances from midspan. The midspan deflections are plotted on the same axis to show the effect of the deflections on the stresses of the steel.

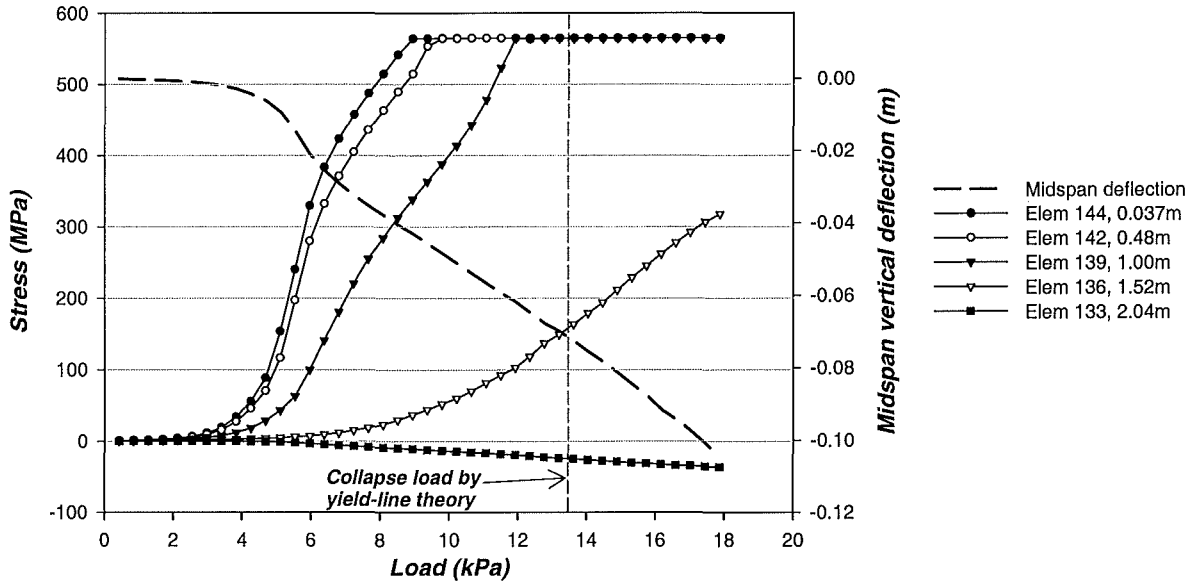

Figure 7-11: Reinforcing stresses in the short span (y-direction) of the slab.

Figure 7-11 shows that under low load levels, the tensile bending stresses were resisted by the concrete in tension and the reinforcing stresses were very low. As the slab was progressively loaded, the tensile stresses at the bottom of the slab increased and exceeded the tensile strength of the concrete, causing the concrete to crack. Between 5kPa and 6kPa, the steel stresses at the midspan region (elements 142 and 144) increased very rapidly when the tensile stresses in the concrete transferred to the reinforcing steel. The cracking of the concrete caused the loss of flexural stiffness and the deflections to increase. First yield occurred at midspan at element 144, under a load of 8.9kPa. The steel at 0.48m and 1.0m from the centre, yielded at 9.8kPa and 11.9kPa, respectively. The computer output also shows that at the theoretical load capacity (13.3kPa), the length of the yield line had formed a metre in both directions from the centre of the slab. The low compression steel stresses at the outer edges (element 133) are considered to be due to the compression ring at the outer edges of the slab.

X-direction stresses

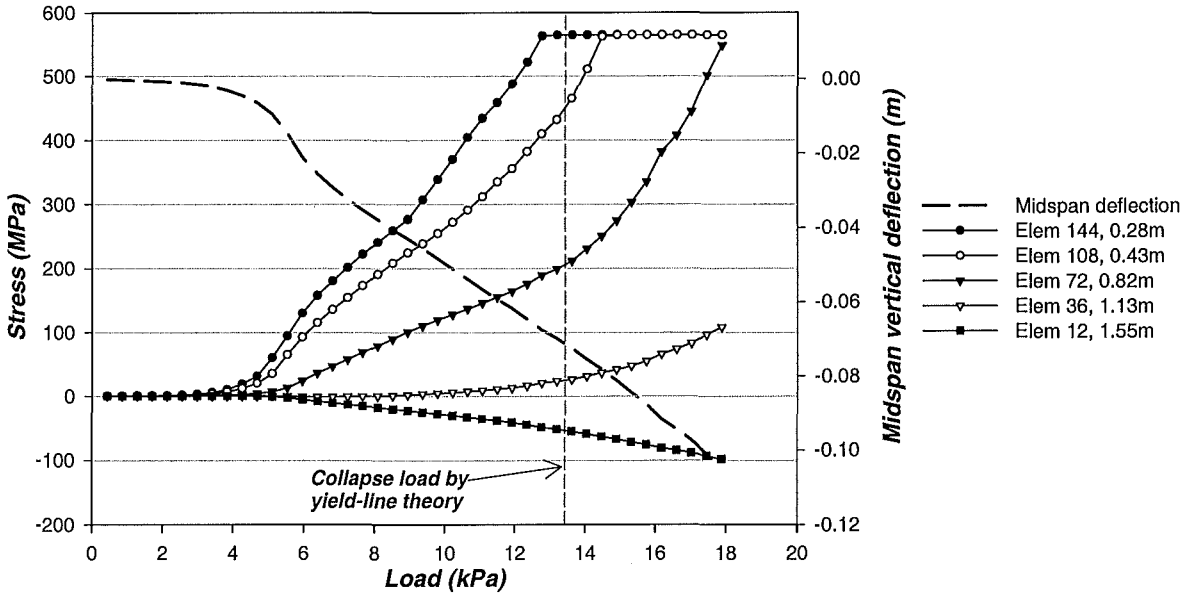

Figure 7-12: Reinforcing stresses in the long span (x-direction) of the slab.

Figure 7-12 shows the variation of the steel stresses across the long span (X-direction). The stresses of the steel across the middle of the long span were plotted for elements 12, 36, 72, 108 and 144 (See Figure 7-10). The graph shows that up to 4kPa, the stresses in the steel were very low as the tensile bending stresses were resisted by the concrete. Beyond 5kPa, the steel stresses at midspan (element 144) gradually increased when the tensile bending stresses transferred from the concrete to the steel as the concrete started to crack. The increase of the steel stresses in the long direction at midspan was not as rapid as observed in the transverse (Y) direction because of the lower moments in the X-direction. The midspan steel yielded at 12.8kPa and the stresses levelled off under increasing load. The computer output shows that the length of the yield line extended up to 0.82m in both directions from the centre when the slab failed. The presence of the compression ring at the edges of the slab is shown by the steadily increasing compression stresses in element 12, located 1.55m from the centre (30mm from the edge of the slab).

Stress distribution

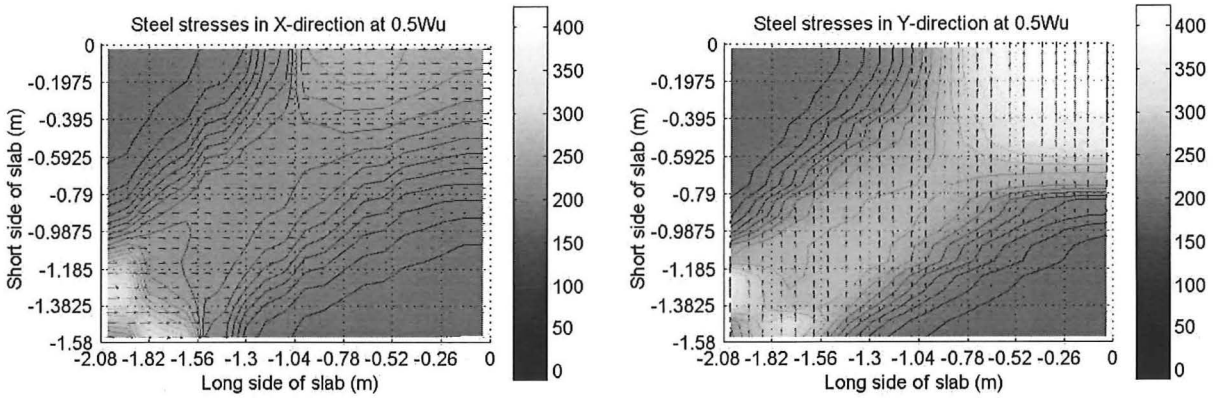

Figure 7-13: Distribution of steel stresses at 50% of the theoretical ultimate load capacity ($0.5w_u$).

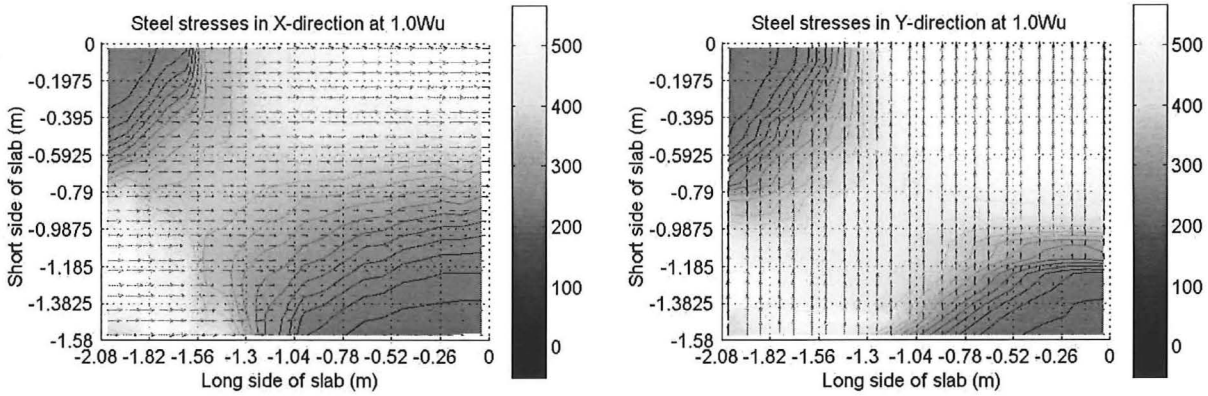

Figure 7-14: Distribution of steel stresses at the theoretical ultimate load capacity ($1.0w_u$).

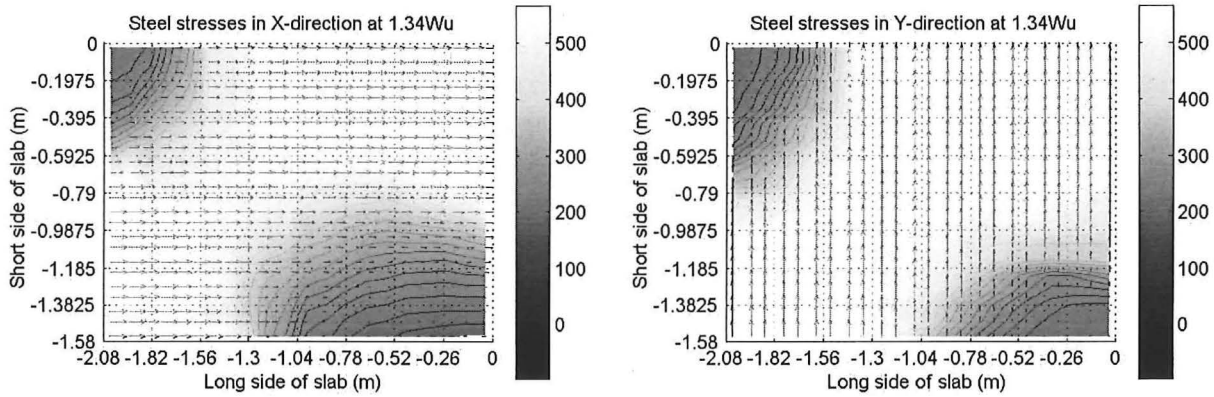

Figure 7-15: Distribution of steel stresses prior to collapse ($1.34w_u$).

Figure 7-13 to Figure 7-15 shows the distribution of the steel stresses in the slab at various load levels. The plots show the steel stresses in the bottom left quadrant of the slab in the X (longitudinal) and Y (transverse) directions. Dark shades indicate low tension and compression stresses and bright shades indicate high tensile stresses.

At 50% of the theoretical load capacity (6.65kPa), Figure 7-13 clearly shows a band of high tensile stresses which extend from the middle (top right corner) to the corner support (bottom left) of the slab. This region of high tensile stresses corresponds to the formation of the yield lines. The tensile stresses in the transverse direction were higher than in the longitudinal direction because the reinforcing bars in the short direction were placed below the bars in the long direction and resisted higher bending moments..

As the applied load was progressively increased to the $1.0w_u$ and $1.34w_u$, the diagonal band of the tensile stresses widened due to spreading of the yield region. Figure 7-14 shows relatively high tensile stresses near the corner support (bottom left), which were due to the high torsional moments at the corners. At collapse ($1.34w_u$), Figure 7-15 shows extensive yielding of the steel throughout the slab, except for the middle region of the slab edges which showed low tension and compression stresses. The low tension and compression stresses at the edges were due to the compression ring forming at the outer edges. At this stage, the slab acted a membrane, resisting the loads by tensile membrane action.

7.2.8. Tractions

Figures 7-15 to 7-17 show the distribution of the membrane tractions in the slab and the N_x and N_y tractions at various stages of loading. The first column (a) shows the principal tractions, N_1 and N_2, in the slab. The tractions, represented by the arrows, are plotted at each surface integration point of the shell element. The arrows are oriented according to their respective principal angles and the lengths of the arrows indicate the magnitude of the tractions. The thick, dark arrows represent compression tractions and the lighter arrows represent tension tractions. The second column (b) shows the distribution of N_x tractions at midspan in the longitudinal direction and the third column (c) shows the N_y tractions in the transverse direction. The tractions at each surface integration point, in either the X or Y direction, is equal to the integral of the stresses over the thickness of the slab, as shown in Equation 7-1.

$$N_i = \int_{-t/2}^{t/2} \sigma_i \, dz \qquad \textbf{Equation 7-1}$$

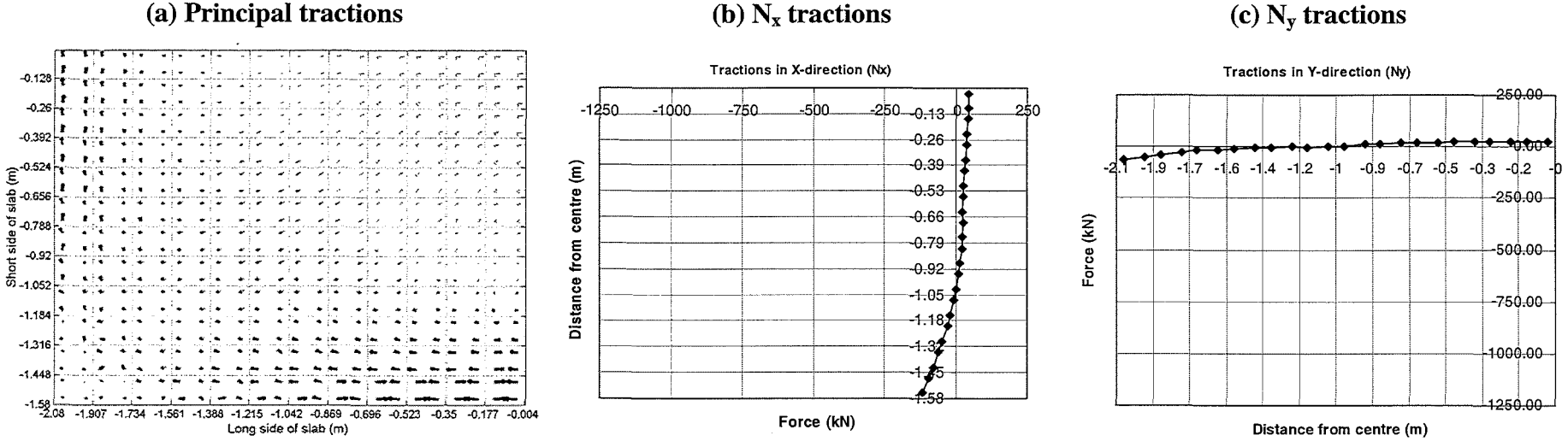

Figure 7-16: Distribution of traction forces at $0.5w_u$ (6.65kPa)

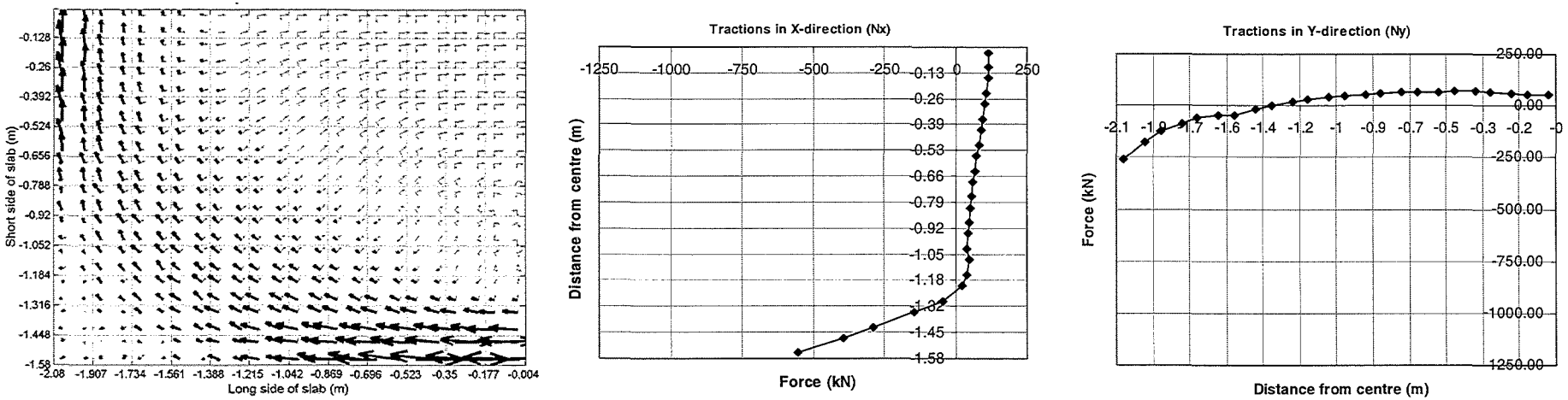

Figure 7-17: Distribution of traction forces at $1.0w_u$ (13.3kPa).

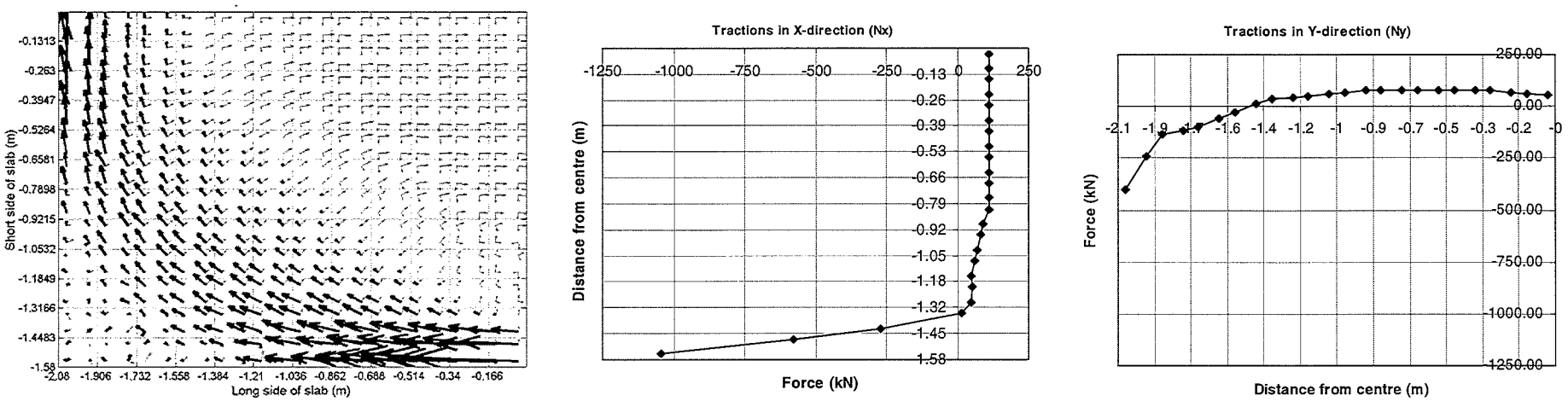

Figure 7-18: Distribution of traction forces at $1.34w_u$ (17.8kPa)

At 50% of the theoretical load capacity ($0.5w_u$), Figure 7-16 shows that the membrane forces in the slab are low, with tension in the middle and compression at the outer edges. During this stage, the loads were mainly resisted by bending action because the flexural strength of the slab was still high. The N_x tension tractions in the longitudinal direction at the middle of the slab were almost constant. The tension tractions changed to compression with increasing distance from the centre of the slab. The width of the compression field at the edges in the X and Y directions are 0.52m and 0.94m, respectively. The sum of the compression tractions, across either the X or Y directions, is equal to the sum of the tension tractions.

At the theoretical ultimate load (13.3kPa), Figure 7-17 shows that the membrane forces had increased significantly, shown by the increasing magnitude of the tension tractions in the middle of the slab and the compression ring at the edges. At this stage, extensive yielding of the reinforcing had occurred at midspan (see Figure 7-14), thus resulting in the high tension tractions in that region. Figure 7-17b shows that the N_x compression tractions at the outer edges of the slab had increased very significantly. The width of the compression region at the edges in the X-direction had decreased from 0.52m at $0.5w_u$, to 0.36m at $1.0w_u$. The increasing deflections increased the size of the tensile field, which in turn decreased the width of the compression ring. This increased the magnitude of the compression tractions at the edges of the slabs to maintain equilibrium with the tension tractions. In the midspan region, the maximum N_x tractions had reached 110kN/m, indicating that the steel had yielded. Note that the yield traction force of the steel is 111kN/m ($198mm^2/m$ x 565MPa). The steel spanning the transverse direction had also yielded (N_y), but the maximum tractions were lower compared to those in the X-direction due to the wider span of the slab; hence the lower force per unit width.

At the point of collapse ($1.34w_u$), Figure 7-18b shows that the N_x compression tractions had increased very significantly, while the width of the compression ring had decreased to 0.24m. The tension tractions in the middle of the slab were constant, indicating extensive yielding of the steel. However, in the transverse direction, the N_y tractions only showed a slight increase from the previous figure.

7.2.9. Reaction force distribution

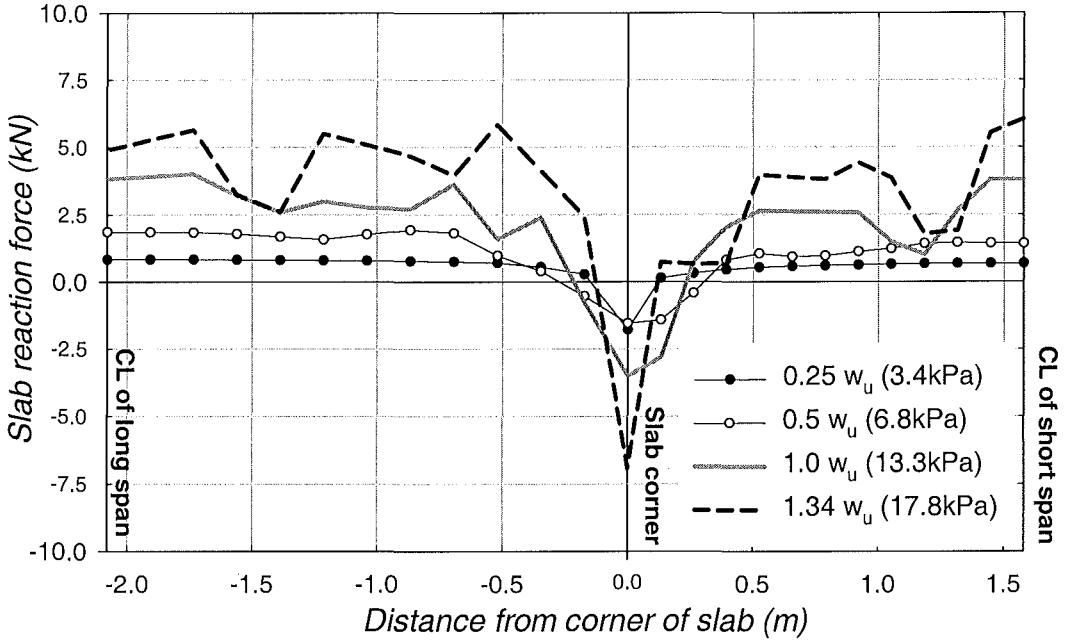

Figure 7-19: Distribution of the reaction forces at the slab supports.

Figure 7-19 shows the distribution of the reaction forces at the slab supports at various load levels. The reaction forces are plotted from the centreline of the long span to the centreline of the short span. Positive reaction force represents upward reaction while negative reaction represents downward reaction. At low load levels (3.4kPa), the graph shows a uniform positive reaction force along the entire length of the support, except at the corner of the slab. Negative reactions formed at the corner of the slab due to the downward reactions against lifting of the corners. As the load was increased, the distribution of the reactions progressively became more erratic. At failure of the slab (17.8kPa), the reaction forces were distributed into bands of high reaction concentrations at the centre of the long and short spans of the slab, and at a quarter of the long and short spans. The corner of the slab also shows a very high and localised downward reaction force.

The graph provides a qualitative representation of the reaction forces at the supports at high load levels and after the slab had suffered extensive yielding and plastification. The precision of the solution of the reaction forces can be increased with a higher number of elements or with increased precision to achieve convergence. However, this would demand large amount of computational resources and require further improvements to the concrete model to allow higher convergence precisions without premature failure.

7.2.10. Conclusions

The analyses in this section have shown that:

- The SAFIR shell element can be used to predict the ultimate load of a simply supported two-way slab at ambient conditons, accounting for the effects of membrane forces and material and geometrical non-linearity.
- SAFIR predicts a higher ultimate load of the slab than predictions made with yield line theory. The increased load carrying capacity is due to enhancement by the in-plane membrane forces.
- Membrane forces form in two-way slabs due to the geometry of the deformations as the slabs deflect downwards. The in-plane membrane forces consist of a compression ring forming at the outer edges of the slab, surrounding a tensile field in the midspan region.
- The coarse mesh with the low precision estimated a much higher load capacity. With a higher precision, the coarse and medium finite element meshes predicted a closer ultimate load to that predicted with the 12x12 mesh. The analyses showed that using a fine mesh, a low precision would provide a close estimate of the ultimate load of the slab.
- Any analysis with the plane stress concrete model at ambient conditions should be performed with a low concrete tensile strength. Large values of concrete tensile strength would underestimate the deflections of the slabs.
- At high load levels, the reaction forces formed localised concentrations along the edge supports.

7.3. The effect of the outer edges on the slab behaviour

7.3.1. Introduction

In this section, the slab is analysed with outer edges to model the presence of the concrete outside the line of the support. The outer edges are included in the analysis to investigate whether they affect the stiffness and load capacity of the slab. The slab is subjected to increasing loads at ambient conditions and is compared with the slab without the outer edges, discussed in section 7.2.

7.3.2. Slab description

The slab measures 4.3m by 3.3m and has a clear span identical to the slab of the previous section, measuring 4.16m by 3.16m, with a 70mm overhang beyond the supporting rollers.

7.3.3. SAFIR structural model

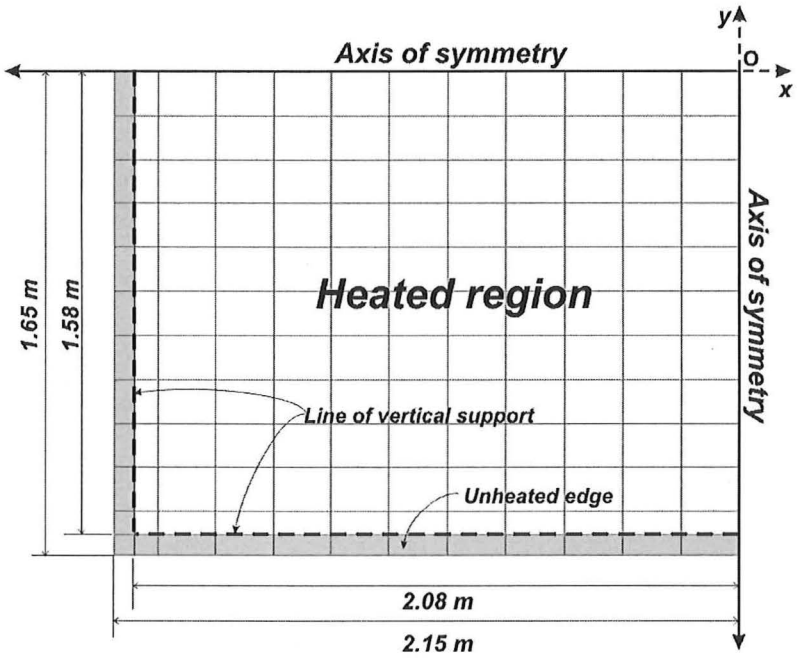

Figure 7-20: Structural model with the edge elements.

Figure 7-20 shows the finite element model of the slab with the outer edges. The model consists of 144 elements in a 12 x 12 grid of shell elements. The outer edges of the slab were modelled with a single row of shell elements. A higher steel content was modelled in the outer edges to represent the trimmer bars built into the actual tested slabs. The clear span of the slab, between the supports, was loaded with a uniformly distributed load, to failure. The

increasing load was not applied to the edges of the slab. The material properties and reinforcing content are identical to the slab of the previous section. The slab is analysed with zero and 0.5MPa concrete tensile strength and the results of the analyses are compared to the slab behaviour in section 7.2.

7.3.4. Midspan deflections

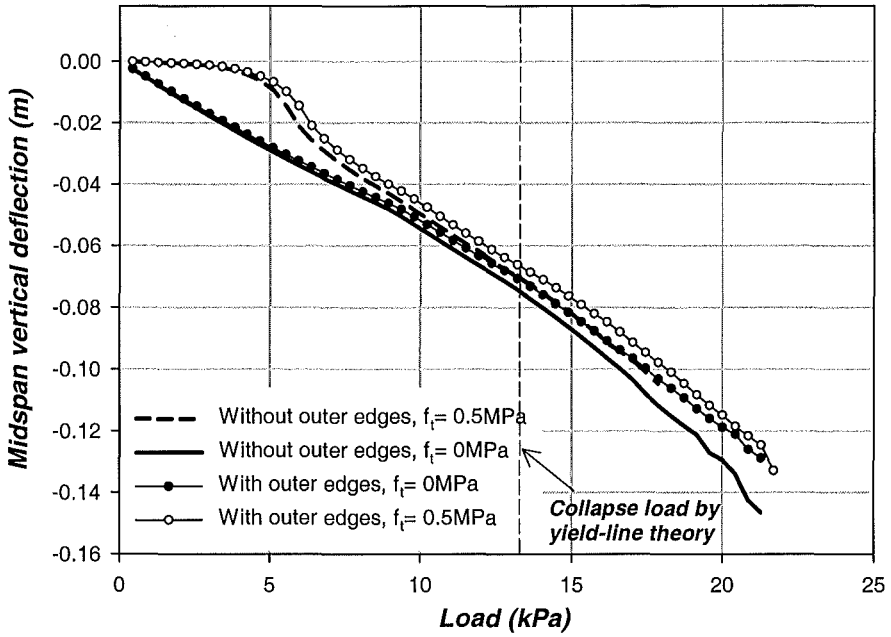

Figure 7-21: Effect of outer edges on the midspan deflections of the D147 flat slab.

Figure 7-21 compares the deflections of the slab with and without the outer edges. With f_t equal to zero, the graph shows that at low load levels, the deflection curves of the slabs with and without the outer edges were almost identical. The outer edges of the slab had very little effect on increasing the stiffness of the slab and only showed some effect on the deflections at higher load levels. The ultimate load capacities of the slabs with and without the edges were identical (21.3kPa) and the difference of the deflections at failure was very small. The deflected shape of the slab with the outer edges, prior to collapse, is shown in Figure 7-22.

The graph shows that with 0.5MPa concrete tensile strength, the slab suffered very small deflections at low load levels because the concrete was uncracked. After cracking of the concrete at 4kPa, the deflection rate increased and the deflections asymptote to the curve of the fully cracked slab. With the outer edges, the program predicted an ultimate load of 21.7kPa, which is similar to the slabs with zero concrete tensile strength. It did not suffer the

convergence problems experienced in the slab without the outer edges which reached an ultimate load of only 17.9kPa.

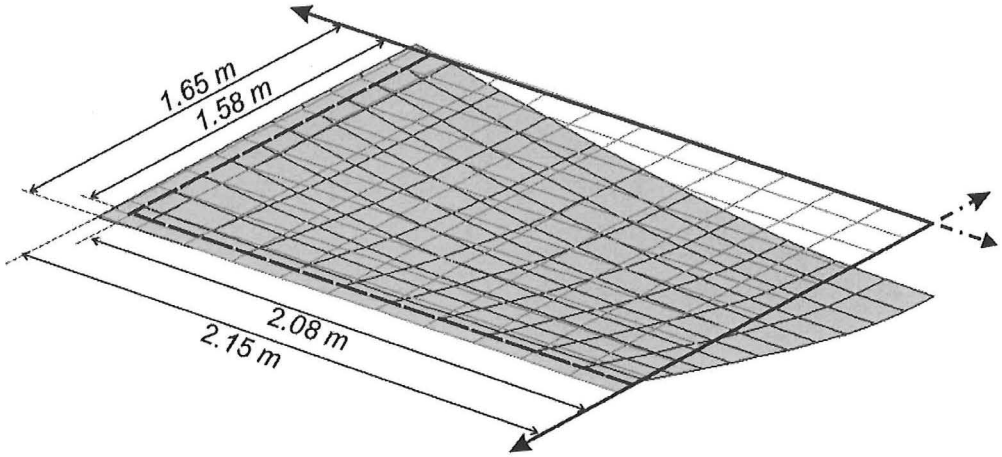

Figure 7-22: Deflected shape of the slab at the point of collapse (Deflections magnified 2 times).

7.3.5. Conclusions

The analyses in this section have shown that the outer edges did not have a significant influence on the stiffness of the slab at ambient conditions. The edges of the slabs reduced the slab deflections slightly at high load levels but did not have any effect at low load levels. The analyses also showed that the outer edges did not have any effect on the ultimate load capacity of the slab.

7.4. Modelling of a one-way composite slab at ambient conditions

7.4.1. Introduction

This section describes the modelling of the Hibond composite slab at ambient conditions. The Hibond slab behaves as an orthotropic slab at ambient conditions, with high flexural strength and stiffness in one direction, but has low strength and stiffness in the perpendicular direction. Under fire conditions, the strength of the slab decreases very rapidly due to the rapid strength degradation of the exposed steel decking. The orthotropic behaviour cannot be modelled with a plain shell element alone without modifying the shell element formulation. Recent work on modelling orthotropic slab behaviour at elevated temperatures has been reported by Huang et al. (2000a). They have used an effective stiffness approach to model the orthotropic behaviour of a similar composite floor system which has proven to be very successful in predicting the behaviour of the Cardington fire tests.

A different approach will be used here to model the composite slab, utilising beam and shell elements. In this section, two experimental tests of one-way Hibond slabs conducted at ambient conditions, will be modelled with SAFIR. The slabs were simply supported and were loaded to failure with a series of point loads. The test will be replicated with SAFIR by modelling the tested slab with shell and beam elements. The purpose of replicating the tests with SAFIR is to verify the model with existing experimental data to assess the accuracy of the model, before extending the model to analyse the 3D behaviour of a 2-way slab under fire conditions, which will be discussed in Chapter 9.

7.4.2. Description of the experimental test

The experimental tests were conducted on two identical one-way simply supported Hibond slabs and the test data was obtained courtesy of Dimond Industries (Mike Klemick, *Pers. Comm.*). The slabs had a clear span of 2.5m and were loaded with two equal point loads as shown in Figure 7-23. Figure 7-24 shows the cross section of the slab, which was 120mm thick and was reinforced with cold-drawn mesh with a steel content of 147mm^2/m. The mesh was placed at approximately 30mm below the top surface of the slab. The concrete strength was 20MPa and the widths of the slabs were 630mm. Before the slabs were tested to their ultimate loads, they were subjected to 10,000 load cycles between 0.5W and 1.5W to represent serviceability loading, where W represents the anticipated applied load.

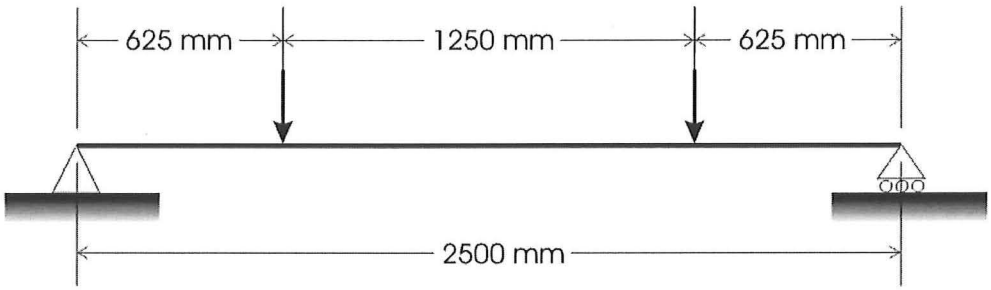

Figure 7-23: Loading of the one-way Hibond slab at ambient conditions.

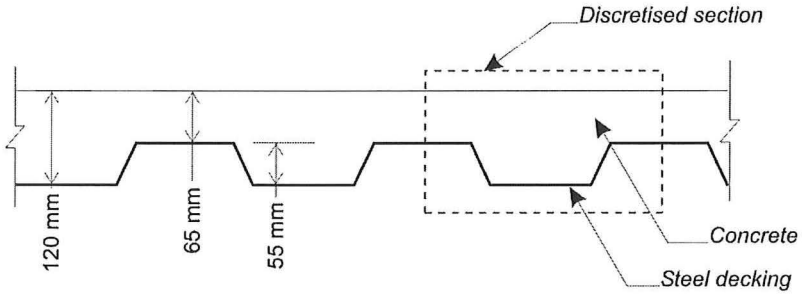

Figure 7-24: Cross section of the Hibond slab for the ambient temperature test.

7.4.3. SAFIR model

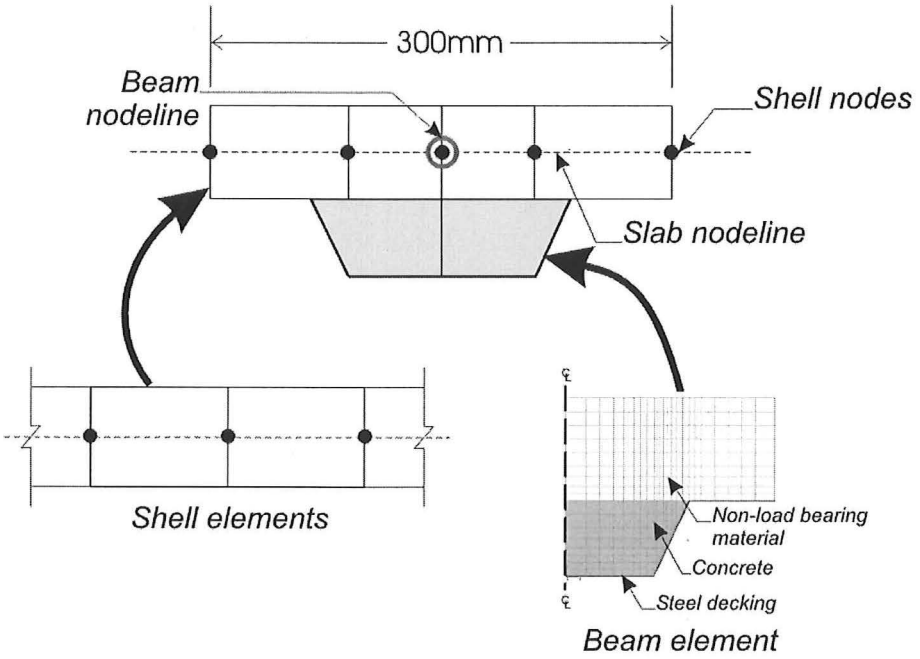

Figure 7-25: Discretisation of the Hibond slab cross section with the shell and beam elements.

Figure 7-25 shows the finite element discretisation of the slab cross section. Only a slice of the actual width of the slab was analysed to reduce the computational effort. The slab was modelled with beam and shell elements. This model assumed that the shell element acted as the flat section of the slab and the beam elements represented the troughs of the slab. The

shell elements were 65mm thick and reinforced with a single layer of mesh, spanning in the same direction as the troughs. The centroid of the reinforcing mesh was positioned at mid-depth of the shell element, which provided a 30mm clear cover from the top of the slab to the top of the mesh.

The cross section of the beam consists of a thin layer of steel at the bottom surface to represent the steel decking, and concrete material properties (shown in grey) to represent the trough of the slab. The flat section of the slab was also included in the discretisation of the cross section for the purposes of thermal analysis, which will be discussed in section 9.4. In the structural analysis, the flat section of the beam element is modelled with non load-bearing material properties so that it does not contribute to the strength and stiffness of the slab. The beam element is coupled to the shell element by aligning the nodeline of the beam with the nodeline of the shell elements (Figure 7-26).

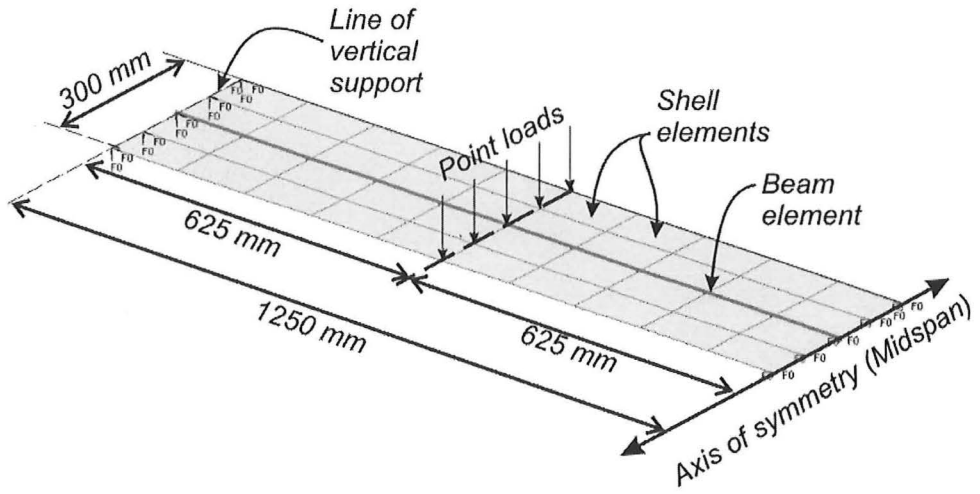

Figure 7-26: SAFIR structural model.

Figure 7-26 shows the SAFIR structural model of the slab. Only half of the full slab length was modelled due to the symmetric load and support conditions. The slab was simply supported at both end supports and was rotationally restrained at the mid-span axis of symmetry to model flexural continuity. Only the width of a single trough (300mm) was modelled. The self weight is imposed in addition to a series of point loads across the width of the slab at quarter span, to represent the point load application in the test. The finite element model assumes full composite action between the steel deck and the concrete and does not account for any slippage between the concrete and the steel deck or with the reinforcing.

7.4.4. Results of analysis

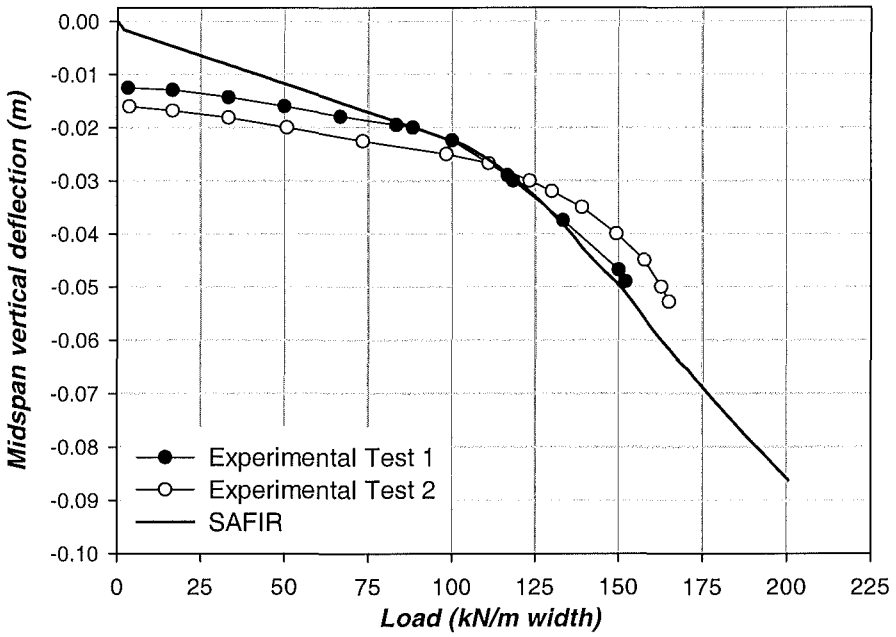

Figure 7-27: Comparison of SAFIR predictions with test results.

Figure 7-27 compares the midspan deflections predicted by SAFIR, with the experimental results. The graph shows that during the initial stages of loading, SAFIR underestimated the deflections of the slab. Under the slabs' self-weight, SAFIR predictd a midspan deflection of only -2mm, compared with the initial deflections of -12.5mm and -16mm in *Test 1* and *Test 2*, respectively. The higher initial deflections of the experimental tests were possibly due to the cyclic tests performed on the slabs prior to the load test. The cyclic tests would have cracked the concrete and broken some of the shear bond between the concrete and the steel deck, causing loss of stiffness of the slab and irrecoverable deformation.

The graph shows that when the loads were increased, SAFIR predicted a linear deflection which converged towards the experimental deflection curves with increasing load. Beyond 85kN/m, the SAFIR results showed very good agreement with the deflections of *Test 1*. After 105kN/m, the deflection rates predicted by SAFIR and *Test 1* increased very substantially due to yielding at midspan of the steel decking at the bottom of the trough. The loading phase of *Test 1* ceased at 152kN and the test slab was subsequently unloaded. The unloading phase of the slab was not modelled with SAFIR and the analysis proceeded until failure occurred at 201kN/m when the concrete at midspan crushed, resulting in a plastic hinge forming at midspan.

The deflections of *Test 2* were consistently larger than *Test 1* during the initial loading phase, but were smaller after yielding of the steel decking. The slab in *Test 2* had a slightly higher yield load of 111kN/m compared with 105kN/m of *Test 1*. Even though both of the tested slabs were identical, they had different deflection curves and ultimate loads, possibly due to the different stiffnesses in the slab after the cyclic tests which were performed earlier. The analysis with SAFIR showed good agreement with the deflections of *Test 1* but showed a slight difference compared with *Test 2*.

7.4.5. Conclusions

The analysis of the one-way composite slab with SAFIR showed good agreement with the experimental results. The analysis showed that the load-deflection characteristics and the load capacity of the composite slab can be predicted with a reasonable level of accuracy by coupling the beam elements to the shell elements.

7.5. Conclusions

- The SAFIR shell element looks good for predicting the behaviour of two-way slabs at ambient temperature.
- The SAFIR shell element can be used to predict the ultimate load of a simply supported two-way slab at ambient conditons, accounting for the effects of membrane forces and material and geometrical non-linearity.
- The analysis of the one-way composite slab using SAFIR shell and beam elements showed good agreement with experimental results.

8. 3D MODELLING OF TWO-WAY SLAB BEHAVIOUR UNDER FIRE CONDITIONS

8.1. Introduction

This chapter presents the 3D modelling of two-way reinforced concrete slabs under fire conditions with the SAFIR shell element. The purpose of the modelling is to study the behaviour of two-way reinforced concrete slabs under fire conditions using the SAFIR shell element. The slab is modelled with different finite element mesh sizes and different levels of precision to investigate their effects on the predicted results. The effects of different concrete tensile strengths and the unheated outer edges are also investigated. The results of the 3D analyses are compared with the experimental results in Chapter 9. Modelling of slabs with different support conditions is presented in chapter 10.

8.2. Slab properties

The properties of the slab are based on one of the tested flat slabs, the D147 slab, described in Chapter 6 and are identical to those in section 7.2. The slab was loaded with a constant uniformly distributed load of 5.4kPa and was exposed to the ISO fire for up to four hours or until the slab failed, whichever occurred first.

Slab geometry	
Length, L_y	4.16m
Width, L_x	3.16m
Slab thickness, h	100mm
Concrete properties	
Compressive strength (ambient temperature) f'_c:	36 MPa
Maximum concrete tensile strength, f_t	3.0 MPa ($0.5\sqrt{f'_c}$)
Concrete model (thermal and mechanical):	Siliceous aggregate (EC2, 1995)
Concrete cover, c_c	25mm
Reinforcing steel properties	
Reinforcing mesh	198mm^2/m in both directions
Yield strength (ambient temperature), $f_{y,o}$:	565 MPa
Steel model (thermal and mechanical):	Hot-rolled steel (EC2, 1995)
Loads	
Self weight	2.4 kPa
Live load	3.0 kPa
Total applied load	5.4 kPa

8.3. Finite element model

8.3.1. Thermal model

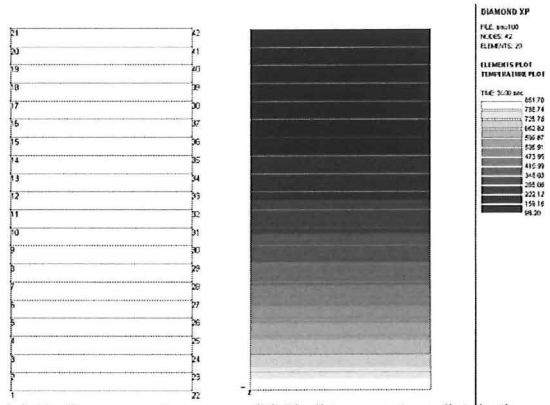

(a) Shell cross section (b) Shell temperature distribution

Figure 8-1: Cross section of the slab for determining the temperature distribution in the shell.

The temperatures across the shell elements were determined from the thermal analysis of a slice of the slab. The thermal analysis was performed by discretising the cross section with four node quadrilateral elements (Figure 8-1a). Figure 8-1b shows the typical temperatures in the 100mm slab when it is subjected to uniaxial heat flux from the bottom of the slab. The analysis assumes that the temperatures only vary across the thickness and do not vary in the longitudinal direction. The reinforcing bars were not included in the thermal analysis and were assumed not to affect the temperature distribution of the concrete. The temperatures of the reinforcing bars were assumed to be equal to the temperatures of the concrete at the level of the slab.

8.3.2. Structural model

The structural model is based on the model in section 7.2.3. A quarter of the slab was analysed due to the symmetric load and support conditions. The effect of different number of elements will be discussed in section 8.5.

8.3.3. Assumptions of the analyses

In addition to the other assumptions of the SAFIR analyses described in chapter 4, the following assumptions are made in the analyses:

- The reinforcing bars of the tested slabs were approximated with a smeared layer of steel in the shell elements.

- The analysis assumes that the horizontal movements of the slabs at the supports were unrestrained. In the actual tests, there was some friction between the slab and the steel clamps which held the corners down.
- The loads from the water drums in the experimental tests were approximated as a uniformly distributed surface load in the analyses.

8.4. Slab temperatures

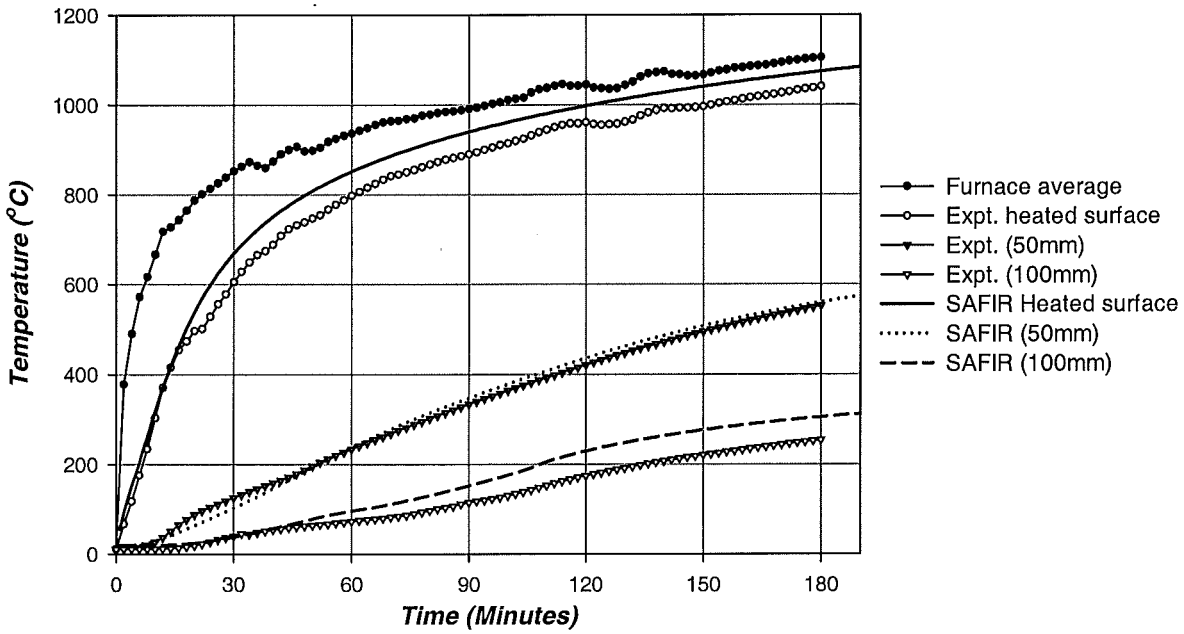

Figure 8-2: Comparison of temperatures from fire test and SAFIR analysis for a 100mm thick slab exposed to the ISO fire.

Figure 8-2 shows the variation of the temperatures across the depth of the slab. The temperatures calculated with SAFIR were compared with the temperatures obtained from the fire tests of the HD12 flat slab, from Chapter 6. The variation of the temperatures with time in the fire was plotted at the heated surface, mid-depth and the unheated surface. The graph shows that at the heated surface, the SAFIR predictions matched the measured experimental temperatures very closely during the first 20 minutes. After that, the measured temperatures dropped off slightly and lagged behind the SAFIR temperatures for the remainder of the fire by approximately 30 to 50 degrees. Nevertheless, the predicted temperatures and the measured temperatures showed very similar trends.

At mid-depth (50mm), the SAFIR temperatures showed very good agreement with the measured temperatures throughout the entire fire duration. On the unheated surface (100mm),

the predicted temperatures showed very good agreement with the measured temperatures during the first 45 minutes. After that, SAFIR predicted slightly higher temperatures than the measured temperatures for the remainder of the fire.

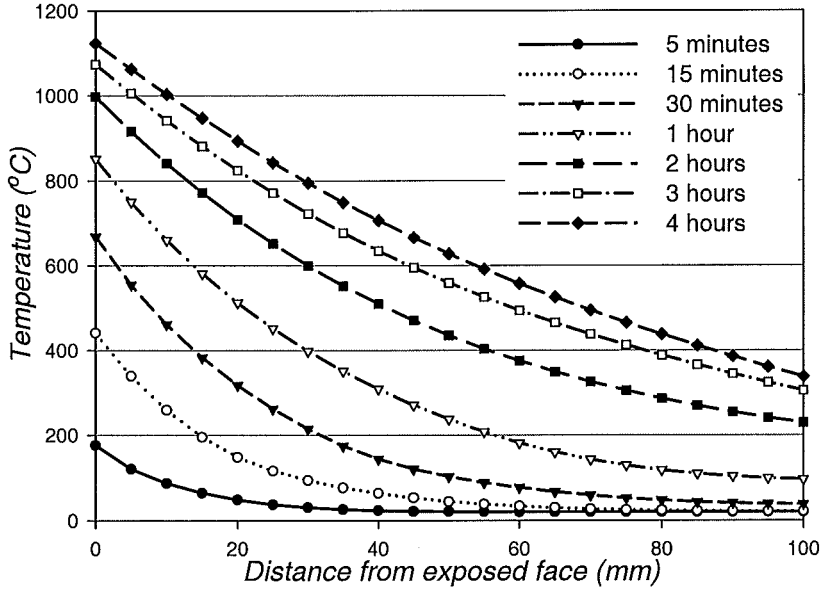

Figure 8-3: Temperature distributions across the 100mm slab, calculated with SAFIR.

Figure 8-3 shows the temperature distributions across the 100mm thick slab at various times during the ISO fire exposure. The temperatures were determined with the SAFIR analysis. The graph shows very high temperature gradients across the slab during the first hour. After that, the steepness of the temperature gradients decreased and approached a linear distribution by 4 hours.

8.5. Effect of number of elements

The section presents the analysis of the slab with SAFIR is conducted with a different number of shell elements and mesh sizes. The purpose of this is to investigate the effect of the different number of elements on the predictions of the slab behaviour at elevated temperatures. The three different grid sizes are shown below (Figure 8-4 to Figure 8-6). The slabs were analysed with zero concrete tensile strength and with a precision of 0.010.

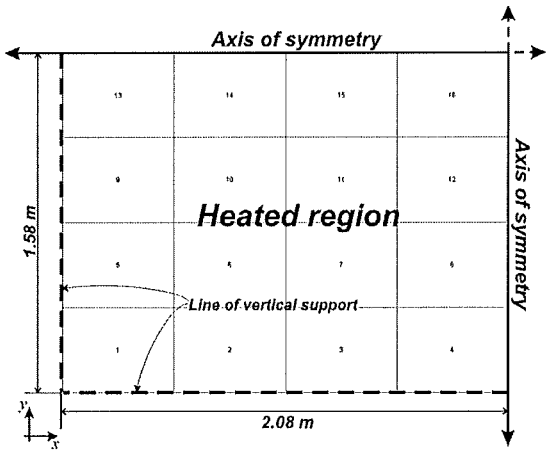

Figure 8-4: 4 x 4 mesh

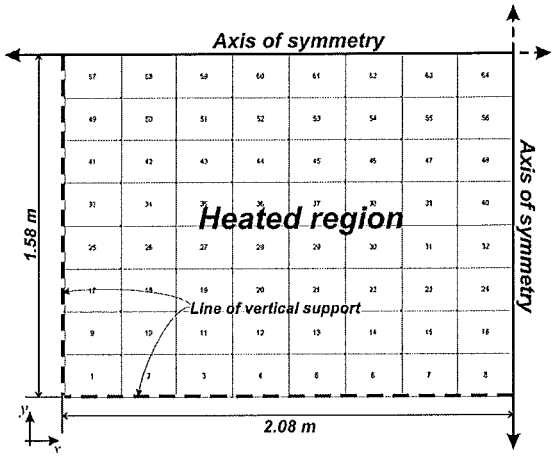

Figure 8-5: 8 x 8 mesh

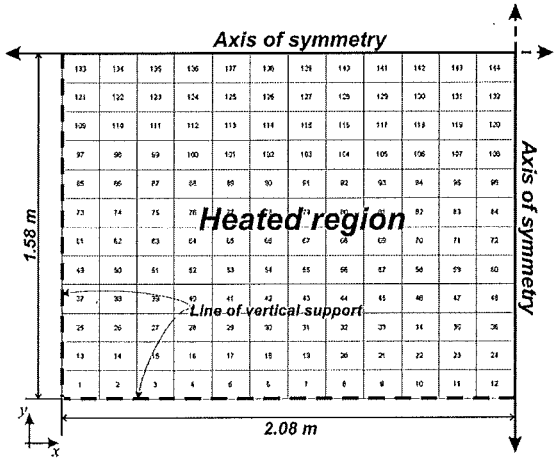

Figure 8-6: 12 x 12 mesh

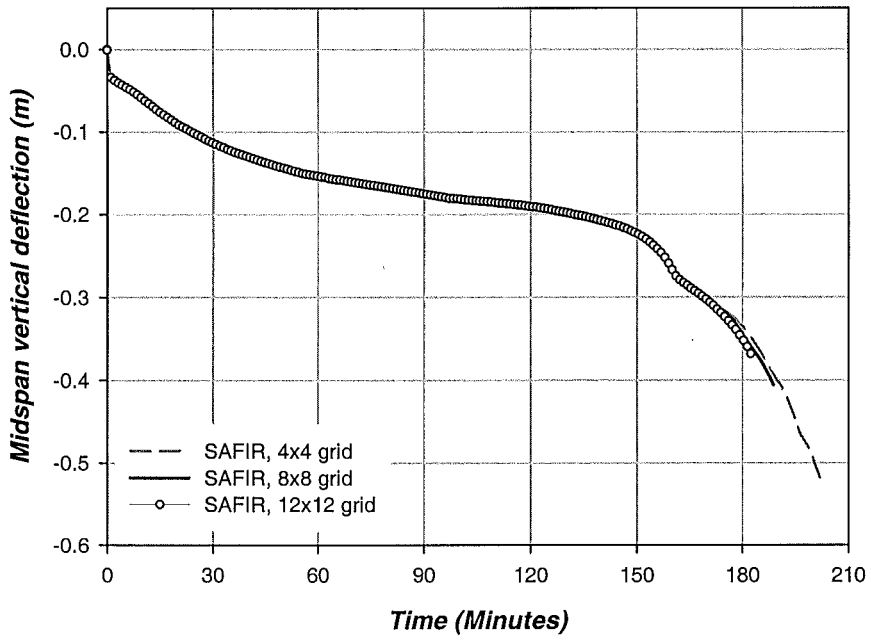

Figure 8-7: Comparison of midspan deflections with different grid resolutions.

Figure 8-7 compares the midspan vertical deflections calculated with different number of elements in the finite element mesh. The graph shows that the deflections of the slab, calculated with the different grid sizes, were almost identical. The effects of the different grid sizes only appeared at the end of the analyses, as the slabs approached failure.

The slabs had an initial midspan deflection of -34mm. As the fire progressed, the slabs deflected downwards very rapidly and appeared to asymptote to a limiting deflection of -200mm. However, after 125 minutes, the deflection rate of the slabs increased again, leading to runaway failure. The failure times predicted with the 4x4, 8x8 and 12x12 grids are 202 minutes, 189 minutes and 185 minutes, respectively. The corresponding deflections at failure of the slabs were -502mm, -406mm and -385mm, respectively. Failure of the slabs occurred due to rupture of the reinforcing bars at midspan. The analyses showed that as the number of elements was increased, the times to failure and the maximum deflections at failure, decreased. With a higher number of elements, failure occurred earlier when rupture of the reinforcing was detected with the higher number of integration points. With fewer elements, the integration points had a sparser distribution and did not detect rupture of the reinforcing bars until a later stage.

The analyses showed that the coarse finite element grid produced deflections consistent with the finer meshes. The effect of the different number of elements only appeared when the slabs approached failure, with the coarser grid predicting higher failure times at larger deflections. The coarser grid has the advantage of requiring only a smaller amount of computer memory and a faster run time. But, in order to predict failure of slab accurately, a finer grid would be required.

8.6. Effect of concrete tensile strength

This section investigates the behaviour of the slab with different values of concrete tensile strength. The concrete tensile strength is varied from zero to 3MPa ($0.5\sqrt{f'_c}$). The analysis of the slab is performed with the 12x12 finite element mesh.

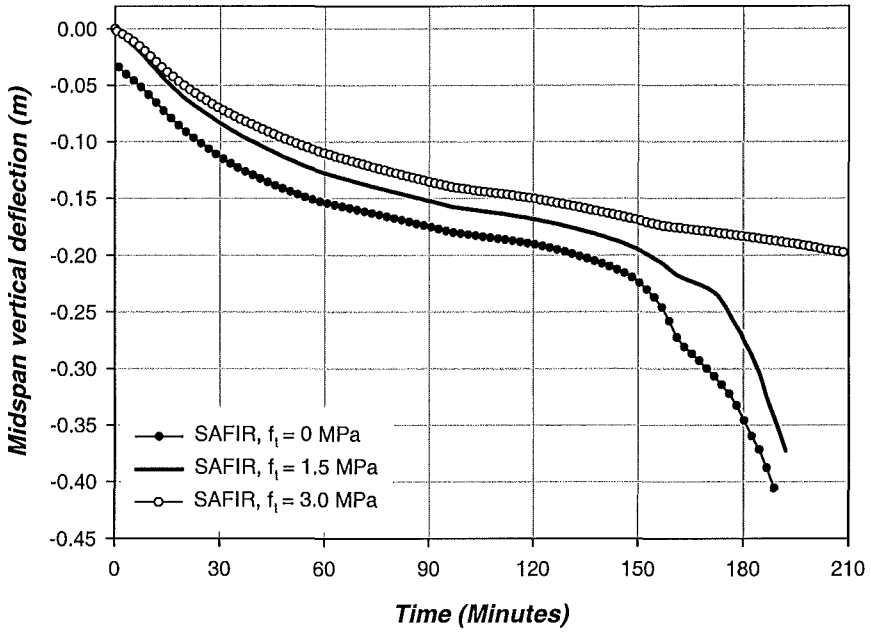

Figure 8-8: Midspan vertical deflections with different values of concrete tensile strength

Figure 8-8 shows the effect of different values of concrete tensile strength on the deflections of the slab. The graph shows that with zero concrete tensile strength, SAFIR predicts a deflection of -34mm at the very start of the fire, due to the gravity loads on the slab. With 1.5MPa and 3MPa concrete tensile strength, SAFIR predicts a much lower initial deflection of -3mm. As the fire progressed, the slab with 0MPa and 1.5MPa tensile strength produced similar deflection trends. The slabs deflected at a very gradual rate during up to 150 minutes. Beyond that, the deflection rates of the slabs increased markedly and runaway failure occurred.

The graph shows that with 3MPa concrete tensile strength, the deflection trend of the slab was very similar to the slab with 1.5MPa during the first 10 minutes of the fire. After that, the deflection curves started to diverge. With f_t equal to 3MPa, the deflections of the slab asymptote towards -200mm and did not show a runaway failure as shown by the slabs with zero and 1.5MPa concrete tensile strength.

As with the analysis of the slab at ambient conditions (Section 7.2.6), the slab with 3MPa ($0.5\sqrt{f'_c}$) concrete tensile strength showed much lower deflections at fire conditions, particularly at the advanced stages of the fire. The reason for this, as demonstrated by the earlier analyses in section 7.2.6, is that the concrete model is very ductile in tension, especially for high levels of tensile strength.

8.7. Membrane traction distributions

This section investigates the distribution of the membrane tractions in the slab during the fire exposure. The traction forces are shown for a slab analysed with zero concrete tensile strength with a 12 x 12 finite element grid.

Figure 8-9 to Figure 8-14 show the distribution of the membrane tractions at the bottom quarter of the slab at various times during the fire. Column (a) shows the distribution of the principal tractions. The dark and thick arrows represent compression tractions and the thinner arrows represent tension tractions. Column (b) shows the distribution of the N_x tractions in the longitudinal direction at midspan and column (c) shows the distribution of the N_y tractions in the transverse direction at midspan.

During the initial stages (1 minute), Figure 8-9 shows low tensile tractions in the midspan region and low compression forces at the outer edges of the slab. At this stage, the deflections of the slab were still very small and the loads were mainly resisted by bending action. Ten minutes after the fire started, Figure 8-10 shows that significant membrane forces had formed in the slab with a wide band of compression tractions forming a ring around the edges of the slab. At this stage, the compression tractions in the slab were very low. Figure 8-10b shows that the N_x tractions formed a parabolic distribution in the longitudinal direction. The maximum tension force formed at midspan and decreased with increasing distance from midspan, to compression at the outer edge. In the transverse direction, the N_y tractions had a similar distribution to that of the N_x tractions, but the highest tension force formed 0.7m from the centre. Figure 8-10 shows that the overall tractions in the longitudinal direction were higher than in the transverse direction, due to the narrower span of the slab which resulted in a higher force per unit width.

(a) Principal tractions **(b) Tractions across the long span (Nx)** **(c) Tractions across the short span (Ny)**

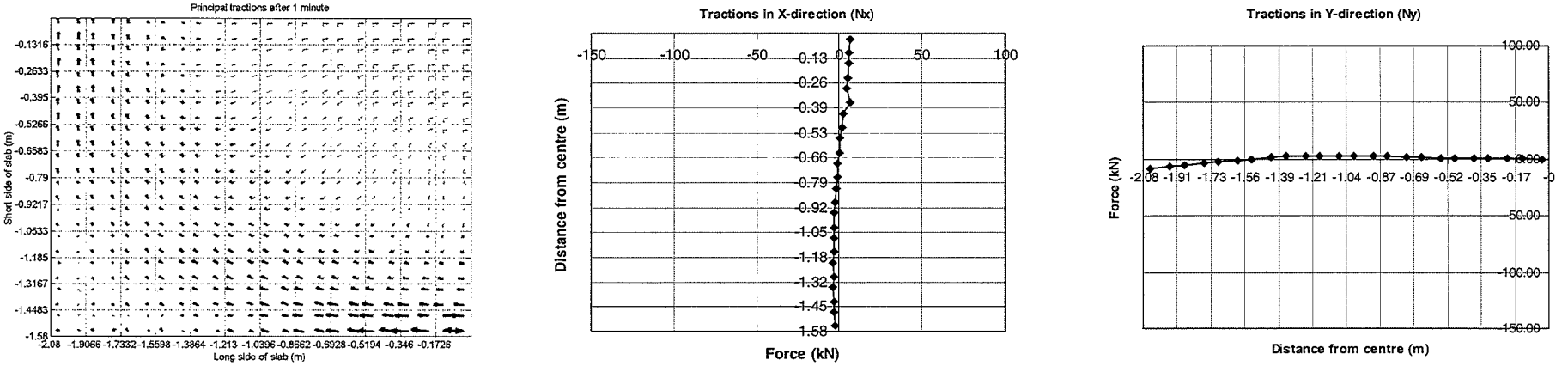

Figure 8-9: Distribution of traction forces at the start of the fire (1 minute)

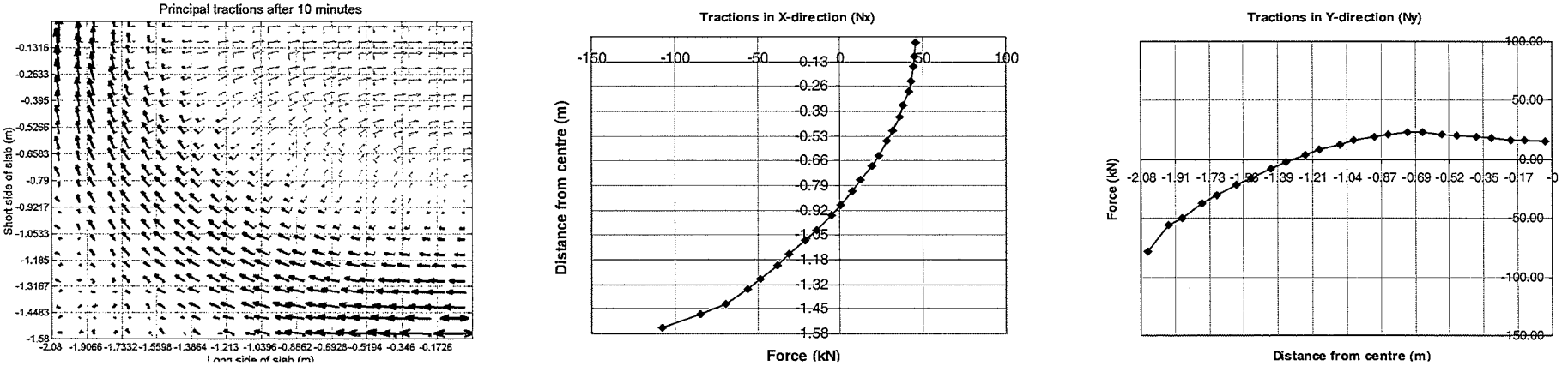

Figure 8-10: Distribution of traction forces after 10 minutes

(a) Principal tractions

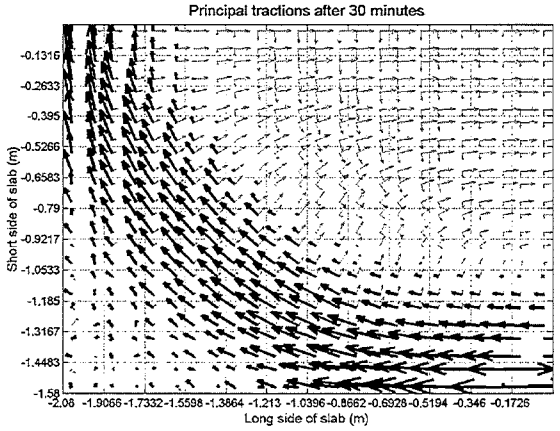

(b) Tractions across the long span (Nx)

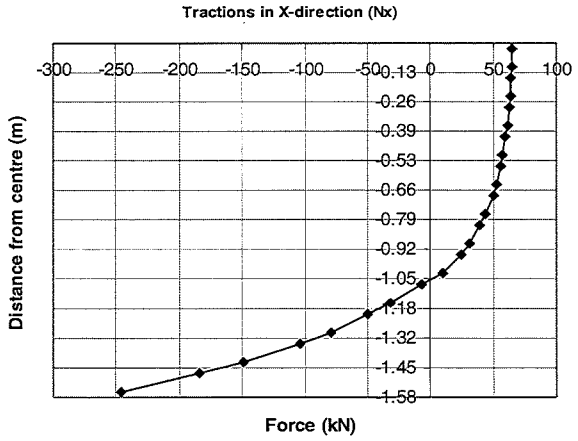

(c) Tractions across the short span (Ny)

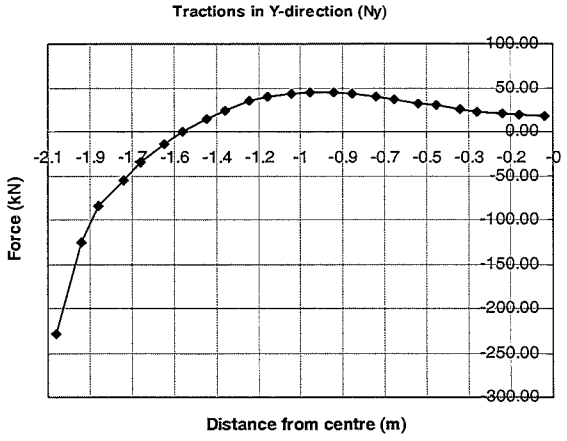

Figure 8-11: Distribution of traction forces after 30 minutes

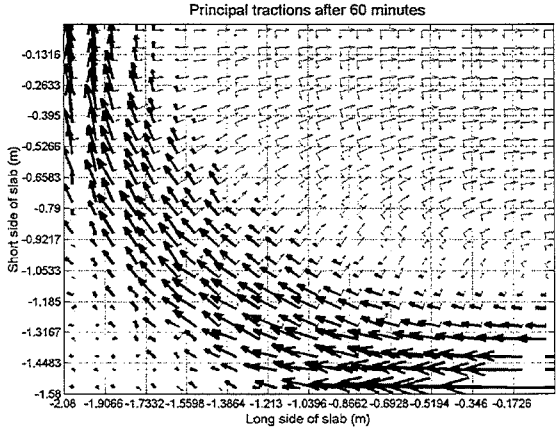

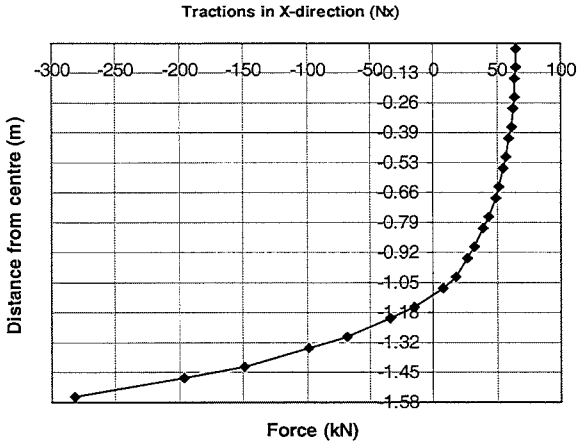

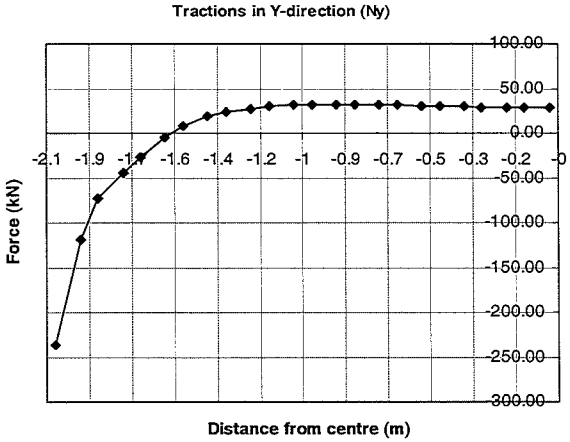

Figure 8-12: Distribution of traction forces after 1 hour

(a) Principal tractions

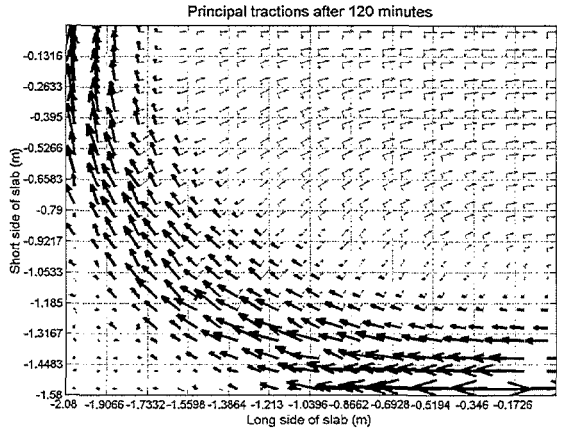

(b) Tractions across the long span (Nx)

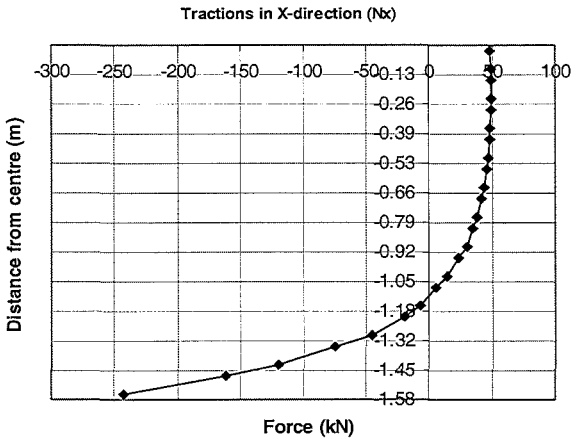

(c) Tractions across the short span (Ny)

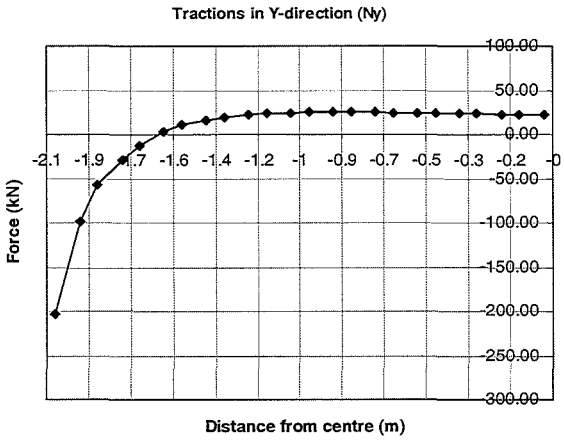

Figure 8-13: Distribution of traction forces after 2 hours

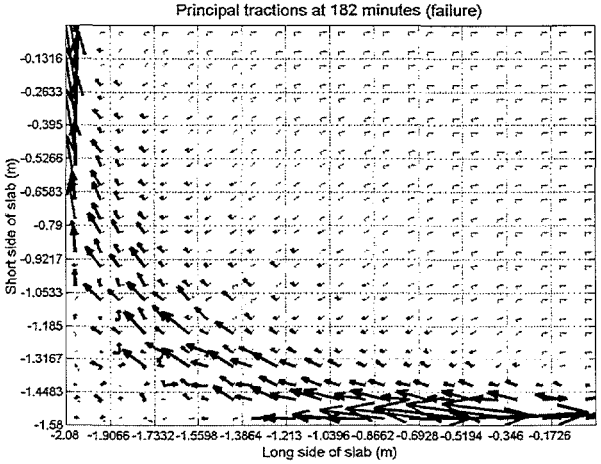

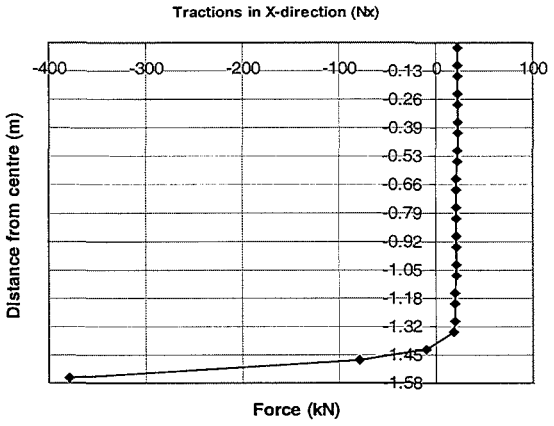

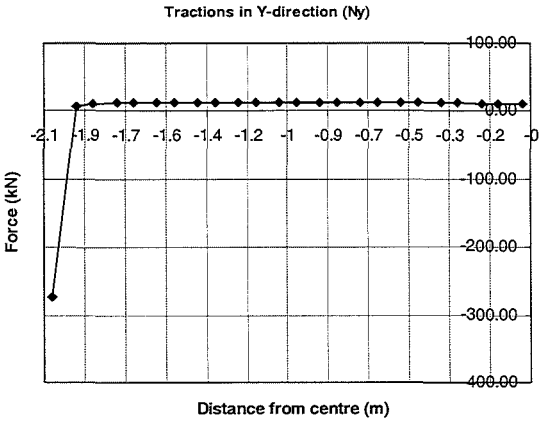

Figure 8-14: Distribution of traction forces at failure (3 hours 2 minutes)

After 30 minutes, the magnitudes of the compression and tension tractions had increased significantly, forming a very well defined compression ring around the edges and a tension field at midspan. In the middle region of the slab, column (b) shows that the N_x tension tractions had formed a uniform distribution at the midspan region. The maximum N_x compression force at the outer edge had increased very significantly from -108kN/m at 10 minutes, to -245kN/m. The N_y tractions showed that the maximum tension tractions formed 1m from the centre of the slab while the maximum N_y compression force at the outer edge had increased from -78kN/m at 10 minutes to -228kN/m.

After 1 hour, Figure 8-12 shows a similar distribution of traction forces to that observed at 30 minutes. Across the short span, the N_y tension tractions had formed a more uniform distribution but the maximum value of the tension tractions had decreased. As the fire progressed up to 2 hours, Figure 8-13 shows that the width of the tension field had widened and the distributions of the tension tractions become more uniform.

At failure of the slab (3 hours and 2 minutes), Figure 8-14 shows that the width of the compression ring had decreased very substantially and had shifted noticeably to the outer edges of the slab. Figure 8-14b and c shows constant tension tractions in the longitudinal and transverse directions and large compression tractions at the edges of the slab. The width of the tension field had increased significantly at this stage. This was caused by the high deflection rate in the last 30 minutes which led to large slab deflections. The reduced width of the compression ring caused the magnitudes of the compression tractions to increase, in order to maintain equilibrium with the tension tractions.

8.8. Variation of membrane tractions with time

The following section discusses the variation of the membrane tractions with time at several locations in the slab. The variation of the membrane tractions in the x and y directions will be plotted at midspan (L/2), quarter span (L/4) and at the support along the middle of the long and short spans, as shown in Figure 8-15.

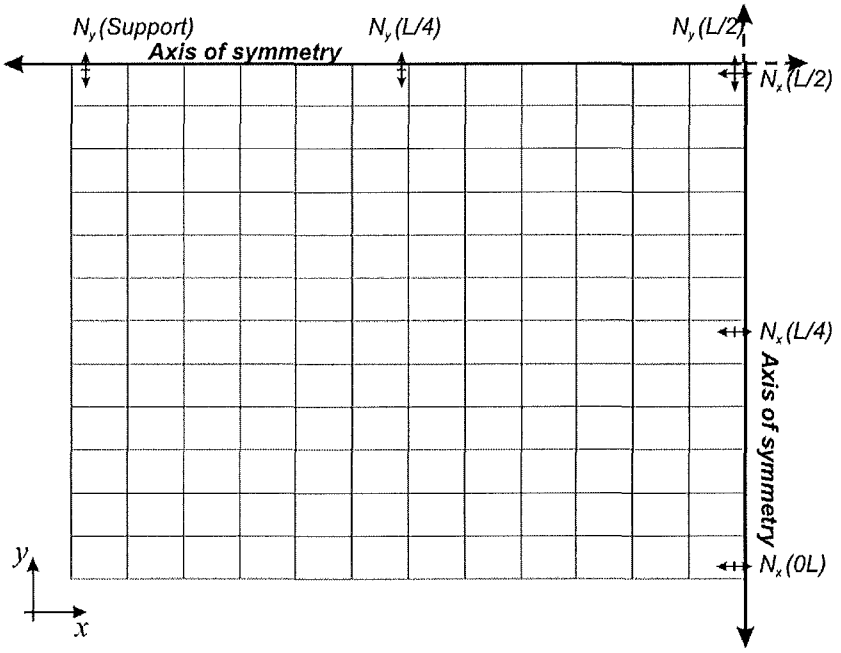

Figure 8-15: Locations where the membrane tractions are plotted.

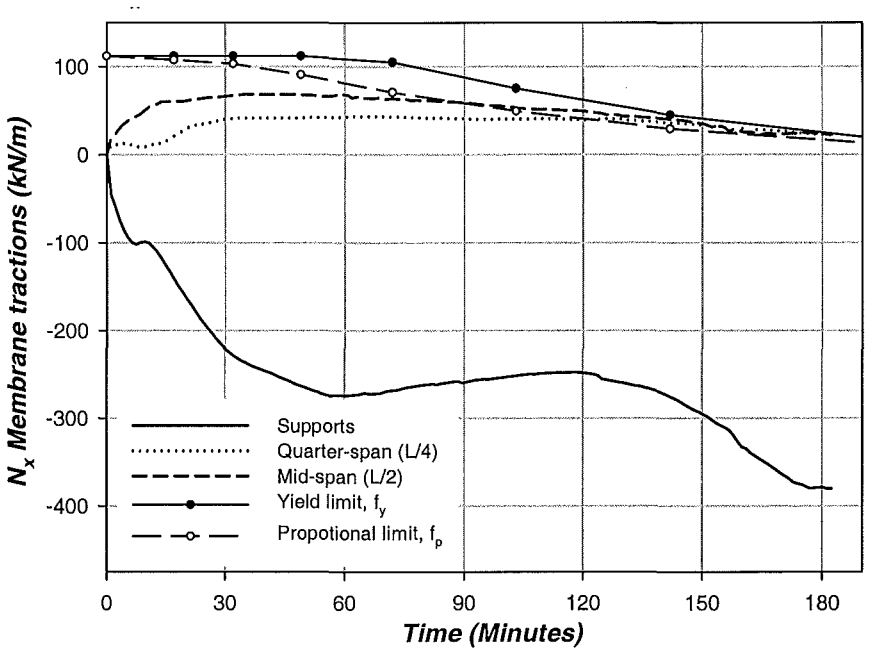

Figure 8-16: Variation of the N_x tractions in longitudinal direction, across the long span.

Figure 8-16 shows the variation of the N_x tractions at the support, midspan (L/2) and quarter span (L/4) of the slab. Also plotted on the graph are the elastic proportional and yield tensile limits of the tractions which decrease with time in the fire due to the increasing temperatures.

At midspan, the tension tractions increased very rapidly, reaching a peak of 68kN/m after 37 minutes. The tension tractions remained constant and started to decrease after 65 minutes. At quarter-span, the tension tractions remained relatively constant during the first 15 minutes of the fire. The tractions increased slightly and levelled off at 30 minutes. The tractions remained constant until 120 minutes, when they started to decrease. The tractions at L/2 and L/4 exceeded the proportional limits at 90 minutes and 123 minutes, respectively, and decreased between the envelopes of the yield and proportional limits during the final stages.

Figure 8-16 shows that compression tractions formed very rapidly at the edges of the slab during the initial stages of the fire, reaching a peak of -274kN/m after 1 hour. The compression tractions dropped slightly after reaching its peak and increased again during the last hour, reaching a second peak of -382kN/m at 3 hours. The increase of the compression tractions during the last 30 minutes was caused by the increased deflection rate which caused the size of the tension field to increase and the width of the compression ring to decrease (refer Figure 8-14).

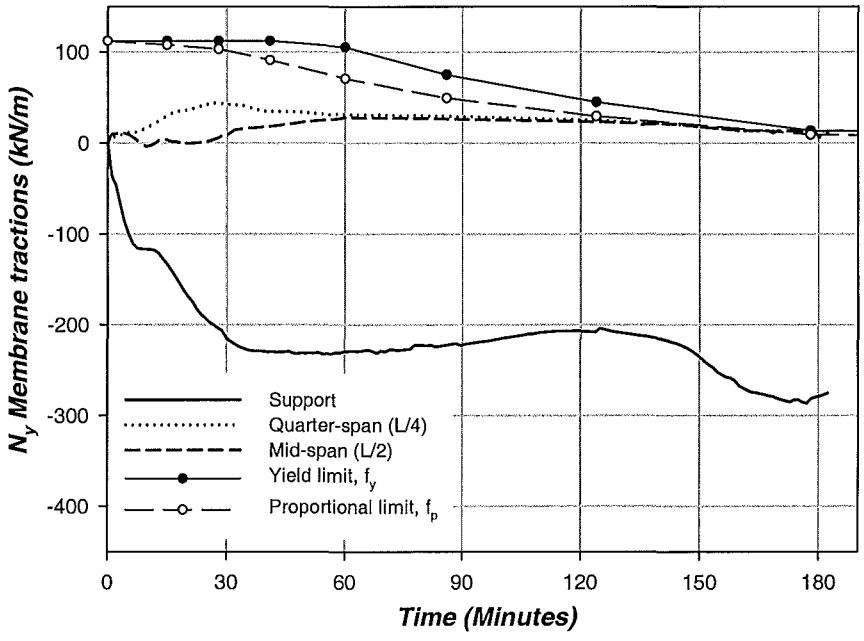

Figure 8-17: Variation of the N_y tractions in transverse direction, across the short span.

Figure 8-17 shows the variation of the N_y tractions in the transverse direction at midspan. The tractions were plotted at the supports, midspan (L/2) and quarter-span (L/4). The graph shows that during the initial stages, the tractions at quarter-span were much higher than the midspan tractions, which is the opposite of the N_x tractions which showed the midspan tractions increase first. After 60 minutes, the tension tractions formed a uniform distribution (See Figure 8-12c) which resulted in equal tractions at midspan and quarter-span. During the final stages of the fire, the tension tractions at quarter-span and midspan reached the proportional limit at 140 minutes, and continued to decrease within the limits of the yield and proportional limits. The N_y tension tractions reaching the proportional limit at 140 minutes caused the deflection rate of the slab to increase very markedly (See Figure 8-8). The increased deflections caused the size of the tension field to increase and the width of the compression ring to decrease. Consequently, the compression tractions in both Y and X directions increased again during the last 30 minutes of the fire.

8.9. Effect of the thermal strain and mechanical strains on the slab behaviour

This section investigates the effects of thermal strain and the gravity loads on the behaviour of the slab. The total strains in SAFIR are expressed by the following equation:

$$\varepsilon_{total} = \varepsilon_{\sigma} + \varepsilon_{cr} + \varepsilon_{i} + \varepsilon_{th}$$

where:

ε_{total} = Total strain

ε_{σ} = Stress related strain (Mechanical strain)

ε_{cr} = Creep strain

ε_{i} = Initial strain

ε_{th} = Thermal strain

The creep strains have been implicitly included in the stress-strain curves of the material properties and are incorporated with the mechanical strains. The initial strains are due to other forces such as external prestressing. For the slabs in this discussion, the initial strains are zero since the slabs are not subjected to other external forces. The effects of the thermal strain and the mechanical strain on the behaviour of the slab are considered separately in this section.

In order to investigate the effects of the thermal and mechanical strains, the slab will be analysed with their mechanical and thermal strains suppressed in separate analyses. To consider the effects of the thermal strains only, the mechanical strains were suppressed by analysing the slab without the gravity loads during the fire.

8.9.1. Effect of thermal strains

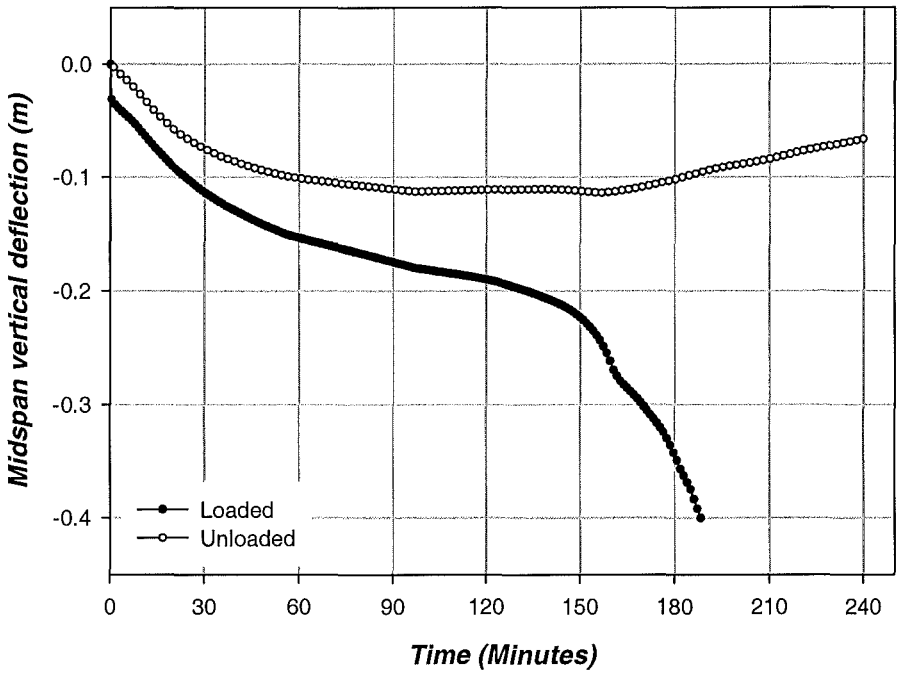

Figure 8-18: Effect of thermal strains on the slab behaviour.

Figure 8-18 shows the effect of the thermal strain on the behaviour of the two-way slab when it was exposed to the ISO fire. An unloaded slab was analysed to minimise the mechanical strains and to show the effect of the thermal expansion in the slab. The deflections of the unloaded slab were compared with the loaded slab. Both slabs were analysed with zero concrete tensile strength.

The graph shows that without any applied loads, the slab had zero deflections at the start of the fire while the gravity loads imposed an initial deflection of -31mm on the loaded slab. The graph shows that during the initial stages, the unloaded and loaded slabs deflected with a similar trend, indicating that the deflections of the slab during the initial stages were dominated by the thermal strains. The deflections were caused by the non-linear thermal expansion across the depth of the concrete slab. Between 60 and 160 minutes, the deflections of the unloaded slab levelled off while the deflections of the loaded slab continued to increase. At 160 minutes, the deflection rate of the loaded slab increased very significantly due to runaway failure while the unloaded slab started to deflect upwards.

8.9.2. Effect of suppressing the thermal strains

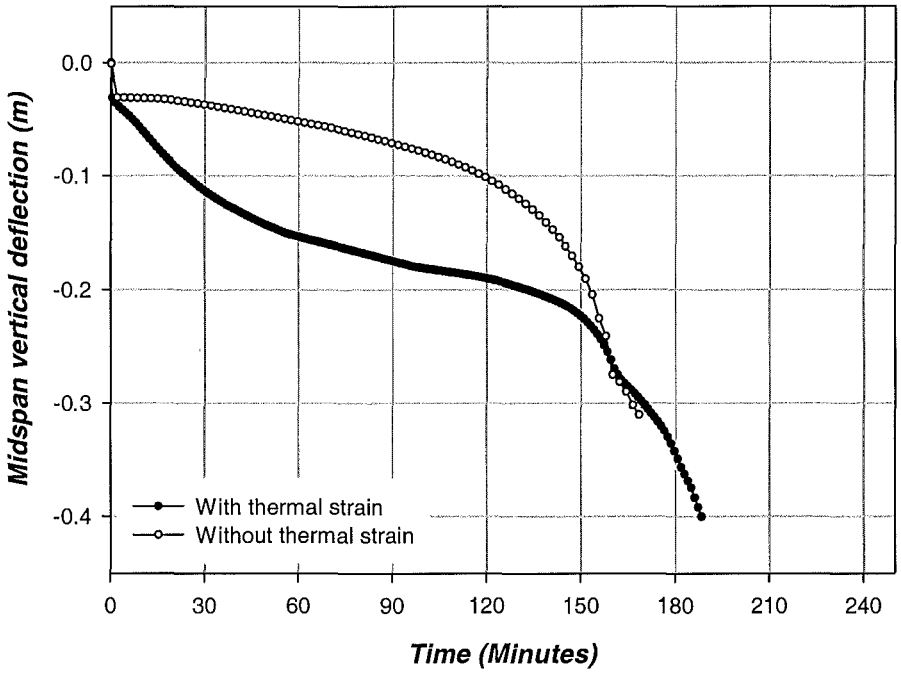

Figure 8-19: Effect of the suppressing the thermal strains on the slab behaviour.

Figure 8-19 shows the effect of suppressing the thermal strains on the behaviour of the slab. The slab with the thermal strains suppressed was compared with the slab with both thermal strains and gravity loads. The graph shows that the slabs with and without the thermal strains had similar deflections at the very start of the fire. As the fire progressed, the slab with the thermal strains started to deflect downwards very rapidly due to thermal bowing. The slab without the thermal strains initially showed very small deflections, but they later increased at an exponential rate, eventually leading to runaway failure and collapse at 169 minutes. The increasing deflections were due stiffness degradation of the reinforcing steel caused by the temperature effects. Runaway failure occurred when the slab lost significant stiffness and strength.

This comparison has shown that the thermal strains dominate the deflections of the slab during the initial stages due to the steep thermal gradients in the slab, shown in Figure 8-3. As the fire progresses, the thermal gradients become less steep and reduced the thermal bowing deflections, as seen in Figure 8-18. At the advanced stages of the fire, the stiffness of the reinforcing steel decreases as a result of the thermal effects. Runaway deflections occur at the final stages when the reinforcing steel has lost significant stiffness and strength.

8.10. Effect of the outer edges on two-way slab behaviour in fire conditions

In this section, the effects of the outer edges in the tested slabs are analysed and compared with the slab without the outer edges analysed in section 8.6. The overall dimensions of the slab are 3.3m by 4.3m, with a clear span of 3.16m by 4.16m. The clear span of the slab is the fire-exposed region of the slab while the outer edges, located over the line of vertical support, measure 70mm wide and is not heated. The unheated outer edges of the slabs may also be considered to represent the edges of a slab supported over a fire-protected beam in a real structure.

The heated region of the slab is loaded with its self weight and a live load of 3.0kPa while the outer edge is only loaded with its self weight. The slab is reinforced with D147 mesh and has a concrete compressive strength of 36MPa. A higher amount of reinforcement was modelled in the outer edges to represent the perimeter trimmer bars that were present in the tested slab.

8.10.1. Finite element structural model

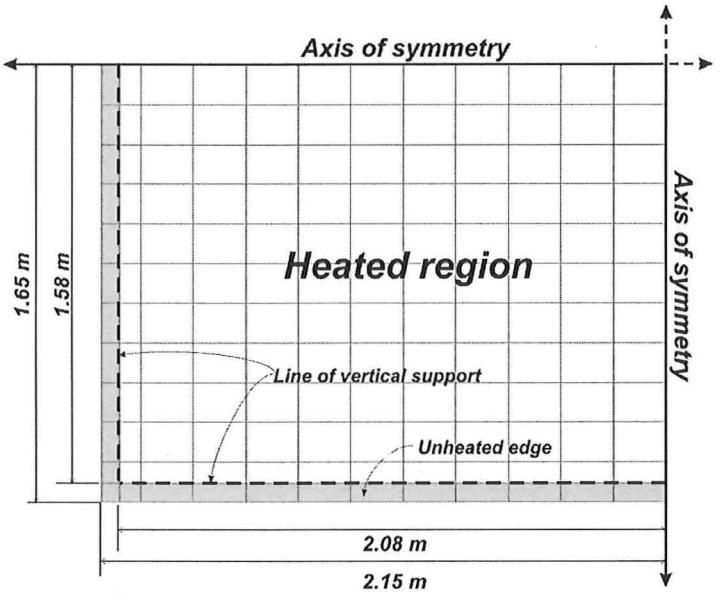

Figure 8-20: Finite element discretisation of the slab with outer edges.

Figure 8-20 shows the SAFIR finite element discretisation of the slab, which consists of 144 elements. A quarter of the slab was analysed due to the symmetric loading and support conditions. The light coloured mesh represents the heated section of the slab while the shaded region represents the unheated edges of the slab. The line of vertical support at the outer perimeter is shown by the dashed line.

8.10.2. Midspan vertical deflections

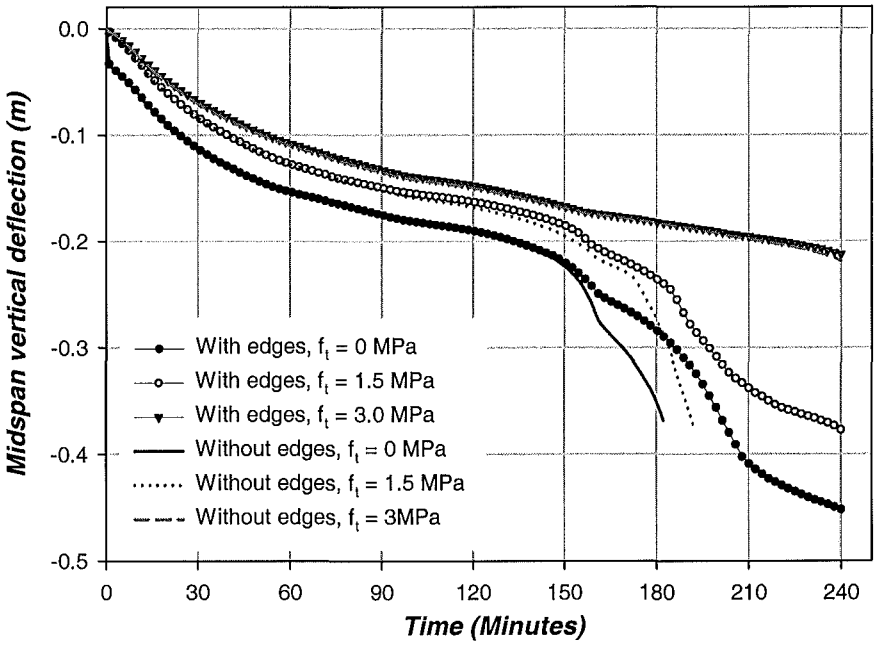

Figure 8-21: The effect of the outer edge elements on the midspan deflections.

Figure 8-21 shows the effect of the outer edges on the deflections of the slabs. The deflections of the slabs, with and without the outer edges are plotted for different values of concrete tensile strength.

Figure 8-21 shows that the edges did not have any effect on reducing the deflections during the initial stages which were caused by thermal bowing. They only had an effect on the deflections at the advanced stages, after 150 minutes. The effect of the outer edges appeared only for the slabs which had concrete tensile strength of 0MPa and 1.5MPa. The slabs without the outer edges deflected more rapidly after 150 minutes and failed after 180 hours. The outer edges enabled the slabs to survive the fire for up to 4 hours without collapse. Between 180 minutes and 210 minutes, the deflection rates of both slabs increased very markedly but reduced again during the final 30 minutes. In the slab with 3MPa concrete tensile strength, the outer edges had no effect on the deflections as the slabs with and without the outer edges had identical deflection curves.

8.10.3. Tractions

This section shows the distribution of the traction forces during the fire in the slab with the outer edges. The tractions of the slab with zero concrete tensile strength are shown.

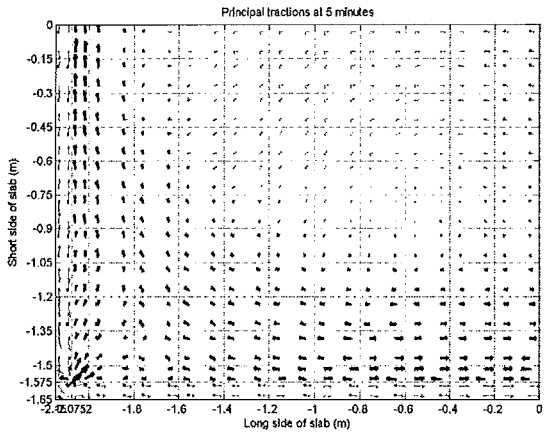

(a) 5 minutes

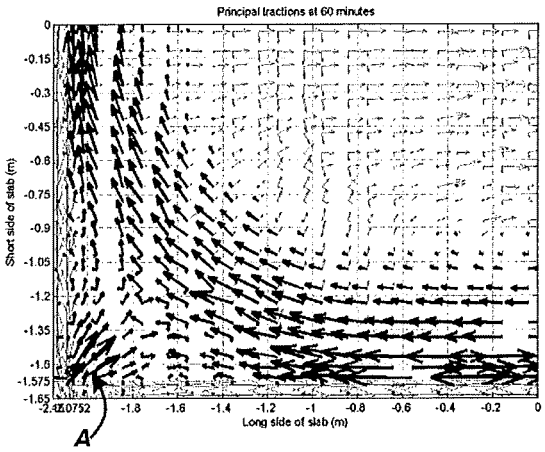

(b) 1 hour

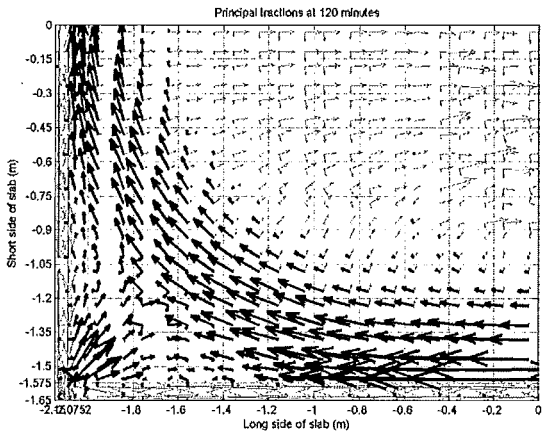

(c) 2 hours

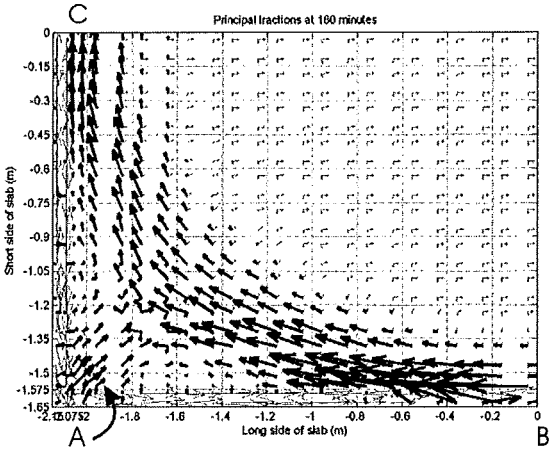

(d) 3 hours

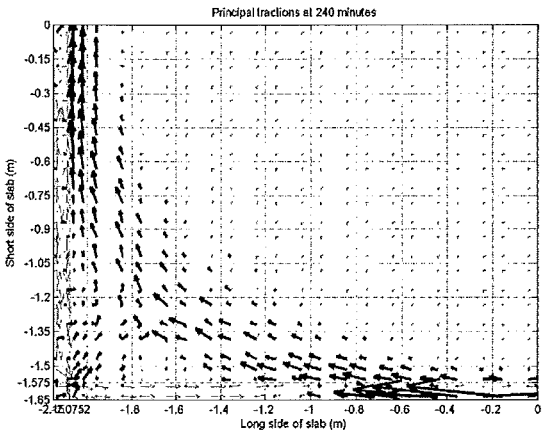

(e) 4 hours

Figure 8-22: Distribution of the tractions in the slab with the outer edges during the ISO fire.

Figure 8-22 shows the distribution of the principal tractions in the slab with the outer edges during the ISO fire. The thick dark arrows represent the compression tractions and the light arrows represent tension tractions. The traction distribution during the fire is similar to the slab without the outer edges, shown in section 8.7. Five minutes after the start of the fire, very small membrane forces formed in the slab. As the fire developed, a tension field formed at the midspan region where the maximum deflection occurred. The tension field was surrounded by a compression ring on the outer perimeter of the heated region.

During the first two hours of the fire, the compression ring was confined to the heated region by a thin tension ring which formed at the unheated outer edges. This tension ring formed due to the tensile resistance of the unheated outer edges against thermal expansion of the heated central region. The tensile tractions in the outer unheated edges were resisted by the perimeter trimmer bars. Figure 8-22b shows that large compressive forces formed at the corner support (Point A) due to the reaction to the tensile ring restraining the expansion of the heated central region.

After three hours, the width of the compression ring and the magnitude of the reaction forces at the corner of the slab (Point A of Figure 8-22d) had decreased substantially. The compression ring had also shifted to the unheated outer edges along the centre of the long span (Point B) which was previously in tension. Along the centre of the edges of the short span (Point C), the outer edges were still in tension. The magnitude of the tension tractions in the central midspan of the slab had decreased markedly due to the decreasing yield strength of the reinforcing mesh. By four hours, the compression ring had clearly moved to the unheated outer edges of the slab. The magnitudes of the compression tractions at the outer edges and the tension tractions in the middle of the slab had decreased very significantly.

The analyses in this section showed that the unheated outer edges of the slab increased the fire resistance of the slab very substantially. The outer edges did not have any effect on the slab deflections during the initial stages of the fire. However, they significantly reduced the deflections of the slab during the advanced stages of the fire and prevented collapse.

8.11. Conclusions

The analyses of the slabs with the SAFIR shell element have shown that:

- The two-way slab carried the loads in excess of 3 hours in the ISO fire, despite suffering large vertical deflections and significant loss of flexural strength. The high fire resistance of the slab was due to tensile membrane action.
- The coarser finite element mesh predicted higher fire resistances than a finer mesh.
- The deflections of the lightly reinforced slab were sensitive to the value of concrete tensile strength used in the analysis.
- Membrane forces formed in two-way slabs as a result of the geometry of deformations as the slabs deflect downwards. The membrane forces comprised a tensile field at the midspan region, surrounded by a compression ring at the outer edges. The magnitudes of the membrane forces decreased during a fire, due to strength degradation of the reinforcing steel.
- The initial deflections of the slab were attributed to thermal bowing of the slab as a result of the non-linear thermal expansion of the concrete. At the advanced stages of the fire, the deflections were due to stiffness degradation of the reinforcing caused by the increasing temperatures in the steel.
- SAFIR predicted that failure occurred when the reinforcing steel at midspan ruptured.
- The fire resistances of the slabs were further increased by the outer edges of the slabs. The outer edges prevented runaway failure during the advanced stages of the fire.

9. COMPARISON OF SAFIR MODELLING WITH TEST RESULTS

9.1. Introduction

This chapter presents the 3D modelling of several of the tested slabs. Five of the tested slabs, comprising the three solid flat slabs, the Hibond and the Speedfloor slab are modelled. The purpose of this is to predict the behaviour of the tested slabs during the fire test. The different slabs are modelled with several different finite element models using the SAFIR shell and beam elements. The results of the SAFIR modelling will be compared with the experimental test results.

9.2. Two-way behaviour of the D147 slab under fire conditions

This section compares the SAFIR analyses of the D147 slab with the experimental results. The comparison will be performed using the SAFIR structural models with and without the outer edges which have been presented and discussed in sections 8.10 and 8.6, respectively.

9.2.1. Comparison of the test results with the SAFIR analyses without the outer edges

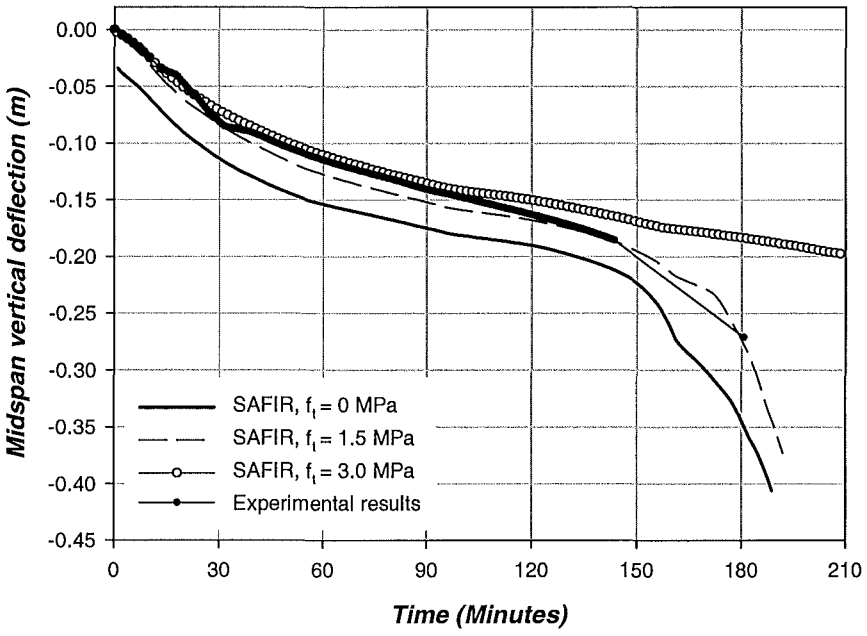

Figure 9-1: Comparison of the experimental results with the SAFIR analyses without the outer edges.

Figure 9-1 compares the experimental results with the SAFIR predictions using the model without the outer edges. The slab was analysed with different values of concrete tensile strength, ranging from 0MPa to 3MPa.

The graph shows that with zero tensile strength in the concrete, the analysis results were consistently larger than the experimental results throughout the entire fire duration. The deflections predicted by SAFIR were similar to the experimental results, showing a high deflection rate during the first 30 minutes, followed by a gradual deflection rate up to 150 minutes and finally increasing again from 150 minutes to 180 minutes. The SAFIR analysis stopped at 182 minutes when the reinforcing steel at midspan ruptured. The larger deflections predicted by SAFIR were attributed to the slab being fully cracked and being more flexible.

With a concrete tensile strength of 1.5MPa, SAFIR showed good agreement with the tested slab throughout the entire fire duration. SAFIR predicted low deflections before the fire started, when the concrete was uncracked, followed by thermal bowing deflections during the initial stages of the fire, leading to final failure of the slab at 189mins.

With a concrete tensile strength of 3MPa, the deflections predicted by SAFIR showed good agreement with the experimental test results during the first 100 minutes. Beyond that, the deflections started to diverge as the predicted deflections asymptote to -200mm while the experimental deflection rate increased. It shows that the current concrete model with full tensile strength in SAFIR is very ductile in tension as the concrete does not crack sufficiently at the later stages of the fire.

9.2.2. Comparison of the test results with the SAFIR analyses with outer edges

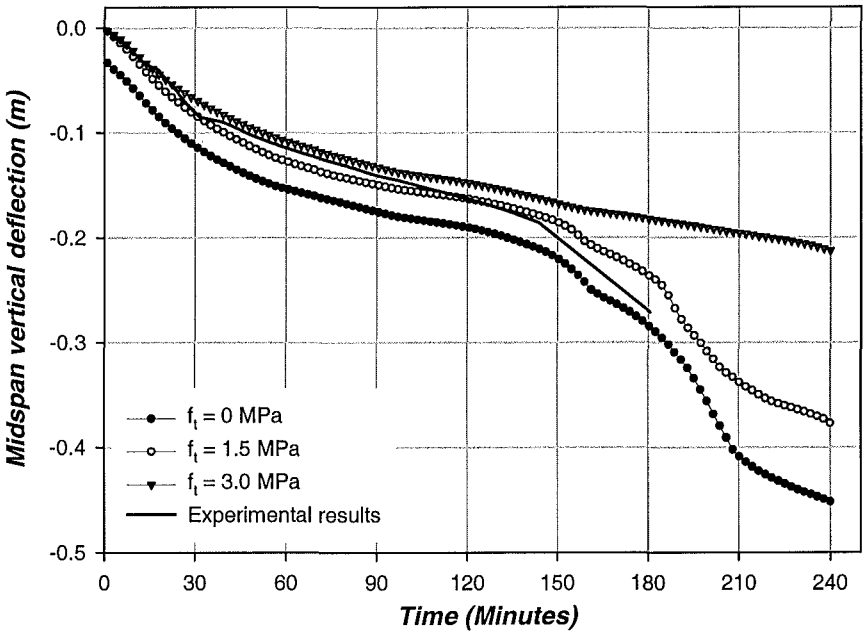

Figure 9-2: Comparison of the experimental results with the SAFIR analyses with outer edges.

Figure 9-2 compares the experimental results with the SAFIR predictions using the model with outer edges. Similarly with the results shown in section 9.2.1, the graph shows that the predictions made with 1.5MPa concrete tensile strength showed good agreement with the experimental results during the initial stages. However, during the advanced stages of the fire, the calculated deflections were substantially lower than the experimental results; unlike the slab without the edges which showed close agreement throughout the entire fire duration. The final deflection of the tested slab was between the predictions made with 0MPa and 1.5MPa concrete tensile strength.

9.2.3. Conclusions

The comparison of the experimental fire tests and the SAFIR analyses of the D147 slab showed that:

- The models with and without the outer edges showed good agreement with the experimental results when 1.5MPa ($0.25\sqrt{f'_c}$) concrete tensile strength was used.
- Analysing the slab with the outer edges and with 1.5MPa concrete tensile strength produced slightly lower deflections during the advanced stages of the fire.
- With 3MPa concrete tensile strength, SAFIR showed good agreement during the initial stages but underestimated the experimental results at the advanced stages of the fire.

9.3. Two-way flat slab behaviour with different reinforcing steel contents

9.3.1. Introduction

This section compares the SAFIR results with the testing of two-way flat slabs with different amounts of reinforcing steel.

9.3.2. Description of the slabs

The slabs were modelled using the finite element mesh shown in Figure 8-20 which includes the outer edges. Except for the higher steel content, the material properties are identical to the D147 slab (See section 8.2). The steel content of the slabs with the 661 mesh and HD12 mesh are 295mm^2/m and 565mm^2/m, respectively, which are 150% and 285% greater than the steel content of the D147 mesh. A concrete compressive strength of 36MPa was used in the analysis. The concrete tensile strength used in the analyses ranged from zero (fully cracked) to 3MPa ($0.5\sqrt{f'_c}$).

In the experimental tests, the corners of the 661 slab and the HD12 slab were not held down and were allowed to deflect upwards (See section 6.4.4). However, in the finite element model, the slabs were modelled as simply supported and the corners were prevented from lifting. The slabs in the experimental fire tests were tested for up to 3 hour exposure to the ISO fire but the analyses with SAFIR were conducted for up to four hour exposure or until failure of the slab, whichever occurred first.

9.3.3. 661 flat slab

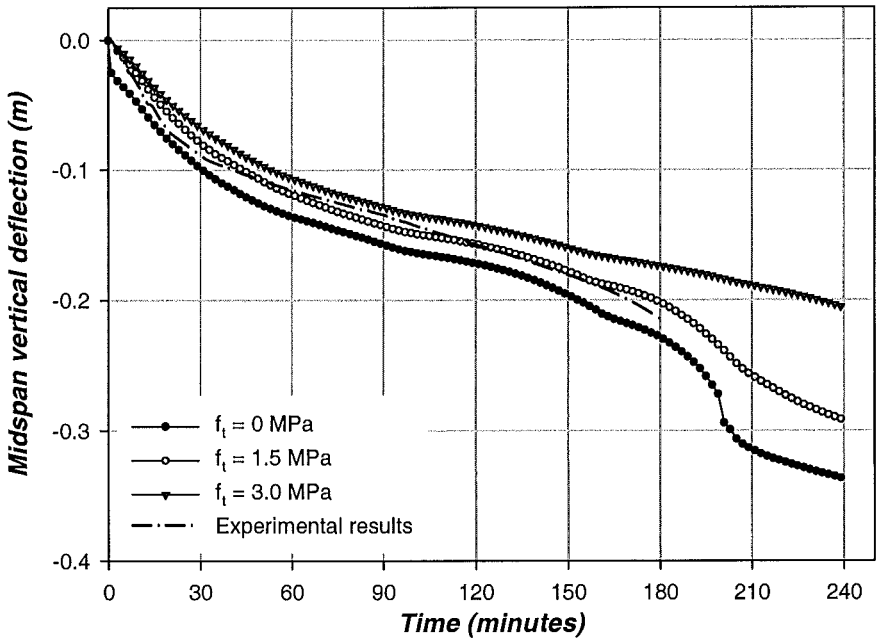

Figure 9-3: Midspan vertical deflections of the 661 slab during the ISO fire.

Figure 9-3 compares the deflections from the SAFIR modelling of the 661 slab with the experimental results. The graph shows that without concrete tensile strength, SAFIR predicted higher deflections than the experimental results throughout the entire fire duration. The analysis with SAFIR reached four hours without collapse. At 200 minutes, the deflection rate increased very significantly for a brief period causing sudden increase in deflections. The deflection rate decreased again, causing the deflection trend to level off during the last 30 minutes. This behaviour is similar to that seen in the analyses of the D147 slab (section 9.2.2).

With f_t equal to 1.5MPa, the experimental and SAFIR results showed good agreement for most of the fire duration. During the initial stages of the fire however, the tested slab deflected at a higher rate and produced larger deflections than those predicted with SAFIR. A possible reason for this is due to the corners of the tested slab being free to lift off the supports; whereas the slab modelled in SAFIR had its corners clamped. The clamped corners in the numerical model increased the stiffness of the slab, and produced smaller deflections compared with the tested slab. At the advanced stages of the fire, the SAFIR deflections showed very good agreement with the test results and showed that the holding down of the corners had a lesser effect on the deflection trend of the slab. The deflection rate of the slab increased slightly between 180 minutes and 210 minutes but it was not as significant as that seen in the D147 slab.

With 3MPa concrete tensile strength, the deflections predicted with SAFIR showed a similar trend to the test results but were consistently smaller. The graph shows that after 90 minutes, SAFIR predicted a linear deflection trend and did not show a sudden increase in the deflection rate between 180 and 210 minutes, as observed in the slabs with 0MPa and 1.5MPa concrete tensile strength.

9.3.4. HD12 flat slab

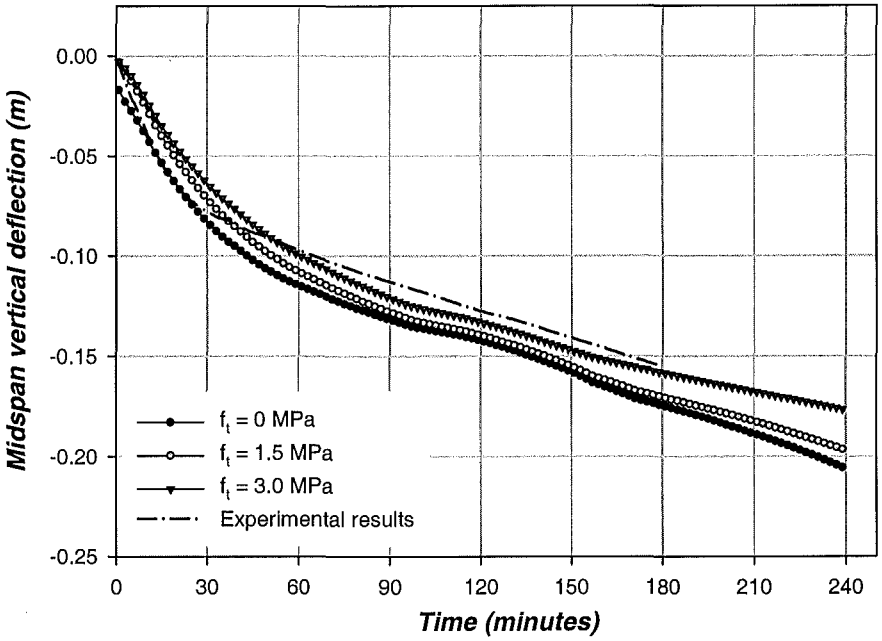

Figure 9-4: Midspan vertical deflections of the HD12 slab during the ISO fire.

Figure 9-4 compares the deflections from the SAFIR modelling of the HD12 slab with the experimental results. The graph shows that the predicted deflections of the slabs using different values of concrete tensile strength were very similar to each other. During the first 30 minutes, the tested slab showed a significantly higher deflection rate than the SAFIR predictions, producing deflections equal to the slab analysed without concrete tensile strength. After the first 30 minutes, the deflection rate of the tested slab reduced markedly and deflected at a linear rate for the remainder of the fire test. After the first hour, all the SAFIR predictions were greater than the experimental deflections. The high deflection rate of the tested slab during the initial stages is probably due to the corners of the tested slab being free to lift. The analyses of the HD12 slab with zero and 1.5MPa concrete tensile strength did not show the increased deflection rate at the later stages of the fire as seen in the D147 and 661 slabs.

The small difference of the deflections in the slab with zero and full concrete tensile strength indicates that concrete tensile strength has little effect on the deflections of a slab with high steel content. Conversely, the deflections of the slabs with low steel contents were strongly influenced by the amount of concrete tensile strength, as shown in the analysis of the D147 slab in section 9.2.

9.3.5. Conclusions

The analyses of the flat slabs with the 661 mesh and the HD12 mesh have shown that:

- The SAFIR analyses of the slab with the 661 mesh showed good agreement with the fire test results.
- The analyses of the slab with the HD12 mesh overestimated the test results during the later stages of the fire.
- The unclamped corners of the tested slabs produced higher initial deflection rates than the SAFIR model which had clamped corners.
- The deflections of slabs with high steel ratios were less sensitive to the amount of concrete tensile strength, compared with slabs with low steel ratios.

9.4. Behaviour of the two-way Hibond slab under fire conditions

This section compares the modelling of the two-way Hibond slab with the results of the fire resistance tests. Recent modelling of two-way composite slabs under fire conditions has been reported by O'Callaghan et al. (2000), Gillie et al. (2002) and Huang et al. (1999; 2000; 2001; 2002). Huang et al. (2000a) have modelled the orthotropic behaviour of the composite slabs with an effective stiffness approach. A different approach will be presented here, which utilises beam and shell elements.

9.4.1. Slab properties

The properties of the concrete and reinforcing in the Hibond slab are based on the material properties of the tested slab and are shown below. The loading and support conditions of the slab are identical to the slabs analysed in the previous sections. The tested slab was exposed to the ISO fire for 3 hours while the SAFIR analysis was performed up to 4 hours or until failure of the slab, whichever occurred first.

Slab geometry	
Length, L_y	4.16m
Width, L_x	3.16m
Overall thickness	130mm
Concrete properties	
Compressive strength (ambient temperature), f'_c:	32 MPa
Maximum concrete tensile strength, f_t	2.8 MPa ($0.5\sqrt{f'_c}$)
Concrete model (thermal and mechanical):	Siliceous aggregate (EC2, 1995)
Concrete cover, c_c	20mm above steel trough
Reinforcing steel properties	
Reinforcing mesh	198mm^2/m in both directions
Yield strength (ambient temperature), $f_{y,o}$:	565 MPa
Steel model (thermal and mechanical):	Hot-rolled steel (EC2, 1995)
Steel deck properties	
Thickness	0.75mm
Yield strength (ambient temperature), $f_{y,o}$:	550 MPa
Loads	
Self weight	2.43 kPa
Live load	3.0 kPa
Total applied load	5.43 kPa

9.4.2. Thermal model

The cross section of the slab that was modelled is shown in Figure 9-5. It is similar to the slab which was modelled in section 7.4, except with an overall thickness of 130mm.

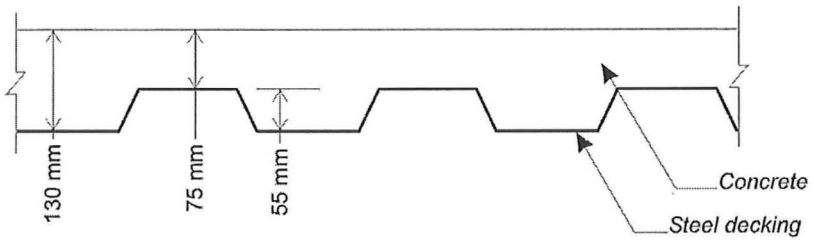

Figure 9-5: Cross section of the Hibond slab for the ambient temperature test.

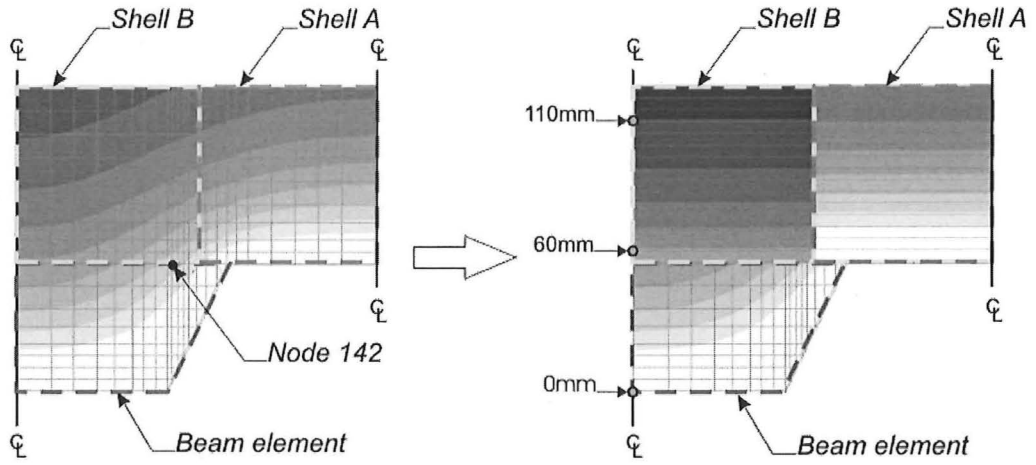

(a) Thermal distribution of Hibond slab ***(b) Discretisation with beam and shells***

Figure 9-6: Structural representation of the composite section with beam and shell elements.

Figure 9-6a shows the finite element discretisation and the temperature gradients of the Hibond slab. The composite section was discretised with concrete and steel material properties and was heated with the ISO fire at the bottom surface. The thicker section of the slab above the trough is cooler and the temperature gradients are not as steep as those in the thin section. Until now, the structural analyses in the previous sections assumed that the temperatures at any height across the plan of the slab were uniform. This assumption is valid for the analysis of plain flat slabs but is not valid for the Hibond slab due to the different thickness of the trapezoidal profile. Therefore, the different temperatures in the thick and thin parts of the Hibond slab would have to be considered in order to perform the structural analysis.

To account for the different temperatures across the section in the structural analysis, a combination of shell elements with different temperature exposures and beam elements were

used, as shown in Figure 9-6a. As each shell element can only be exposed to uniaxial heat flux and only consider temperature variations across the thickness of the shell, two different levels of heat fluxes were used to model the temperatures in the thin and thick sections, labelled *Shell A* and *Shell B*, respectively. *Shell A* is exposed to the ISO fire from below and *Shell B* is modelled with a lower temperature-time curve, taken from the temperatures of Node 142 in Figure 9-6a. The temperatures at Node 142 were used for the temperature input for *Shell B* as it provided a good estimate of the temperature variation above the trough.

The temperature curves which will be exposed to shells *A* and *B* are shown in Figure 9-7. Figure 9-6b shows the representation of the cross section of the Hibond slab with the shell elements and the beam elements. The trough of the slab is modelled with a beam finite element, which can consider fire exposure from more than one face.

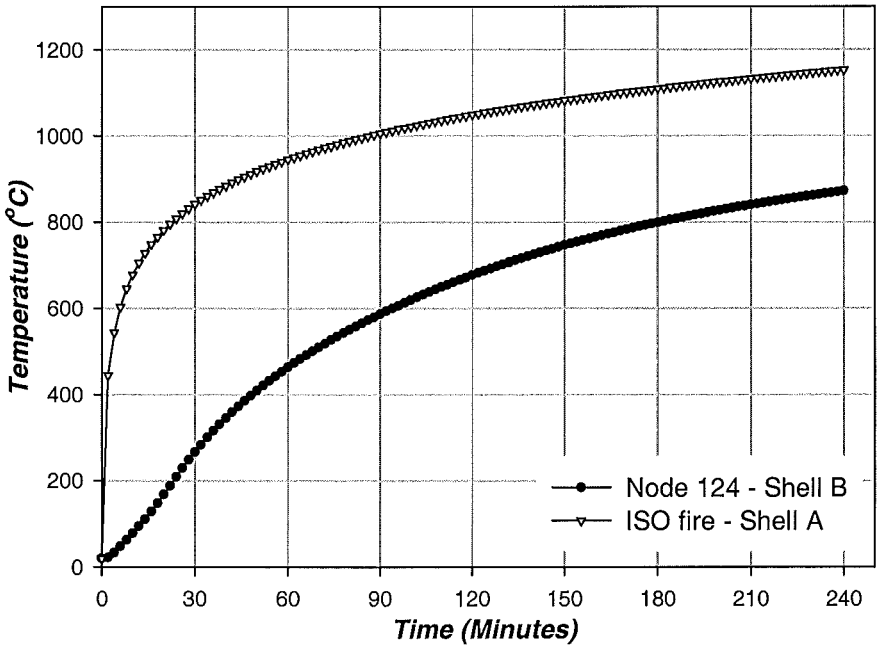

Figure 9-7: Temperature-time curves for exposure to Shells A and B.

9.4.3. Slab temperatures

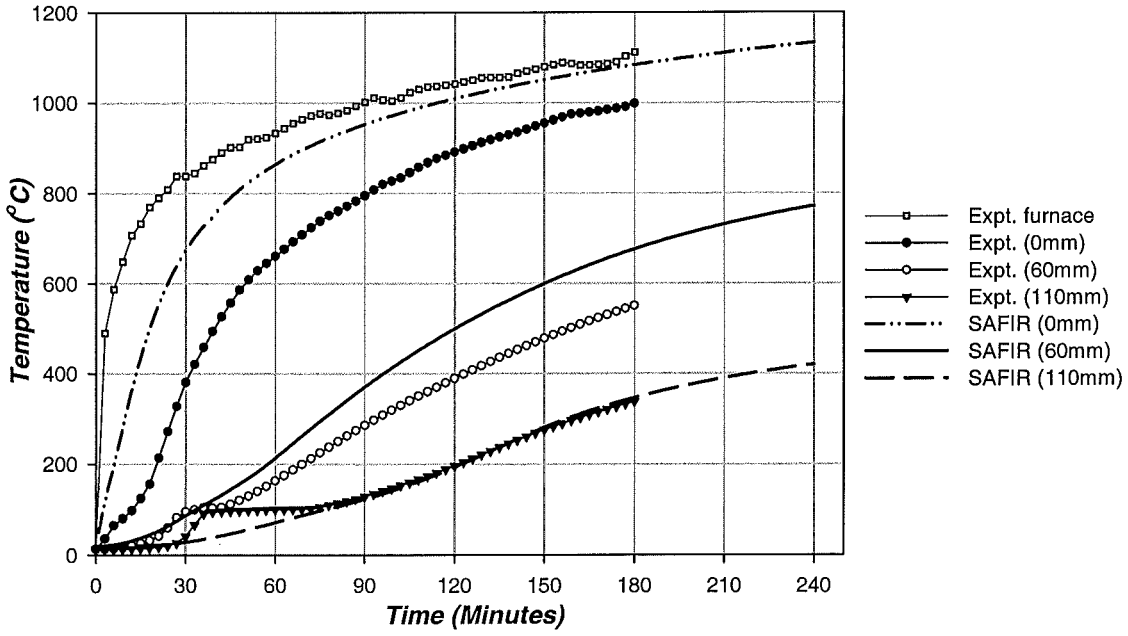

Figure 9-8: Temperatures in the Hibond slab from the fire tests and from SAFIR.

Figure 9-8 shows the temperatures in the Hibond slab during the ISO fire. The temperatures from the SAFIR thermal analysis were compared with the temperatures obtained from the fire tests. The temperatures from the tests and SAFIR were measured in the centre of the trough, as shown in Figure 9-6b, on top of the steel decking and at 60mm and 110mm from the bottom surface.

At the bottom of the trough (0mm), SAFIR predicted a logarithmic temperature rise, similar to the ISO fire curve, starting with a linear increase followed by a non-linear rise. The temperatures of the tested slab showed a slower linear increase during the initial 18 minutes. After that, the temperatures rose in a similar trend as predicted with the SAFIR, but lagged the SAFIR temperatures throughout the entire fire duration.

At 60mm from the bottom of the trough, the measured temperatures showed good agreement with the SAFIR temperatures during the initial stages. At approximately 30 minutes, the experimental temperatures levelled off briefly at approximately 100°C. The temperature plateau at 100°C was due to moisture accumulation at that height. When the free moisture at that height has been driven off, the temperatures increased again after 45 minutes but lagged behind the SAFIR temperatures for the remainder of the fire. The temperatures at 110mm from the exposed face showed very good agreement with the measured temperatures for most

of the fire duration, except when the temperatures levelled off at 100°C between 38 minutes and 75 minutes.

The difference between the SAFIR and experimental temperatures on the exposed face was most probably due to the debonding of the steel decking and concrete, from the bottom of the slab. The concrete, which was mechanically anchored to the decking, was ripped from the slab due to the release of steam. The release of steam was due to the high moisture content at the bottom surface, trapped by the decking. When the steel deck debonded from slab, it created a layer of air between the steel deck and the slab which acted as a layer of insulation and reduced the temperature rise at the bottom of the slab. Therefore, the temperature rise at the bottom of the tested slab was due to radiation and convection from the heated steel deck, rather than by direction conduction through the steel deck. The mode of heat transfer in the SAFIR analysis is by conduction and could not account for the insulating layer of air due to debonding of the steel deck from the slab, hence the higher calculated temperatures.

9.4.4. Structural model

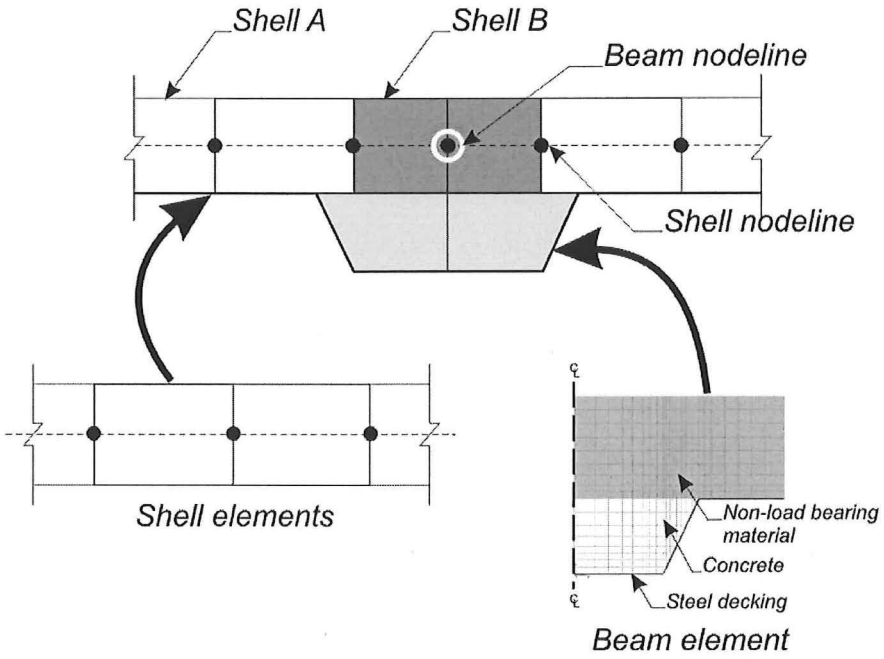

Figure 9-9: Discretisation of the Hibond slab cross section with the shell and beam elements.

Figure 9-9 shows a schematic of the structural representation of the Hibond slab. The flat deck of the slab was modelled with shell elements with different levels of fire exposure to represent the temperatures in the thin and thick sections. The trough of the slab, which consisted of concrete and the steel decking, was modelled with a beam element. The trough of

the beam element was modelled with concrete and steel properties. The flat section of the beam element (shown in grey) was modelled with non load-bearing material so that it did not contribute to the strength and stiffness of the slab, which was already provided by the shell elements. The nodeline of the beam elements was aligned with the nodeline of the shell elements.

Figure 9-10 shows the plan view of the finite-element mesh for the Hibond slab. The analysis was performed for a quarter of the slab without the outer edges. The discretisation consisted of shell elements with two different temperature exposures (designated *Shell A* and *Shell B*) and beam elements to represent the troughs. The beam elements were modelled at the positions of the troughs of the slab, at 300mm centres. The analysis of the 3D beam elements also involved evaluating the torsional stiffness of the beam element. The torsional stiffness of the beam was evaluated for ambient conditions but does not vary with time and temperature during the analysis. Therefore, a reduction factor was applied to the ambient torsional stiffness and was assumed to remain constant during the entire analysis. The torsional stiffness of the troughs was reduced to 10% of its stiffness at ambient conditions to simulate its stiffness under fire conditions.

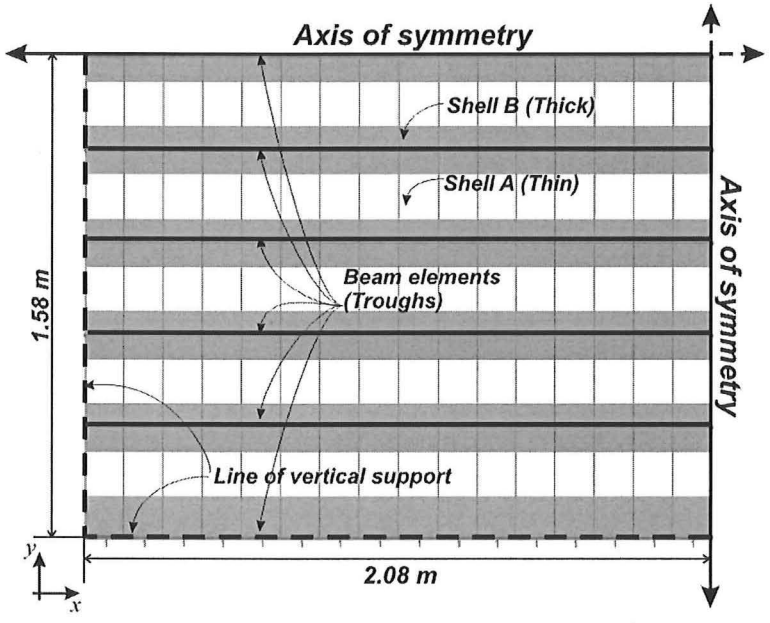

Figure 9-10: Finite element discretisation of the Hibond slab with beam and shell elements.

9.4.5. Deflections

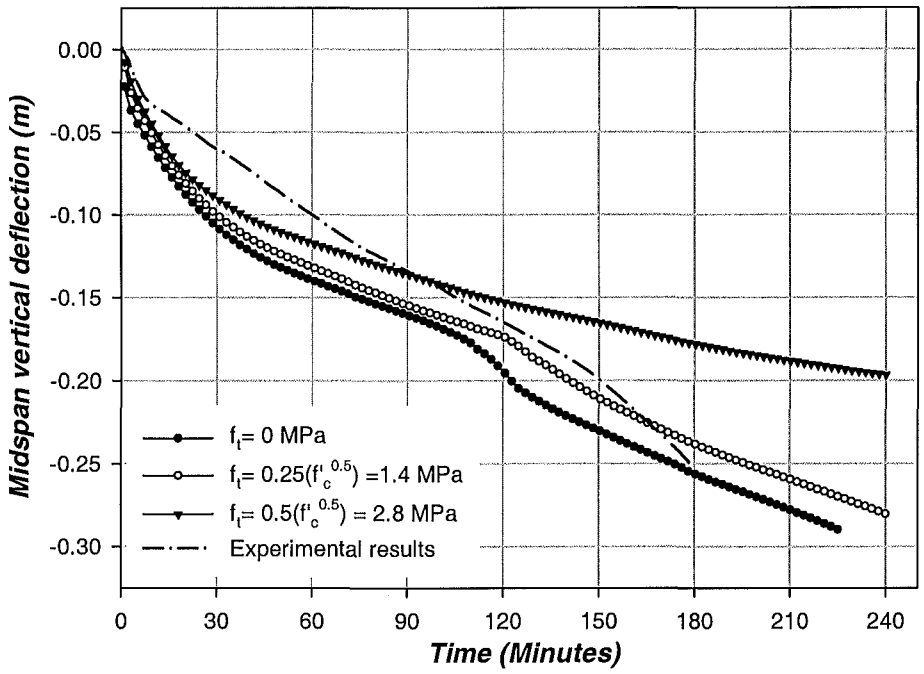

Figure 9-11: Midspan vertical deflections of the Hibond slab during the ISO fire.

Figure 9-11 compares the midspan deflections from the experimental results with the deflections predicted using SAFIR. The analyses using SAFIR were conducted with values of concrete tensile strength ranging from 0 MPa to 2.8 MPa.

The slabs with different concrete tensile strengths had similar deflection trends during the initial stages of the fire. The effect of different values of f_t only appeared at the later stages. With f_t equal to zero, the slab deflected very rapidly during the initial stages. Its deflection rate gradually decreased until it reached a constant and linear rate after 45 minutes. At 112 minutes, the deflection curve showed a dip in the deflection trend as the deflection rate increased briefly. At 125 minutes, the deflection rate decreased again and the slab continued to deflect at a linear rate until 226 minutes, when the analysis was stopped. The analysis stopped when the stresses of the steel decking in one of the beam elements reached the descending branch of its stress-strain curve. The analysis could not converge to a solution and could not iterate further.

With f_t equal to 1.4MPa, the slab showed a similar deflection trend to the fully cracked slab (f_t=0MPa), but with lower deflections due to the effect of the concrete tensile strength. With f_t equal to 2.8MPa, the slab deflected similarly to the other slabs during the initial stages. After

45 minutes, the deflection rate decreased and the slab deflected at a constant rate, reaching -197mm at 4 hours.

The SAFIR results differed quite markedly from the experimental results and showed close comparison only during the first 10 minutes. After that, the deflection rate of the tested slab decreased very noticeably, producing much lower deflections than the SAFIR predictions. At 150 minutes, the deflection rate of the tested slab increased slightly, but the slab still continued to deflect in a linear trend until reached -253mm after 3 hours. The increase of the deflection rate in the tested slab at 150 minutes showed some similarity to the analytical deflection trends of the slabs with f_t of zero and 1.4MPa, whose deflection rates increased briefly at approximately 2 hours. The final deflection of the tested slab was close to the slabs with zero and 1.4MPa concrete tensile strength.

The most obvious difference between the test and the numerical results occurred during the initial stages when the deflections were sensitive to the temperature distributions. The slower temperature rise at the bottom surface of the tested slab reduced the rate of thermal bowing and produced lower deflections, whereas SAFIR cannot account for debonding of the steel deck and predicted a faster temperature rise. At the later stages, the deflections were more sensitive to the stiffness of the reinforcing steel; therefore, the numerical results showed some similarity to the test results. To predict the deflections accurately with SAFIR, the thermal analysis of the slab has to account for the insulating effects of the steel deck debonding from the concrete slab.

9.4.6. Conclusions

The analyses of the Hibond slab showed that:

- The SAFIR analyses overestimate the deflections of the Hibond test results during the initial stages of the fire. The analyses results show better agreement at the advanced stages of the fire.
- The behaviour of the composite slab with steel decking is difficult to predict, particularly during the initial stages of the fire because of the debonding of the steel decking which affects the thermal distributions in the slabs.

9.5. Behaviour of the two-way Speedfloor slab under fire conditions

This section compares the results of the SAFIR analyses of the Speedfloor slab with the experimental results.

9.5.1. Slab properties

The properties of the Speedfloor slab are based on the properties of the tested slab and are shown below:

Slab geometry	
Length, L_y	4.3m
Width, L_x	3.3m
Slab thickness, h	90mm
Concrete properties	
Compressive strength (ambient temperature) f'_c:	37.6 MPa
Maximum concrete tensile strength, f_t	3.1 MPa ($0.5\sqrt{f'_c}$)
Concrete model (thermal and mechanical):	Siliceous aggregate (EC2, 1995)
Concrete cover, c_c	25mm
Reinforcing steel properties	
Yield strength (ambient temperature), $f_{y,o}$:	565 MPa
Reinforcing mesh	295mm^2/m in both directions
Steel model (thermal and mechanical):	Hot-rolled steel (EC2, 1995)
Steel joist properties	
Joist depth	250mm
Joist spacing	1.28m c/c, spanning the long direction
Joist thickness	3mm
Yield strength, $f_{y,o}$:	350 MPa
Steel model (thermal and mechanical):	Hot-rolled (EC3, 1995)
Loads	
Self weight	2.16 kPa
Live load	3.0 kPa
Total applied load	5.26kPa

9.5.2. Thermal model

This section discusses the thermal analysis of the Speedfloor slab to determine the temperatures of the exposed steel joist and the steel embedded in the concrete. The cross section of the slab which was modelled is shown in Figure 9-12. The slab consists of a 90mm concrete slab with a 250mm deep joist. The joists spanned across the long direction in the

tested slab and were spaced at 1.28m centres. For the thermal analysis of the cross section, a single joist with a slice of the concrete slab was modelled, as shown in Figure 9-13a. The reinforcing mesh shown in Figure 9-12 was not included in the thermal analysis of the concrete slab. The joist was exposed to three-sided heating and the slab was heated only at the bottom surface. Figure 9-13b shows the temperature distribution in the slab and joist after an hour exposure to the ISO fire. The temperatures of the exposed joist were very high, in excess of 900°C, while the embedded steel in the slab was relatively cool.

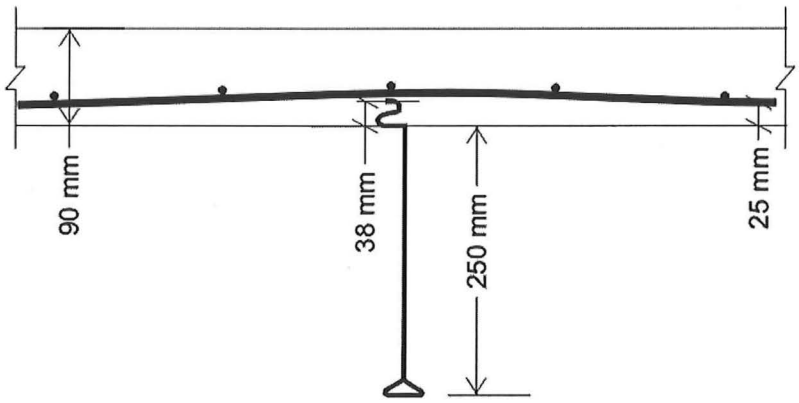

Figure 9-12: Cross section of the Speedfloor slab.

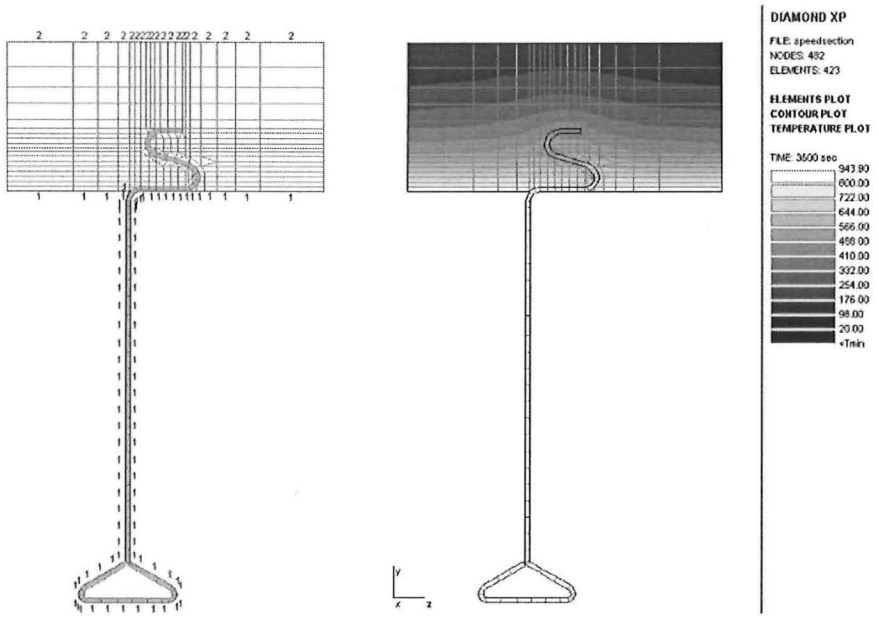

(a) Finite element mesh of the joist and slab

(b) Thermal gradients in the slab after 1 hour exposure to the ISO fire

Figure 9-13: Finite element mesh and typical thermal gradients in the composite slab.

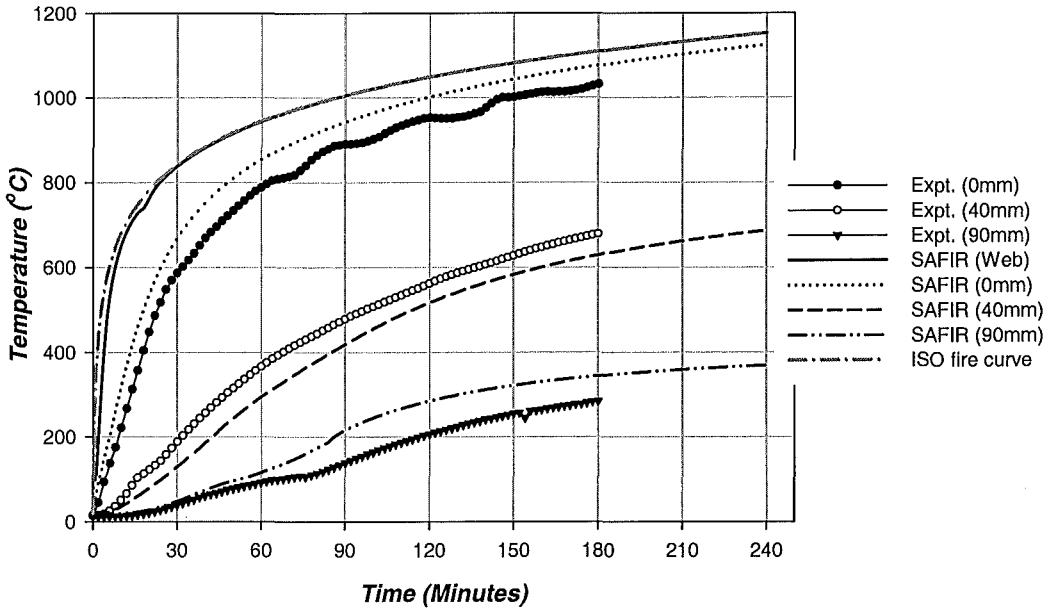

Figure 9-14: Temperatures in the Speedfloor slab from the fire tests and from SAFIR.

Figure 9-14 shows the temperatures in the slab and the steel joist, calculated from SAFIR and measured during the experimental fire tests. The temperatures were plotted at the heated surface (0mm) of the slab and at 40mm and 90mm from the heated surface. The calculated temperatures at the web of the steel joist were also plotted. The SAFIR analysis shows that the temperatures in the joist were almost equal to the gas temperatures. On both the heated and unheated surfaces of the slab, SAFIR predicted slightly higher temperatures than the measured temperatures. But, in the middle region (40mm), SAFIR underestimated the measured temperatures.

9.5.3. Structural model

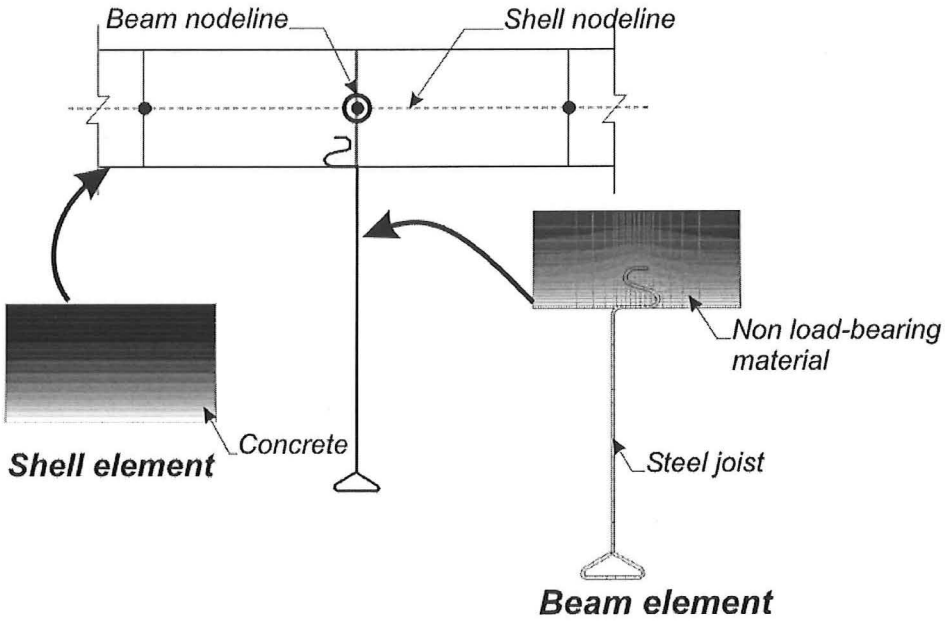

Figure 9-15: Discretisation of the Speedfloor slab cross section with the shell and beam elements.

Figure 9-15 shows a schematic of the cross section of the Speedfloor slabs for the structural analysis. The concept of the model is similar to the Hibond slab (Section 9.4.4). The beam elements, which represent the joists, act in full composite action with the shell elements which form the slab. The joist of the beam element was modelled with hot-rolled steel properties from EC3 (1995). The hot-rolled steel was used based on the assumption that the mechanical properties of the cold-formed joist would quickly revert to that of the hot-rolled steel during the early stages of the fire when the joist was exposed to high temperatures. The concrete slab of the beam element, which the top of the joist was embedded, was represented with non load-bearing material. The shell elements had concrete properties and were used to represent the slab in the structural analysis. The circular penetrations in the webs of the joists were not taken into consideration in the structural analysis.

Figure 9-16 shows the plan view of the finite element mesh for the structural analysis of the Speedfloor slab which consists of shell and beam elements. Unlike the analyses of the slabs in the previous sections, half of the Speedfloor slab was modelled due to the asymmetric cross section of the joist located at the centre of the slab. The beam elements spanned in the long direction and were spaced at 1.28m centres. The model also included the outer edges which were not heated. The slab was simply supported at four sides, 70mm from the edges. Similarly with the analysis of the Hibond slab, the torsional stiffness of the beam elements

was reduced to 10% of its initial ambient stiffness to simulate its stiffness under fire conditions. The heated region of the slab was loaded with a live load of 3.0 kPa, in addition to its self-weight. The live load was not applied to the outer edge elements.

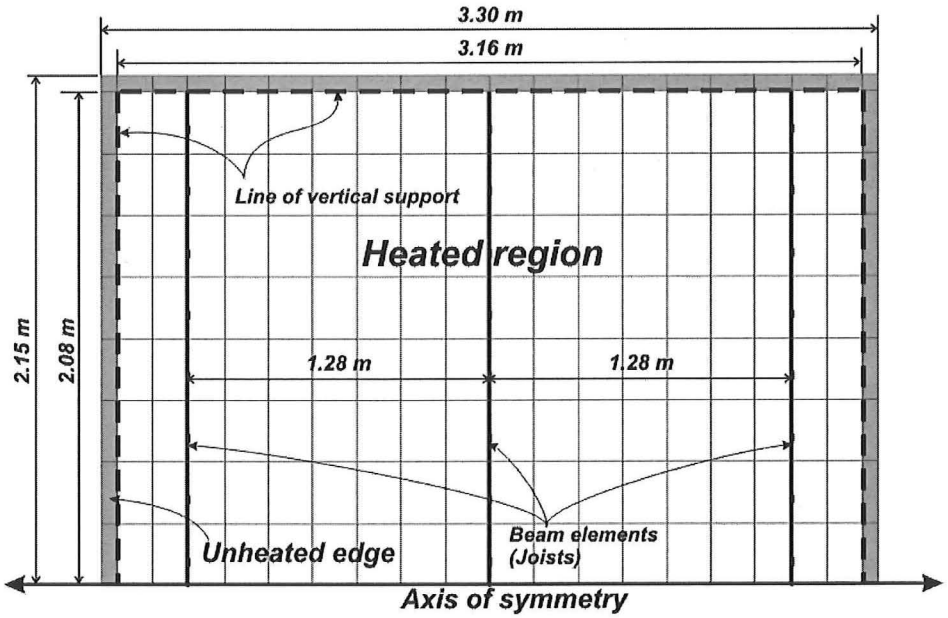

Figure 9-16: Finite element discretisation of the Speedfloor slab with beam and shell elements.

9.5.4. Deflections

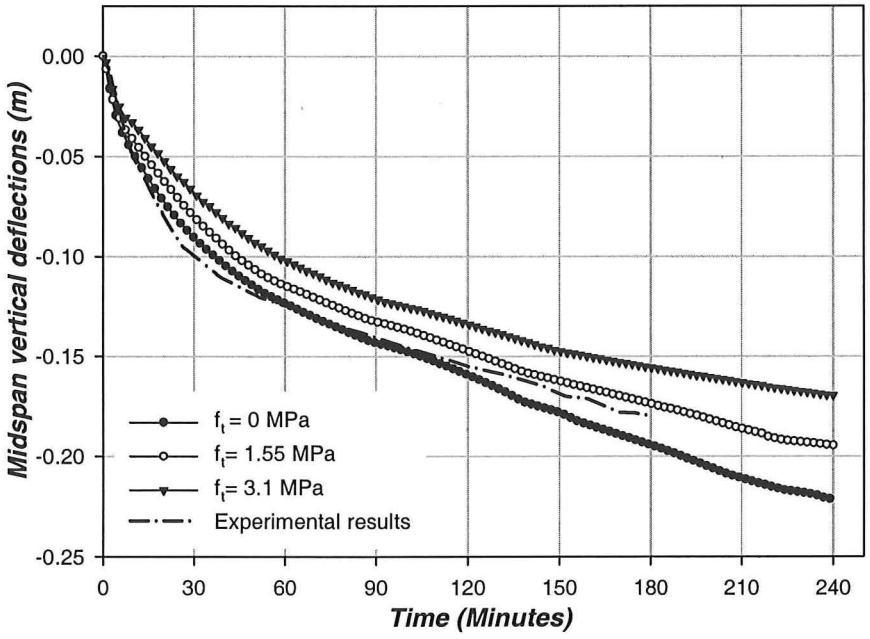

Figure 9-17: Midspan vertical deflections of the Speedfloor slab during the ISO fire.

Figure 9-17 compares the midspan vertical deflections predicted by SAFIR with the experimental results. The analyses with SAFIR were performed with values of concrete

tensile strength ranging from zero to 3.1MPa ($0.5\sqrt{f'_c}$). The graph shows that the SAFIR results showed very good agreement with the test deflection throughout the entire fire duration. However, the analyses with different values of concrete tensile strength underestimated the deflections of the tested slab during the initial stages. The graph shows that during the initial stages, there was little difference in the deflections with different values of concrete tensile strength.

The high deflection rate of the slab during the initial stages was caused by thermal bowing of the heated slab and the expansion of the joists. After the first 30 minutes, the test results and the SAFIR analyses showed a marked decrease in the deflection rate. At the advanced stages of the fire, the variation of the deflections in the slabs with different concrete tensile strengths increased. The slab with 1.55MPa ($0.25\sqrt{f'_c}$) concrete tensile strength showed the closest agreement with the tested slab. The analyses of all the slabs with SAFIR continued up to 4 hours without failure. The deflected shape of the slab with 1.55MPa concrete tensile strength after four hours exposure to the ISO fire is shown in Figure 9-18.

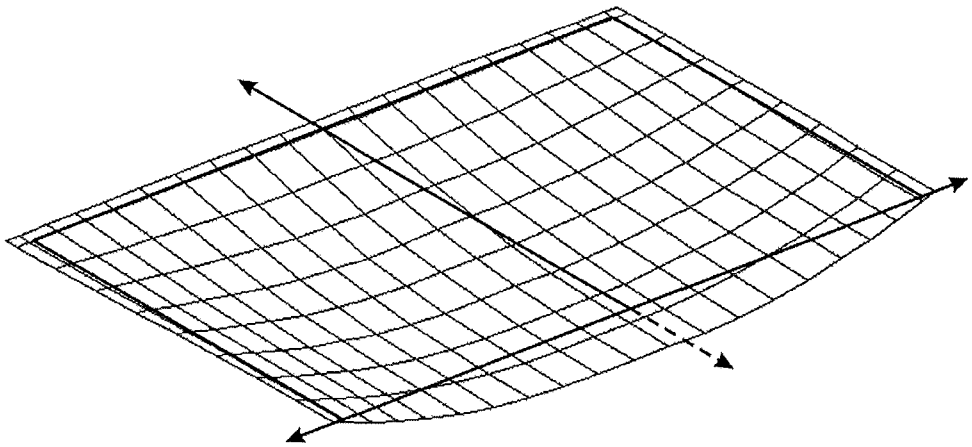

Figure 9-18: Deflected shape of the Speedfloor slab after 4 hours exposure to the ISO fire.

9.5.5. Conclusions

The analyses of the Speedfloor slab with SAFIR shows good agreement with the experimental test results. The analyses show that the composite slab with the steel joists can be accurately modelled by combining the beam and shell elements.

9.6. Conclusions

The finite element modelling of the tested slabs with SAFIR have shown that:

- SAFIR can be used to accurately predict the 3D behaviour of two-way solid flat slabs and composite slabs under fire exposure.
- SAFIR analyses showed good agreement with the test results.
- For lightly reinforced slabs, the SAFIR predictions were sensitive to the amount of concrete tensile strength. The deflections of the slabs were less sensitive to the amount of concrete tensile strength for highly reinforced slabs.
- The analyses with concrete tensile strength of $0.5\sqrt{f'_c}$ underestimated the test results for most of the analyses.
- Using zero concrete tensile strength predicted much larger deflections than the test results Zero concrete tensile strength can be used as a conservative estimate for analysing existing structures which have already suffered cracking.
- A concrete tensile strength of $0.25\sqrt{f'_c}$ showed good agreement with most of the test results and is recommended for the analysis of uncracked concrete slabs exposed to fire.
- The unclamped corners of the 661 and HD12 slabs in the experimental fire tests produced higher deflection rates than the SAFIR predictions during the initial stages.
- The behaviour of the Hibond slab with the steel decking is difficult to predict with SAFIR because the numerical analysis does not account for the debonding of the steel decking which affectes the temperature distributions in the slabs.

10. THE BEHAVIOUR OF FIRE-EXPOSED TWO-WAY SLABS WITH VARIOUS SUPPORT CONDITIONS

10.1. Introduction

The fire behaviour of two-way slabs with various configurations and support conditions will be analysed in this chapter using SAFIR. The purpose is to investigate whether tensile membrane action can increase the fire resistance of reinforced concrete slabs with different configurations and support conditions. Their behaviour will be compared to the 3.16m x 4.16m slab analysed in section 8.6. The different slabs which will be analysed are summarised in Table 10-1.

Section	Slab	Support condition	Slab size
10.4	One-way slab	One-way, simply supported	3.16m
10.5	Three sided support	Simply supported on three sides	3.16m x 4.16m
10.6	Effect of aspect ratio	Simply supported on 4 sides	3.16m x 8.0m 3.16m x 12.0m
10.7	Slab on beams	Simply supported on 4 sides on beams	3.16m x 4.16m

Table 10-1: Slab configurations to be analysed.

10.2. Slab properties

The properties of the slabs that will be analysed in the following sections are identical to those described in section 8.2. The slabs are 100mm thick and are reinforced with D147 mesh (198mm^2/m) spanning in two directions. The compressive strength of the concrete is 36MPa and its tensile strength is 1.5MPa. 1.5MPa concrete tensile strength was chosen as it showed good agreement with the test results of the D147 slab (Section 9.2). The full details of the slab properties can be found in section 8.2.

10.3. Thermal model

The slab is assumed to be uniformly heated with the ISO fire from below. The thermal analysis for the slabs in this chapter is identical to that of section 8.3.

10.4. One-way slab behaviour

This section compares the behaviour of a one-way slab with a two-way slab exposed to the ISO fire. In this section, the two-way slab (Figure 10-1A) discussed in chapter 8 is assumed to span only in one direction, across the short span (Figure 10-1B). The one-way slab is simply supported at both ends and has a 3.16m span. A metre width of the one-way slab is analysed with section properties identical to that of the two-way slab. The reinforcing mesh spans only in one direction and has a 25mm cover. The slab is loaded with a uniformly distributed load of 5.4kPa and is subjected to the ISO fire from below.

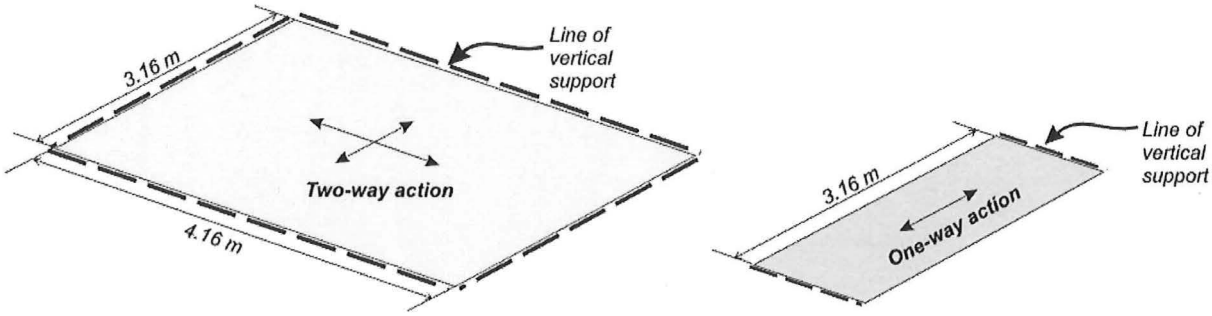

(A) Two-way slab, simply supported on four edges *(B) One-way slab, simply supported on two edges*

Figure 10-1: Two-way and one-way action.

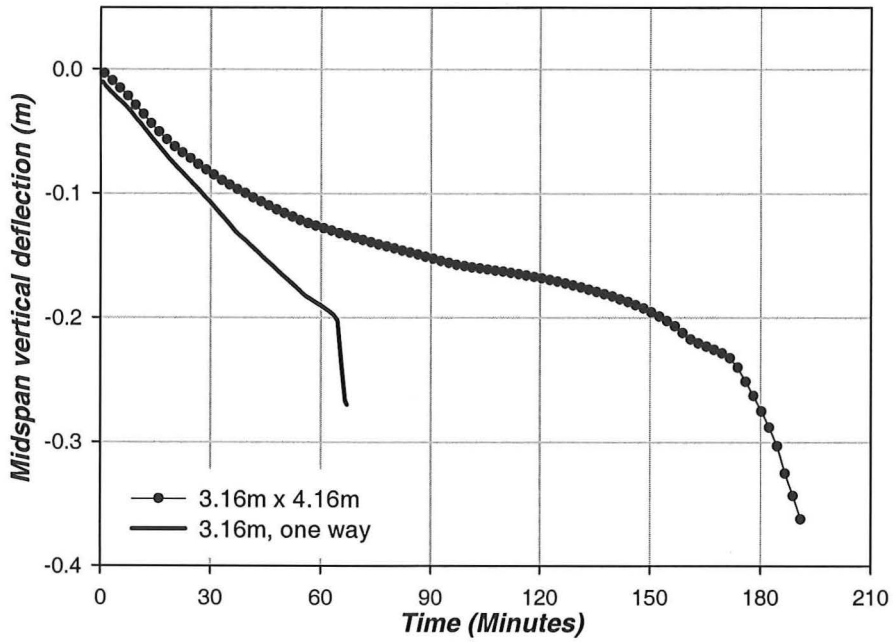

Figure 10-2: Comparison of the behaviour of one-way and two-way fire-exposed slabs.

Figure 10-2 compares the midspan vertical deflections of the two-way slab with the one-way slab during the ISO fire. The graph shows that the one-way slab had a significantly lower fire

resistance than the two-way slab. The slab deflected very rapidly during the start of the fire, due to thermal bowing. During the first 15 minutes, the deflection rates of the one-way and two-way slabs were identical. After that, the deflection rate of the two-way slab decreased while the one-way slab continued at the same rate. At 64 minutes, the deflection rate of the slab increased very rapidly due to runaway failure. Failure occurred at 67 minutes, which is approximately a third of the failure time of the two-way slab. The analysis shows that the two-way slab had a much higher fire resistance than the one-way slab. The higher fire resistance of the two-way slab was due to membrane enhancement which prevented collapse after the slab had lost its bending resistance. The one-way slab cannot develop tensile membrane action and relies only on its flexural strength to resist collapse.

10.5. Fire-exposed slab supported on three sides

10.5.1. Introduction

The fire behaviour of a slab supported on three sides is described in this section. The purpose of this analysis is to simulate a slab supported on three fire protected beams which provide rigid vertical support. The unsupported edge represents an unprotected beam that is assumed to be unable to support the slab during the fire.

10.5.2. Structural model

The structural model of the slab is shown in Figure 10-3. The slab is simply supported on three sides, on two of the long edges and one of the short edges. The unsupported edge of the slab is between *A* and *C*. Half of the slab was modelled due to symmetry of the slab about the long span. The model consists of 112 shell elements in a 7 x 16 grid.

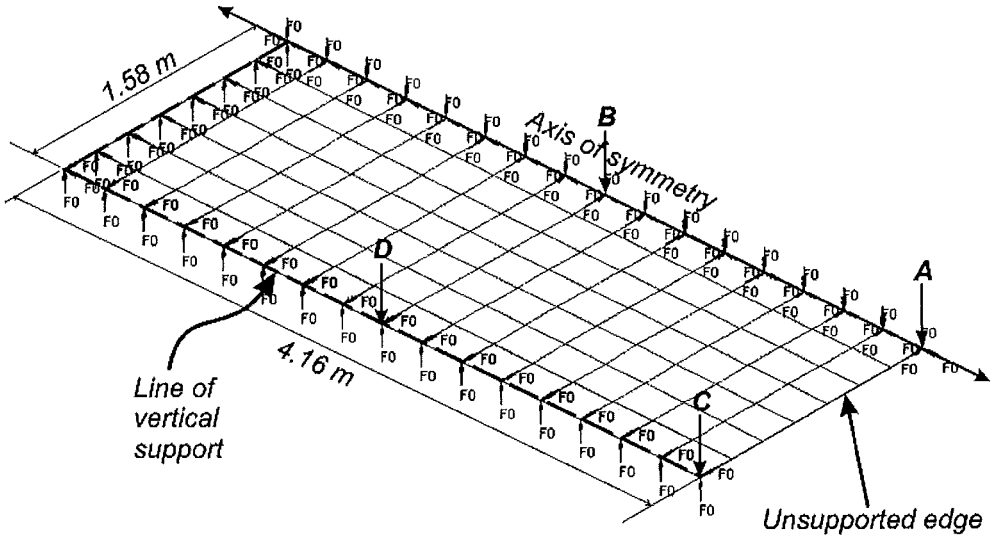

Figure 10-3: Structural model of the slab supported on three sides.

10.5.3. Deflections

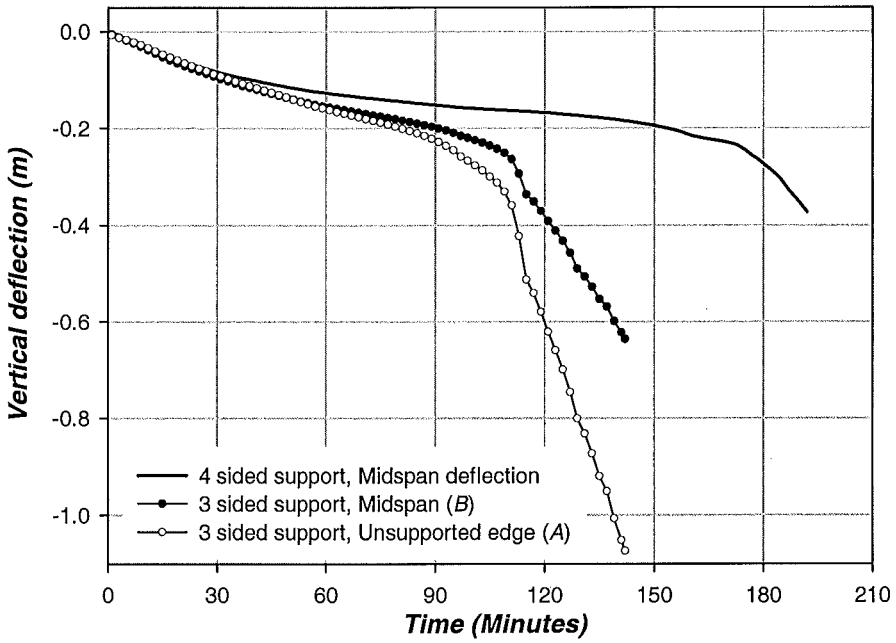

Figure 10-4: Variation of vertical deflections with time.

Figure 10-4 shows the variation of the vertical deflections at the middle of the unsupported edge and at midspan. The unsupported edge and midspan correspond to points *A* and *B* of Figure 10-3, respectively. Also plotted on the graph are the midspan vertical deflections of the slab supported on four edges.

During the initial stages of the fire, the deflections at the unsupported edge and at midspan were very similar to the midspan deflections of the slab supported on 4 sides. The midspan

deflections were initially slightly larger than the unsupported edge deflections. After 45 minutes, the unsupported edge deflections surpassed the midspan deflections as it deflected at a higher rate. At 112 minutes (1 hour and 52 minutes), the deflection rates increased very markedly due to runaway failure. At the last time step (142 minutes), the deflections at the unsupported edge and midspan had reached -1.07m and -0.64m, respectively. The reason for the runaway failure at 112 minutes was due to crushing of the concrete at the unsupported edge which will be discussed in section 10.5.5.

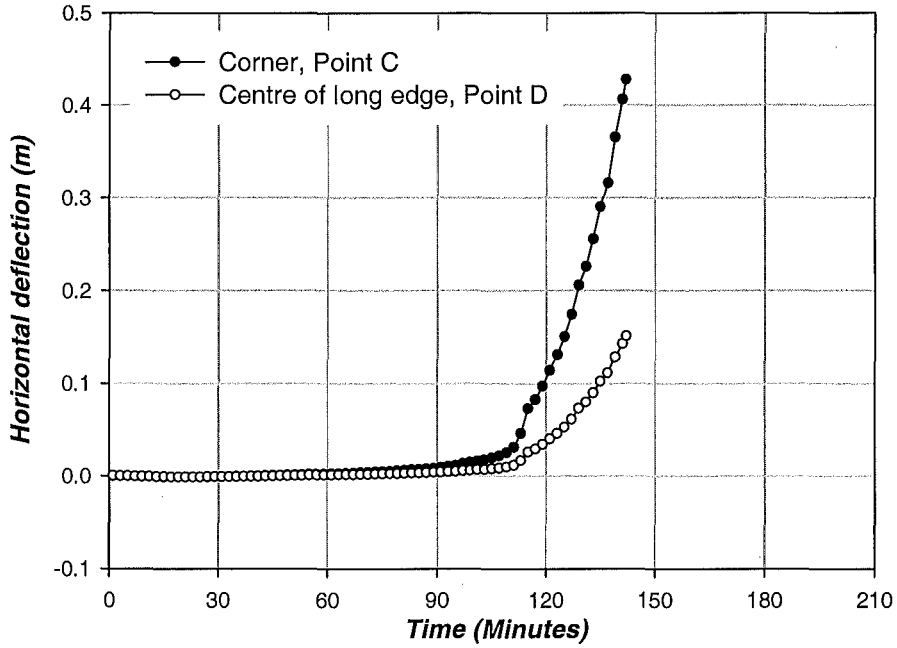

Figure 10-5: Lateral deflections at the supported edges of the slab.

Figure 10-5 shows the lateral deflections of the supported edges along the long span, at points *C* and *D* of Figure 10-3. The lateral deflections refer to the horizontal deflections in the transverse direction of the slab. Positive deflection indicates inward contraction and negative deflection indicates outward expansion.

During the initial stages of the fire, the long sides of the slab had very small deflections. As the vertical deflection rate increased, the inward deflections of the supported edges gradually increased. The horizontal deflections increased very markedly at 112 minutes when runaway failure occurred due to the edges being pulled inwards. The final inward deflection sustained at points *C* and *D* were 0.43m and 0.15m, respectively.

Figure 10-6 shows the deflected shape of the slab after an hour exposure to the fire. The original shape of the slab is superimposed onto the deflected shape of the slab. At this stage, the deflections at midspan and at the free edge were almost identical. Figure 10-7 shows the deflections of the slab when it failed at 142 minutes. The large vertical deflections caused the supported edges to pull inwards and the slab to fold as indicated by the runaway vertical and horizontal deflections.

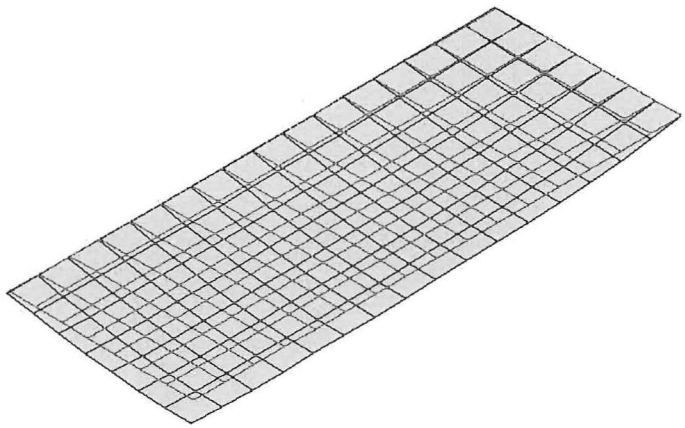

Figure 10-6: Deflected shape of the slab after an hour exposure to the ISO fire.

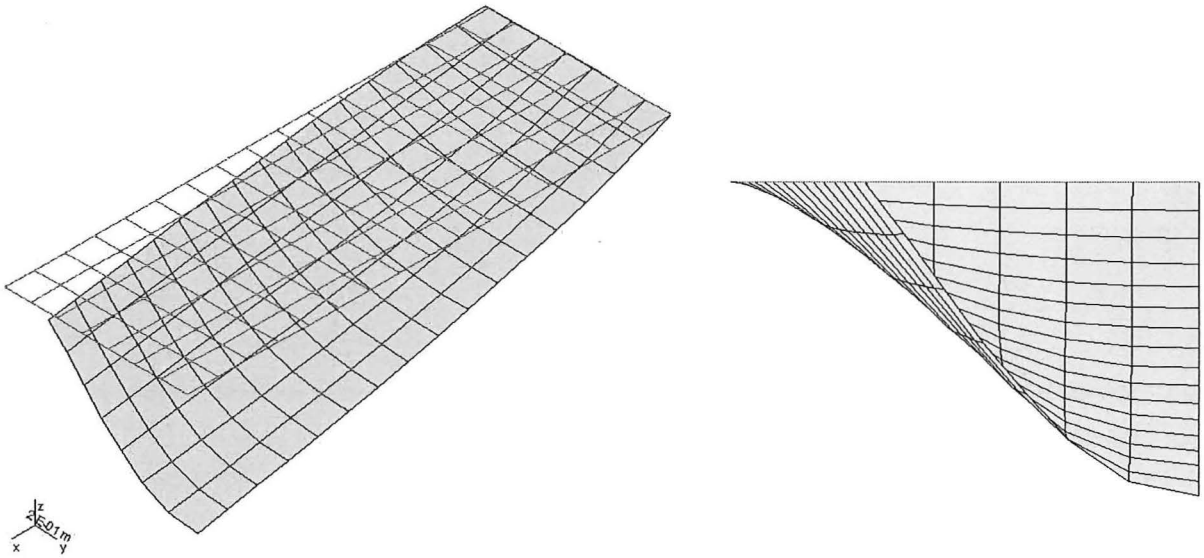

Isometric view **Front view**

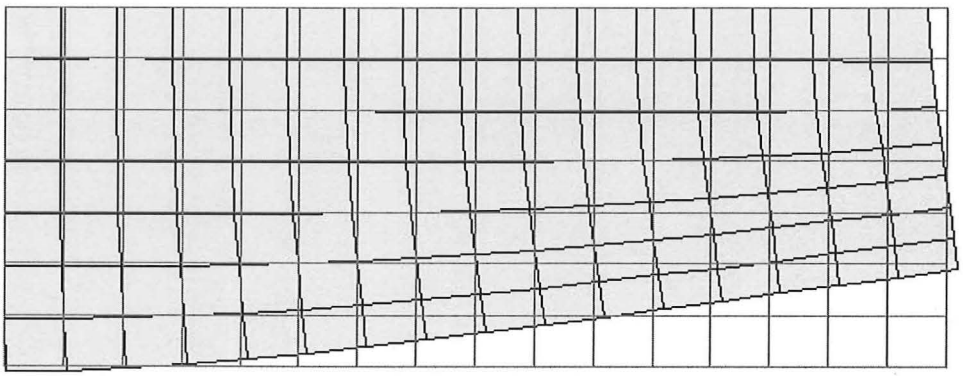

Top view

Figure 10-7: Deflected shape at failure (142 minutes).

10.5.4. Traction distribution

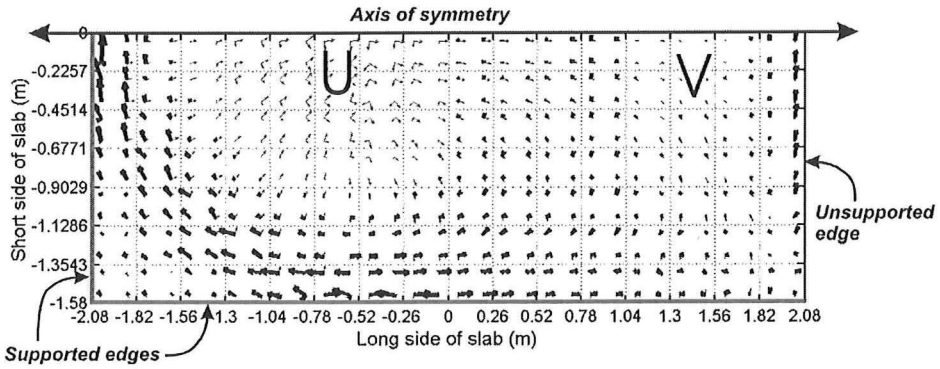

Figure 10-8: Traction distribution after 5 minutes fire exposure.

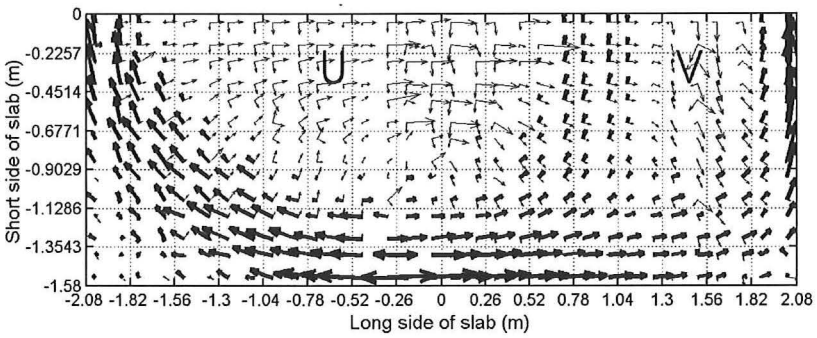

Figure 10-9: Traction distribution after 60 minutes fire exposure.

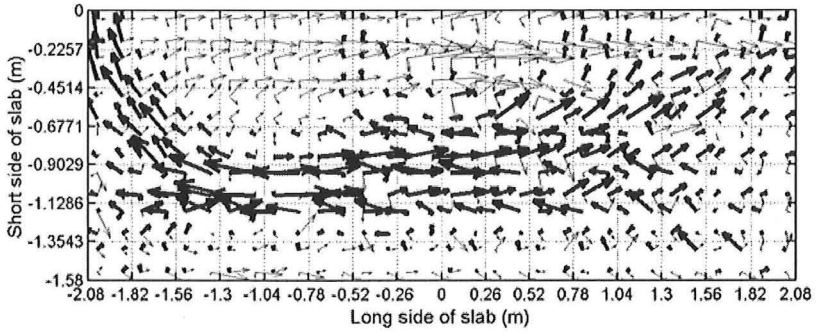

Figure 10-10: Traction distribution after 120 minutes fire exposure.

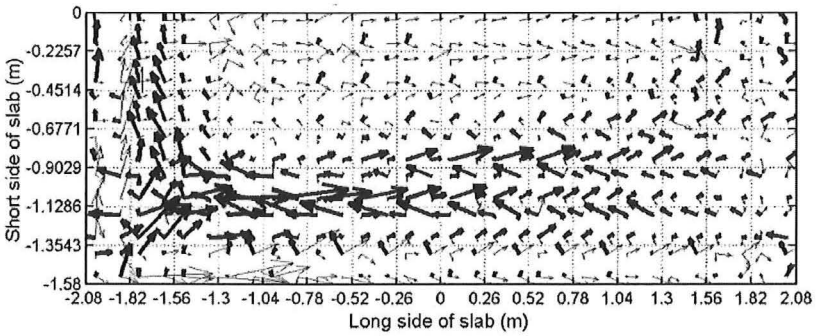

Figure 10-11: Traction distribution at failure (142 minutes).

Figure 10-8 to Figure 10-11 show the distribution of the principal tractions in the slab during the fire. The positions of the supported and unsupported edges of the slab are shown in Figure 10-8.

Figure 10-8 shows that 5 minutes after the fire had started, membrane forces had formed in the slab. Up to the first 60 minutes, Figure 10-8 and Figure 10-9 show that two tension fields, marked *U* and *V*, had formed in the slab and were surrounded by a large compression ring. The compression ring formed around the edges of the slab and was divided by a narrow compression band, forming between the two tension fields. The increasing vertical deflections at the unsupported edge caused a thin band of high compression membrane tractions to form along the unsupported edge of the slab.

Figure 10-10 shows that after 2 hours, the compression ring had shifted inwards from the edges of the slab to the central region of the slab. The main compression ring was divided by several bands of compression tractions across the short span. The main compression ring, which had shifted inwards, was due to the in-plane resistance of the slab against runaway failure as the long sides folded inwards. Figure 10-11 shows that at failure, the bands of compression tractions across the main compression ring seen in Figure 10-10 had disappeared, leaving only one main compression ring. The compression ring had also developed in-plane reaction compression forces thrusting into the corner of the supported edges.

10.5.5. Variation of the stresses at the unsupported edge

This section describes the variation of the stresses across the short span, at point *A* of Figure 10-3, which is located in the middle of the unsupported edge. The stresses at the top surface of the concrete slab were plotted because they were the most critical position which would cause failure of the slab. Figure 10-12 shows the exact position where the stresses are plotted in the finite element mesh.

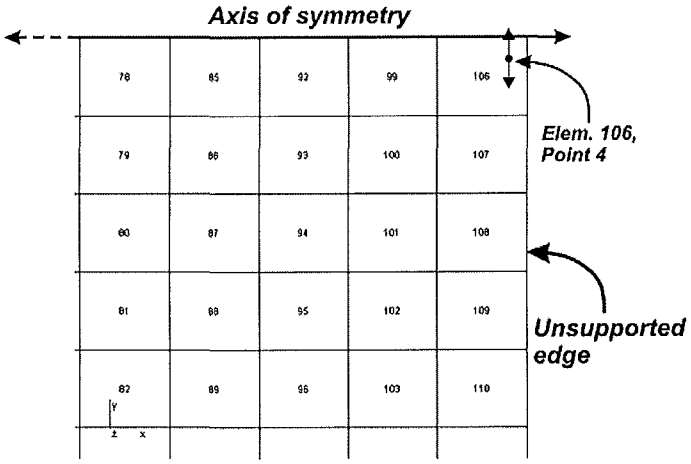

Figure 10-12: Detail of the finite element mesh at the unsupported edge and the axis of symmetry.

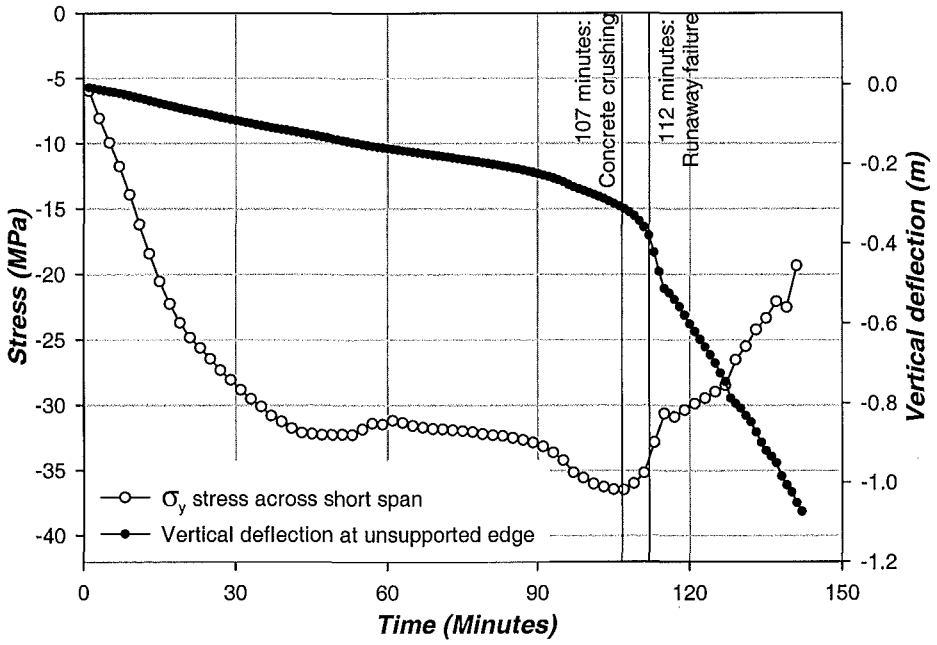

Figure 10-13: Variation of concrete stresses at the top surface across the short span.

Figure 10-13 shows the variation of the stresses along the unsupported edge of the top surface of the slab (Element 106, point 4). The vertical deflections at the centre of the unsupported edge are also plotted. The graph shows that the compression stresses increased very rapidly in a linear trend during the initial stages. The high compression stresses at the edges correspond to the high compression membrane tractions along the unsupported edge, shown in Figure 10-9. After 19 minutes, the rate of rise of the concrete compressive stress decreased slightly and levelled off at 43 minutes. The stress remained fairly constant until 90 minutes when it increased again. At 107 minutes, the concrete stress at the middle of the unsupported edge reached its ultimate strength and crushed. Therefore, the compression ring which formed

around the perimeter could not be sustained. After that, the compressive stresses decreased very rapidly, accompanied by runaway deflection after 112 minutes.

10.5.6. Theoretical ultimate load

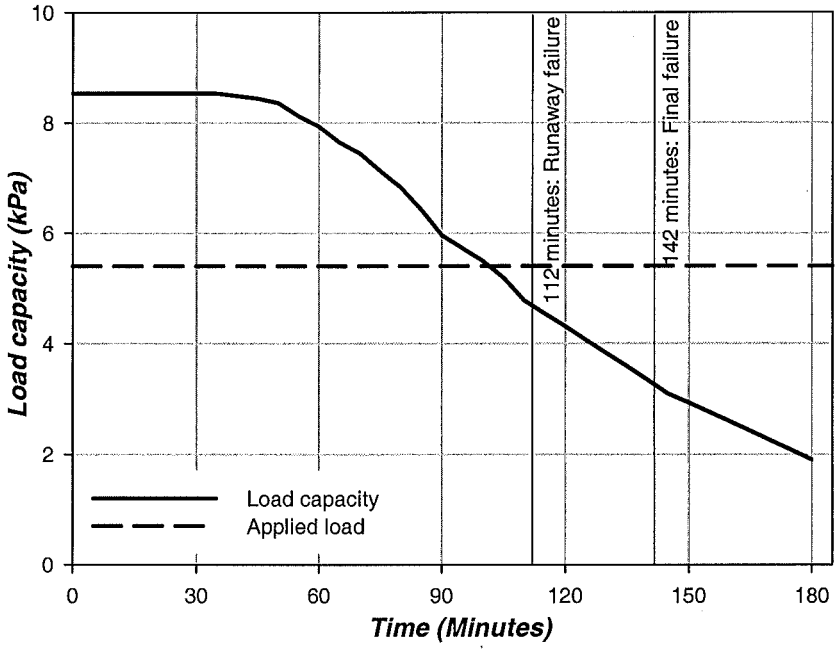

Figure 10-14: Theoretical load capacity with time in the fire.

Figure 10-14 shows the variation of the theoretical load capacity of the slab during the fire. The theoretical load capacity was calculated with yield line theory using the reduced strengths of the reinforcing steel. The level of the applied load, and the times to runaway failure and final failure predicted by the SAFIR analysis, are also shown. The graph shows that during the first 40 minutes, the theoretical yield-line capacity remained constant but dropped off linearly after that.

Based on yield-line theory, the slab should collapse when the load capacity of the slab dropped below the level of the applied loads at 101 minutes. SAFIR showed that runaway failure commenced at 112 minutes, which is only slightly later than predicted with yield line theory. This comparison shows that the slab supported on three sides did not have significant enhancement due to tensile membrane action, resulting in a much lower fire resistance than if it was supported on four sides.

10.5.7. Conclusions

The analysis of the slab which was supported on three sides showed that:

- The fire resistance of the slab supported on three sides was significantly less than the slab supported on four sides.
- Runaway failure of this slab occurred when the concrete at the unsupported edge crushed.
- SAFIR predicted runaway failure occurring at a similar time based on yield-line theory. The similar times indicate that the slab did not have significant tensile membrane enhancement as yield-line theory does not account for membrane effects.

10.6. Fire-exposed two-way slabs with different aspect ratios

10.6.1. Introduction

The behaviour of two-way slabs with different aspect ratios under fire conditions is investigated in this section. Two different geometries will be analysed to investigate the extent which tensile membrane action can increase the fire resistances of the slabs. As the aspect ratio (L_y/L_x) of a two-way slab increases, the behaviour of the slab should approach that of a one-way slab and the enhancement by tensile membrane action on the fire resistance of the slab should decrease. Design standards provide a limiting aspect ratio to which a slab can be treated as a two-way slab. The Concrete Structures Standard of New Zealand (SNZ, 1995) and FIP (1978) recommend that slabs with aspect ratios of greater than 2 be designed as one-way slabs.

10.6.2. Properties

The geometries of the slabs that will be analysed are shown in Table 10-2.

	L_x	L_y	L_y/L_x
Slab 1	3.16m	8.0m	2.53
Slab 2	3.16m	12.0m	3.80

Table 10-2: Geometries of the slabs to be analysed.

10.6.3. Structural models

The finite element meshes used in the structural analyses of the 3.16m x 8m slab and the 3.16m x 12m slab are shown in Figure 10-15 and Figure 10-16, respectively. The 8m and 12m slabs were analysed with 112 and 168 shell elements, respectively. Only a quarter of the slabs were analysed due to the symmetry of the support and loading conditions. At the axes of symmetry, the horizontal, rotational and drilling degrees of freedom were restrained.

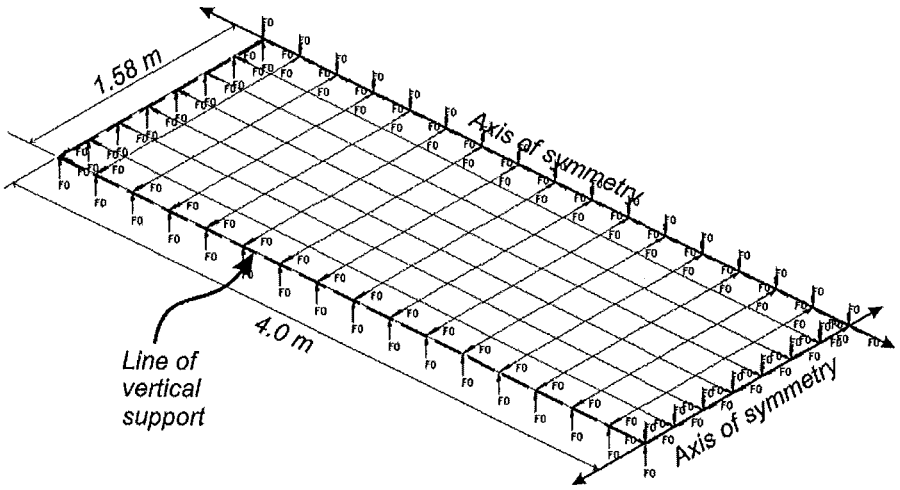

Figure 10-15: Finite element mesh for the structural analysis of the 3.16m x 8.0m slab.

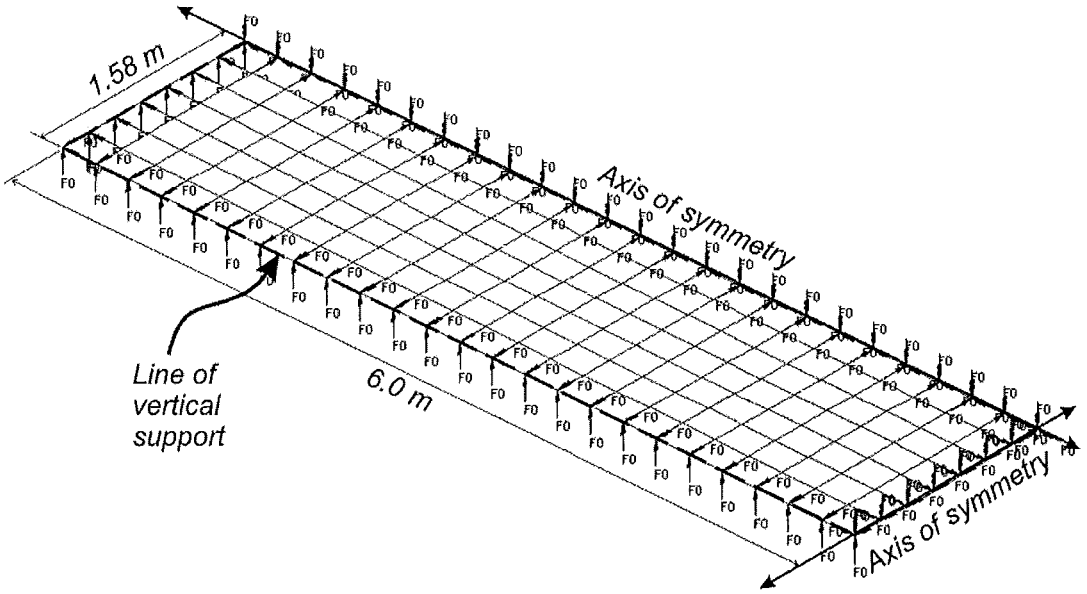

Figure 10-16: Finite element mesh for the structural analysis of the 3.16m x 12.0m slab.

10.6.4. Deflections

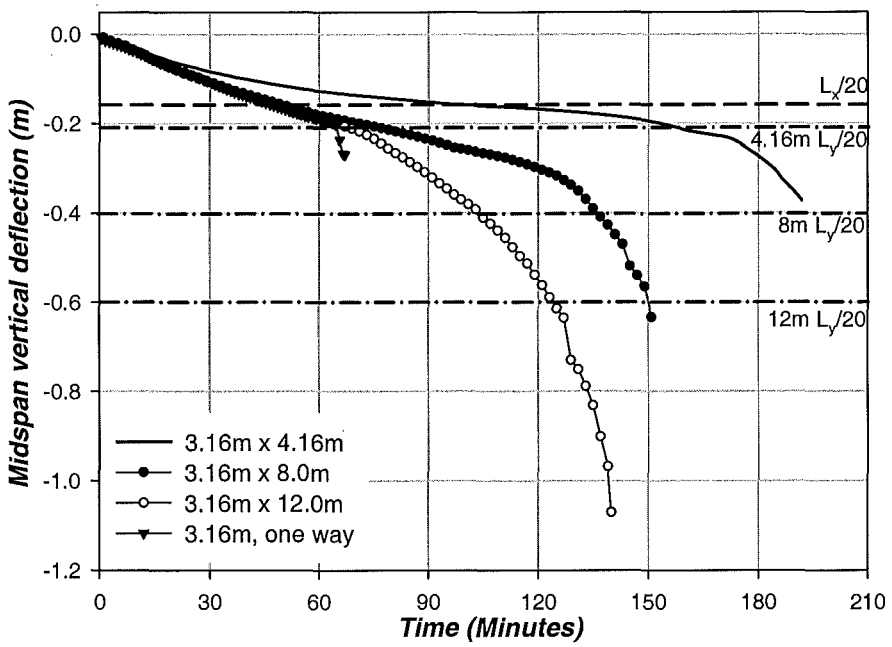

Figure 10-17: Variation of midspan vertical deflections of the slabs with different aspect ratios.

Figure 10-17 shows the variation of the midspan vertical deflections of the slabs with different aspect ratios. The deflection curves of the one-way 3.16m slab (Section 10.4) and the 3.16m x 4.16m slab supported on four sides (Section 8.6) are also plotted. Also plotted on the graph are the $L_y/20$ deflection limits for each of the slabs with different aspect ratios and the $L_x/20$ limit.

The graph shows that during the first 20 minutes, all the slabs had a similar rate of deflection. After 20 minutes, the deflections of the 3.16m x 4.16m diverged from the other slabs due to reduction of its deflection rate. The one-way slab and the 8m and 12m two-way slabs had identical deflection trends, until runaway failure of the one-way slab occurred at 64 minutes. The deflection rate of the 3m x 12m slab increased at 73 minutes, soon after the one-way slab failed, and progressively led to runaway failure. The 3m x 12m slab reached its $L_y/20$ deflection limit of -0.6m at 124 minutes and failed at 140 minutes when the midspan deflection reached -1.07m. For the 3m x 8m slab, runaway failure commenced after 130 minutes. The slab reached its $L_y/20$ deflection limit of -0.4m at 136 minutes and failed at 152 minutes, when the program failed to converge to a solution.

Figure 10-18 and Figure 10-19 show the deflected shapes of the slabs after an hour exposure and when the slabs collapsed. The deflected shapes showed that both slabs had identical midspan deflections after one hour, as shown in the deflection versus time plot in Figure 10-17. When the slabs failed, the edges of the long span had deflected inwards as they were pulled inwards when the slab collapsed downwards. The lateral deflections of the long edges of the 12m slabs were much larger than the 8m slab. The large deflection of the 12m slab is very similar to a one-way slab undergoing runaway failure.

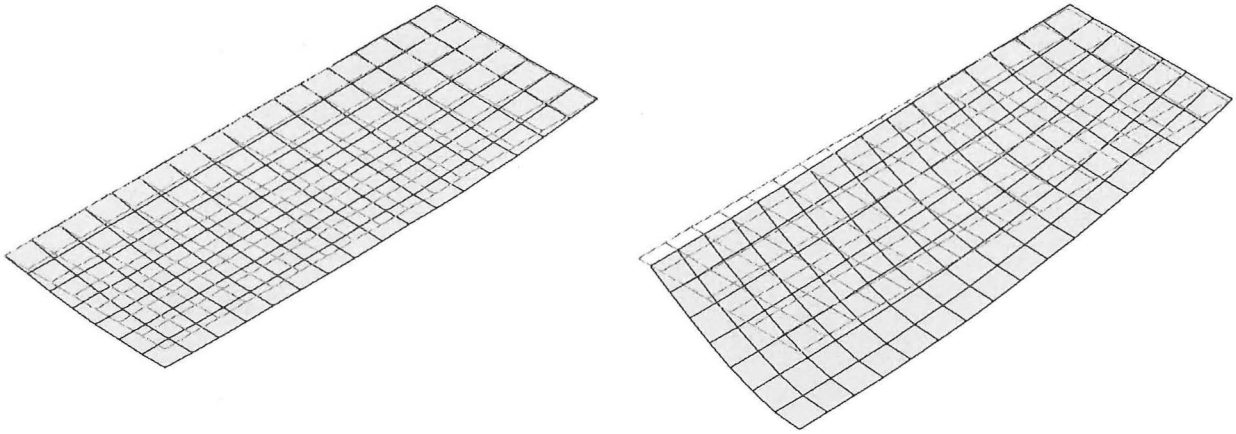

After 1 hour exposure **At failure (152 minutes)**

Figure 10-18: Deflected shape of the 3m x 8m slab.

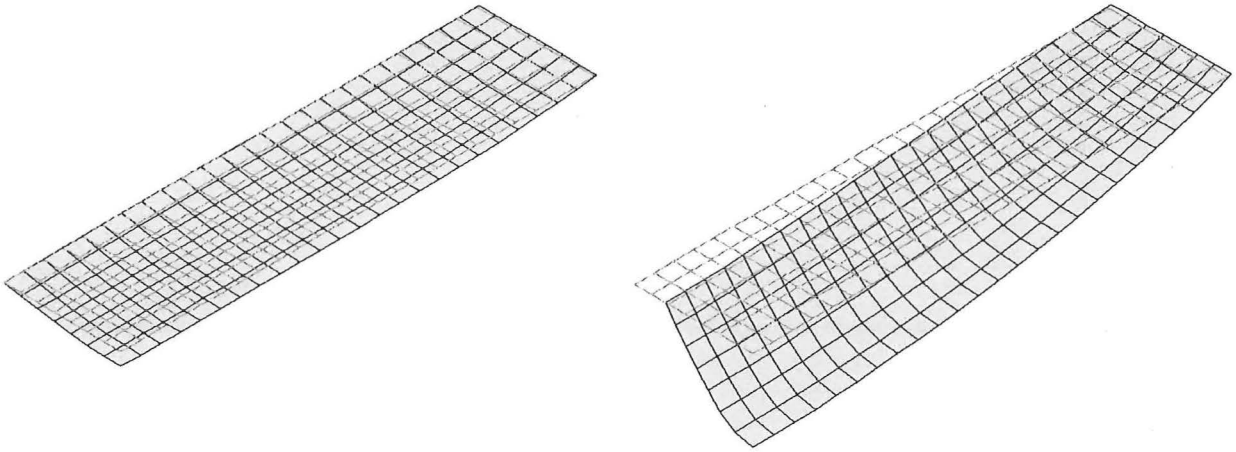

After 1 hour exposure **At failure (140 minutes)**

Figure 10-19: Deflected shape of the 3m x 12m slab.

	L_x	L_y	L_y/L_x	Time to $L_x/20$ (-0.158m)	Time to failure
Slab 1	3.16m	4.16m	1.31	87 minutes	192 minutes
Slab 2	3.16m	8.0m	2.53	47 minutes	152 minutes
Slab 3	3.16m	12.0m	3.80	45 minutes	140 minutes
Slab 4	3.16m	-	-	44 minutes	67 minutes

Table 10-3: Time to reach the limiting deflections for the slabs with different aspect ratios.

Table 10-3 shows the times for the slabs to reach the L_x limiting deflection. Slab 1 had the greatest fire resistance as it took the longest time to exceed the $L_x/20$ deflection criteria, due to its low aspect ratio and its ability to mobilise tensile membrane action. As the aspect ratio of the slab was increased to 2.53 and 3.80, the times when the limiting deflection were exceeded decreased significantly to 47 minutes and 45 minutes, respectively. These times are almost identical to that of the one way slab (Slab 4). By measuring the fire resistances based on the $L_x/20$ criteria, slabs with aspect ratios equal or greater than 2.5 should be considered as one-way slabs as they showed similar behaviour to the one-way slab.

10.6.5. Traction distributions

The principal tractions in the 3m x 8m slab and the 3m x 12m slabs are presented in this section. Figure 10-20 to Figure 10-27 show the distribution of the membrane tractions in the 3m x 8m and the 3m x 12m slab. The following discussion summarises the observations of the membrane tractions in both slabs during the fire.

During the initial stages of the fire (15 minutes), Figure 10-20 and Figure 10-24 show a circular tension field forming near the ends of both slabs, marked '*A*'. The tension field is surrounded by high compression tractions which spread into the middle sections of the slabs. After 30 minutes, the magnitudes of the tractions in the tension field at the ends of both slabs and the surrounding compression tractions increased very substantially. Several bands of compression tractions also formed across the short span of the slabs. After 60 minutes, the compression bands across the short span disappeared but compression tractions had started to form along the long edges. At failure, very high compression tractions formed along the edges of both slabs but the compression tractions at the ends of the slabs had decreased significantly.

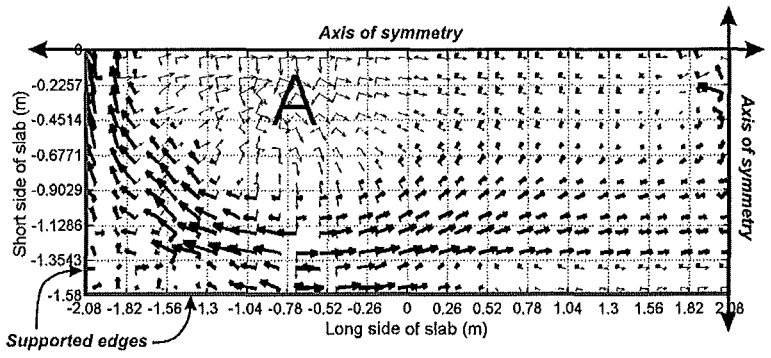

Figure 10-20: Traction distribution after 15 minutes for 3.16m x 8m slab.

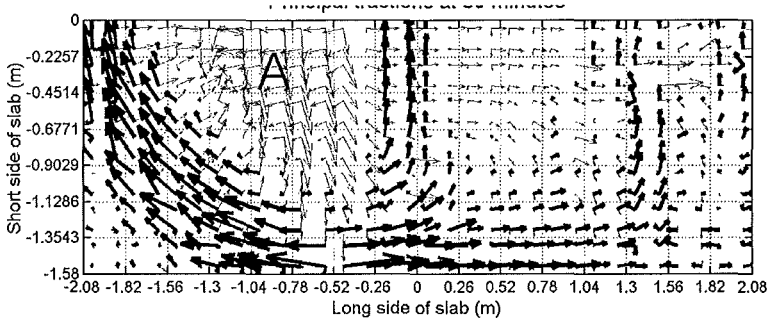

Figure 10-21: Traction distribution after 30 minutes for 3.16m x 8m slab.

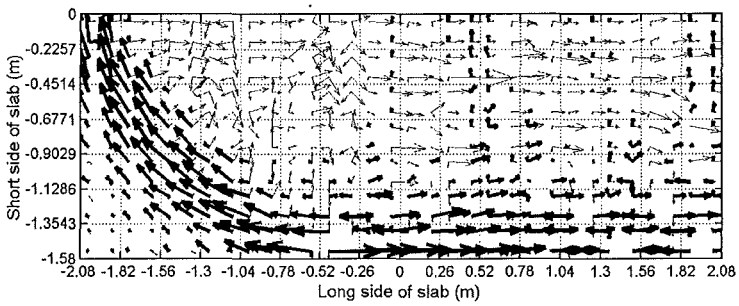

Figure 10-22: Traction distribution after 60 minutes for 3.16m x 8m slab.

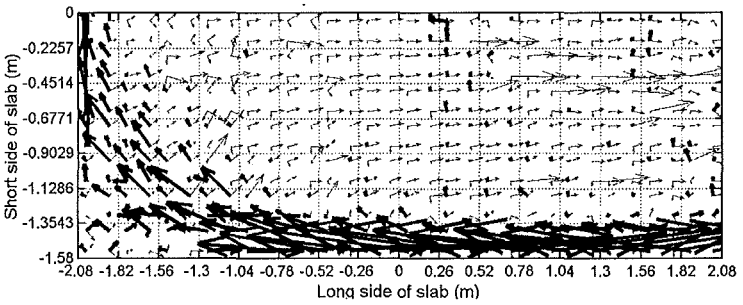

Figure 10-23: Traction distribution at failure (159 minutes) for 3.16m x 8m slab.

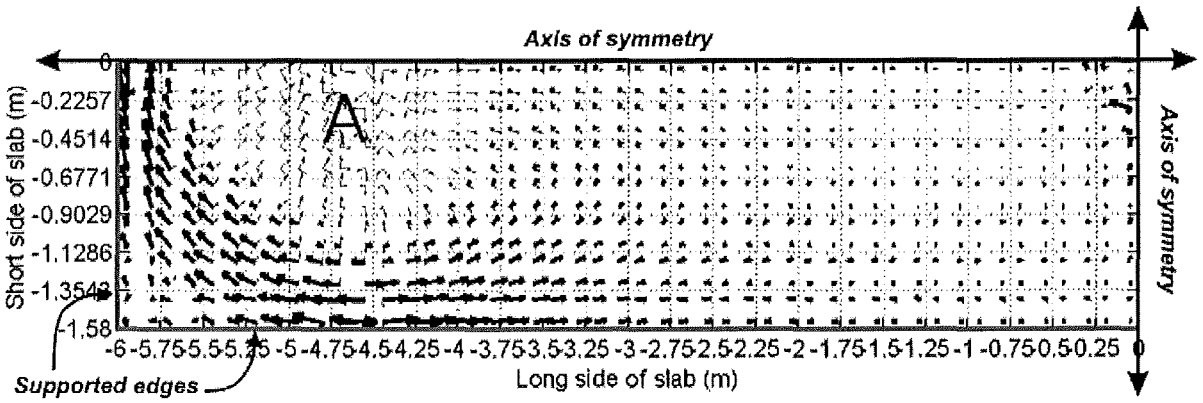

Figure 10-24: Traction distribution after 15 minutes for 3.16m x 12m slab.

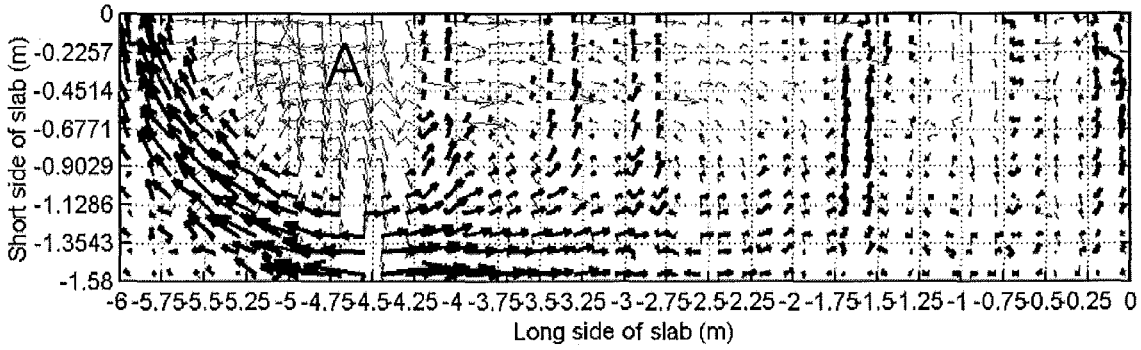

Figure 10-25: Traction distribution after 30 minutes for 3.16m x 12m slab.

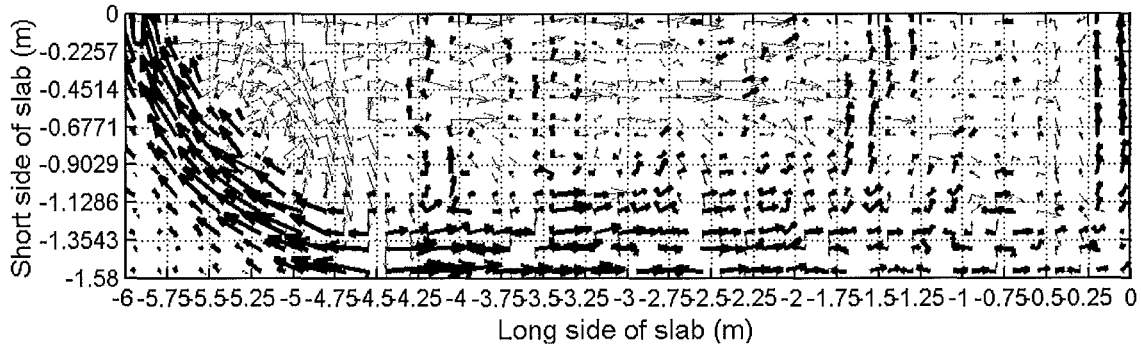

Figure 10-26: Traction distribution after 60 minutes for 3.16m x 12m slab.

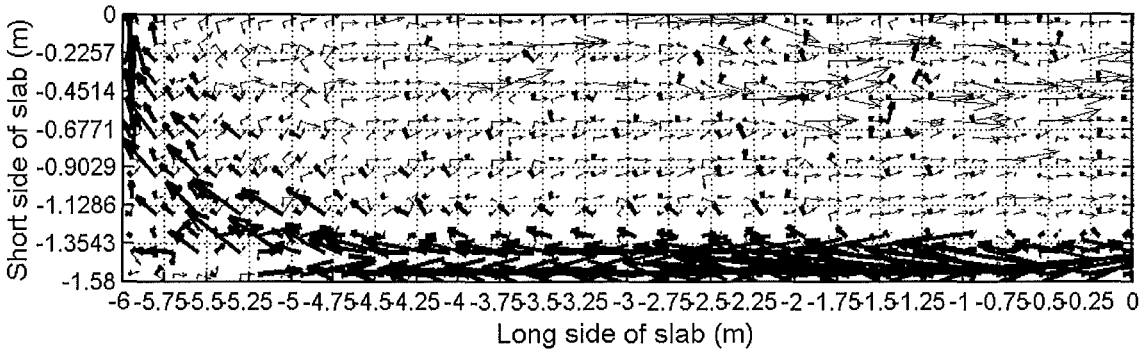

Figure 10-27: Traction distribution at failure (149 minutes) for 3.16m x 12m slab.

The pattern of the membrane tractions in the 3m x 8m and 3m x 12m slabs is similar to those seen in section 8.7 and is attributed to the large vertical deflections of the slab. The large sagging deflections at midspan produced the tension tractions in the middle which were balanced by the compression ring at the outer perimeter. Large spurious tension tractions had also formed in the central region after 60 minutes fire exposure, shown by the large thin arrows. The large tension tractions do not show up if a higher precision is used in the analysis. Conversely, the higher precision may result in convergence problems which may cause the program to terminate the analysis prematurely.

10.6.6. Comparison with yield-line predictions

The variation of the yield line load capacities of the different slabs is presented in this section and is compared with the failure times predicted by SAFIR. This comparison is performed to investigate the accuracy of yield-line theory in predicting the fire resistances of slabs with high aspect ratios.

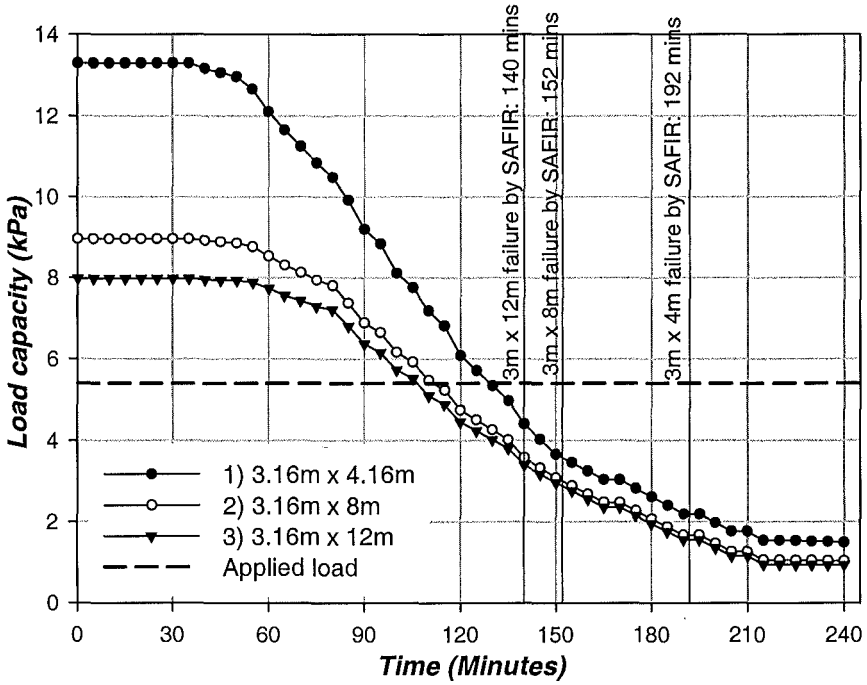

Figure 10-28: Variation of the load capacities of two-way slabs calculated with yield-line theory.

Figure 10-28 shows the variation of the load capacities of the different slabs based on yield-line theory. The variation of the load capacities were calculated using the reduced strengths of the heated reinforcing steel. The initial load capacities of slabs 1, 2 and 3 at ambient conditions were 13.3kPa, 9.0kPa and 8.0kPa, respectively. The graph shows that the yield-line

load capacities of slabs 2 and 3 reached the level of the applied load at 113 minutes and 106 minutes, respectively. Theoretically, the slabs should collapse when the load capacities of the slabs drop below the level of the applied load. However, SAFIR predicted failure much later in the fire at 152 minutes and 140 minutes for the 8m and 12m slabs, respectively. For the 3.16m x 4.16m slab, the difference between the yield-line predictions and the SAFIR predictions was greater, due to tensile membrane action in the slab. Yield-line theory predicted earlier failure in the slabs because it does not account for membrane action.

10.6.7. Conclusions

The analyses of the slabs with the different aspect ratios showed that:

- The fire resistances of the two-way slabs decreased with increasing aspect ratio.
- Slabs with aspect ratios equal or greater than 2.5 can be classified as one-way slabs, based on the $L_x/20$ deflection criteria. However, these slabs showed much higher fire resistances than one-way slabs as they failed much later under very large deflections. Limited tensile membrane action in these slabs increased the fire resistances of the slabs.
- Even though yield-line theory underestimates the actual collapse times of the slabs, it can still be used as a conservative estimate of the fire resistances of two-way slabs.

10.7. The fire behaviour of two-way slabs supported on beams

10.7.1. Introduction

In the previous sections, the slabs were supported on rigid supports that did not deflect during the fire. This section investigates the behaviour of two-way slabs supported on unprotected fire exposed beams that will deflect in a fire situation. The beams are exposed to the ISO fire and are vertically supported on columns at the corners of the slab. The purpose of this is to investigate if slabs on flexible supports can develop tensile membrane action to increase its fire resistance.

10.7.2. Scope

In section 10.7.3, the slabs will be analysed with different beam sizes to investigate its effect on the behaviour of the slabs. In this section, only one type of beam connection to the vertical support will be used.

Section 10.7.4 will investigate the behaviour of the slab with different types of connections from the beams to the corner supports. These connections simulate different horizontal and rotational restraint conditions, with one beam size.

10.7.3. Different beam sizes

The behaviour of a slab supported on beams of different sizes is investigated in this section. Three different beam sizes will be investigated for one slab configuration. The section sizes of the universal beams are shown in Table 10-4 and were obtained from the *Hot-rolled and Structural Products* by BHP Steel (1994). The same beam size will be used to support the slab on the long and short spans. The beams were exposed to the ISO fire from one side and from the bottom, as shown in Figure 10-29, to simulate the heating conditions of a compartment fire under the slab.

Beam	Weight	Overall Depth	Flange width	Elastic Section modulus, Z_{ex}
460UB82	82 kg/m	460 mm	191 mm	1610,000 mm^3
360UB51	51 kg/m	356 mm	171 mm	798,000 mm^3
250UB31	31 kg/m	252 mm	146 mm	354,000 mm^3

Table 10-4: Properties of the beams to be used in the analyses.

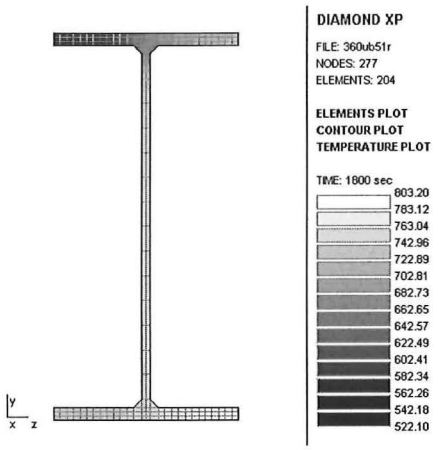

Figure 10-29: Thermal analysis of the 360UB beam exposed to 2 sided heating.

Structural model

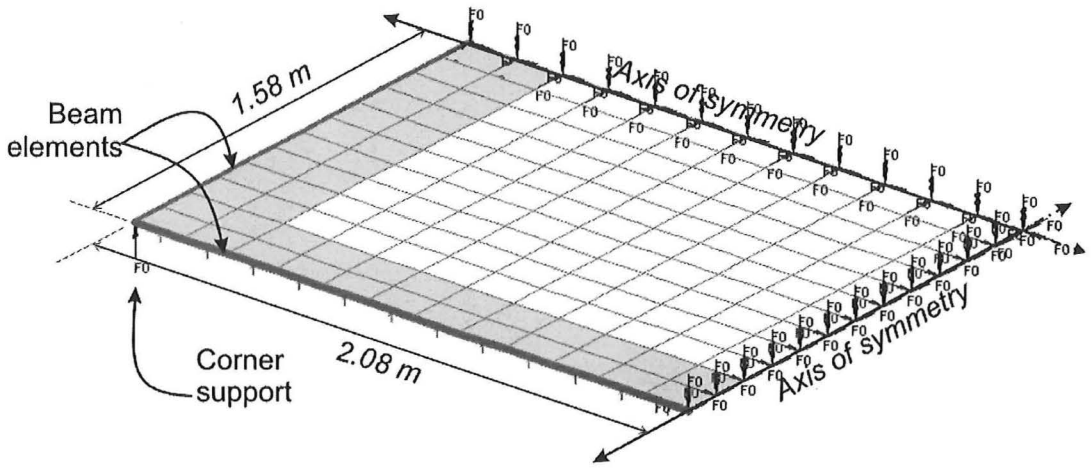

Figure 10-30: Structural model of the slab supported on the beams.

Figure 10-30 shows the SAFIR structural model of a quarter of the slab supported on beams. The lines at the outer edges of the slab in the model represent the beam elements which were vertically supported at the four corners of the slab. The vertical supports at the corners represent protected columns which do not deflect during the fire. The beams were horizontally and rotationally unrestrained at the corner support, but with warping restraint of the beams imposed. The shaded shell elements represent the slab with top and bottom reinforcing steel while the light coloured elements represent the slab reinforced with bottom steel only.

Deflections of the slab on the 360UB beam

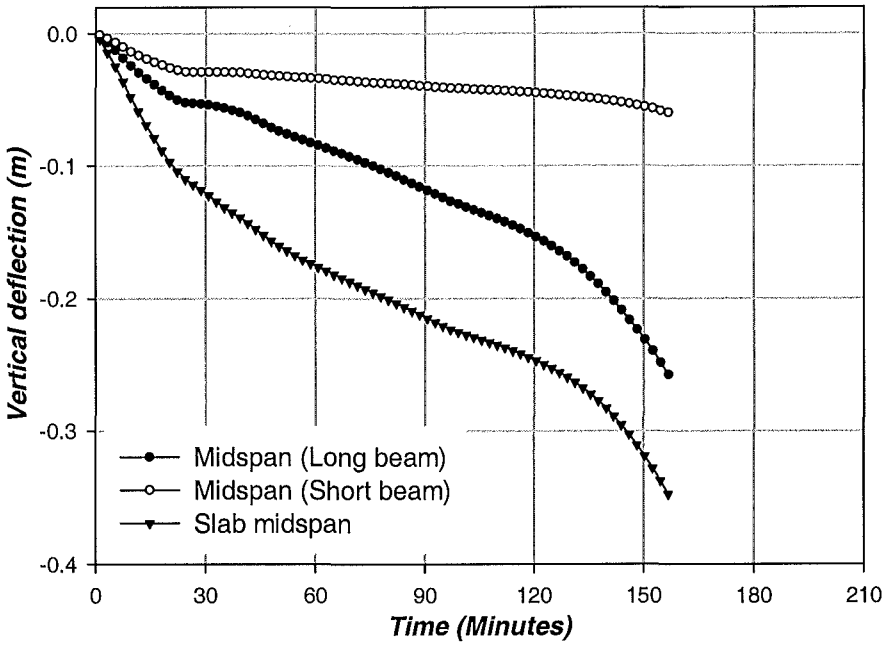

Figure 10-31: Vertical deflections of the slab supported on the 360UB beams.

Figure 10-31 shows the variation of the vertical deflections of the slab supported on the 360UB beams. The deflections at the middle of the slab and at the middle of the long and short spans of the beams were plotted. The graph shows that the slab had a similar deflection trend to the longer beam but with larger deflections. This indicates that the slab deflections were governed by the deflections of the longer beam. The slab deflected in a bilinear manner, with a high deflection rate initially followed by a lower rate. At 135 minutes, the deflection rate increased again due to a plastic hinge forming at midspan of the long beams. The plastic hinge at midspan of the beam caused the slab to fold in half across the long span, as shown in Figure 10-32. The shorter beam suffered much smaller deflections than the longer beam and did not exhibit runaway failure at the end of the analysis.

The analysis stopped at 157 minutes when the stresses of the bottom flange of the long beam at the support yielded in compression and reached the descending branch of the stress-strain curve. This caused convergence problems and the analysis could not carry on. In a real beam, the high compressive stresses and strains can be accommodated by local buckling of the bottom flange. However, the beam finite element cannot account for local buckling of the flange, therefore resulting in the high compressive strains and convergence problems.

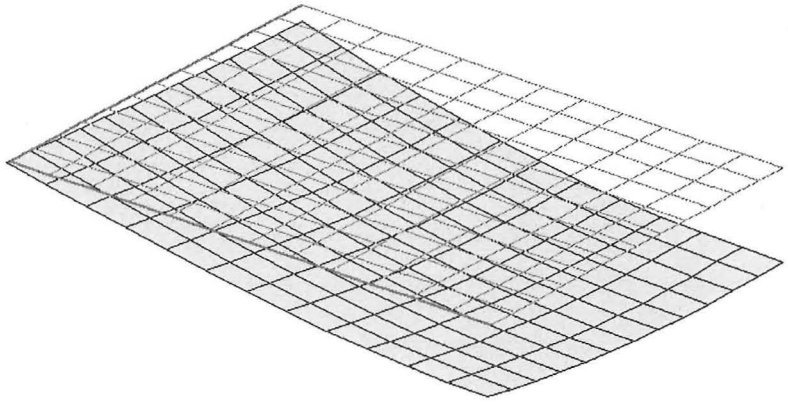

Figure 10-32: Final deflected shape of the slab supported on the 360UB beam.

Deflections of the slab on different sized beams

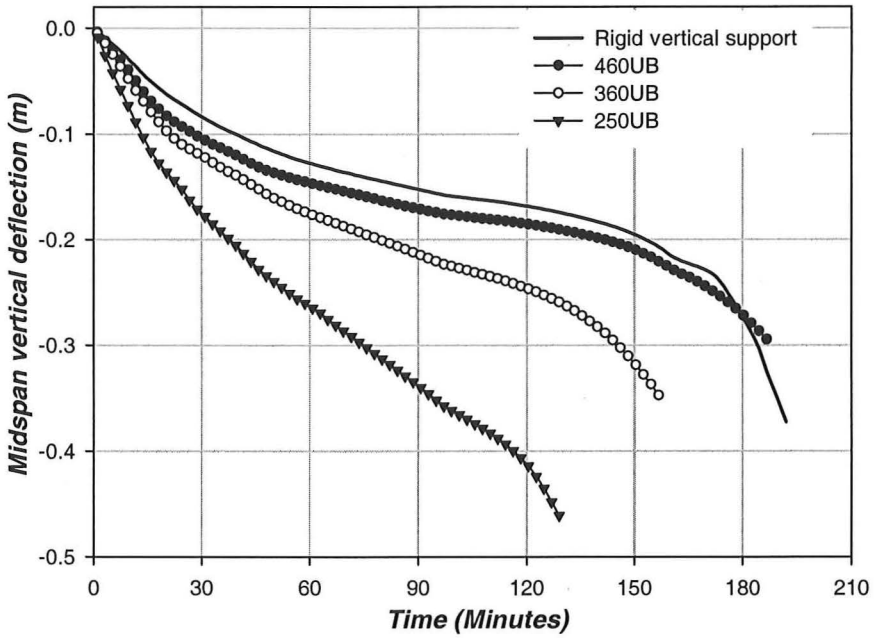

Figure 10-33: Midspan deflections of the slabs supported on different sized beams.

Figure 10-33 shows the variation of the midspan vertical deflections of the slab supported on different sized beams. The slab supported on rigid vertical supports, analysed in section 8.6, is also plotted for comparison. The slab supported on the 460UB beams showed very close agreement to the slab supported on rigid vertical supports. As the beam size decreased, failure of the slabs occurred earlier with larger slab deflections. Final failure of the slabs on the 360UB and 250UB beams were due to compressive stresses of the bottom flange of the long beam at the supports reaching the descending branch of the stress strain curve, which occurred after runaway failure commenced. This caused the slab to deform in single curvature

and fold in half. The 460UB beam was strong and stiff enough to resist failure and allowed the slab to behave similarly as if it was on rigid vertical supports. Failure occurred for the slab on the 460UB beams when the reinforcing steel at midspan ruptured, instead of forming at the beams.

Traction distributions

Figure 10-34 to Figure 10-36 show the distributions of the principal traction forces in the slab supported on the 360UB beam. Figure 10-34 shows that during the initial stages of the fire, high tensile tractions formed in the slab and propagated from the corner support to the central region of the slab. A thick band of compression tractions formed diagonally between the long and short beams. This was possibly due to the in-plane restraint provided by the beams against the thermal expansion of the heated slab. At this early stage, the beams were stiff and could provide substantial lateral restraint. This pattern was observed during the first 30 minutes and progressively changed to the pattern shown in Figure 10-35.

At 45 minutes, the slab had sustained significant deflections and had deformed into double curvature. The sagging deflections of the slab at midspan produced a tension field in the middle of the slab and a compression ring at the outer edges, as shown in Figure 10-35. The in-plane compression forces between the long and short beams which formed under small vertical deflections were relieved by the large deflections of the slab. The slab showed the same pattern of tractions until the end of the fire when the slab collapsed (Figure 10-36).

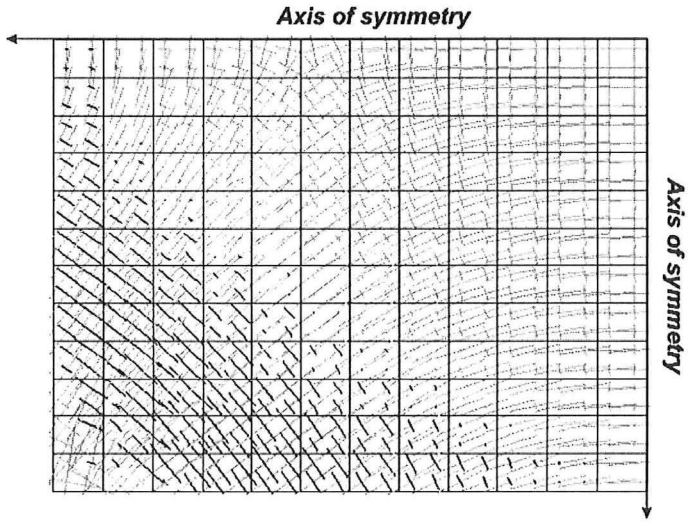

Figure 10-34: Distribution of tractions after 5 minutes.

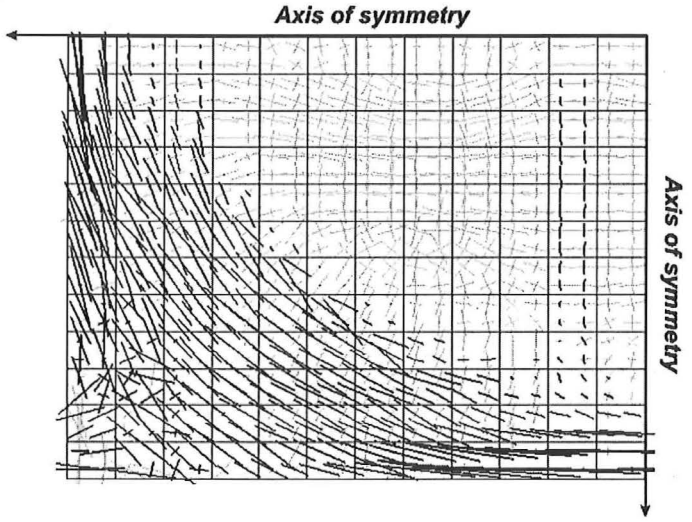

Figure 10-35: Distribution of tractions after 45 minutes.

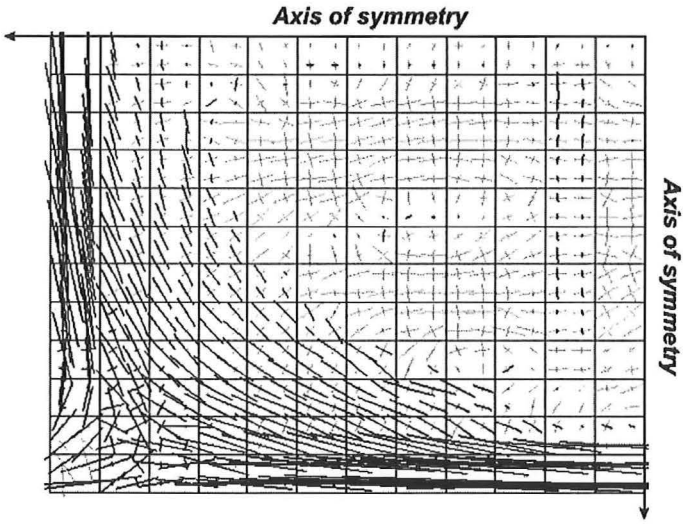

Figure 10-36: Distribution of tractions at failure.

10.7.4. Different corner restraint conditions

The behaviour of the slab with different boundary conditions at the corner supports is investigated in this section. The slab is analysed with one beam size, 360UB, with different connections between the beam and the vertical supports. The different cases that are analysed are shown in Table 10-5.

Slab	Connections between beam and corner support	
	Rotational restraint	Horizontal restraint
1: Fix-slide	Yes	No
2: Pin-roller	No	No
3: Pin-pin	No	Yes
4: Rigid supports, No beams	No	No

Table 10-5: Cases analysed with different beam-support connections.

Structural model

Figure 10-37 shows the support conditions for the fix-slide slab (slab 1), with rotationally fixed connections between the beam and the supports but is free to move horizontally. This restraint condition simulates a column which provides low axial restraint but is connected to the beam with rotationally fixed connections. Slab 2 has the same support conditions to the slab which has been analysed in the previous section (section 10.7.3). Figure 10-38 shows the support condition for slab 3 which prevents horizontal movement at the corner support but is rotationally unrestrained. This restraint condition simulates a column which provides very high axial restraint but is connected to the beam with pinned connections.

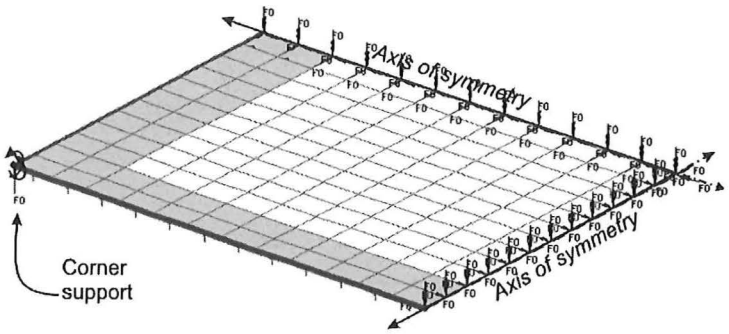

Figure 10-37: Structural model for the slab with rotationally fixed corner supports (Slab 1).

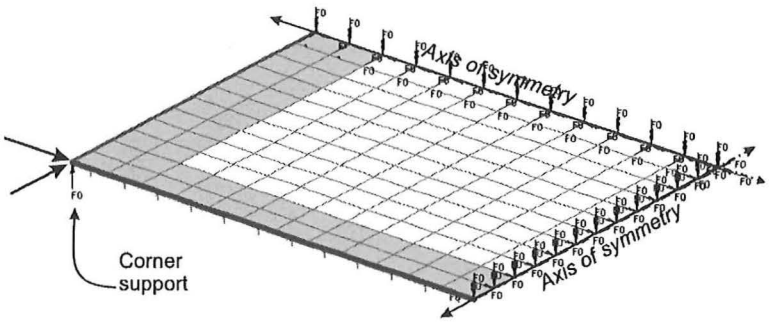

Figure 10-38: Structural model for the slab with axially restrained corner support (Slab 3).

Deflections

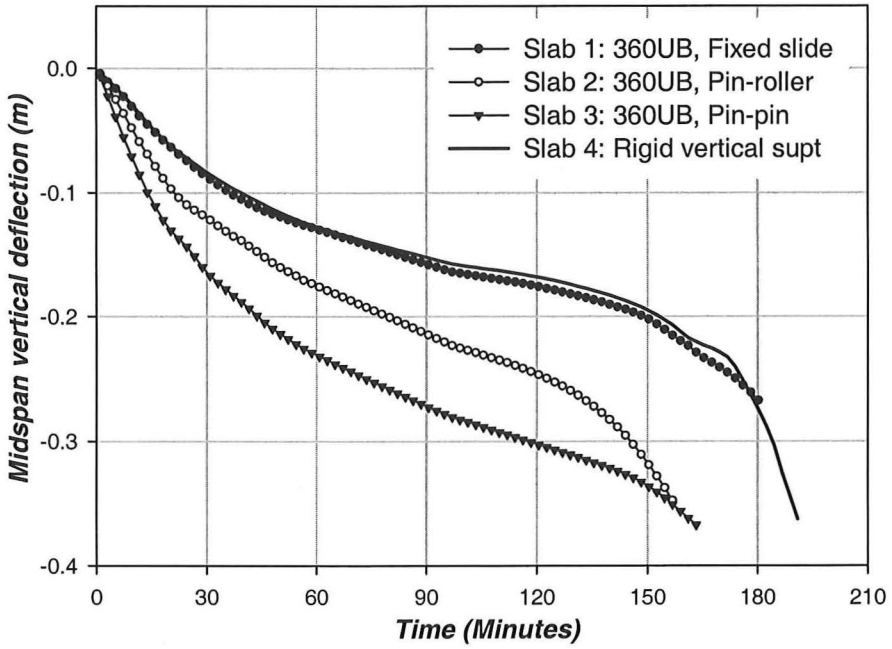

Figure 10-39: Deflections of the slab with different boundary conditions at the corner support.

Figure 10-39 shows the behaviour of the slab with various types of boundary conditions between the beam and the vertical supports. The deflections of the slab on rigid vertical supports (from section 8.6) are plotted. The behaviour of the slab on the pin-roller corners (Slab 2) has been discussed in section 10.7.3.

The analysis shows that the deflections of the slab with rotationally fixed connections (Slab 1) are very similar to the slab on rigid supports (Slab 4). The higher structural redundancy of the supports due to the rotational restraint of the connections increased the stiffness of the beams and prevented large deflections of the supporting beams. This enabled the slab to deform into double curvature and mobilise tensile membrane action. This prevented the collapse mode

observed in Case 2 (Pin-roller support) whereby failure of the floor system was initiated by a plastic hinge forming at midspan of the longer beam and caused the slab to fold in half.

The slab on pin-pin corner supports (Slab 3) showed a very high deflection rate during the initial stages. The high deflection rate was attributed to the high in-plane forces imposed by the corner restraint which forced the slab to deflect downwards rapidly. The axial restraint by the corner support prevented horizontal deflection of the slab due to thermal expansion. Therefore, the increased length of the slab caused by thermal expansion was accommodated by the large vertical deflections.

10.7.5. Conclusions

The analyses in this section have shown that:

- The fire resistances of the floor systems decreases as the size of the supporting beams decreased.
- Weak supporting beams resulted in the slabs failing as a one-way slab across the long span. Very strong and rigid supporting beams on all four edges of the slab enabled it to deform into double curvature and mobilise tensile membrane action, preventing the slab from folding in half.
- The behaviour of the slabs was very sensitive to the corner restraint and the type of beam-column connection. Rotationally restrained connections at the corner supports produced very similar behaviour to the slab on rigid vertical supports and had much smaller deflections than if rotational fixity was not imposed.
- The pin-pin corner connections produced high compression forces in the slab during the initial stages of the fire which caused compressive yielding of the supporting beams.
- The different beam-column connections produced different amounts of slab deflection but did not have a significant effect on the fire resistances of the slabs.

11. CONCLUSIONS AND RECOMMENDATIONS

11.1.Introduction

This research project was conducted to study the behaviour of reinforced concrete slabs under fire conditions. The main objectives of this research were to investigate the influence of compressive membrane action and tensile membrane action on the behaviour of reinforced concrete slabs subjected to fire conditions. The study on compressive membrane action was performed on one-way slabs with 2D finite element analyses using SAFIR. The investigation on tensile membrane action was performed on two-way slabs, focussing on two-way behaviour under large deflections without horizontal axial restraint. The study was performed with experimental fire tests and 3D finite element analyses using SAFIR.

11.2.Compressive membrane action of fire exposed one-way concrete slabs

An analytical study has been carried out into the structural behaviour of one-way reinforced concrete floor systems exposed to fire on the underside, with various stiffnesses of axial and flexural restraint at the supports.

11.2.1. Main conclusions

The main findings of the research on one-way slabs are follows:

i) The behaviour of one-way slabs under fire conditions is very sensitive to their end support conditions and the axial restraint stiffness.

ii) Slabs with rotational restraint at both end supports have much better behaviour and significantly higher fire resistance than pin-supported slabs.

iii) The behaviour of a slab under compressive restraint is not easy to quantify and model, even with a sophisticated finite element program. Computer modelling of restrained reinforced concrete floor systems is difficult because of poor information about the actual boundary conditions in real construction, especially the likely height of the axial restraint force, which may change in location during fire exposure.

11.2.2. Pin-supported slabs with fixed line of thrust

The analyses of pin-supported slabs with fixed line of thrust have shown that:

vi) The behaviour of axially restrained pin-supported slabs under fire conditions is very sensitive to the position of the line of thrust at the supports and the stiffness of the axial restraint.

vii) High compressive axial restraint does not always increase the fire resistance of one-way pin-supported slabs. High compressive restraint is beneficial only if the line of thrust at the supports is located well below the centroidal axis and when the centroidal axis of the slab remains above the line of thrust during the fire exposure.

viii) High compressive axial restraint produces poor slab behaviour if the line of thrust at the supports is located close to the centroidal axis. In this case, high compressive restraint increases the vertical deflections of the slab and decreases the time to plastic hinge formation.

ix) For pin-supported slabs with the line of thrust fixed and located close to the soffit (up to 50mm above the soffit), high axial restraint ($\Delta L/L \leq 0.001$ and $k \geq 40\%$) produces good behaviour and high fire resistance. With intermediate or low axial restraint stiffness ($\Delta L/L > 0.001$ and $k < 40\%$), the slab deforms into a catenary, resulting in axial tensile forces being generated. If the slab does not have sufficient axial tensile capacity at the supports to resist the tensile forces, it will collapse.

x) The behaviour of a pin-supported slab in a real fire is no worse than in a long duration ISO fire. In many cases, better slab behaviour was observed in the decaying fire compared with a long duration ISO fire.

11.2.3. Rotationally restrained slabs

The analyses of rotationally restrained slabs have shown that:

iv) Slabs with flexural continuity have excellent behaviour under fire conditions.

v) Rotationally restrained slabs with low axial restraint have better fire resistance than simply supported slabs and have smaller deflections than equivalent pin-supported slabs.

vi) Rotationally restrained slabs with top steel curtailed according to code recommendations (SNZ, 1995) showed similar behaviour to those with top steel over the full length of the slab.

11.2.4. Pin-supported slabs with moveable line of thrust

Pin-supported slabs with moveable line of thrust refer to slabs modelled to simulate cast-in-situ reinforced concrete slabs (See Section 5.8 and 5.9 for details). The analyses have shown that:

i) Compressive restraint increases the fire resistance of pin-supported slabs with moveable line of thrust if the axial restraint stiffness is high ($\Delta L/L \leq 0.001$ and $k \geq 40\%$). For slabs with high axial restraint, compressive restraint is beneficial to the slab behaviour if the vertical deflections are small and if the line of thrust at the end supports is located below the centroidal axis. The beneficial effects of compressive restraint are lost if the centroidal axis of the slab drops below the line of thrust.

ii) For slabs with low and intermediate axial restraint stiffness ($\Delta L/L > 0.001$ and $k < 40\%$), compressive axial restraint produces worse behaviour than the *pin-roller* (unrestrained) condition.

iii) Compared with the rotationally restrained slabs, the time to failure of these slabs can be very low if there is no top steel anchored into the supports.

iv) The fire behaviour of these slabs with low and intermediate axial restraint stiffnesses is sensitive to the length of the top steel at the supports. The fire resistance of these slabs increases as the length of the top steel increase. Slabs with high axial restraint are less sensitive to the lengths of the top steel at the supports.

v) The thrust-expansion results from the SAFIR analyses of slabs with moveable line of thrust showed a similar trend to the results of the PCA tests.

vi) The PCI hand calculation method is not recommended for assessing the required stiffness to enhance the fire resistance of pin-supported slabs, because it is an over-simplification of slab behaviour in fire.

11.2.5. Recommendations for design and construction of one-way slabs

The hierarchy of design recommendations for fire resistance of one-way slabs is as follows:

i) One-way slabs have excellent fire behaviour if they are designed as continuous slabs with their top steel curtailed according to current code recommendations such as the Concrete Structures Standard (NZS, 1995) and have low axial restraint ($\Delta L/L \geq 0.0055$ and $k \leq 1\%$).

- The top reinforcement bars at the supports should not be severely curtailed, to allow redistribution of the moments to increase the fire resistance of the slabs.
- The top reinforcement bars at the supports must be able to withstand high strains due to the large rotations. Ductile reinforcing bars must be used rather than cold-formed mesh.

ii) For slabs without flexural continuity (pin-supported), fire resistance can be increased by supporting the slab at all four edges to provide some two-way action (See section 11.3.4).

iii) Slabs without flexural continuity or two-way action should be designed as simply supported slabs with sufficient strength to resist the loads for the expected fire duration. Simple hand methods, found in references such as CRSI (1980), Purkiss (1996), Buchanan (2001) and Fleischmann et al. (2002), can be used.

iv) If compressive axial restraint is required to increase the fire resistance of pin-supported slabs, the following details must be applied:

- The horizontal movement of the slab at its supports must be less than 0.001L and the axial restraint stiffness must be greater than 40% of the axial stiffness of the heated slab.
- The supports must be detailed to maximise the distance between the line of thrust at the supports and the centroidal axis of the slab. Support details with the line of thrust located close to the centroidal axis (e.g.: flange mounted double tees with webs cut away) must be avoided.
- Some of the reinforcing of the slab must be anchored into the supports to prevent catastrophic collapse should the slabs deform into catenary mode.

11.3.Tensile membrane action in fire exposed two-way concrete slabs

The study into tensile membrane action in unrestrained two-way slabs under fire conditions was conducted with experimental fire tests and 3D finite element analyses. The experimental tests consisted of fire tests of six concrete slabs conducted on a fire resistance furnace. The slabs comprised three flat slabs and three composite steel-concrete slabs. The slabs were simply supported at all four edges and were horizontally unrestrained. They were loaded with a constant live load and were exposed to the ISO standard fire for three hours. The 3D finite element analyses were performed with SAFIR using shell and beam elements, to predict the behaviour of the tested slabs and to model slabs with different geometries and support conditions.

11.3.1. Main conclusions

The main findings of the study are as follows:

i) Two-way simply supported slabs have much greater fire resistance than one-way simply supported slabs. The high fire resistance of two-way slabs is due to tensile membrane action.

ii) The SAFIR shell element can be used to accurately model the 3D behaviour of flat slabs and composite slabs under fire conditions. Modelling of the tested slabs with the SAFIR shell element showed good agreement with the experimental results.

iii) The behaviour of two-way slabs under fire conditions is sensitive to the aspect ratio of the slabs and their support conditions.

11.3.2. 3D modelling of slabs with SAFIR

i) SAFIR can be used to predict the behaviour of two-way slabs at ambient and fire conditions while taking account of material and geometrical non-linearities.

ii) SAFIR predicted higher ultimate loads in two-way slabs at ambient conditions compared with yield line predictions. The higher predicted load capacity was due to in-plane membrane forces not included in yield-line analysis.

iii) The behaviour of composite slabs at ambient and fire conditions can be modelled by combining beam and shell elements. The behaviour of composite slabs with steel decking is difficult to predict accurately because the numerical analysis cannot account for slippage and debonding of the steel decking from the slab.

iv) The results of the SAFIR analyses were sensitive to the concrete tensile strength, particularly in lightly reinforced slabs. Any analysis with the plane stress concrete model should be performed with concrete tensile strength not greater than $0.25\sqrt{f'_c}$. Zero concrete tensile strength can be used as a conservative value to predict the behaviour of existing structures which have suffered cracking.

11.3.3. The behaviour of two-way slabs under fire conditions

The experimental fire tests of two-way slabs showed that:

i) The slabs supported the applied loads for the entire duration of the fire without collapse despite suffering large deflections. The good behaviour of the slabs is due to tensile membrane action.

ii) The cold-drawn mesh used in the fire tests did not rupture because the fire tests were stopped before rupture occurred. The high temperatures increased the ductility of the steel and enabled to the steel to resist high tensile strains without rupture.

iii) The tests showed that the amount of reinforcement in the slab is important for maintaining the integrity of the slabs. Slabs with light reinforcement and large bar spacings (three times the slab thickness) suffered large, full-depth cracks. With smaller bar spacings (up to two times the slab thickness) the slabs only suffered superficial cracking.

iv) The test of the Hibond composite slab showed that under prolonged fire exposure, holes can form in the steel decking due to oxidisation, potentially causing integrity failure.

The SAFIR analyses of two-way slabs in fire conditions showed that:

i) Significant membrane forces formed in the slab during the fire. The membrane forces comprise a tensile field at the midspan region, surrounded by a compression ring at the outer edges. The magnitudes of the membrane forces decreased during a fire, due to strength degradation of the reinforcing steel.

ii) The analyses showed that the initial deflections were due to thermal bowing. At the advanced stages of a fire, the slab deflections were caused by stiffness degradation of the reinforcing steel. SAFIR showed that failure occurred when the steel at midspan ruptures.

iii) The extent of tensile membrane enhancement in two-way slabs is dependent on their aspect ratio. Slabs with high aspect ratios ($L_y/L_x \geq 2.5$) have lower tensile membrane enhancement, and their behaviour approach that of a one-way slab.

iv) Tensile membrane enhancement of two-way slabs requires stiff vertical beam supports on all four edges of the slab. Strong and stiff supporting beams are required to enable the slab to deform into double curvature in order to mobilise tensile membrane action.

v) Tensile membrane enhancement cannot be mobilised if one or more supporting beams deflects excessively.

vi) The fire behaviour of the slabs is very sensitive to the corner restraint and the beam-column connection. Different beam-column connections produced similar fire resistances but with different amounts of deflections.

11.3.4. Recommendations for design and construction of two-way slabs

This section presents the recommendations for design and construction of two-way slabs based on the experimental fire tests and finite element analyses of the slabs conducted in this study.

i) Two-way slabs with supports on all four edges and no axial restraint have excellent fire resistance provided there is sufficient reinforcing to develop tensile membrane action for the duration of the fire.

ii) Either hot-rolled reinforcing bars or cold-drawn mesh may be used as the bottom reinforcement for two-way slabs. The steel content in the slab has to be at least $300mm^2/m$ and the bar spacings not greater than two times the slab thickness. The cover to the reinforcement should be based on current code recommendations such as the Concrete Structures Standard (NZS, 1995).

iii) Two-way slabs with high aspect ratios ($L_y/L_x \geq 2.5$) behave similarly to one-way slabs. Fire protection must be applied to the appropriate supporting beams to avoid high aspect ratios of the slabs under fire conditions.

iv) The supporting beams of the slabs must be well protected to provide stiff vertical support to the slabs in order to mobilise tensile membrane action.

v) If two-way action cannot be provided, fire resistance can be increased by adding top steel at the supports of the slabs to provide flexural continuity (See section 11.2.5 for details). The top steel must be curtailed according to code recommendations.

vi) The beam-column connections must be designed to resist high tension forces if the beams deform into catenary mode.

11.4.Recommendations for future research

The following areas should be investigated in future research projects:

i) The behaviour of one-way and two-way slabs with unsymmetrical distributed or point loads.

ii) The effect of different slenderness ratios in fire-exposed slabs with compressive axial restraint.

iii) 2D finite element analyses of fire-exposed double tee and hollow-core slabs with compressive axial restraint.

iv) Determine the effect of elevated temperatures on the ductility of cold-formed mesh.

REFERENCES

1. Anderberg, Y. (1973) Fire-exposed hyperstatic concrete structures. *Bulletin 32*, Division of Structural Mechanics and Concrete Construction, Lund Institute of Technology, Lund, Sweden.

2. Anderberg, Y. (1978) 'Fire-exposed hyperstatic concrete structures: An experimental and theoretical study'. In: *Analytical design of fire exposed concrete structure Bulletin 65*. Eds: Y. Anderberg, S.E. Magnusson, S. Thelandersson, O. Petterson, U. Wickström. Lund Institute of Technology, Lund, Sweden.

3. Anderberg, Y. (1991) SUPER-TEMPCALC. A commercial and user-friendly computer program with automatic FEM-generation for temperature analysis of structures exposed to heat. Fire Safety Design, Lund, Sweden.

4. Anderberg, Y., Thelandersson, S. (1976) Stress and deformation characteristics of concrete at high temperatures, *Bulletin 54*, Division of Structural Mechanics and Concrete Construction, Lund Institute of Technology, Lund, Sweden.

5. Anderberg, Y. and Forsen, N.E. (1982) Fire Resistance of Concrete Structures, Division of Structural Mechanics and Concrete Construction, Lund Institute of Technology, Lund, Sweden.

6. ASTM (1999) Standard test methods for fire tests of building construction and materials, E119-98. American Society for Testing and Materials. Philadelphia, U.S.A.

7. Bailey, C.G., Lennon, T. and Moore, D.B. (1999) The behaviour of full-scale steel-framed buildings subjected to compartment fires. *The Structural Engineer*. Vol. 77 No. 8. pp. 15-21.

8. Bailey, C.G., White, D.S. and Moore, D.B. (2000) The tensile membrane action of unrestrained composite slabs simulated under fire conditions. *Engineering Structures*. Vol. 22 No. 11. pp 1583-1595.

9. Bailey, C.G. and Moore, D.B. (2000a) The structural behaviour of steel frames with composite floorslabs subject to fire: Part 1: Theory. *The Structural Engineer*. Vol. 78 No. 11. pp. 19-27.

10. Bailey, C.G. and Moore, D.B. (2000b) The structural behaviour of steel frames with composite floorslabs subject to fire: Part 2: Design. *The Structural Engineer*. Vol. 78 No. 11. pp. 28-33.

11. Bailey, C.G. (2001) Membrane action of unrestrained lightly reinforced concrete slabs at large displacements. *Engineering Structures*. Vol. 23. No. 5. pp. 470-483.

12. Batoz, J.L. and Tahar, M.B. (1982) Evaluation of a new quadrilateral thin plate bending element. *Int. J. Num. Meth. Eng.*, Vol. 18, pp. 1655-1677.

13. Bazant, P.Z. and Nilson A.H. (1982) *Finite element analysis of reinforced concrete,* American Society of Civil Engineers. New York.

14. Bazant, P.Z. and Kaplan, M.F. (1996) *Concrete at High Temperatures: Material Properties and Mathematical Models,* Concrete Design and Construction Series, Longman Group Limited, U.K.

15. Becker, J. and Bresler, B. (1974) FIRES-RC. A computer program for the fire response of structures-Reinforced Concrete Frames. University of California, Berkeley.

16. BHP Steel (1994) *Hot Rolled and Structural Steel Products.* BHP Co. Pty. Ltd. Australia.

17. Blundell, R., Diamond, C. and Browne, R.G. (1976) The properties of concrete subjected to elevated temperatures, *Technical Note No. 9,* CIRIA Underwater Engineering Group, London.

18. Browne, R.D. (1972) Thermal movement of concrete, *Concrete,* Vol. 6, No.11, 51-53.

19. Buchanan, A.H. (2001) *Structural Design for Fire Safety.* John Wiley & Sons, Ltd. U.K.

20. BIA (1992) *New Zealand Building Code Handbook and Approved Documents.* Building Industry Authority, Wellington.

21. Carlson, C.C., Selvaggio, S.L. and Gustaferro, A.H. (1965) A review of studies of the effects of restraint on the fire resistance of prestressed concrete. *Proc. Symposium on Fire Resistance of Prestressed Concrete, Germany.* International Federation for Prestressing (F.I.P.) Germany. Reprinted as PCA Research Department Bulletin 206.

22. Cembureau and FIP (1979) *Concrete for fire resistant construction.* Cement and Concrete Association, Wexham Springs, Slough. U.K.

23. Clifton, G.C. and Beck, C. (2003) Design of Multi-Storey Steel Framed Buildings with Unprotected Secondary beams or joists for Dependable Inelastic Response in Severe Fires: Second Edition. *HERA Steel Design and Construction Bulletin No. 71,* HERA, Manukau City, New Zealand.

24. Cooke G.M.E. (1993) Results of tests on end-restrained reinforced concrete floor strips exposed to standard fires. Report prepared for the Construction Directorate of the Department of the Environment. Fire Research Station, Hertfordshire, U.K.

25. Crisfield, M.A. (1981) A fast incremental/iterative solution procedure that handles "snap-through". *Computers and Structures.* Vol. 13. pp. 55-52.

26. CRSI (1980) *Reinforced Concrete Fire Resistance.* Concrete Reinforcing Steel Institute, Chicago, USA.

27. Cruz, C.R. and Gillen, M. (1980) Thermal expansion of Portland cement paste, mortar and concrete at high temperatures. *Fire and Materials,* Vol. 4, No. 2, pp. 66- 70.

28. Dimond Industries (1997) *Manual No. 7 Hibond Design Manual*, Dimond Industries. New Zealand.

29. EC2 (1995). Eurocode 2: Design of concrete structures. ENV 1992: Part1-2: General rules- Structural fire design, European Committee for Standardization, Brussels.

30. EC3 (1995). Eurocode 3: Design of steel structures. ENV 1993 Part1-2: General rules- Structural fire design, European Committee for Standardization, Brussels.

31. Ehm, C. and Schneider, U. (1985) The high temperature behaviour of concrete under biaxial conditions. *Cement and Concrete Research.* Vol. 15 No. 1 pp. 27-34.

32. Elghazouli, A.Y., Izzuddin, B.A. (2001) Analytical assessment of the structural performance of composite floors subject to compartment fires. *Fire Safety Journal.* Vol. 36 No. 8. pp. 769-793.

33. Feasey, R. and Buchanan A.H. (2002) Post-flashover fires for structural design. *Fire Safety Journal.* Vol. 37. pp. 83-105.

34. FIP (1978) *Report on methods of assessment of the fire resistance of concrete structural members.* Alden Press, Great Britain.

35. FIP (1986) *Design of multi-storey precast concrete structures,* FIP Commission on Prefabrication, Thomas Telford, London.

36. Fleischmann, C. and Buchanan, A. (2002) 'Analytical methods for determining fire resistance of concrete members'. In: *The SFPE Handbook of Fire Protection Engineering, Third Edition.* Ed: P.J. DiNenno. National Fire Protection Association, Massachusetts. pp. 4-239 to 4-256.

37. Forgan Jones Structural Ltd (1996) *Traydec 300 Specification and Design Manual*, Silverdale, New Zealand.

38. Franssen, J.M. (1990) The unloading of building materials submitted to fire. *Fire Safety Journal*, Vol. 16. No. 3 pp. 213-227.

39. Franssen, J.-M., Kodur, V.K.R. and Mason J. (2002a) *User's manual for SAFIR2001 free: A computer program for analysis of structures at elevated temperature conditions.* University of Liege, Department Structures de Genie Civil, Service Ponts et Charpentes, Belgium.

40. Franssen, J.-M., Kodur, V.K.R. and Mason J. (2002b) *Elements of theory for SAFIR2001 free: A computer program for analysis of structures at elevated temperature conditions.* University of Liege, Department Structures de Genie Civil, Service Ponts et Charpentes, Belgium.

41. Gillie, M., Usmani, A., Rotter, M. and O'Connor, M. (2001) Modelling of heated composite floor slabs with reference to the Cardington experiments. *Fire Safety Journal* Vol. 36. No. 8 pp 745-767.

42. Gillie, M., Usmani, A. and Rotter, M. (2002) Bending and membrane action in concrete slabs. *Proc. Second Structures in Fire Workshop*. Ed: P. J. Moss. (Christchurch, New Zealand), March 2002. pp 95-114.

43. Guice, L.K., Slawson, T.R. and Rhomberg, E.J. (1989) Membrane analysis of flat plate slabs. *ACI Structural Journal.* Title no. 86-S10. pp. 83-92.

44. Gustaferro, A. and Martin, L.D. (1989) *Design for Fire Resistance of Precast Prestressed Concrete, Second Edition.* Prestressed Concrete Institute, Illinois, USA.

45. Harmathy, T.Z. (1970) Thermal properties of concrete at elevated temperatures. *ASTM Journal of Materials*, Vol.5. No.1, pp.47-74.

46. Harmathy, T.Z. (1993) *Fire Safety Design & Concrete*, Concrete Design and Construction Series, Longman Group Limited, U.K.

47. Harmathy, T.Z., Allen L.W. (1973) Thermal properties of selected masonry unit concretes. *Journ. Amer. Concr. Inst.*, Vol.70. No.2, pp. 132-142.

48. Hayes B. (1968) Allowing for membrane action in the plastic analysis of rectangular reinforced concrete slabs. *Magazine of Concrete Research.* Vol. 20. No. 65, pp. 205-212.

49. Herlihy, M.D. (1999) Precast Concrete Floor Support and Diaphragm Action, Ph.D. Thesis, University of Canterbury, Chrischurch, New Zealand.

50. Huang, Z., Burgess, I.W. and Plank, R.J. (1999a) Nonlinear analysis of reinforced concrete slabs subjected to fire. *ACI Structural Journal.* Vol. 96 No.1 pp. 127-135.

51. Huang, Z., Burgess, I.W. and Plank, R.J. (1999b) Three-dimensional modelling of two full-scale fire tests on a composite building. *Proceedings of the Institution of Civil Engineers Structures and Buildings.* Vol. 134 pp. 243-255.

52. Huang, Z., Burgess, I.W. and Plank, R.J. (2000a) Effective stiffness modelling of composite concrete slabs in fire. *Engineering Structures.* Vol. 22 pp. 1133-1144.

53. Huang, Z., Burgess, I.W. and Plank, R.J. (2000b) Non-linear modelling of three full-scale structural fire tests. *Proc. of the First International Symposium of Structures in Fire. (Copenhagen, Denmark)* pp. 53-70.

54. Huang, Z., Burgess, I.W. and Plank, R.J. (2001a) Non-linear structural modelling of a fire test subject to high restraint. *Fire Safety Journal.* Vol. 36 No. 8 pp 795-814.

55. Huang, Z., Burgess, I.W., Plank, R.J. and Bailey, C.G. (2001b) Strategies for fire protection of large composite buildings. *Proc. Interflam Conference 2001 (Edinburgh, U.K.)* pp. 395-406.

56. Huang, Z., Burgess, I., Plank, R. and Bailey, C. (2002) Comparison of BRE simple design method for composite floor slabs in fire with non-linear FE modelling. *Proc. Second Structures in Fire Workshop*. Ed: P. J. Moss. (New Zealand), March. pp. 83-94.

57. Iding, R.J., Bresler, B. and Nizamuddin, Z. (1977) FIRES-T3, A computer program for the fire response of structures-thermal. Report No. UCB FRG77-15. Department of Civil Engineering, University of California, Berkeley, USA.

58. Institution of Structural Engineers (1975) *Fire Resistance of Concrete Structures.* Report of a Joint Committee of the Institution of Structural Engineers and the Concrete Society, London.

59. Institution of Structural Engineers and The Concrete Society (1975) *Fire resistance of concrete structures.* The Institution of Structural Engineers. London, U.K.

60. ISO (1975) *Fire resistance tests - elements of building construction.* ISO 834-1975. International Organization for Standardization.

61. Issen, L.A., Gustaferro, A.H. and Carlson, C.C. (1970) Fire tests of concrete members; An improved method for estimating thermal restraint forces. *Fire Test Performance, ASTM, STP 464,* American Society for Testing and Materials, pp. 153-185.

62. Jiang, S.C. (2001) Theoretical and experimental research on fire resistance of steel-concrete composite floor system. Ph.D. Thesis. Tonji University, Shanghai, China.

63. Jeanes, D.C. (1985) 'Computer modelling the fire endurance of floor systems in steel framed buildings'. In: *Fire Safety: Science and Engineering.* Ed: T.Z. Harmathy. ASTM Committee E-5 and SFPE. Denver, USA.

64. Jeanes, D.C. (1986) 'Developing design concepts for structural fire endurance using computer models'. In: *Design of Structures against Fire.* Eds: R.D. Anchor, H.L. Malhotra, and J.A. Purkiss. Elsevier Applied Science Publishers, U.K.

65. Khennane, A. and Baker, G. (1992a) Plasticity models for the biaxial behaviour of concrete at elevated temperatures, Part I: Failure criterion. *Computer Methods in Applied Mechanics and Engineering*, Vol. 100 No. 2, pp. 207-223.

66. Khennane, A. and Baker, G. (1992b) Plasticity models for the biaxial behaviour of concrete at elevated temperatures, Part II: Implementation and simulation tests. *Computer Methods in Applied Mechanics and Engineering*, Vol. 100 No. 2, pp. 225-248.

67. Khoury, G.A., Grainger, B.N. and Sullivan, P.J.E, (1985a) Transient thermal strain of concrete: Literature review, conditions within specimen and behaviour of individual constituents, *Magazine of Concrete Research*, Vol.37. No. 132, pp.131-144.

68. Khoury, G.A., Grainger, B.N. and Sullivan, P.J.E, (1985b) Strain of concrete during first heating to 600°C under load, *Magazine of Concrete Research*, Vol.37. No, 133, pp.195-215.

69. Khoury, G.A., Grainger, B.N. and Sullivan, P.J.E, (1986) Strain of concrete during first cooling from 600°C under load, *Magazine of Concrete Research*, Vol.38. No. 134, pp. 3 -12.

70. Kirby, B.R. and Preston, R.R. (1988) High temperature properties of hot-rolled structural steels for use in fire engineering design studies. *Fire Safety Journal*, Vol. 13, pp. 27-37.

71. Lamont, S., Usmani, A.S. and Drysdale, D.D. (2001) Fire protection of steel beams in composite framed structures. *Proc. Interflam Conference 2001 (Edinburgh, U.K.)* pp. 407-418.

72. Lim, L. and Wade, C. (2002) Experimental fire tests of two-way concrete slabs. Fire Engineering Research Report 02/12. University of Canterbury and BRANZ Ltd, New Zealand.

73. Lin, T.D. and Abrams, M.S. (1983) 'Simulation of realistic thermal restraint during fire tests of floors and roofs'. In: *Fire Safety of Concrete Structures*. Ed: M.S. Abrams. Publication SP-80. American Concrete Institute, Detroit.

74. Malhotra, H.L. (1984) Spalling of concrete in fires, *Technical Note No.118*, Construction Industrial Research and Information Association (CIRIA)

75. Mindess, S. and Young, J.F. (1981) *Concrete.* Prentice-Hall Inc., New Jersey. U.S.A.

76. Moss, P.J. and Clifton, G.C. (2002) Modelling of the Cardington LBTF steel frame building fire tests. *Proc. Second Structures in Fire Workshop*. Ed: P. J. Moss. (Christchurch, New Zealand), March. pp 193-209.

77. Newman, G.M., Robinson, J.T. and Bailey, C.G. (2000) *Fire Safe Design: A New Approach to Multi-Story Steel-Framed Buildings.* The Steel Construction Institute, Berkshire, U.K.

78. NZCS-NZNSEE (1999) *Guidelines for the use of structural precast concrete in buildings, Second Edition.* Centre for Advanced Engineering, University of Canterbury, Christchurch, New Zealand.

79. O'Callaghan, D.J. and O'Connor, M.A. (2000) Comparison of finite element models of composite steel framed buildings behaviour in fire. *Proc. of the First International Symposium of Structures in Fire. (Copenhagen, Denmark)* pp. 41-52.

80. Park, R. (1964a) Ultimate strength of rectangular concrete slabs under short term uniform loading with edges restrained against lateral movement. *Proc. Inst. Civ. Eng.*, Vol. 28. pp. 125-150.

81. Park, R. (1964b) The ultimate strength and long term behaviour of uniformly loaded two-way concrete slabs with partial lateral restraint at all edges. *Magazine of Concrete Research.*, Vol. 16, No. 48. pp. 139-152.

82. Park, R. (1964c) Tensile membrane behaviour of uniformly loaded rectangular reinforced concrete slabs with fully restrained edges. *Magazine of Concrete Research.* Vol. 16. No. 46, pp. 39-44.

83. Park, R. and Gamble, W. (2000) *Reinforced Concrete Slabs.* John Wiley and Sons, Inc.

84. Purkiss, J.A. (1996) *Fire Safety Engineering Design of Structures.* Butterworth-Heinemann, Oxford. U.K.

85. Routley, G.J., Jennings, C. AND Chubb, M. (1991) High-rise Office Building Fire, One Meridian Plaza, Philadelphia, Pennsylvannia, Report 049. Federal Emergency Management Agency, National Fire Data Centre, Maryland, U.S.A.

86. Sanad, A.M., Rotter, J.M., Usmani, A.S. and O'Connor, M.A. (1999) Finite Element Modelling of Fire Tests on the Cardington Composite Building. *Proc of Interflam '99 International Fire Science and Engineering Conference.* (Edinburgh, Scotland) 29 June-1 July. pp. 1045-1056.

87. Sawczuk, A., Winnicki L. (1965) Plastic behaviour of simply supported reinforced concrete plates at moderately large deflections. *International Journal of Solids and Structures.* Vol. 1. pp. 97-111

88. Schneider, U. (1985), Behaviour of Concrete at High Temperatures, RILEM Committee 44- PHT.

89. Selvaggio, S.L. and Carlson, C.C. (1963) Effect of restraint on fire resistance of prestressed concrete, American Society for Testing and Materials, STP 344, pp. 1-25. Reprinted as PCA Research Department Bulletin 164.

90. Speedfloor Holdings Ltd. *Speedfloor Design Manual.* Auckland. New Zealand.

91. Standards Australia (1997) AS1530 Methods of fire tests on building materials, components and structures. Part 4: Fire resistance tests of elements of building construction. Standards Australia, New South Wales.

92. SNZ (1995) NZS 3101: Part1: 1995. *The Design of Concrete Structures*, Standards New Zealand, Wellington.

93. Sullivan, P.J.E., Terro, M.J. and Morris, W.A. (1994) Critical review of fire-dedicated thermal and structural computer programs. *Journal of Applied Fire Science.* Vol. 3 No. 2, pp. 113-135.

94. Taylor, R. (1965) A note on a possible basis for a new method of ultimate load design of reinforced concrete slabs. *Magazine of Concrete Research.* Vol. 17, No. 53. pp 183-186.

95. Talamona, D., Franssen, J.M. (2000) New quadrangular shell element in Safir. *Proc. of the First International Symposium of Structures in Fire. (Copenhagen, Denmark)* pp. 195-210.

96. Terro, M.J. (1998) Numerical modelling of the behavior of concrete structures. *ACI Structural Journal.* Vol. 95 No. 2. pp. 183-193.

97. UL (1988). *Fire Resistance Directory*, Underwriters Laboratories Inc., USA.

98. Vecchio, F.J. and Collins, M.P. (1990a) Investigating the collapse of a warehouse. *Concrete International.* Vol. 12. No. 3. pp. 72-78.

99. Vecchio, F.J. and Tang, K. (1990b) Membrane action in reinforced concrete slabs. *Canadian Journal of Civil Engineering*. Vol. 17. pp. 686-697.

100. Wang, Y.C. (1994) Predicting the Behaviour of Reinforced Concrete Slabs at Elevated Temperatures Using Finite Shell Element Analysis. *Proc. of the Fourth International Symposium of Fire Safety Science (Ottawa, Canada).* pp. 1077-1088.

101. Wade, C.A. (1992) Fire Resistance of New Zealand Concretes- Part 2, Building Research Association of New Zealand, BRANZ Study Report SR 40. Judgeford.

102. Wickström, U. (1979) TASEF-2 A Computer Program for the Temperature Analysis of Structures Exposed to Fire, Lund Institute of Technology, Sweden.

103. Wickström, U. (1986) A very simple method for estimating temperatures in fire exposed structures, In: *New Technology to Reduce Fire Losses and Costs*, Elsevier Applied Science, London, pp. 186-194.

104. Wood, R.H. (1961) *Plastic and elastic design of slabs and plates, with particular reference to reinforced concrete slabs*. Thames and Hudson. London.

105. Woodson, S. and Krauthammer, T. (1999) 'Design for severe dynamic loads'. In: *The design of two-way slabs, SP-183*. Ed: T.C. Schaeffer, American Concrete Institute. USA. pp. 17-35.

APPENDIX

Typical input file for thermal analysis

```
100mm concrete section exposed to the ISO fire from below

    NPTTOT       782
     NNODE   42
      NDIM    2
 NDIMMATER    1
   NDDLMAX    1
      FROM    1   TO    42 STEP     1 NDDL     1
  END_NDDL
  TEMPERAT
      TETA       0.9
  TINITIAL      20.0
  MAKE.TSH
 LARGEUR11    190000
 LARGEUR12       100
   NORENUM
slab100.tsh
      NMAT    1
  ELEMENTS
     SOLID   20
        NG    2
     NVOID    0
  END_ELEM
     NODES
      NODE    1      -0.05     -0.025
     GNODE   21       0.05     -0.025
      NODE   22      -0.05      0.025
     GNODE   42       0.05      0.025
 FIXATIONS
   END_FIX
NODOFSOLID
      ELEM    1    1   22   23    2    1    0
     GELEM   20   20   41   42   22    1    0    1
  FRONTIER
         F    1      FISO        NO        NO        NO
         F   20        NO        NO       F20        NO
 END_FRONT
  SYMMETRY
   END_SYM
 PRECISION     1.E-3
 MATERIALS
SILCONCEC2
92      25         9       0.5
      TIME
                  1.        15.
                 15.      1800.
                 30.     14400.
   ENDTIME
IMPRESSION
 TIMEPRINT       60.
```

Typical input file for 2D structural analysis with beam elements

```
Pin supported slab slab
Line of thrust=-50mm from yo, R=0.5, 200mm doubly reinforced
100 percent axial spring

    NPTTOT       5000
     NNODE    50
      NDIM     2
 NDIMMATER     1
   NDDLMAX     3
      FROM     1   TO    49 STEP     2 NDDL     3
      FROM     2   TO    48 STEP     2 NDDL     1
      FROM    50   TO    50 STEP     1 NDDL     3

    STATIC
     NLOAD     1
   OBLIQUE     0
  COMEBACK       0.01
 ARCLENGTH      0.002
 LARGEUR11        514
 LARGEUR12         50
   NORENUM
      NMAT     4
  ELEMENTS
      BEAM    24     2
        NG     2
    NFIBER   220
     TRUSS     1     1

     NODES
      NODE     1    0.00000  -0.05000
      NODE     5    0.00000   0.00000     1
      NODE    45    5.00000   0.00000     1
      NODE    49    5.00000  -0.05000     1
      NODE    50    6.00000  -0.05000
 FIXATIONS
     BLOCK     1              F0         F0
     BLOCK    49                         F0
     BLOCK    50              F0         F0         F0

 NODOFBEAM
ipe600-nf.tem
 TRANSLATE     1     1

slab200_125x2-12.tem
 TRANSLATE     1     2
 TRANSLATE     2     3

    1     1     2     3     1
    2     3     4     5     1     2
    3     5     6     7     2
   22    43    44    45     2     2
   23    45    46    47     1
   24    47    48    49     1     2
NODOFTRUSS
                          0.001          0     4
    1    49    50     1
 PRECISION      1.e-5
```

```
     LOADS
  FUNCTION      FLOAD
 DISTRBEAM          3          0.       -863
 DISTRBEAM         22          0.       -863     1

 MATERIALS
  STEELEC3
    2120e9         .3    800.E+6
SILCONCEC2
    20.E+9         .2     30.E+6                                          -1
  STEELEC2
   210.E+9         .3    430.E+6
   ELASTIC
  9.73E+10         .3
      TIME
                  30.      1800.
                  30.     14400.
   ENDTIME
LARGEDISPL
     EPSTH
IMPRESSION
 TIMEPRINT        60.
PRINTREACT
   PRINTMN
```

Typical input file for 3D structural analysis with shell elements

```
IN file for the 3m x 4m slab subjected to the ISO fire
144 elements modelled for a quarter of the slab
D147 reinforcing mesh

    NPTTOT   6912
     NNODE  169
      NDIM    3
 NDIMMATER    2
   NDDLMAX    6
EVERY_NODE    6
  END_NDDL
    STATIC
     NLOAD    1
   OBLIQUE    0
  COMEBACK 0.001
NARCLENGTH
 LARGEUR11 67268
 LARGEUR12   126
 READRENUM
      NMAT    3
  ELEMENTS
     SHELL  144   1
   NGTHICK   10
    NGAREA    2
   NREBARS    2
  END_ELEM
     NODES
      NODE    1  -2.08  -1.58  0
     GNODE   13    0.0  -1.58  0   1
    REPEAT   13    0.0 0.13167 0  12
 FIXATIONS
 BLOCK   1  NO  NO  F0  F0  F0  NO
 BLOCK   2  NO  NO  F0  NO  F0  NO
 BLOCK   3  NO  NO  F0  NO  F0  NO
 BLOCK   4  NO  NO  F0  NO  F0  NO
 BLOCK   5  NO  NO  F0  NO  F0  NO
 BLOCK   6  NO  NO  F0  NO  F0  NO
 BLOCK   7  NO  NO  F0  NO  F0  NO
 BLOCK   8  NO  NO  F0  NO  F0  NO
 BLOCK   9  NO  NO  F0  NO  F0  NO
 BLOCK  10  NO  NO  F0  NO  F0  NO
 BLOCK  11  NO  NO  F0  NO  F0  NO
 BLOCK  12  NO  NO  F0  NO  F0  NO
 BLOCK  13  F0  NO  F0  NO  F0  F0
 BLOCK  14  NO  NO  F0  F0  NO  NO
 BLOCK  26  F0  NO  NO  NO  F0  F0
 BLOCK  27  NO  NO  F0  F0  NO  NO
 BLOCK  39  F0  NO  NO  NO  F0  F0
 BLOCK  40  NO  NO  F0  F0  NO  NO
 BLOCK  52  F0  NO  NO  NO  F0  F0
 BLOCK  53  NO  NO  F0  F0  NO  NO
 BLOCK  65  F0  NO  NO  NO  F0  F0
 BLOCK  66  NO  NO  F0  F0  NO  NO
 BLOCK  78  F0  NO  NO  NO  F0  F0
 BLOCK  79  NO  NO  F0  F0  NO  NO
 BLOCK  91  F0  NO  NO  NO  F0  F0
 BLOCK  92  NO  NO  F0  F0  NO  NO
```

```
 BLOCK 104   F0   NO   NO   NO   F0   F0
 BLOCK 105   NO   NO   F0   F0   NO   NO
 BLOCK 117   F0   NO   NO   NO   F0   F0
 BLOCK 118   NO   NO   F0   F0   NO   NO
 BLOCK 130   F0   NO   NO   NO   F0   F0
 BLOCK 131   NO   NO   F0   F0   NO   NO
 BLOCK 143   F0   NO   NO   NO   F0   F0
 BLOCK 144   NO   NO   F0   F0   NO   NO
 BLOCK 156   F0   NO   NO   NO   F0   F0
 BLOCK 157   NO   F0   F0   F0   NO   F0
 BLOCK 158   NO   F0   NO   F0   NO   F0
 BLOCK 159   NO   F0   NO   F0   NO   F0
 BLOCK 160   NO   F0   NO   F0   NO   F0
 BLOCK 161   NO   F0   NO   F0   NO   F0
 BLOCK 162   NO   F0   NO   F0   NO   F0
 BLOCK 163   NO   F0   NO   F0   NO   F0
 BLOCK 164   NO   F0   NO   F0   NO   F0
 BLOCK 165   NO   F0   NO   F0   NO   F0
 BLOCK 166   NO   F0   NO   F0   NO   F0
 BLOCK 167   NO   F0   NO   F0   NO   F0
 BLOCK 168   NO   F0   NO   F0   NO   F0
 BLOCK 169   F0   F0   NO   F0   F0   F0
   END_FIX
NODOFSHELL
slab100_198.tsh
 TRANSLATE    1    1
 TRANSLATE    2    2
 END_TRANS
      ELEM    1    1    2   15   14    1
     GELEM   12   12   13   26   25    1   1
    REPEAT   12   13                      11
 PRECISION     10e-3
     LOADS
  FUNCTION FLOAD
 DISTRSH       1    0.    0.   -5400.
GDISTRSH     144    0.    0.   -5400.    1
  END_LOAD
 MATERIALS
 SILCONC2D
       0.2     36.6E6     1.5e6     1
  STEELEC2
 210000.E6        0.3    565.E6
SILCONCEC2
       0.2     30.0E6     0.0e6    1
      TIME
              .025   5.00
              1.    20.00
              4.    32.00
              8.   1200.0
              8.   3600.0
              8.  14400.0
  END_TIME
LARGEDISPL
     EPSTH
IMPRESSION
 TIMEPRINT   64.0
PRNNXSHELL
```

FIRE ENGINEERING RESEARCH REPORTS

95/1	Full Residential Scale Backdraft	I B Bolliger
95/2	A Study of Full Scale Room Fire Experiments	P A Enright
95/3	Design of Load-bearing Light Steel Frame Walls for Fire Resistance	J T Gerlich
95/4	Full Scale Limited Ventilation Fire Experiments	D J Millar
95/5	An Analysis of Domestic Sprinkler Systems for Use in New Zealand	F Rahmanian
96/1	The Influence of Non-Uniform Electric Fields on Combustion Processes	M A Belsham
96/2	Mixing in Fire Induced Doorway Flows	J M Clements
96/3	Fire Design of Single Storey Industrial Buildings	B W Cosgrove
96/4	Modelling Smoke Flow Using Computational Fluid Dynamics	T N Kardos
96/5	Under-Ventilated Compartment Fires - A Precursor to Smoke Explosions	A R Parkes
96/6	An Investigation of the Effects of Sprinklers on Compartment Fires	M W Radford
97/1	Sprinkler Trade Off Clauses in the Approved Documents	G J Barnes
97/2	Risk Ranking of Buildings for Life Safety	J W Boyes
97/3	Improving the Waking Effectiveness of Fire Alarms in Residential Areas	T Grace
97/4	Study of Evacuation Movement through Different Building Components	P Holmberg
97/5	Domestic Fire Hazard in New Zealand	KDJ Irwin
97/6	An Appraisal of Existing Room-Corner Fire Models	D C Robertson
97/7	Fire Resistance of Light Timber Framed Walls and Floors	G C Thomas
97/8	Uncertainty Analysis of Zone Fire Models	A M Walker
97/9	New Zealand Building Regulations Five Years Later	T M Pastore
98/1	The Impact of Post-Earthquake Fire on the Built Urban Environment	R Botting
98/2	Full Scale Testing of Fire Suppression Agents on Unshielded Fires	M J Dunn
98/3	Full Scale Testing of Fire Suppression Agents on Shielded Fires	N Gravestock
98/4	Predicting Ignition Time Under Transient Heat Flux Using Results from Constant Flux Experiments	A Henderson
98/5	Comparison Studies of Zone and CFD Fire Simulations	A Lovatt
98/6	Bench Scale Testing of Light Timber Frame Walls	P Olsson
98/7	Exploratory Salt Water Experiments of Balcony Spill Plume Using Laser Induced Fluorescence Technique	E Y Yii
99/1	Fire Safety and Security in Schools	R A Carter
99/2	A Review of the Building Separation Requirements of the New Zealand Building Code Acceptable Solutions	J M Clarke
99/3	Effect of Safety Factors in Timed Human Egress Simulations	K M Crawford

99/4	Fire Response of HVAC Systems in Multistorey Buildings: An Examination of the NZBC Acceptable Solutions	M Dixon
99/5	The Effectiveness of the Domestic Smoke Alarm Signal	C Duncan
99/6	Post-flashover Design Fires	R Feasey
99/7	An Analysis of Furniture Heat Release Rates by the Nordtest	J Firestone
99/8	Design for Escape from Fire	I J Garrett
99/9	Class A Foam Water Sprinkler Systems	D B Hipkins
99/10	Review of the New Zealand Standard for Concrete Structures (NZS 3101) for High Strength and Lightweight Concrete Exposed to Fire	M J Inwood
99/12	An Analytical Model for Vertical Flame Spread on Solids: An Initial Investigation	G A North
99/13	Should Bedroom Doors be Open or Closed While People are Sleeping? - A Probabilistic Risk Assessment	D L Palmer
99/14	Peoples Awareness of Fire	S J Rusbridge
99/15	Smoke Explosions	B J Sutherland
99/16	Reliability of Structural Fire Design	JKS Wong
99/17	Heat Release from New Zealand Upholstered Furniture	T Enright
00/1	Fire Spread on Exterior Walls	FNP Bong
00/2	Fire Resistance of Lightweight Framed Construction	PCR Collier
00/3	Fire Fighting Water: A Review of Fire Fighting Water Requirements (A New Zealand Perspective)	S Davis
00/4	The Combustion Behaviour of Upholstered Furniture Materials in New Zealand	H Denize
00/5	Full-Scale Compartment Fire Experiments on Upholstered Furniture	N Girgis
00/6	Fire Rated Seismic Joints	M James
00/7	Fire Design of Steel Members	K R Lewis
00/8	Stability of Precast Concrete Tilt Panels in Fire	L Lim
00/9	Heat Transfer Program for the Design of Structures Exposed to Fire	J Mason
00/10	An Analysis of Pre-Flashover Fire Experiments with Field Modelling Comparisons	C Nielsen
00/11	Fire Engineering Design Problems at Building Consent Stage	P Teo
00/12	A Comparison of Data Reduction Techniques for Zone Model Validation	S Weaver
00/13	Effect of Surface Area and Thickness on Fire Loads	H W Yii
00/14	Home Fire Safety Strategies	P Byrne
00/15	Accounting for Sprinkler Effectiveness in Performance Based Design of Steel Buildings in Fire	M Feeney
00/16	A Guideline for the Fire Design of Shopping Centres	J M McMillan
01/1	Flammability of Upholstered Furniture Using the Cone Calorimeter	A Coles
01/2	Radiant Ignition of New Zealand Upholstered Furniture Composites	F Chen

01/3	Statistical Analysis of Hospitality Industry Fire Experience	T Y A Chen
01/4	Performance of Gypsum Plasterboard Assemblies Exposed to Real Building Fires	B H Jones
01/5	Ignition Properties of New Zealand Timber	C K Ngu
01/6	Effect of Support Conditions on Steel Beams Exposed of Fire	J Seputro
01/7	Validation of an Evacuation Model Currently Under Development	A Teo
01/8	2-D Analysis of Composite Steel - Concrete Beams in Fire	R Welsh
01/9	Contribution of Upholstered Furniture to Residential Fire Fatalities in New Zealand	C R Wong
01/10	The Fire Safety Design of Apartment Buildings	S Wu
01/11	Smoke Alarm Ownership in Relation to Socio-Economic Factors in Christchurch	N Buchanan
01/12	Accounting for Sprinkler Effectiveness in Performance Based Design of Steel Buildings for Fire	M Feeney
01/13	Equivalent Fire Resistance Ratings of Construction Elements Exposed to Realistic Fires	J Nyman
02/1	Performance of Expanded Polystyrene Insulated Panel Exposed to Radiant Heat	G Baker
02/2	A Comparison Between Predicted and Actual Behaviour of Domestic Smoke Detectors in a Realistic House Fire	D Brammer
02/3	Development of Bench-Scale Testing of Sprinkler and Smoke Detector Activation/Response Time	K S Chin
02/4	The Effect of Door Angle on Fire Induced Flow Through a Doorway	L R Clark
02/5	Implementation of a Glass Fracture Module for the BRANZ Fire Compartment Fire Zone Modelling Software	R Parry
02/6	Assessing the Feasibility of Reducing the Grid Resolution in FDS Field Modelling	N Patterson
02/7	Fire Safety Design of Ferrymead Heritage Park	M Rangi
02/8	Experimental Results for Pre-Flashover Fire Experiments in Two Adjacent ISO Compartments	L Rutherford
02/9	Measurement of Magnitude and Direction of Hot Gas Flow in a Fire Compartment with a Five-hole Probe	J Schulz
02/10	Assessment of the Current False Alarm Situation from Fire Detection Systems in New Zealand and the Development of an Expert System for Their Identifications	Y F Tu
02/11	Performance of Unprotected Steel and Composite Steel Frames Exposed to Fire	C Wastney
02/12	Experimental Fire Tests of Two-Way Concrete Slabs	L Lim
03/1	Modelling the Effects of Fuel Types and Ventilation on Post-Flashover Compartment Fires	Ee H Yii
03/2	Membrane Action in Fire Exposed Concrete Floor Systems	L Lim

School of Engineering
University of Canterbury
Private Bag 4800, Christchurch, New Zealand

Phone 643 364-2250
Fax 643 364-2758